

***IN SITU* AND LABORATORY STUDIES OF POTASH DEFORMATION**

With Reference to Saskatchewan Potash

by

**Rui Chen**

A Thesis Presented to the Faculty of Graduate Studies  
in Partial Fulfillment of the Requirements for the Degree of

**Doctor of Philosophy**

Department of Civil Engineering  
the University of Manitoba  
Winnipeg, Manitoba

February, 1993



National Library  
of Canada

Acquisitions and  
Bibliographic Services Branch

395 Wellington Street  
Ottawa, Ontario  
K1A 0N4

Bibliothèque nationale  
du Canada

Direction des acquisitions et  
des services bibliographiques

395, rue Wellington  
Ottawa (Ontario)  
K1A 0N4

*Your file* *Votre référence*

*Our file* *Notre référence*

The author has granted an irrevocable non-exclusive licence allowing the National Library of Canada to reproduce, loan, distribute or sell copies of his/her thesis by any means and in any form or format, making this thesis available to interested persons.

L'auteur a accordé une licence irrévocable et non exclusive permettant à la Bibliothèque nationale du Canada de reproduire, prêter, distribuer ou vendre des copies de sa thèse de quelque manière et sous quelque forme que ce soit pour mettre des exemplaires de cette thèse à la disposition des personnes intéressées.

The author retains ownership of the copyright in his/her thesis. Neither the thesis nor substantial extracts from it may be printed or otherwise reproduced without his/her permission.

L'auteur conserve la propriété du droit d'auteur qui protège sa thèse. Ni la thèse ni des extraits substantiels de celle-ci ne doivent être imprimés ou autrement reproduits sans son autorisation.

ISBN 0-315-81742-9

Canada

Name \_\_\_\_\_

*Dissertation Abstracts International* is arranged by broad, general subject categories. Please select the one subject which most nearly describes the content of your dissertation. Enter the corresponding four-digit code in the spaces provided.

CIVIL ENGINEERING

SUBJECT TERM

0543 UMI

SUBJECT CODE

**Subject Categories**

**THE HUMANITIES AND SOCIAL SCIENCES**

**COMMUNICATIONS AND THE ARTS**

Architecture .....0729  
 Art History .....0377  
 Cinema .....0900  
 Dance .....0378  
 Fine Arts .....0357  
 Information Science .....0723  
 Journalism .....0391  
 Library Science .....0399  
 Mass Communications .....0708  
 Music .....0413  
 Speech Communication .....0459  
 Theater .....0465

**EDUCATION**

General .....0515  
 Administration .....0514  
 Adult and Continuing .....0516  
 Agricultural .....0517  
 Art .....0273  
 Bilingual and Multicultural .....0282  
 Business .....0688  
 Community College .....0275  
 Curriculum and Instruction .....0727  
 Early Childhood .....0518  
 Elementary .....0524  
 Finance .....0277  
 Guidance and Counseling .....0519  
 Health .....0680  
 Higher .....0745  
 History of .....0520  
 Home Economics .....0278  
 Industrial .....0521  
 Language and Literature .....0279  
 Mathematics .....0280  
 Music .....0522  
 Philosophy of .....0998  
 Physical .....0523

Psychology .....0525  
 Reading .....0535  
 Religious .....0527  
 Sciences .....0714  
 Secondary .....0533  
 Social Sciences .....0534  
 Sociology of .....0340  
 Special .....0529  
 Teacher Training .....0530  
 Technology .....0710  
 Tests and Measurements .....0288  
 Vocational .....0747

**LANGUAGE, LITERATURE AND LINGUISTICS**

Language  
 General .....0679  
 Ancient .....0289  
 Linguistics .....0290  
 Modern .....0291  
 Literature  
 General .....0401  
 Classical .....0294  
 Comparative .....0295  
 Medieval .....0297  
 Modern .....0298  
 African .....0316  
 American .....0591  
 Asian .....0305  
 Canadian (English) .....0352  
 Canadian (French) .....0355  
 English .....0593  
 Germanic .....0311  
 Latin American .....0312  
 Middle Eastern .....0315  
 Romance .....0313  
 Slavic and East European .....0314

**PHILOSOPHY, RELIGION AND THEOLOGY**

Philosophy .....0422  
 Religion  
 General .....0318  
 Biblical Studies .....0321  
 Clergy .....0319  
 History of .....0320  
 Philosophy of .....0322  
 Theology .....0469

**SOCIAL SCIENCES**

American Studies .....0323  
 Anthropology  
 Archaeology .....0324  
 Cultural .....0326  
 Physical .....0327  
 Business Administration  
 General .....0310  
 Accounting .....0272  
 Banking .....0770  
 Management .....0454  
 Marketing .....0338  
 Canadian Studies .....0385  
 Economics  
 General .....0501  
 Agricultural .....0503  
 Commerce-Business .....0505  
 Finance .....0508  
 History .....0509  
 Labor .....0510  
 Theory .....0511  
 Folklore .....0358  
 Geography .....0366  
 Gerontology .....0351  
 History  
 General .....0578

Ancient .....0579  
 Medieval .....0581  
 Modern .....0582  
 Black .....0328  
 African .....0331  
 Asia, Australia and Oceania .....0332  
 Canadian .....0334  
 European .....0335  
 Latin American .....0336  
 Middle Eastern .....0333  
 United States .....0337  
 History of Science .....0585  
 Law .....0398  
 Political Science  
 General .....0615  
 International Law and Relations .....0616  
 Public Administration .....0617  
 Recreation .....0814  
 Social Work .....0452  
 Sociology  
 General .....0626  
 Criminology and Penology .....0627  
 Demography .....0938  
 Ethnic and Racial Studies .....0631  
 Individual and Family Studies .....0628  
 Industrial and Labor Relations .....0629  
 Public and Social Welfare .....0630  
 Social Structure and Development .....0700  
 Theory and Methods .....0344  
 Transportation .....0709  
 Urban and Regional Planning .....0999  
 Women's Studies .....0453

**THE SCIENCES AND ENGINEERING**

**BIOLOGICAL SCIENCES**

Agriculture  
 General .....0473  
 Agronomy .....0285  
 Animal Culture and Nutrition .....0475  
 Animal Pathology .....0476  
 Food Science and Technology .....0359  
 Forestry and Wildlife .....0478  
 Plant Culture .....0479  
 Plant Pathology .....0480  
 Plant Physiology .....0817  
 Range Management .....0777  
 Wood Technology .....0746  
 Biology  
 General .....0306  
 Anatomy .....0287  
 Biostatistics .....0308  
 Botany .....0309  
 Cell .....0379  
 Ecology .....0329  
 Entomology .....0353  
 Genetics .....0369  
 Limnology .....0793  
 Microbiology .....0410  
 Molecular .....0307  
 Neuroscience .....0317  
 Oceanography .....0416  
 Physiology .....0433  
 Radiation .....0821  
 Veterinary Science .....0778  
 Zoology .....0472  
 Biophysics  
 General .....0786  
 Medical .....0760

Geodesy .....0370  
 Geology .....0372  
 Geophysics .....0373  
 Hydrology .....0388  
 Mineralogy .....0411  
 Paleobotany .....0345  
 Paleocology .....0426  
 Paleontology .....0418  
 Paleozoology .....0985  
 Palynology .....0427  
 Physical Geography .....0368  
 Physical Oceanography .....0415

**HEALTH AND ENVIRONMENTAL SCIENCES**

Environmental Sciences .....0768  
 Health Sciences  
 General .....0566  
 Audiology .....0300  
 Chemotherapy .....0992  
 Dentistry .....0567  
 Education .....0350  
 Hospital Management .....0769  
 Human Development .....0758  
 Immunology .....0982  
 Medicine and Surgery .....0564  
 Mental Health .....0347  
 Nursing .....0569  
 Nutrition .....0570  
 Obstetrics and Gynecology .....0380  
 Occupational Health and Therapy .....0354  
 Ophthalmology .....0381  
 Pathology .....0571  
 Pharmacology .....0419  
 Pharmacy .....0572  
 Physical Therapy .....0382  
 Public Health .....0573  
 Radiology .....0574  
 Recreation .....0575

Speech Pathology .....0460  
 Toxicology .....0383  
 Home Economics .....0386

**PHYSICAL SCIENCES**

**Pure Sciences**  
 Chemistry  
 General .....0485  
 Agricultural .....0749  
 Analytical .....0486  
 Biochemistry .....0487  
 Inorganic .....0488  
 Nuclear .....0738  
 Organic .....0490  
 Pharmaceutical .....0491  
 Physical .....0494  
 Polymer .....0495  
 Radiation .....0754  
 Mathematics .....0405  
 Physics  
 General .....0605  
 Acoustics .....0986  
 Astronomy and Astrophysics .....0606  
 Atmospheric Science .....0608  
 Atomic .....0748  
 Electronics and Electricity .....0607  
 Elementary Particles and High Energy .....0798  
 Fluid and Plasma .....0759  
 Molecular .....0609  
 Nuclear .....0610  
 Optics .....0752  
 Radiation .....0756  
 Solid State .....0611  
 Statistics .....0463

**Applied Sciences**

Applied Mechanics .....0346  
 Computer Science .....0984

Engineering  
 General .....0537  
 Aerospace .....0538  
 Agricultural .....0539  
 Automotive .....0540  
 Biomedical .....0541  
 Chemical .....0542  
 Civil .....0543  
 Electronics and Electrical .....0544  
 Heat and Thermodynamics .....0348  
 Hydraulic .....0545  
 Industrial .....0546  
 Marine .....0547  
 Materials Science .....0794  
 Mechanical .....0548  
 Metallurgy .....0743  
 Mining .....0551  
 Nuclear .....0552  
 Packaging .....0549  
 Petroleum .....0765  
 Sanitary and Municipal .....0554  
 System Science .....0790  
 Geotechnology .....0428  
 Operations Research .....0796  
 Plastics Technology .....0795  
 Textile Technology .....0994

**PSYCHOLOGY**

General .....0621  
 Behavioral .....0384  
 Clinical .....0622  
 Developmental .....0620  
 Experimental .....0623  
 Industrial .....0624  
 Personality .....0625  
 Physiological .....0989  
 Psychobiology .....0349  
 Psychometrics .....0632  
 Social .....0451



**IN SITU AND LABORATORY STUDIES OF POTASH DEFORMATION  
WITH REFERENCE TO SASKATCHEWAN POTASH**

**BY**

**RUI CHEN**

**A Thesis submitted to the Faculty of Graduate Studies of the University of Manitoba in partial fulfillment of the requirements for the degree of**

**DOCTOR OF PHILOSOPHY**

**© 1993**

**Permission has been granted to the LIBRARY OF THE UNIVERSITY OF MANITOBA to lend or sell copies of this thesis, to the NATIONAL LIBRARY OF CANADA to microfilm this thesis and to lend or sell copies of the film, and UNIVERSITY MICROFILMS to publish an abstract of this thesis.**

**The author reserves other publications rights, and neither the thesis nor extensive extracts from it may be printed or otherwise reproduced without the author's permission.**

## ABSTRACT

This thesis attempts to address certain stress-history and time dependent properties of potash in underground mining environment that have been ignored in the existing literature, including relaxation properties, bimodularity (the property of having different Young's moduli and Poisson's ratios in tension and in compression), and progressive deformation in potash yield pillars.

Compared with creep properties, stress relaxation has been overlooked in research on salt rocks. In this thesis, potash relaxation properties were studied by multiple-stage repeated relaxation tests along a reverse loading path. The testing results suggest that potash has no creep limit. A uniaxial constitutive equation was extended to include confining pressure and was fitted into the experimental data.

Besides relaxation, another largely ignored aspect is bimodularity. This property was demonstrated by a new testing technique that measures deformation moduli in tension and in compression on the same specimen and in the same compressive loading frame. Analytical solutions and a finite element program were developed to include bimodular effects. The practical significance of bimodularity was illustrated with regard to the interpretation of indirect rock tensile strength tests and mine roof behavior.

The specific *flow* property of potash is extensively used in yield pillar design for room-and-pillar operations in potash mining. However, the deformational mechanisms within yield pillars are still poorly understood. Yield pillar deformation was investigated in this thesis by *in situ* mapping of yield pillars, rock fabric analyses and finite element simulation. Progressive pillar deformation has been interpreted by a four-stage deformational model that involves bulk rock flattening, the development of shear zones at pillar corners and shear wedges at pillar margins, the detachment of shear wedges into adjacent rooms, and the development of second-generation shear zones.

TO MY PARENTS  
with cheer and with mourning

## ACKNOWLEDGEMENTS

I would like to express my sincere thanks to my advisor, Dr. Brian Stimpson, for his advice and guidance throughout my study and research at UM and for his course in ground support that guided my entry into rock engineering. I would also like to thank Dr. Emery Z. Lajtai for opening up my way towards this degree and a career in Canada, and for years of support and enthusiastic help; Dr. W.C. Brisbin for his criticisms, encouragements, never ending patience, and his guidance on understanding yield pillar deformation; and Dr. De Souza for his time and effort in reviewing this thesis.

My special thanks are due to Dr. M. Laoucet Ayari for his FEM program, SIMEX, and Yanguang Yuan for his endless help. Their inexhaustible wisdom freed me from many predicaments throughout my thesis work, particularly, in numerical modeling.

Many thanks to Dr. Bruce J. Carter and Dr. E.J. Scott Duncan whose help made my experience in complicated laboratory rock testing less painful.

I would like to thank Mr. M. Grajewski for his patient advice and technical assistance during the *in situ* investigations, sample preparation and laboratory testing. I would also like to thank Mr. David Mackintosh, chief engineer at the Cominco Mine, for his cooperation and assistance during underground mapping and sampling.

I also wish to thank Ingrid Trestrail, Tracy Wang, Min Liao, and Fariba Sadaad for their understanding and friendship, which made my stressful study life enjoyable.

The financial support of the University of Manitoba, Duff-Roblin Graduate Fellowship and the research support from NSERC, Cominco Fertilizer's Limited and the Potash Corporation of Saskatchewan are gratefully acknowledged.

Finally, I would like to thank my only sister, Yin Chen, who has always been trying to cheer me up with all her love and care.

## TABLE OF CONTENTS

ABSTRACT	i
DEDICATION	ii
ACKNOWLEDGEMENTS	iii
TABLE OF CONTENTS	iv
LIST OF FIGURES	xi
LIST OF TABLES	xxiii
CHAPTER 1 INTRODUCTION	
1.1 General Background	1
1.2 Statement of the Problem	2
1.3 Thesis Organization	3
CHAPTER 2 LITERATURE SURVEY	
2.1 Introduction	6
2.2 Stress History and Rate Dependent Properties of Salt	7
2.2.1 Experimental investigations	8
2.2.2 Theoretical investigations	10
2.3 Response of Underground Openings to Excavation	13
2.3.1 Single openings	14
2.3.2 Multiple openings and pillar design	16

## CHAPTER 3 POTASH IN SASKATCHEWAN

### - Mechanical Behavior and Mining Methods

3.1	Introduction	22
3.2	Challenges Facing the Potash Industry in Saskatchewan	24
3.3	Mining Methods	26
3.4	Rock Mechanics Related Research in Saskatchewan Potash Mining	32

## CHAPTER 4 CRITIQUE AND OBJECTIVES OF THESIS

4.1	Critique	38
4.2	Research Objectives	40

## CHAPTER 5 VISCOPLASTICITY OF SALT - Experimental Program I

5.1	Introduction	42
5.2	Testing Equipment, Data Acquisition and Sample Preparation	44
5.2.1	Testing equipment	44
5.2.2	Data acquisition	45
5.2.3	Specimen preparation	46
5.3	Reverse Loading Triaxial Tests	47
5.3.1	Test procedure	47
5.3.2	Testing results	48
5.4	Multiple-Stage Repeated Relaxation Test	53
5.4.1	Test procedure	53

5.4.2 Test results	56
5.4.3 Discussion on potash behavior in multiple-stage repeated relaxation tests	62
5.5 Discussion on Stress-Strain Relationship and Material Parameters	68
5.5.1 Constitutive model based on Haupt (1991)	68
5.5.2 Determination of material parameters	70
5.6 Chapter Summary	71
<b>CHAPTER 6 BIMODULARITY OF EVAPORITES - Experimental Program II</b>	
6.1 Introduction	75
6.2 Development of Testing Technique	77
6.2.1 Testing equipment and data acquisition	78
6.2.2 Specimen geometry and preparation	78
6.2.3 Experimental procedure	82
6.3 Experimental Results	91
6.3.1 Results on Cominco halite	91
6.3.2 Results on Cominco potash	95
6.3.3 Results on Lac du Bonnet granite	99
6.3.4 Results on Tyndall limestone	100
6.4 Discussion of Experimental Results	101
6.5 Implications of Bimodular Behavior of Rock	103
6.6 Chapter Summary	107

## CHAPTER 7 IMPLICATIONS OF ROCK BIMODULAR BEHAVIOR

7.1	Introduction	108
7.2	Review of Constitutive Equations for Bimodular Materials	110
7.2.1	General constitutive relationships in plane problems	110
7.2.2	Constitutive relation for bimodular materials	110
7.2.3	Review of material bimodular models	111
7.3	Analytical Solutions for Simple Structures	116
7.3.1	Solution of bimodular beam	118
7.3.2	Hydraulic extension of bimodular, thick-walled cylinder	128
7.4	Finite Element Implementation of Bimodularity	130
7.5	Effect of Bimodularity on Indirect Measurement of Rock Tensile Strength	134
7.5.1	Indirect determination of rock tensile strength	135
7.5.2	Influence of rock bimodularity	140
7.5.3	Application of indirect tensile tests	145
7.6	Influence of Material Bimodularity on Roof Behavior	147
7.7	Chapter Summary	151

## CHAPTER 8 DEFORMATION AND FRACTURE OF POTASH YIELD PILLARS

8.1	Introduction	152
8.2	Background	153
8.3	Study Methods	154

8.3.1	Object shape method	156
8.3.2	Centre-to-centre method	158
8.3.3	Evaluation of three-dimensional strain	161
8.4	Results from Pillar 1	163
8.4.1	Dimensional changes and mesoscopic structures	163
8.4.2	Microfabric	168
8.5	Results from Pillar 2	172
8.5.1	Dimensional changes and mesoscopic structures	173
8.5.2	Microfabric	178
8.6	Results from Pillar 3	178
8.6.1	Dimensional changes and mesoscopic structures	179
8.6.2	Microfabric	182
8.7	Strain Partitioning, Deformational Mechanisms and Finite Strain	
	Measurement	183
8.7.1	Mineral components and strain partitioning	183
8.7.2	Fabric anisotropy, deformational mechanisms and finite strain	
	measurement	188
8.8	Interpretation of Progressive Pillar Failure	192
8.9	Chapter Summary	195

CHAPTER 9 NUMERICAL SIMULATION OF DEFORMATION AND FRACTURE  
IN POTASH YIELD PILLAR

9.1	Introduction	197
9.2	Introduction to SIMEX (SIMulation of Mining EXcavation)	199
9.3	Basic Concepts	200
9.3.1	Basic concepts in Linear Elastic Fracture Mechanics (LEFM)	201
9.3.2	Basic concepts of elasto-plasticity	204
9.3.3	Basic concepts of elasto-viscoplasticity	205
9.3.4	Strain localization and instability	208
9.4	LEFM Simulation of Corner Shear Zones	210
9.5	Viscoplastic Modelling Procedure with SIMEX	216
9.6	Results of Viscoplastic Simulation	218
9.6.1	Fracture pattern	218
9.6.2	Stress distribution	225
9.6.3	Convergence	233
9.7	Discussion	233
9.7.1	Effect of clay layers	233
9.7.2	Discrepancies between field observations and FEM results	236
9.7.3	Effects of viscoplastic roof and floor	240
9.8	Chapter Summary	245

CHAPTER 10	DISCUSSION, CONCLUSIONS AND FUTURE WORK	
10.1	Discussion	252
10.1.1	Deformational properties of salt	252
10.1.2	Underground excavation in salt	256
10.1.3	Numerical modelling in salt excavation	258
10.2	Conclusions	259
10.3	Recommendation for Further Research	263
REFERENCES		267

## LIST OF FIGURES

<u>Figures</u>		<u>Page</u>
2.1	Axial stress-axial strain curve from the standard uniaxial compression and direct tension tests for halite from Cominco Mine at Vanscoy, Saskatchewan.	8
2.2	Parallel-room technique for stabilizing protected room separated from preliminary room by a yield pillar. Deformation of yield pillar permits development of the secondary stress envelope (after Serata 1983).	20
3.1	Isopach map of the Prairie Evaporite Formation (after Holter 1969). The unit of isopaches is feet.	22
3.2	Columnar section showing Middle Devonian Evaporite cycles in Saskatchewan. Potash layer occurs at a depth of 1100 Meters (after Lane 1959).	23
3.3	Detailed columnar section of mining area in Cominco Mine at Vanscoy, Saskatchewan (edited according to borehole #16-6-35-8 from Vanscoy).	25
3.4	Formation of stress-relieved ground for stabilizing mine openings by the <i>stress relief</i> technique of stress control (after Serata 1983).	28
3.5	Stabilized condition after excavation of protected room in the <i>time control</i> technique illustrated by profiles of vertical and lateral stresses, indicating formation of a secondary stress envelope (after Serata 1983).	29
3.6	Mining sequences and the development of stress envelopes of a 5-entry mining system used in Cominco Mine at Vanscoy, Saskatchewan.	31
3.7	Stress-strain curves from a uniaxial compression test of the ductile Lanigan potash rock displaying all stages of fracture; initiation ( $C_i$ ), yielding ( $C_y$ ), damage ( $C_d$ ) and failure (after Lajtai et al. 1991a).	36
3.8	Triaxial fracture parameters for Lanigan potash rock, a salt rock from Saskatchewan (after Lajtai et al. 1991a).	36
5.1	Idealized stress-strain diagram with an assumed creep limit ( $\dot{\sigma}=0$ , $\dot{\epsilon}=0$ ) and with curves of relaxation and creep tests. A relaxation test will always terminate on the creep limit, but a creep test may not reach the creep limit (after Haupt and Natau 1988).	43

5.2	Stress versus axial (A), lateral (L) and volumetric (V) strain curves at various stress rates from reverse loading triaxial tests on Saskatchewan potash. Tests REV26 and REV24 were from Duncan (1990). The general characteristics of these curves are similar to those obtained from conventional compression tests (See Figure 3.7) and show a dependence on stress rate.	50
5.3	Dependence of initial axial deformation moduli on stress rate at which deviatoric stress was applied to the specimen from the reverse loading tests on Saskatchewan potash.	52
5.4	Effect of stress rate on the deviatoric stress at the ductile yield point for Saskatchewan potash from reverse loading tests.	52
5.5	Normalized stress drop ( $\sigma_l/\sigma_a$ , where $\sigma_l$ is the axial stress at any time during relaxation and $\sigma_a$ is the axial stress at the beginning of the relaxation cycle) and the total axial strain versus time for Test RLX5, Stage 6 ( $q=29$ MPa). The figure shows 5 relaxation cycles. The first four lasted for one day each and the last one was prolonged for 5 days.	55
5.6	Deviatoric stress versus axial strain curve for Test RLX3. The inserted relaxation tests are indicated by stage numbers. The axial strain was measured by LVDT. The inserted relaxation phases have no significant influence on the stress-strain curve.	58
5.7	Total vertical strain and normalized stress drop versus time from Test RLX3. The stress relaxation of potash increases significantly as deviatoric stress increases and the deformation shows a steady-state stage prior to failure.	59
5.8	Linear relationship between normalized stress drop and logarithm of time at all stages from relaxation tests on Specimen RLX3, suggesting no creep limit exists for Lanigan potash. $q$ is the deviatoric stress level. Numbers indicate the sequence ( $N_r$ ) of repeated relaxation cycles at each deviatoric stress level.	60
5.9	Deviatoric stress versus axial strain curve for Test RLX5. The inserted relaxation tests are indicated by stage numbers. They have no significant influence on the stress-strain curve.	62
5.10	Total vertical strain and normalized stress drop versus time for Test RLX5. The stress relaxation increases significantly as deviatoric stress increases and the deformation shows a steady-state stage prior to failure.	63

5.11	Linear relationship between normalized stress drop and logarithm of time for specimen RLX5. $q$ is the deviatoric stress level. Numbers indicate the sequence of repeated relaxation cycles at each deviatoric stress level.	64
5.12	Relationship between normalized axial stress and logarithm of time for the elongated relaxation cycles (5 days) at various stages for Tests RLX4 and RLX5, showing the effect of stress rate on potash relaxation curves. Number in parentheses indicate stage numbers as shown in Figure 5.9.	65
5.13	The effect of stress rate on stress drop after 5 days of relaxation at various deviatoric stress level, showing that the higher stress rate induces a larger stress drop.	67
5.14	Relationship between the stress drop after 24 hours of relaxation and the number of repeated relaxation cycles, showing a decreasing stress drop with increasing relaxation number at low deviatoric stress. However, stress drop is equivalent for all the relaxation cycles near failure at higher stress level ( $q \geq 15$ MPa).	67
5.15	Stress rate versus stress for determining relaxation parameters in Equation (5.15).	72
5.16	Diagram for the determination of relaxation parameters $A$ and $B$ .	72
6.1	(a) Specimen geometry and (b) loading for tension test (after Luong 1988).	79
6.2	Modified specimen geometry for the new, combined compression-tension test. The exposed surface of the middle rock annulus permits the attachment of axial and lateral electrical resistance strain gauges to measure deformation moduli.	80
6.3	Platen and loading configuration for tensile loading in the combined compression-tension test.	83
6.4	Platen and loading configuration for compressive loading in the combined compression-tension test.	84
6.5	Set-up of tension test in a compressive loading frame.	85
6.6	Set-up of compression test in the same compressive loading frame as in tension test.	86

6.7	Principal stress trajectories for tensile loading in the combined compression-tension test. The specimen configuration converts the applied compressive load on the specimen into a state of uniform tensile stress beneath the strain-gauged area.	87
6.8	Principal stress trajectories for compressive loading in the combined compression-tension test, showing a uniform compressive stress state beneath the strain-gauged area.	88
6.9	Halite axial stress-axial strain curves from the standard tension and compression tests. The specimen was loaded under tension or compression continuously to the final failure. $E_t$ and $E_c$ are Young's moduli in tension and in compression, respectively, measured as the slope of the linear portion of the stress strain curves.	94
6.10	Halite axial stress-axial strain curves from the combined compression-tension test. $E_t$ and $E_c$ are Young's moduli in tension and in compression, respectively, measured as the slope of the linear portion of the stress strain curves.	95
6.11	Potash axial stress-axial strain curves from the standard tension and compression tests. $E_t$ and $E_c$ are Young's moduli in tension and in compression, respectively, measured as the slope of the linear portion of the stress strain curves.	98
6.12	Potash axial stress-strain curves from the combined compression-tension test. $E_t$ and $E_c$ are Young's moduli in tension and in compression, respectively, measured as the slope of the linear portion of the stress strain curves.	98
6.13	Contour map of the maximum tensile principal stress in tensile loading test by the combined compression-tension technique, indicating high stress concentrations around the notches at the ends of the drilling slots.	104
6.14	Photo of specimen G1 after testing. The specimen was taken to failure by rupturing at the blind end of the inner slot.	105
7.1	Compliances of bimodular constitutive relation (after El-Tahan et al. 1989). (a) Ambartsumyan model, the cross compliance, $C_{12}$ , is not continuous in the principal stress space; (b) WCM model, the cross compliance is continuous, but its slope is not continuous.	112
7.2	Cross compliance in MWCM bimodular material model, both the cross compliance and its slope are continuous (after El-Tahan et al. 1989).	113

7.3	The principal stress-space representation of various cases of (a) plane stress, and (b) plane strain. There are three cases for a plane stress problem and four cases for a plane strain problem according to the signs of the principal stresses.	114
7.4	Simply supported beam with uniformly distributed load $q$ , a rectangular cross section (height $h$ , width $b$ ), and span $L$ .	117
7.5	Cross section of a thick-walled cylinder.	117
7.6	A beam under pure bending: (a) longitudinal, vertical section (plane of symmetry), and (b) transverse section. $c$ is the distance of the neutral axis from the top of the beam, $\rho$ is the curvature of the deformed neutral axis, and $y$ is the vertical coordinate starting from the neutral axis.	119
7.7	Portion ACC'A' in a cantilever beam for deriving shearing stress $\tau_{xy}$ .	121
7.8	Forces acting on the free body ACC'A' for deriving shear stress $\tau_{xy}$ .	121
7.9	The shear force $\Delta H$ exerts on a portion of length $\Delta X$ of the horizontal cut through C'.	122
7.10	Analytical results showing the influence of moduli ratio, $k$ , on beam deflection, $y(x)$ (normalized by beam height, $h$ ). Negative sign denotes downward displacement. Beam deflection increases significantly as $k$ decreases.	125
7.11	Analytical solution showing the distribution of $\sigma_x$ at the central height of the beam along the beam span with various deformation moduli ratio, $k$ . $L$ is beam span, $h$ is beam height, $q$ is applied load/unit length on the top surface. The origin of $x$ and $y$ is at the left bottom corner of the beam.	126
7.12	Analytical solution showing the distribution of $\sigma_x$ at the centre span of the beam along the beam height as moduli ratio, $k$ , varies. $h$ is beam height and $L$ is beam span.	127
7.13	Analytical solution showing the distribution of $\sigma_{xy}$ at the right end of the beam along the beam height as moduli ratio, $k$ , varies.	128
7.14	Radial and tangential stress distribution in a thick hollow cylinder. $\sigma_\theta$ is the tangential stress, $\sigma_r$ is the normal stress, $P_i$ is the internal pressure, $P_o$ is the external pressure, $r_i$ is the internal radius, $r_o$ is the external radius, and $k$ is moduli ratio.	129

7.15	Radial and tangential stress around a wellbore. $\sigma_\theta$ is the tangential stress, $\sigma_r$ is the normal stress, $P_i$ is the internal pressure, $P_o$ is the external pressure, $r_i$ is the internal radius, $r_o$ is the external radius, and $k$ is moduli ratio.	129
7.16	Flow-chart of the finite element program for bimodular materials. Names in capital form are names of subroutines in the FEM code.	132
7.17	Comparison of beam deflection from FEM and analytical solutions for a simply supported beam with uniformly distributed load.	133
7.18	Comparison of FEM and analytical solutions of the maximum beam deflection with various deformation moduli ratio ( $k$ ).	133
7.19	Three point bending test of a beam with rectangular cross section. The maximum tensile stress, $\sigma_t$ , is developed at the extreme-most fibre on the convex side of the beam. Dashed lines show deformed shape of the beam.	136
7.20	Hydraulic extension of a ring. Tensile stress, $\sigma_t$ , is developed in the tangential direction and is the maximum at the inner surface.	137
7.21	Brazilian test. A constant tensile stress, $\sigma_t$ , is developed in the central portion of the disc along the loaded diameter.	137
7.22	Ring test. A maximum tensile stress is developed at the intersection of the central hole and the loaded diameter.	139
7.23	Analytical results showing the influence of moduli ratio, $k$ , on the normalized maximum tensile stress, $\sigma_t/\sigma_{t(k=1)}$ , for a beam bending test.	142
7.24	Analytical solution of the relationship between moduli ratio, $k$ , and the normalized maximum tensile stress, $\sigma_t/\sigma_{t(k=1)}$ , in a hydraulic extension test. $m$ is the ratio of the external and internal radii.	142
7.25	Finite element mesh for the Brazilian test.	144
7.26	Finite element results showing the influence of moduli ratio, $k$ , on the normalized maximum tensile stress, $\sigma_x/\sigma_{x(k=1)}$ , in a Brazilian disc.	146
7.27	Finite element results showing the influence of moduli ratio, $k$ , on the normalized maximum tensile stress, $\sigma_t/\sigma_{t(k=1)}$ , in the ring test.	146

7.28	Finite element mesh of a single rectangular opening (25m × 5m). Arrows represent applied load.	148
7.29	Finite element solution showing the influence of moduli ratio, $k$ , on the maximum roof deflection at various horizontal to vertical principal stress ratios, $m$ .	150
7.30	Finite element solution showing the influence of moduli ratio, $k$ , on the maximum tensile stress at the middle span of the opening and on crack initiation load ( $m=0$ ).	150
8.1	Cross section showing the original 5-entry potash openings and the later cross cut. Mining sequence of the original openings is shown by numbers.	153
8.2	The mean axial ratio of deformed elliptical markers as determined using $A$ , $G$ and $H$ compared to the tectonic strain ratio (after Lisle 1977).	157
8.3	Section through a deformed aggregate. The partially deformed spheres have undergone partial pressure solution along their mutual contacts (after Ramsay 1967).	159
8.4	Examples of Fry centre-to-centre plot (a) and normalized Fry centre-to-centre plot (b).	160
8.5	Geometry of the original sphere and the deformed ellipsoid for deriving three dimensional strains.	161
8.6	Photograph of the cross section of Pillar 1. There is one metre between every two black dots. Black circles are sample locations. The revealed pillar section is about two thirds of the upper part of the original pillar.	164
8.7	Mapped cross section of Pillar 1. A-halite unit; B-first clay layer; C-potash; D-second clay layer; E-potash; F-third clay layer; G-potash. (a) Fabric anisotropy ellipsoids from the shape method for sylvite grains. (b) Fabric anisotropy ellipsoids from the centre-to-centre method. All the ellipsoids are centred at sample locations. See Table 8.1 for the ellipsoid dimensions.	165
8.8	Development of shear zones and shear wedge in another pillar at the Vanscoy Mine. (a) Photo; (b) Sketch.	167
8.9	The Flinn diagram for representing the shape of strain ellipsoids (after Ramsay 1983). $\text{inf}=\text{infinite}$ .	171

- 8.10 Flinn diagram for strain measured in pillar 1. Most ellipsoids are located very close to the horizontal axis, signifying apparent flattening. inf=infinite. 173
- 8.11 Photograph of the cross section of Pillar 2. There is one metre between every two black dots. Black circles are sample locations. The revealed pillar section is about two thirds of the upper part of the original pillar. 174
- 8.12 Mapped cross section of Pillar 2. A - halite unit; B - first clay layer; C - potash; D - second clay layer; E - potash; F - third clay layer; G - potash. (a) Fabric anisotropy ellipsoids from the shape method for sylvite grains. (b) Fabric anisotropy ellipsoids from the centre-to-centre method. All the ellipsoids are centred at sample locations. See Table 8.3 for the ellipsoid dimensions. 175
- 8.13 Flinn diagram for Pillar 2. Most of the strain ellipsoids are located very close to the horizontal axis, signifying apparent flattening. inf=infinite. 179
- 8.14 Photograph of the cross section of Pillar 3. There is one metre between every two black dots. Black circles are sample locations. The revealed pillar section is about two thirds of the upper part of the original pillar. 180
- 8.15 Mapped cross section of Pillar 3. A - halite unit; B - first clay layer; C - potash; D - second clay layer; E - potash; F - third clay layer; G - potash. (a) Fabric anisotropy ellipsoids from the shape method for sylvite grains. (b) Fabric anisotropy ellipsoids from the centre-to-centre method. All the ellipsoids are centred at sample locations. See Table 8.5 for the ellipsoid dimensions. 181
- 8.16 Flinn diagram for Pillar 3. Most strain ellipsoids are located very close to the horizontal axis, signifying apparent flattening of rock. inf=infinite. 184
- 8.17 Strain partitioning results from Sample 4, from near corner ductile shear zone in Pillar 1. (a) Tracing of grain shapes, darker grains are sylvite, lighter grains are halite; (b) Contour map of dimensional ratios of grains, contour interval equals 1; (c) Relief map of dimensional ratios of grains. Peaks correspond to areas of sylvite concentration, valleys correspond to areas of halite grains. 185
- 8.18 Strain partitioning results from Sample 3, This sample is located in the central part of pillar 1. (a) Tracing of grain shapes, darker grains are sylvite, lighter grains are halite; (b) Contour map of dimensional ratios 186

	of grains, contour interval equals 1; (c) Relief map of dimensional ratios of grains. Peaks correspond to areas of sylvite concentration, valleys correspond to areas of halite grains.	
8.19	Strain partitioning results from Sample 10, locating at the centre of shear wedge in Pillar 1. (a) Tracing of grain shapes, darker grains are sylvite, lighter grains are halite; (b) Contour map of dimensional ratios of grains, contour interval equals 1; (c) Relief map of dimensional ratios of grains. Peaks correspond to areas of sylvite concentration, valleys correspond to areas of halite grains.	187
8.20	A sample of undeformed potash collected from a fresh mining surface. The scale is centimetres.	189
8.21	Samples of deformed potash collected from yield pillars after 8 years of deformation. Sylvite is dark and flattened; halite occurs as light and broken aggregates in the shape of augen. The scale is centimetres. (a) Deformed potash equivalent in grain size to Figure 8.20; (b) Deformed potash coarser grained than Figure 8.20.	190
8.22	Proposed model of progressive pillar deformation. C marks the centre line of the pillar and parallel vertical lines mark the position of the original pillar width. The principal strain values are based on shape changes in sylvite and represent interpretation of sylvite strain in the centre of the pillars.	193
9.1	Fundamental modes of fracture in 2D, (a) Mode I (Opening Mode), (b) Mode II (Shearing Mode).	202
9.2	Crack tip coordinates, stresses, and node numbers.	202
9.3	Rheological analogue of elasto-plastic material.	206
9.4	Rheological analogue of elasto-viscoplastic material.	206
9.5	Axial stress-axial plastic strain curve of Saskatchewan potash for calibrating post yield hardening and softening behaviour. It is from a conventional triaxial compression test with 0.5 MPa confining pressure and a strain rate of $1.75 \mu\epsilon \cdot s^{-1}$ . The specimen was cylindrical with diameter of 5 cm and height of 10 cm (after Duncan 1990).	208
9.6	Finite element mesh geometry, supports and loading conditions of pillar model for simulating corner shear zones based on the theory of linear	213

elastic fracture mechanics. Load was applied as distributed edge load shown by the arrows at the top.

- 9.7 Principal stress distribution showing stress concentration at room corner. 213
- 9.8 Generation of corner diagonal crack with refined mesh and imposed singularity elements (special quarter point triangular elements, their nodes are shown by black dots). 214
- 9.9 At a load of 25 MPa, the corner fracture extended to the middle height of the pillar. 214
- 9.10 Principal stress distribution after corner diagonal crack extended to the middle height of the pillar. A zone was isolated by the corner fracture and stresses in this isolated area were relieved. 215
- 9.11 Finite element model configuration for simulating viscoplastic pillar deformation and fracturing, including dimensions, supports and loading conditions. A - weak, elastic layer representing overlying and underlying strata. B - weak, viscoplastic potash layer. 217
- 9.12 Finite element mesh showing opening, yield pillar, abutment pillar, and surrounding strata. Numbers and letters show the locations of stress and convergence histories in Figures 9.20 and 9.26, respectively. 219
- 9.13 Plastic strain distribution immediately after room excavation, signifying the initiation of corner ductile shear zone. The size of black dots is proportional to the magnitude of plastic strain at the Gauss points. 221
- 9.14 Localizations of plastic strain along diagonal directions at pillar edges 60 days after room excavation, symbolizing the failure pattern of corner ductile shear zones observed from field observations in Chapter 8. 222
- 9.15 Principal stress distribution (green lines) in the yield pillar and accumulated plastic strain (red dots). 223
- 9.16 Second generation of plastic strain localization (70 days after room excavation). 224
- 9.17 Third generation of plastic strain localization. Fracture pattern appears to be stable in the yield pillar (110 days after room excavation). 226

9.18	Variation of vertical stress ( $\sigma_y$ ) distribution along the central height of the potash zone, (a) 10 days after excavation, (b) 30 days after excavation, (c) 60 days after excavation.	227
9.19	Variation of vertical stress ( $\sigma_y$ ) distribution along the central height of the potash zone, (a) 70 days after excavation, (b) 110 days after excavation, (c) 690 days after excavation.	228
9.20	History of vertical stress ( $\sigma_y$ ) at various locations shown by numbers in Figure 9.12. I - Removal of first set of shear wedges, II - Removal of second generation of shear wedges.	230
9.21	Contour map of vertical stress prior to room excavation, showing uniform <i>in situ</i> stress of around 25 MPa (equals to the applied boundary stress).	231
9.22	Contour map of vertical stress immediately after room excavation (after 10 days). Vertical stress increased in the pillars and decreased at roof and floor.	231
9.23	Contour map of vertical stress 30 days after room excavation. Two peak stresses occurred in the yield pillar, stresses near pillar edges dropped due to yield.	232
9.24	As pillar deformation increased (60 days after room excavation), the entire pillar yielded, forming a single peak stress at pillar centre.	232
9.25	As pillar deformation increased further (120 days after excavation), zone of yielding ground increased, stress relieved ground over all three openings, and the location of peak compressive stress moved away from the openings.	234
9.26	History of convergence between roof and floor at various pairs of locations shown by letters in Figure 9.12.	235
9.27	Finite element mesh showing clay layers, openings, yield pillar, abutment and surrounding rock.	237
9.28	Localization of plastic strain 60 days after room excavation in the yield pillar model that includes clay layers at the top and bottom of the potash ore zone (see Figure 9.27). Comparing to Figure 9.14, the plastic strain near top and bottom reduced due to the presence of clay layers.	238

9.29	Distribution of plastic strain 70 days after the initial room excavation in the yield pillar model that includes the effect of clay layers at the top and bottom of the potash zone.	239
9.30	Plastic strain distribution immediately after room excavation in the model with viscoplastic roof and floor. It signifies the initiation of corner ductile shear zones. Local plastic strain also occurs in the roof and floor.	242
9.31	Localization of plastic strain in diagonal directions at pillar edges 60 days after room excavation in the model with viscoplastic roof and floor. Failure also occurs in the roof and floor areas.	243
9.32	Third generation of plastic localization for the model with viscoplastic roof and floor. Fracture pattern appears to be stable in the yield pillar (110 days after initial room excavation).	244
9.33	Vertical stress ( $\sigma_y$ ) distribution along the central height of the potash zone for the model with viscoplastic roof and floor. (a) 10 days after excavation, (b) 30 days after excavation, (c) 60 days after excavation.	246
9.34	Vertical stress ( $\sigma_y$ ) distribution along the central height of the potash zone for the model with viscoplastic roof and floor. (a) 70 days after excavation, (b) 110 days after excavation, (c) 690 days after excavation.	247
9.35	History of vertical stress at various locations shown by the numbers in Figure 9.12 for the model with viscoplastic roof and floor. I - Removal of first set of shear wedges, II - Removal of second generation of shear wedges.	248
9.36	Modified yield pillar deformation model. Finite element simulation reproduced all four stages pillar deformation proposed in Figure 8.22. An additional deformation stage may be included (Stage 5), indicating a final stable failure mode.	250

## LIST OF TABLES

<u>Table</u>		<u>Page</u>
5.1	Reverse loading triaxial tests.	49
5.2	Multiple-stage repeated relaxation tests.	54
6.1	Young's moduli in tension and compression collected by Haimson and Tharp (1974).	76
6.2	Results on halite in the uniaxial tension tests.	92
6.3	Results on halite in the uniaxial compression tests.	92
6.4	Results on halite from the new technique.	93
6.5	Results on potash from uniaxial tension tests.	96
6.6	Results on potash from uniaxial compression test.	96
6.7	Results on potash from the new technique.	97
6.8	Step loads and Young's moduli for Lac du Bonnet granite.	99
6.9	Step loads and Young's moduli for Tyndall limestone.	100
6.10	Summary of Young's moduli in tension and in compression.	102
8.1	Ellipsoid dimensions of Pillar 1 with Z normalized to unity.	169
8.2	Three dimensional strain of Pillar 1.	170
8.3	Ellipsoid dimensions of Pillar 2 with Z normalized to unity.	176
8.4	Three dimensional strain results of Pillar 2.	177
8.5	Ellipsoid dimensions of Pillar 3 with Z normalized to unity.	182
8.6	Three dimensional strain results of Pillar 3.	183

## 1. INTRODUCTION

### 1.1 General Background

The demand in modern society for energy and raw materials has generated an increasing number of underground excavations in rock for the exploitation of natural resources and for the permanent isolation of nuclear waste products. As both a raw material and a storage medium, evaporitic rocks such as potash, gypsum and halite have been extracted at increasing rates over the last few decades. These activities have stimulated interest in research into the deformational properties of evaporitic rocks and their response to underground excavation.

Mining of evaporites dates back as far as the middle Neolithic Period (3500 B.C. - 2500 B.C.), while potash mining, which began some 100 years ago at Stassfurt, Germany, is relatively new (Bieniawski 1984). Since mining in salt rock started there have been specific engineering problems associated with mining of such rock due to its unique mechanical properties, i.e., the slow but continuous *flow* around mined-out openings which causes gradual closure. Laboratory research revealed that salt rocks are highly ductile and creep significantly. Such behavior has also been demonstrated *in situ* by salt glaciers and flowage patterns observed in salt domes (Baar 1977).

Although considerable research has been conducted on salt deformation, the complicated time and stress history dependent properties of such rock continue to cause engineering problems in practice. The proper design of long term excavations in salt cannot be carried out unless the material deformational characteristics can be evaluated

for a wide range of conditions. The evaluation of such deformational characteristics for potash, *in situ* and in the laboratory, is a major concern in the research program described in this thesis.

## 1.2 Statement of the Problem

Since 1985, a research project on mining stability in Saskatchewan potash mines has been carried out in the Departments of Civil and Geological Engineering at the University of Manitoba, with the cooperation of Cominco Fertilizers Ltd, the Potash Corporation of Saskatchewan and NSERC. The research presented in this thesis was partly supported by this university/industry cooperative research project. Problems to be studied in this thesis have been selected based on the requirements of the project as well as the state-of-the-art research on potash behavior. Therefore, the objectives have been laid out based on a critical examination of the existing literature and the realistic consideration of the specific engineering problems in potash mining in Saskatchewan. These include three aspects: the rate dependent deformational characteristics of potash through stress relaxation tests; rock bimodularity (the property of having different Young's moduli and Poisson's ratio in tension and in compression) and its practical significance; and the progressive deformation of potash yield pillars at the Cominco Mine. The work presented is basically curiosity-driven research and does not attempt to solve specific mining problems. Any application to mining situation must take into account various assumptions and simplifications that have been used.

### 1.3 Thesis Organization

This thesis is subdivided into 10 chapters, Chapters 1-4 act as a preface, Chapters 5-9 form the principal part of this research, and Chapter 10 summarizes the research.

- Chapter 1 is an introduction that provides an overview of the problem being investigated and the organization of the thesis.
- Chapter 2 provides a survey of the literature relevant to the deformational properties of salt rocks and the response of such rocks around excavations.
- Chapter 3 introduces challenges, mining methods and rock mechanics related research in potash mining in Saskatchewan.
- Chapter 4 critiques on the state-of-the-art research on the mechanical properties of evaporitic rocks; summarizes the specific rock mechanics problems associated with potash mining in Saskatchewan, and therefrom, elaborates research objectives for this thesis.
- Chapter 5 describes the initial laboratory experimental study. The viscoplastic properties of potash and salt is addressed by reverse loading triaxial tests and by relaxation tests at various stages before and after yielding along a reverse loading path. The existence of a creep limit and the relaxation behavior of potash before and near failure are discussed. A uniaxial, strain-hardening constitutive law has been extended to incorporate the effect of confining pressure and the experimental results have been approximated by the proposed constitutive model.
- Chapter 6 is the second experimental program of this thesis. It addresses a stress history dependent property, namely *bimodularity* - the property of having different

deformational moduli in tension and in compression. A new testing technique is developed that permits the direct determination of deformational moduli in compression and in tension on the same specimen and in the same compressive loading frame. The results of tests on halite, potash, granite and limestone are presented and compared with previously published data and data from the standard direct compression and direct tension tests.

- Chapter 7 implements a bimodular constitutive relation for a finite element program and derives analytical solutions that incorporate material bimodularity for simple structures. Then, the practical significance of rock bimodularity is evaluated through estimating its influence on roof failure and on indirect rock tensile strength tests such as the beam bending, hydraulic extension, Brazilian and ring tests.
- Chapter 8 addresses the phenomenon of long-term deformation in pillars through the examination of yield pillars in which eight years of deformation has taken place in the Cominco Mine by *in situ* mapping of deformational structures, by determining changes in pillar width and in thicknesses of potash and of interbedded clay layers, and by rock fabric analyses as an indication of accumulated finite strains. Pillar deformation has been shown to involve progressive bulk rock flattening, followed by the development of shear zones at pillar corners, by the development of shear wedges at pillar margins, and by the detachment of these wedges into adjacent rooms. These effects appear to be sequential and repetitive. Finally, a hypothesis of long-term potash yield pillar deformation has been postulated.

- Progressive deformation and failure of a three-entry potash mining panel is simulated numerically in Chapter 9. The deformation model of potash yield pillar proposed in Chapter 8 is analyzed and modified. The initiation and extension of corner ductile shear zones are modelled in terms of narrow bands of *strain localization* - shear bands. Stress variations and long-term stability are discussed.
- Finally, chapter 10 summarizes the research by discussing data from the previous chapters, indicating possible directions for future research, and drawing together the major conclusions.

## 2. LITERATURE SURVEY

### 2.1 Introduction

Underground rock excavations disturb the *in situ* state of stress in rock masses and as a result deformation and, in some cases, fracturing occur around the new openings. This process of stress adjustment may lead to instabilities which may cause injuries and loss of production. Better understanding of the mechanical behavior of rocks around underground openings has increasingly promoted better design, prediction and control, and therefore, greatly benefitted both safety and productivity in rock excavation. This has led to a relatively new field of study called *rock engineering*. Although the practice of rock engineering can be traced back to the earliest days of mining and civil engineering, the theoretical exposition of rock engineering has developed only in the last three decades. Since the First International Congress on Rock Mechanics in Portugal in 1966, the body of literature has been expanding at an accelerating pace, with an ever-increasing number of conferences and technical journals devoted to this and other closely related themes. In addition to technical journals and conference proceedings, there are also some discipline monographs that expound rock engineering in a systematic fashion, e.g. Hoek and Brown (1980), Bieniawski (1984), Brady and Brown (1985), Goodman and Shi (1985), Brown (1987), and Franklin and Dusseault (1989 and 1991).

Interest in salt rock deformation and its application to underground engineering started in the late 1950's after the Academy of Sciences of the United States recommended guidelines for permanent isolation of nuclear waste products in deep bedded salt deposits, salt domes and other sedimentary rocks. Progress in this field is recorded

best in two conference proceedings on the mechanical behavior of salt (Hardy and Langer 1984 and 1988), by the proceedings of the First International Conference on Potash Techniques (McKercher 1983), and by the proceedings of the 1st-7th International Symposium on Salt. In this chapter, the relevant literature is reviewed briefly from two major aspects: (1) experimental and theoretical analyses of the mechanical properties of salt rocks; (2) responses of underground openings to excavation, including *in situ* documentation, theoretical analyses, and physical and numerical simulation on the deformation and fracturing around single as well as multiple underground openings.

Saskatchewan potash was deposited in evaporate sequences. It has many microstructural and deformational characteristics in common with other evaporites, such as halite, anhydrite, and gypsum. In most literature, *salt* has been used in a general sense to represent all these evaporites and the term will be used similarly in the following review.

## **2.2 Stress History and Rate Dependent Properties of Salt**

Since the beginning of the laboratory research on rock salt, it has been realized that salt rocks are highly ductile, easily deformed, and creep significantly. These characteristics are reflected in the non-linear, inelastic and finite deformational characteristics evident in general stress-strain curves in both uniaxial compression and uniaxial tension (Figure 2.1). For decades experimental and theoretical investigations on the deformation of salt rocks have been to define such mechanical properties, mainly by uniaxial creep tests, and to a lesser extent, by triaxial tests with various loading paths.

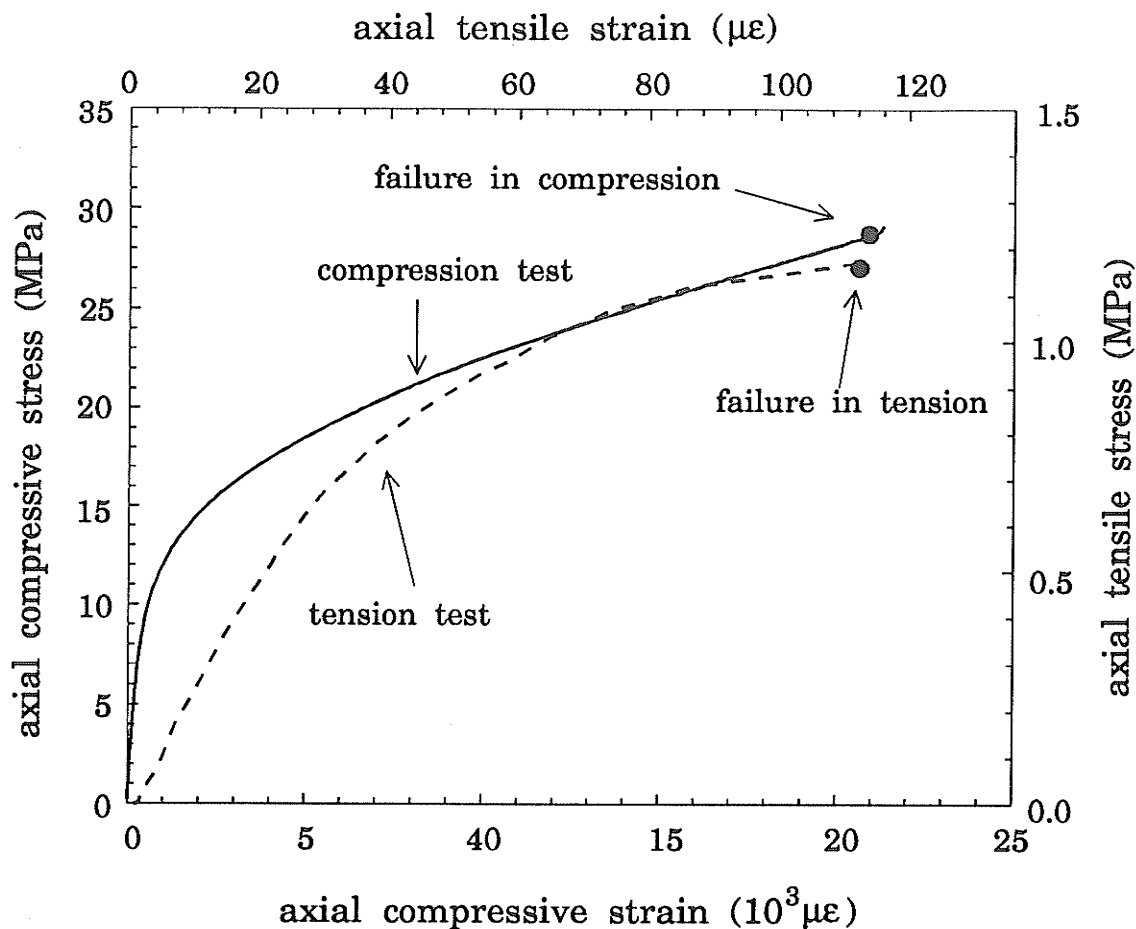


**Figure 2.1** Axial stress-axial strain curve from the standard uniaxial compression and direct tension tests for halite from Cominco Mine at Vanscoy, Saskatchewan.

### 2.2.1 Experimental investigations

There is an extensive body of literature on the experimental investigations of salt rock. A large volume of experimental data is contained in reports by Sandia National Laboratories (Herrman et al. 1980; Herrman and Lauson 1981) and RE/SPEC Inc. (Hansen and Mellegard 1980; Mellegard et al. 1981; Van Sambeek et al. 1992). Most of the research has been focused on the creep and failure behavior of salt (e.g., Carter

and Hansen 1983; Lux and Heusermann 1983; Hambley et al. 1988; Bakhtar et al. 1988; Senseny 1988; Wawersik and Zeuch 1986; and Wawersik 1988 for creep tests, and Serata et al. 1972; Lajtai and Duncan 1988; Hunsche 1991*a* and 1991*b*; Hunshe and Albrecht 1990 for failure behavior).

The test specimens are usually cylindrical cores. Various sizes are used because there has been no standardization of test methods and because of the variety of testing equipment available. The effect of specimen size on creep testing was studied by Senseny (1984). He found that during transient creep, the deformation of smaller specimens is larger than that of larger specimens for the same stress state, temperature environment and test duration. During the steady-state stage, the specimen size was found to have little influence. He concluded that constitutive laws based on laboratory data may lead to an overestimation of salt deformation in the field.

The development of equipment for salt rock creep experiments was discussed by Bakhtar (1979). Usually, because of the long duration of such tests (a minimum of a few weeks), several testing machines are used instead of a single apparatus, so that several specimens can be tested simultaneously under a strictly controlled environment (for the effect of test duration, see Mrugala and Hardy 1988). Langer (1984) described a creep testing facility in which a single creep unit can accommodate up to five specimens stacked one on top of the other for simultaneous testing under the same axial load.

The behavior of salt rock is significantly affected by pressure, deviatoric stress, time, temperature and loading path (Wawersik and Hannum 1980). The relatively simple uniaxial constant stress tests appear insufficient for a thorough understanding of the

mechanical behavior of salt rock. Increasingly, triaxial apparatus with temperature and servo-controlled loading system have been used (e.g., Hansen 1977; Hansen and Carter 1984; Hardikar et al. 1987; and Xiong and Hunsche 1988). A laboratory set-up for a long-term, comprehensive creep testing program was discussed by Horseman and Passaris (1984). The testing facility includes a battery of built-in triaxial creep cells with loading jacks and internal dynamometers. It can monitor salt deformation under *in situ* conditions of stress, temperature and induced moisture content. Triaxial tests have permitted a better understanding of the deformational mechanisms of salt in the deep mining environment and enabled the determination of more practical constitutive relations and failure criteria.

In contrast to creep properties, the relaxation characteristics of salt rock have been largely ignored. Only recently, a few attempts have been made to investigate these properties (Balthasar et al. 1987; Haupt and Natau 1988; and Haupt 1991).

### 2.2.2 Theoretical investigations

Mainly based on creep tests, numerous rheological models or constitutive equations have been published to describe salt behavior. However, the mechanical behavior of salt is so complicated that attempts to generalize a material model to adequately describe the rate and stress history dependent properties of salt rocks subject to an arbitrary history of stress have so far proven unsuccessful.

Basically, two approaches have been used for establishing salt rock constitutive relations, namely *empirical* and *rheological*. The empirical model is essentially a curve fitting process attempting to find experimental constants. Carter and Hansen (1983)

provided an excellent review paper on the existing uniaxial constitutive equations. Lindner and Brady (1984) and Mrugala (1985) listed convenient tables of a number of empirical equations. Cristescu (1992) provided a state-of-the-art review on a number of constitutive models, such as various models developed at the Sandia National Laboratories (Wawersik and Preece 1984; Wawersik et al. 1982; Wawersik and Zeuch 1986; Wawersik and Hannum 1980), the BGR-model (Langer 1982 and 1986), models for *fracture* deformation (Dawson and Munson 1983), a model developed by Hansen and Carter (1980), a triaxial model by Desai and Coworkers (Desai et al. 1986; Desai and Zhang 1987 etc), and kinematic viscosity models (Lindner and Brady 1984; Aubertin et al. 1989 and 1991). These models are essentially similar mathematical formulations containing strain rate expressed as a function of stress, time and temperature raised to some power. For example (Herrmann et al. 1980):

$$\dot{\epsilon} = A\sigma^n \exp(-Q/RT) \quad (2.1)$$

where  $\dot{\epsilon}$  is strain rate in strain per hour,  $T$  is temperature in degrees Kelvin,  $\sigma$  is deviatoric stress in MPa, and  $A$ ,  $n$ ,  $Q$  and  $R$  are experimental constants.

The rheological approach employs mechanical analogues assembled from fundamental rheological components such as springs, sliders and viscous dash pots. It has been used widely as a means of characterizing the time-dependent behavior of salt rocks, particularly for continuum stress analysis. some examples of rheological models are a simple Burger's model used by Passaris (1979) and a viscoelastic model used by Boucly (1984) consisting of combined Maxwell and Bingham models. Other examples are the viscoelastic-viscoplastic models proposed by Serata (1968), Winkel et al. (1972), and

Serata and Cundey (1978). Horseman and Passaris (1984) examined a few existing theoretical models and concluded that the models based on the time-hardening hypothesis provided a very poor description of the response of salt to rapidly changing deviatoric stress; models based on the strain-hardening hypothesis were likely to provide a better representation of the data than time-hardening models but tend to underestimate the strain rates produced by sudden increases in deviatoric stress. Viscoelastic models based on the concept of creep as a hereditary process suffered from the major drawback that they predicted unrealistically large time dependent strain recovery during cavity repressurization. Horseman and Passaris (1984) further used the modified superposition integral developed on the basis of Bultzmann's Superposition Principle from the original model of Findley and Khosla (1955) and claimed that a more accurate description of creep under static or increasing deviatoric stress could be obtained.

A recent tendency in constitutive modelling of salt rocks as well as other geological materials, is the use of a synthetic method that combines a number of combined rheological models by curve fitting methods to obtain the best fit of experimental results. It has been known as the generalized model theory or composite model theory (Sobotkal 1985). A more detailed review of rheological models can be found in Duncan (1990).

Another development in rheological rock mechanics is the deformation-mechanism map (Ashby 1972). One important reason for establishing a deformation-mechanism map is that it provides a better way of extrapolating theoretical and experimental data. Particularly, it provides an improved understanding on rheological deformation that

cannot be observed on a realistic experimental time scale. Another valuable contribution of this method is the better understanding of the distribution and variation of deformational mechanisms in a multi-dimensional space of temperature, confining pressure, deviatoric stress, grain size, gas and fluid. However, the construction of such a mechanism map in multi-dimensional space is very difficult. Therefore most of the maps constructed up to now have been presented in non-dimensionalized stress and temperature spaces. The construction of such a map requires enormous amounts of information in the form of constitutive equations (models) and experimental data. It is, however, a powerful methodology for selecting appropriate constitutive models and their regimes of influence. The first deformation-mechanism map for salt was constructed by Verral et al. (1977). Munson (1979) provided a more recent version based on experimental creep data obtained by various researchers. Munson and Dawson (1984) gave a good example of constitutive models developed within the framework of the deformation-mechanism map for salt that permitted unfolding of the rather complicated low temperature steady-state creep behavior by three simple responses involving separate regimes with individual controlling mechanisms. Recently, Senseny et al. (1992) provided an excellent summary on the mechanical behavior of salt and various examples of reported behavior for illustrating phenomena and micromechanics.

### **2.3 Response of Underground Openings to Excavation**

Although the previous section provides a basis for the development of theoretical methods, there remain questions of applying these laboratory and theoretical results to the

observed deformations in underground rock excavations. In fact, it is usually difficult to extrapolate these findings to *in situ* behavior because of the more complicated geometry, loading paths and boundary conditions *in situ*. At this stage, it is more appropriate to perform a synthetic approach that combines laboratory modelling, theoretical analyses, direct observations and numerical simulations on *model openings* with various degrees of sophistication. For the sake of simplicity, such model openings are grouped into two broad categories: single openings and multiple openings. Some of the literature concerning the mechanical behavior of each group is summarized in the following sections.

### 2.3.1 Single openings

Over the years, single cylindrical opening models have been studied in different contexts in several disciplines. Recently this classical problem has been "revisited" due to the emergence of new challenges, especially in the petroleum industry (Roegiers 1990). It is also one of the basic models used to represent underground mine openings. Indeed, most of the laboratory investigations and theoretical analyses have been carried out for single cylindrical openings (Winkel et al. 1972; Rousset et al. 1989; Ewy and Cook 1990; Carter et al. 1991a; Lajtai et al. 1991a; Carter 1992a; Carter et al. 1992). A theoretical basis for these studies is typically the classical problem of a thick-walled cylinder under hydrostatic loading with or without external pressurization (Daemen and Fairhurst 1971; Daemen 1975). Other theoretical bases include a plate with a central hole

and uniaxially loaded; a plate with a central hole and biaxially loaded; a cube with a central hole and tri-axially loaded.

Research on how rock around a cylindrical opening responds to changes in stress provides an important insight into underground rock engineering problems. In fact, an accurate prediction of the stress distribution and the *ground reaction curve* around a single opening is essential to the proper design of support elements for tunnels and shafts (Pan and Dong 1991) and forms the basis for research on the behavior of multiple openings. Investigations include stresses and deformation around openings, convergence, fracture patterns, and failure mechanisms (Hoek and Brown 1980; Pan and Dong 1991; Carter et al, 1991a). Ewy and Cook (1990) reviewed the existing literature, and investigated elastic and inelastic deformation as well as fracturing around cylindrical underground openings on both an experimental and a theoretical level. Roegiers (1990) summarized the existing analytical work on circular openings for two extreme cases, unsupported and supported openings. More recently, Lajtai and coworkers studied fracture patterns and failure mechanisms numerically and experimentally, and mapped fracture stages around cavities in laboratory physical models (Carter and Lajtai 1991; Carter et al. 1991a; Lajtai et al. 1991a). Pan and Dong (1991) proposed a hierarchical approach to model the excavation/construction process during tunnelling in a rock mass with rheological properties. Most of these studies revealed that hole closure is non-linear and time-dependent, especially for unsupported holes and in "squeezing" ground such as salt rock. In order to handle these non-linear properties, elastoplastic, viscoelastic and viscoplastic analyses have been used (e.g., Detournay and Fairhurst 1987; Gumusoglu et al. 1987;

Santarelli and Brown 1987; and Rousset et al. 1989). Numerical approaches such as finite element and boundary element methods have been adopted to solve these non-linear theoretical equations and simulate the progressive failure processes around underground cylindrical openings (e.g. Booker et al. 1989; Sharan 1989).

Another important aspect that needs to be considered in studying the behavior of single cylindrical openings is the presence of discontinuities (Sakurai and Tanigawa 1989). In recent years, considerable progress has been made in devising methods for analyzing the stability of block systems (Goodman & Shi 1985). Discrete or distinct element methods have also been developed (Williams 1988; Cundall 1976; Cundall and Hart 1983; Cundall 1987; and Hart 1990). In addition, some new, statistically based theories have also been used to describe discontinuity systems and to classify rock masses, e.g., the fractal dimensional theory (Mandelbrot 1983; La Pointe 1988).

### **2.3.2 Multiple openings and pillar design**

Most mine openings are multiple openings, although a few structures, such as shafts and exploration drifts, may be sufficiently isolated to be treated as single openings. Pillars are the un-mined rock left between the roof and floor of an underground opening or between openings, which together with the sidewalls (abutments) of the mined area support the overlying strata. The strength and deformational behavior of pillars constitute a most important part of the design of multiple openings.

The simplest method of pillar design and safety assessment is to calculate average vertical pillar stress (assuming a horizontal deposit) and compare this with rock (pillar)

strength. This analysis gives a safety factor as an index of pillar stability. An early review of pillar loading problem by Denkhaus (1962) showed that the only general analytical expression for predicting pillar loading was based on the tributary area method suggested by Duvall (1948). This was further confirmed in a more detailed literature survey by Coates (1965). Later on, Salamon (1967) suggested a method for designing pillar workings based on statistically derived pillar strength formula. Since then, numerous empirical equations have been proposed to calculate the ultimate strength of pillars. Logie and Matheson (1983) examined the fundamental assumptions, limitations, and areas of application of ten design formulae that had been most frequently utilized. They divided the reviewed equations into 4 categories: acceptable, use with caution, unacceptable and no experience. They also provided a convenient table to present their recommendations. Numerous comprehensive *in situ* instrumentation programs were also implemented that provided a mine wide monitoring as well as calibrations for various pillar design approaches (e.g., Dreyer and Borchert 1965; Beek et al. 1984; Lu 1986; Conover et al. 1989). These include the development of data acquisition systems for achieving automation in excavation instrumentation (De Souza, 1992 and 1991).

When mining in soft rocks, such as salt and potash, stresses around underground cavities often exceed the yield limits of the host rocks and the material therefore behaves plastically. The basic theories adopted in pillar design in plastically deforming ground include general elasto-perfectly plastic theory, and elasto-plastic with strain hardening and strain softening after yield. An example of pillar design in plastically deforming rocks was given by Mraz and Eng (1984). The design equations were derived on the basis of

a concept of a generalized perfectly plastic substance and the design procedures were based on both *in situ* measurements and laboratory tests. Mroz and Nawrocki (1989) conducted a theoretical analysis of soft pillar deformation between strong roof and floor based on an elasto-plastic model with strain softening after maximum strength. Pietruszczak and Mroz (1980 and 1981) provided a numerical solution for a similar problem in which strain hardening was also considered. A recent research on the design of pillars in soft rock was given by Hambley (1989). In this paper, the literature on pillar design was systematically examined, starting from a brief review of pillar design methods in hard rock and coal, since these methods are often borrowed for use in salt rock mining. Pillar design methods in salt were reviewed in detail by grouping them into 4 categories: simplistic approaches, confined-core pillar design approaches, approaches involving numerical modelling, and the approach of Mraz and associated researchers. The methods run the gamut from simplistic approaches, using rules of thumb for width/height ratios that result in stable conditions, to sophisticated viscoelastic-viscoplastic computer based numerical analyses. The effects of pillar size and shape on pillar strength were also discussed. A method for designing pillars based on the stress distribution at steady-state conditions was developed with examples provided to demonstrate its application.

General elasto-plastic theory has been found insufficient because of the significant time dependent properties of soft rocks. Pillars in such a medium exhibit conspicuous time-dependent behavior which must be taken into consideration in mine design. Although there has been a wealth of published information on the time-dependent behavior of evaporitic rocks, most of the information has been deduced from laboratory tests on small

specimens. The application of such information to mine practice has usually been hindered due to size effects and the complexity of stress conditions prevailing *in situ*. Because of these problems, the concept of utilizing model pillars for design purposes has attracted considerable attention since its initiation in the middle 1960's (Obert 1964 and 1965; Bradshaw et al. 1964; Lomenick and Bradshaw 1969; King and Acar 1971; King 1973; Russel and Lomenick 1984; Hunsche et al. 1985). Such experiments intend to simulate, to a fair degree of approximation, the behavior of *in situ* pillars considering the effects of constraints supplied by roof and floor. For soft materials like salt, this simulation is of prime importance since the mechanical behavior of roof, pillar and floor is integral.

Today, one of the most important concepts in pillar design in potash and salt mining is *yield pillar*. Over a period of more than 15 years, Mraz and his associates have developed and demonstrated a method that combines laboratory testing, underground observations and theoretical calculations (Mraz and Eng 1984; Mraz and Dusseault 1986a). The design philosophy is based on a stress-relief concept and the use of yield pillars, similar to that of Baar (1977) and Serata (1983). The method is well known as the *stress control method* (Serata 1983). Although there are advantages and disadvantages with this method (See Hambley 1989 for a summary), its application has expanded to a wide variety of underground mine openings in weak and complex ground through more than a decade of field experience. Thus, yield pillars are becoming widely used in underground excavations in a variety of geological conditions.

*Yield pillars* are pillars in the mined panels which are designed to yield at appropriate, designed rates during their service life. Over a period of time, yield pillars transfer load to the adjacent stiff pillars or surrounding rocks so that the entry-pillar system remains stable (though still deforming). As the principal tool of stress control methods, yield pillars are used to induce and control the redistribution of stresses around mine openings. For example, the parallel room technique provides the stress control necessary for room stabilization through the use of yield pillars (Figure 2.2), where a

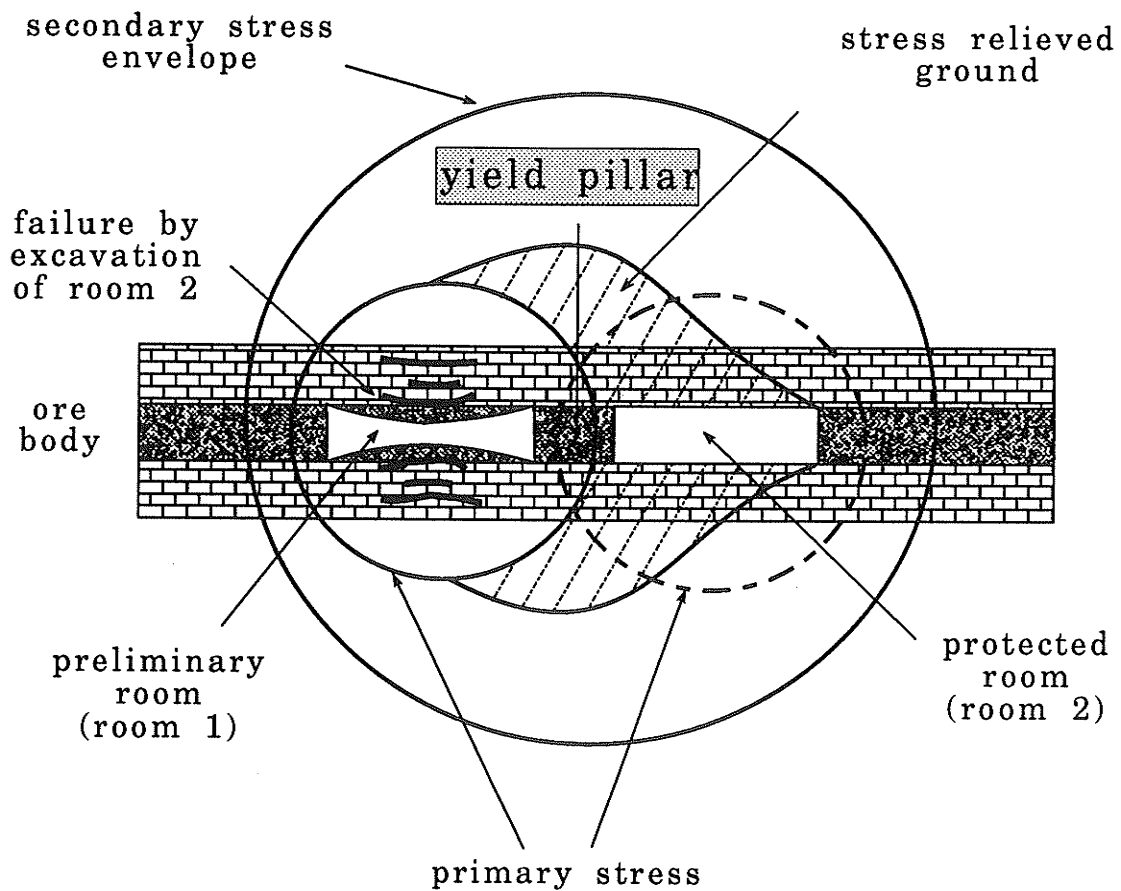


**Figure 2.2** Parallel-room technique for stabilizing protected room separated from preliminary room by a yield pillar. Deformation of yield pillar permits development of the secondary stress envelope (after Serata 1983).

stable second room is achieved by excavating it parallel to a first room excavated earlier, with a narrow yield pillar separating the two. The first room will be damaged by the excavation of the second room close by. The second room, via sacrifice of the first room and the formation of a secondary stress envelope surrounding both rooms, is protected (Serata 1983). Most attention concerning the application of this method has been on the effect of yield pillars on stress redistribution and on the opening itself (Kripakov 1981; Chen and Karmis 1988; and Tsang et al. 1989). Hardly any attempts have been made to study the progressive deformational mechanisms of yield pillars. In the author's opinion, lack of knowledge on yield pillar deformational mechanisms is a deficiency in the research of the stress control methods, because yield pillars play a critical role in the application of these methods. A more detailed review of the development of various stress control techniques will be given in Chapter 3, where the mining methods used in Saskatchewan potash mines are introduced.

### 3. POTASH IN SASKATCHEWAN - Mechanical Behavior and Mining Methods

#### 3.1 Introduction

Potash was first discovered in Saskatchewan in 1943 during oil exploration drilling in the southern part of the province. The first attempt to sink a shaft to the deposit was made in 1952 in Unity, west of the city of Saskatoon. Since then, 11 companies have been involved in Saskatchewan potash mining. A detailed history of company involvements can be found in Fuzesy (1982).

The potash bearing units in Saskatchewan occur in the Prairie Evaporite Formation that extends over 1000 miles from northernmost Alberta to North Dakota (Figure 3.1).

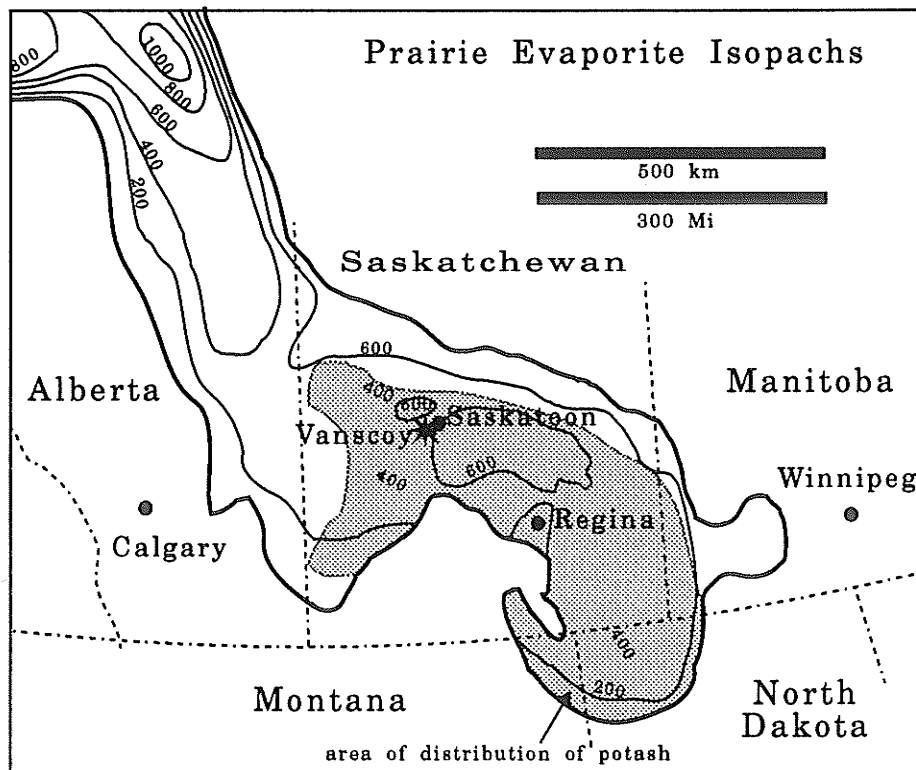


**Figure 3.1** Isopach map of the Prairie Evaporite Formation (after Holter 1969). The unit of the isopachs is feet.

The Formation rests conformably on the older Winnipegosis Formation, is overlain disconformably by the Dawson Bay Formation, and is of middle Devonian age (Figure 3.2). The potash deposit that is currently mined occurs at a depth around 1100 meters. Saskatchewan potash is composed predominantly of medium to coarse grained sylvite (potassium chloride, KCl) and halite (sodium chloride, NaCl) crystals with some carnallite (potassium magnesium chloride,  $KMgCl_3 \cdot 6H_2O$ ) and interstitial clay. A detailed geological background can be found in Worsley and Fuzesy (1979), Dunn (1982), and Dunn (1983). In addition, Mackintosh et al (1983) discussed some geological anomalies observed in the mines and Mollard (1988) introduced the regional tectonic framework in southern Saskatchewan.

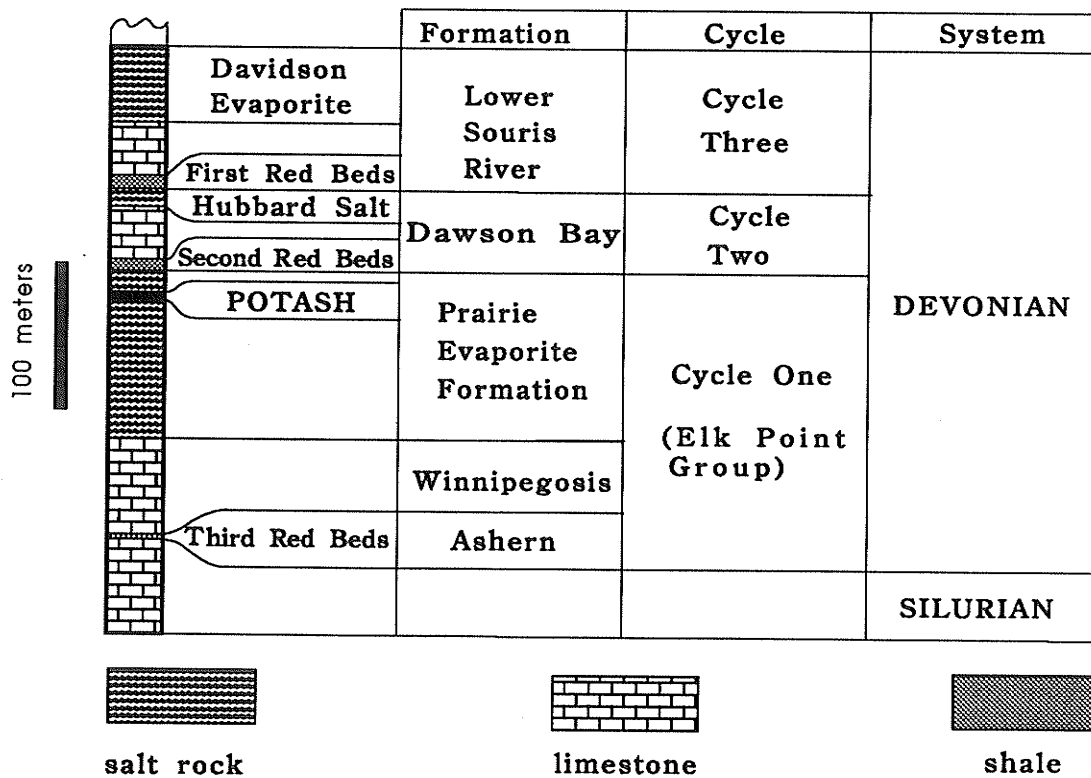


**Figure 3.2** Columnar section showing Middle Devonian Evaporite cycles in Saskatchewan. Potash layer occurs at a depth of 1100 meters (after Lane 1959).

Figure 3.3 provides a detailed stratigraphic column for the immediate mining areas in Cominco Mine at Vanscoy, Saskatchewan. The immediate roof is a salt layer that is usually known as *salt back*. The immediate floor comprises potash layers. Clay seams often present in potash and salt, and in overlying and underlying strata.

### **3.2 Challenges Facing the Potash Industry in Saskatchewan**

In the early years of mining, the most important problem was room stability and convergence. Changes in mining layout and room sequencing are devised to have ameliorated these problems (Serata 1983).

Other critical challenges facing the potash industry in Saskatchewan are water inflow and mining induced seismicity. Ever since potash mining began, the hazard of water inflows has been a major concern. One of the most difficult tasks has been the sinking of shafts due to the presence of water-bearing formations, especially the Blairmore Formation (a poorly consolidated unit of sand and shale). The water pressures in the Blairmore Formation are as high as 5500 KPa (Fuzesy 1982). Of the 17 potash shafts sunk in Saskatchewan, five had major water inflows during shaft sinking. One mine was abandoned completely during production because of water problems (Prugger and Prugger 1991). Another concern is the ever-present hazard of potential brine inflows into mine openings from permeable units in both the hanging wall (carbonates of the Dawson Bay Formation, 15 m to 50 m above the mining level) and the footwall (carbonates of the Winnipegosis Formation, 50 m to 150 m below). The awareness of this hazard has been reflected in conservative overall extraction ratios (35 to 40 percent).



Another challenge, mining induced seismicity, has surfaced in more recent years as the area of mining increased. Mining induced seismicity has been well investigated (Gendzwill 1978, 1984 and 1989; Gendzwill et al. 1982; Gendzwill and Prugger 1987 and 1988; Gendzwill and Lundberg 1989; Sepehr 1988; and Ahmed 1990).

### 3.3 Mining Methods

Saskatchewan potash mining started with a conventional room and pillar mining technique adopted from New Mexico and West German potash mines. However, potash producers in Saskatchewan soon found that this technique was not suitable due to the complicated stratigraphic conditions such as the presence of clay seams, thin saltback, the great mining depth, and the apparent viscoplastic properties of potash. Eventually, the method was abandoned and replaced by various stress-control techniques based on the *stress-relief* concept and the formation of an *effective opening* (Serata 1983). These methods can be grouped into 6 categories - stress relief, parallel room, time-control, compounded time-control, multiple-level, and large room techniques. The theoretical principles of mine design based on laboratory testing of elastic materials, including photo-elastic experiments, postulated vertical normal stress peaks near the walls and horizontal normal stress peaks near the roof and the floor of underground openings (Hoek and Brown 1980). Connecting these peaks tangentially results in a *stress envelope* around mine openings (Baar 1971). According to Serata (1968), creep would be restricted to the interior of such theoretical stress envelopes with the envelope bounding the *effective opening*. Outside this envelope, rock would remain elastic and would provide stable

conditions. This concept, known as *stress relief theory*, states that wider rooms generate a larger stress envelope around the opening compared to narrower rooms. Consequently, the wider room creates a greater stress relieved zone in the roof and floor and the room will be more stable even without the use of yield pillars, provided that the ground is competent and there are no planes of weakness above and below. This is the *stress relief technique* and is shown in Figure 3.4. The method has been successfully used at the IMC's (the International Minerals and Chemical Corp.) mines at Esterhazy, and in the Rocanville Div. of PCS (Potash Corp. of Saskatchewan).

One step beyond the stress relief technique is the *parallel room technique* using yield pillars, which has been briefly introduced in Chapter 2 and illustrated in Figure 2.2. The process shown in Figure 2.2 can be repeated a number of times, forming a multiple-parallel-room entry with the protection of the stress-relieved zone passed in relay fashion to the opening most recently excavated. This method has been frequently applied by Cominco, the Cory Div., Rocanville Div. PCS, and Lanigan of PCS.

In extremely weak ground, often characterized by complex roof strata with clay seams, the parallel room method is insufficient for securing long-term stability. In such cases, the *time-control technique* of stress control has been adopted, which, as the name signifies, requires sequential excavation of parallel openings. Figure 3.5 illustrates a basic application of this method. Two openings are created at some distance apart to form their own stress envelopes with a strain hardened wide pillar in between. After a certain period of time, a third room is excavated through the strain hardened ground. Once the inner opening is created, the pillars yield, forming a larger stress envelope and thus generating

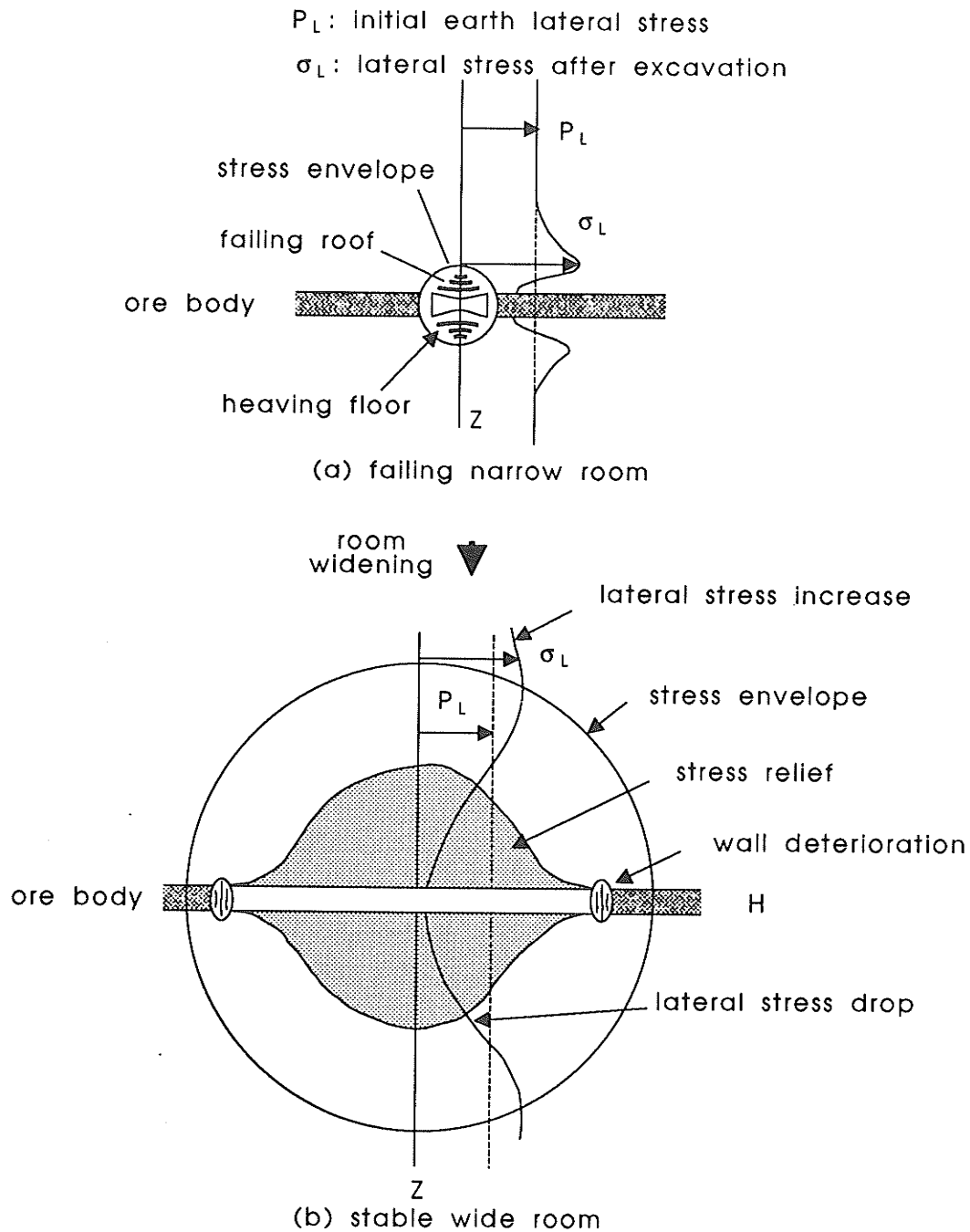


**Figure 3.4** Formation of stress-relieved ground for stabilizing mine openings by the *stress relief* technique of stress control (after Serata 1983).

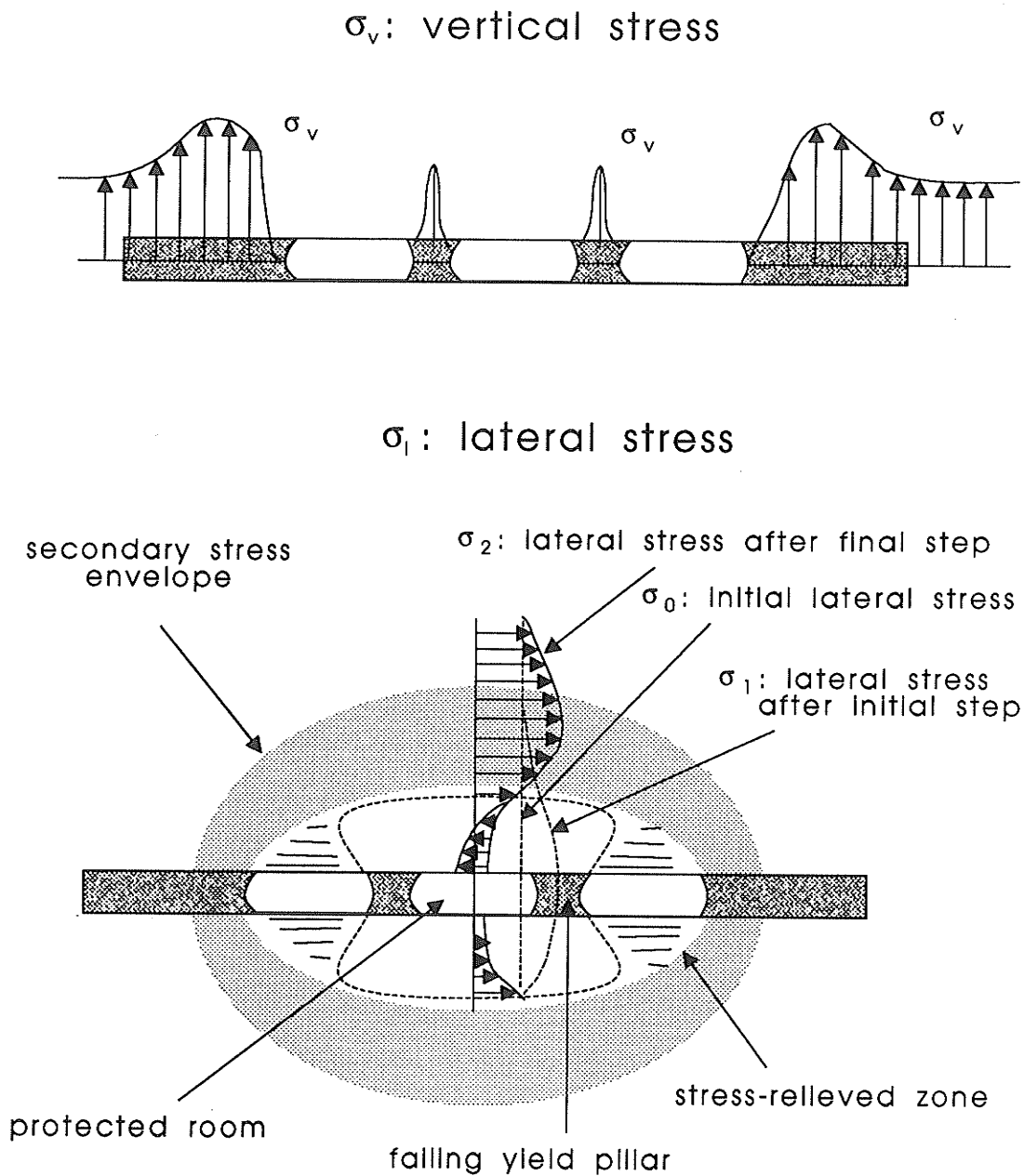


**Figure 3.5** Stabilized condition after excavation of protected room in the *time control* technique illustrated by profiles of vertical and lateral stresses, indicating formation of a secondary stress envelope (after Serata 1983).

a stable central entry. This method is used in sequential cutting of three, four and five entry systems. Generally, in successful use of this technique, the outside entries are cut first, yield pillars are left in between, and finally the middle entry, or entries, are excavated. The technique has been applied successfully at Cominco, PCS Cory, PCS Allan, and Central Canada Potash in Saskatchewan.

Figure 3.6 analyzes the mining sequences and development of stress envelopes of a 5-entry mining system used at the Cominco Mine, where the yield pillar study described in this thesis was conducted. It is actually a combination of the parallel room technique and the time-control technique. The control rooms are two pairs of rooms each excavated by utilizing the *parallel room technique* illustrated in Figure 2.2, in which two *secondary* stress envelopes are formed by yielding of the first yield pillar pair (Figure 3.6a). These two *secondary* stress envelopes are separated by a strain hardened wide pillar. After a certain *delay time*, a fifth room is excavated through the strain hardened wide pillar. The second yield pillar pair is designed to yield immediately upon its formation via the excavation of the inner, protected room. In the pillar yielding process, the separated two *secondary* stress envelopes surrounding the earlier room pairs and a new *primary* stress envelope surrounding the new room are transformed into a single *tertiary* stress envelope, as shown in Figure 3.6b. This *tertiary* stress envelope shields the entire 5-room system, resulting in a stable condition.

Other stress control techniques have also been practiced in Saskatchewan potash mining, including some new techniques which are still at an experimental stage, such as bi-level mining (two potash seams at different depths).

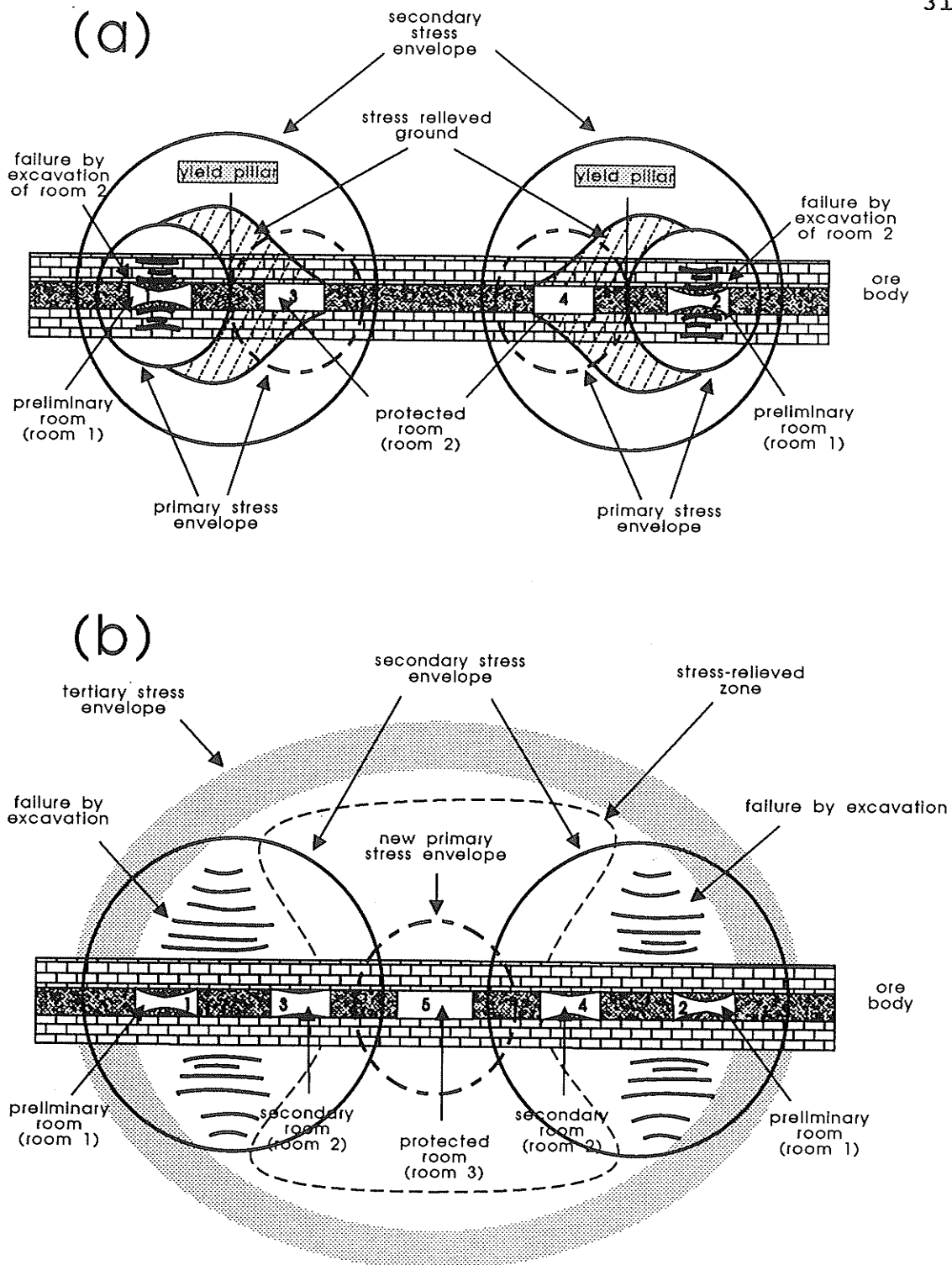


**Figure 3.6** Mining sequences and the development of stress envelopes of a 5-entry mining system used in Cominco Mine at Vanscoy, Saskatchewan.

The process of improving mining methods is essential for increasing extraction ratios commensurate with safety. Various theoretical and experimental rock mechanics research projects have made and will continue to make numerous contributions to this process to improve Saskatchewan potash industry. In the following section, the related research is briefly discussed.

### **3.4 Rock Mechanics Related Research in Saskatchewan Potash Mining**

Research projects on rock mechanics related problems in potash mining in Saskatchewan have been pursued at various levels. One of the examples is a two-year program funded under START (Short Term Assistance in Research and Technology) by the Government of Canada during 1983-1985. The program addressed several topics: regional mine stability, a review of mining options based on potash mining around the world, the development of a two-dimensional finite element model, testing of waste salt as mine backfill, assistance to establish a creep testing facility in Saskatoon, assessment of underground dust levels at work headings, and the evaluation of excavation performance in the field. As summarized by Herget et al. (1985), no final solutions were obtained for all the concerns of the potash industry, relating to ground control and alternatives to present mining methods. However, progress has been made in sharing information on ground control and mining experiences amongst operators.

During 1986 to 1988, a project entitled "identification of input parameters for numerical modelling of potash strata at IMC" was carried out by IMC and Mraz Project Consultants Ltd (MPC). The objective of this project was "to install rock mechanics

instrumentation in selected mining panels and record the pressure changes in the pillars, roof and floor as mining progressed through these panels". As reported in MPC (1988), these results, combined with laboratory testing of core samples from the mining panels, were used to calibrate numerical models. Once the numerical model has been calibrated with this field data, existing mining panel geometries could be characterized and other mining geometries could be tested with an objective to optimize ore recovery under different mining conditions. Instrumented openings have also been implemented in other potash mines.

An earlier example of research on the mechanical properties of Saskatchewan potash can be found in Serata (1968), in which the time-dependent behavior of potash was examined based on tensor analysis and the development of an absolute triaxial testing machine. Material properties, such as octahedral shearing strength, Poisson's ratio, visco-elasticity and visco-plasticity, were identified as fundamental to potash behavior. Since then, a few other laboratory as well as *in situ* investigations have been carried out on potash deformational properties. They yielded quite different values for specific properties which made comparison impossible (e.g. Coolbaugh 1967; Baar 1971, 1972 and 1973; King 1973; Ladanyi and Gill 1983).

Recently, a systematic laboratory investigation on rock mechanics related problems in potash mining in Saskatchewan was carried out in the Departments of Civil and Geological Engineering, University of Manitoba. A three year project entitled "Mine Stability in Potash Mining", was performed under NSERC's University/Industry Cooperative Research Program from 1985 to 1988. The two major components of this

project were the assembly of a finite element computer code to simulate the deformation of mine workings in highly deformable salt rocks and laboratory investigations into the mechanical properties of both the Dawson Bay Formation and potash. Detailed research results were well recorded in the project report (Lajtai et al. 1988), relevant publications (Lajtai and Duncan 1988; Sepehr and Stimpson 1988*a*; Sepehr and Stimpson 1988*b*), and graduate theses (Kroll 1987; Sepehr 1988; Chaudler 1989; and Ahmed 1990). A second phase of the program was operated from 1988 to 1991, with the overall goal of improving the understanding of mining-induced deformation and fracturing around deep underground potash openings. A detailed record of the progress and the initial results can be found in project reports (Lajtai 1989, 1990, and 1991), publications (Lajtai et al 1991*a* and 1991*b*; Carter et al. 1991*a* and 1991*b*; Carter 1992*a*; Carter et al. 1992; Stimpson and Ahmed 1992; Stimpson and Chen 1993; Chen et al. 1993; Chen and Stimpson 1993*a* and 1993*b*) and graduate theses (Duncan 1990; Carter 1992*b*). The research reported in this thesis is also part of the project. In the following paragraphs, the related results are reviewed in more detail.

A laboratory investigation was conducted to establish the mechanical properties of the Dawson Bay limestone (Kroll 1987) and its potential mode of failure due to mining of the potash beneath. Brittle failure of intact carbonate limestone involving the formation of a *dome-shaped* fracture surface was affirmed as a possible mode of failure which would also produce seismicity (Sepehr and Stimpson 1988*a* and 1988*b*; Ahmed 1990; Stimpson and Ahmed 1992). Recently, Morgenstern and Sepehr (1991) published an

extension of Sepehr's earlier finite-element modeling (Sepehr and Stimpson 1988a) to include the effect of ground water pressure on the Dawson Bay carbonates.

As regards the deformation of Saskatchewan potash, a data base has been developed through years of experiments at the University of Manitoba. Potash has a uniaxial compressive strength around 25 MPa, a uniaxial tensile strength 1-2 MPa, a Young's modulus in compression around 20 GPa, and a Poisson's ratio varies from 0.1 to about 0.3 (Carter et al. 1991b). A general potash stress-strain curve under compression was subdivided into three parts: a low stress, quasi-elastic region, an intermediate stress, ductile region, and a high stress, brittle (microfracture) region. Possible deformational and fracturing states around cavities were classified as: pre-fracture (pre-microfracture initiation), yielding, microfracture propagation (initiation to the onset of dilatancy), dilatancy (onset of dilatancy to failure) and post-failure (Lajtai and Duncan 1988). These states are separated by the crack initiation stress ( $C_i$ ), the yield stress ( $C_y$ ), the crack damage stress ( $C_d$ ), and the failure stress (peak strength), respectively (Figure 3.7). Variation of these states with confining pressure was also examined (Figure 3.8) and the maximum principal stress ( $\sigma_1$ ) at crack initiation, yielding, crack damage and failure were found to be functions of the minimum principal stress ( $\sigma_3$ ). Through a curve fitting exercise, a new strength criterion was developed known as the *Rocker* function (Carter et al. 1991b). This criterion was used in a finite element program, originally developed by Ayari (1991) for the SIMulation of Mining EXcavation (SIMEX), to investigate the stability and fracturing of potash openings (Yuan and Lajtai 1991). The viability of the *Rocker* function, fracture propagation criteria, and the finite element program was tested

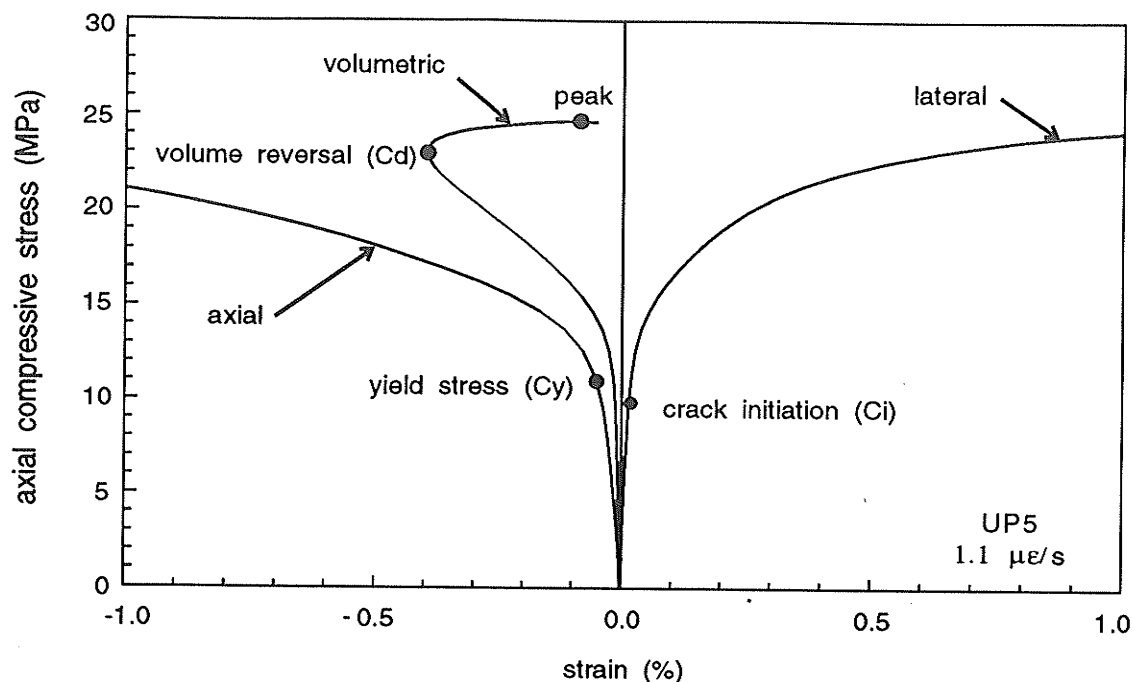


Figure 3.7 Stress-strain curves from a uniaxial compression test of the ductile Lanigan potash rock displaying all stages of fracture: initiation ( $C_i$ ), yielding ( $C_y$ ), damage ( $C_d$ ) and failure (after Lajtai et al. 1991a).

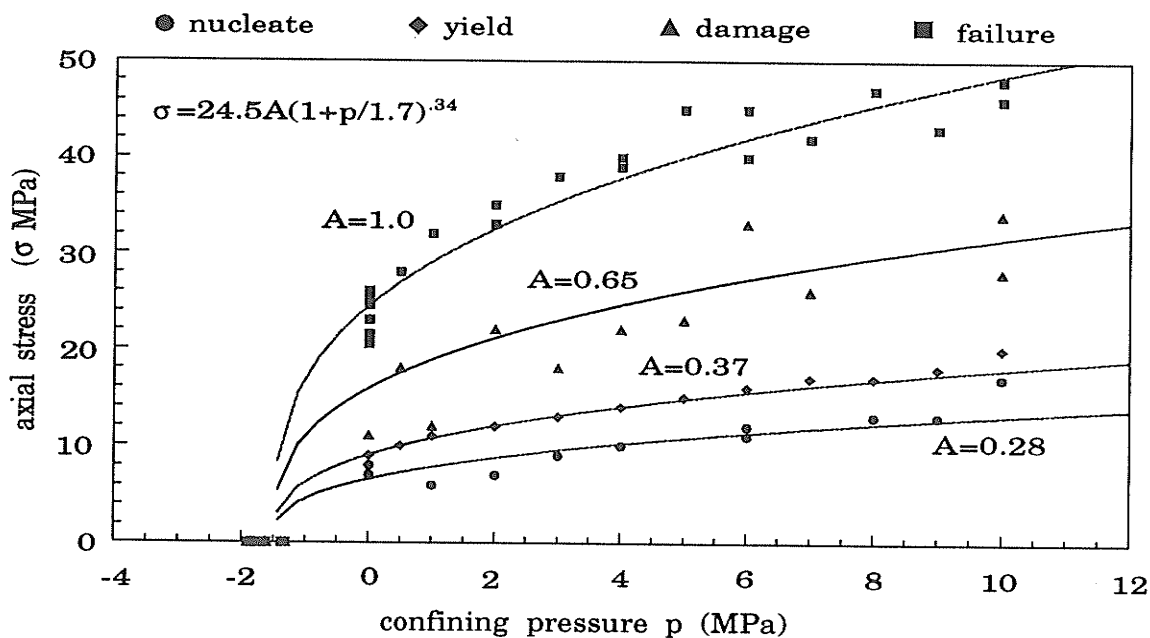


Figure 3.8 Triaxial fracture parameters for Lanigan potash rock, a salt rock from Saskatchewan (after Lajtai et al. 1991a).

by reproducing stress dependent cracking similar to that obtained around cavities in physical models (Carter and Lajtai 1991).

Other testing programs on potash in the Department of Geological Engineering, University of Manitoba, included rate dependent investigations and creep tests. The effect of strain rate on potash strength has been evaluated and incorporated in general strength criteria, including the aforementioned *Rocker* function (Lajtai et al. 1991b). It was found that a potash rock specimen may go through all three stages of creep: primary or transient stage, secondary or steady state stage, and tertiary or accelerating strain stage, depending on the uniaxial stress level (Lajtai and Duncan 1988). In the usual 3 to 5 month tests, both the axial and the lateral creep strains attenuate at the transient stage. At a uniaxial stress above about 13 MPa, the dominant mechanism of deformation is microcracking because lateral and volumetric strain dominates over axial strain. The lateral creep strain curve may then display the transient and the steady-state, or all three stages of creep, while the axial strain usually attenuates or enters tertiary creep directly from the transient stage. Attempts have been made to model a full series of creep curves through a closed-form expression and by a unimodular model for the axial strain and a bimodular model for the lateral strain (Duncan 1990; Duncan and Lajtai 1991).

## 4. CRITIQUE AND OBJECTIVES OF THESIS

### 4.1 Critique

As reviewed in previous sections, there exists an extensive body of literature on the mechanical properties of salt rocks as well as the behavior of mine structures in these rocks. Numerous comprehensive uniaxial and triaxial rock tests have been conducted, various viscoelastic, viscoplastic and superposition integral theoretical models have been established, and multi-dimensional deformation-mechanism maps constructed. As regards mine structure responses to underground excavation, emphasis has been placed on laboratory and theoretical analysis of simplified opening models such as single cylindrical openings and model pillars. Numerical approaches have been adapted for solving non-linear theoretical models, handling complicated opening geometries, and simulating progressive failure processes. Various comprehensive *in situ* measurement programs have also been implemented for the calibration of experimental, theoretical and numerical models. However, there are some problems which have received relatively limited study. Some of these are addressed in this thesis.

Most existing tests involve uniaxial or triaxial creep (change in strain under constant stress, i.e. zero stress rate) and most material models are creep equations. Stress relaxation phenomenon (decrease in stress under constant strain, i.e. zero strain rate) is an alternative reflection of time dependent properties. Relaxation tests might provide another means for understanding rock deformational mechanisms, especially when performed along a reversed loading path (Duncan 1990) similar to the *in situ* loading. Moreover, certain aspects of time-dependent properties, such as the possible existence of

a creep limit (a stress-strain curve on which both stress rate and strain rate are zero), can be proved more easily by relaxation tests than by creep tests (Haupt and Natau 1988). The relaxation phenomenon has not been well addressed in the existing research, although remarkable stress relaxation effects have been observed in rock salt mines (Balthasar et al. 1987).

Another important aspect that has been largely ignored is the possible variation of material constants with the direction and magnitude of the principal stresses. One example of such variation is material bimodularity. *Bimodularity* refers to the property of a material with different Young's moduli and Poisson's ratios in tension and in compression. The bimodular behavior of rock is of practical significance because it influences stress, deformation and fracturing, especially around mine openings and in certain indirect rock tensile tests where there exist bi-axial tension-compression stress states.

Research on the *salt back* (roof) in Saskatchewan potash mining is overlooked, although the roof plays a critical role in overall room stability. Salt bimodularity should be taken into account when analyzing roof behavior.

Although almost all operating potash mines in Saskatchewan use stress-control excavating techniques that involve multiple openings, most of the research has been limited to single excavations. The most important design feature of multiple openings in salt rocks is *yield pillar*. However, the actual nature of deformation within yield pillars is poorly understood. Efforts to address yield pillar deformational mechanisms have been limited to numerical and physical simulations, sometimes with limited and sometimes

inadequate field observations for calibrations. This is because most of the observations are of measured room closure at the initial stage of pillar deformation during mining excavation. Long term pillar deformation has not been documented.

Model pillars made of rock materials from the mines provide simulation of the effects of constraints supplied by roof and floor. However, they do not provide reasonable simulation of the highly time-dependent ductile deformation in potash yield pillars because of the limited laboratory time scale. Physical modelling that meets the similitude requirements using simulated materials are usually costly and troublesome, and have poor repeatability. A computational approach using *numerical experiments* (Fairhurst 1991) would provide much valuable information on progressive pillar deformation, is easier to perform, and will probably be more reliable.

Finally, a systematic analysis that synthesizes experimental investigation, laboratory modelling, theoretical analyses as well as *in situ* observations is desirable for the comprehensive understanding of the response of mine openings to the mechanical properties of their host salt rocks.

## 4.2 Research Objectives

Based on the identification of research deficiencies through the critical examination of the existing literature and the realistic consideration of specific problems in potash mining in Saskatchewan, five major objectives were identified for this study. Each objective defines a specific problem concerning either laboratory or *in situ* deformational

characteristics of Saskatchewan potash and salt rocks. Altogether, they contribute to a greater understanding of the behavior of salt rocks. The objectives are as follows:

1. A laboratory study of the mechanical behavior of potash, especially the general stress relaxation behavior, leading to more incisive understanding of the time dependent properties of potash;
2. Development of a new testing technique for direct determination of the moduli of deformation in compression and in tension and the measurement of rock bimodularity;
3. Evaluation of the practical significance of rock bimodularity, including theoretical analysis on simple structures, the development of a finite element program with bimodular capability for complex geometry and loading conditions, and the influence of bimodularity on the behavior of the salt back in Saskatchewan potash mines and on indirect rock tensile strength tests;
4. Documentation and interpretation of mesoscopic and microscopic deformational features observed within potash yield pillars at the Cominco Mine, including *in situ* mapping, rock fabric analyses, and the development of a hypothesis of progressive pillar deformation;
5. Numerical simulation based on various laboratory and *in situ* results of potash mechanical characteristics to model the progressive potash deformation and failure around underground openings.

## 5. VISCOPLASTICITY OF POTASH - Experimental Program I

### 5.1 Introduction

As reviewed in Chapters 2 and 3, salt rocks show very complex rate and stress-history dependent properties. Although many theoretical and experimental investigations have been performed to describe these properties, the emphasis has been placed only on creep behavior. Stress relaxation has been largely neglected although it has significant influence on the *in situ* stress-strain behavior. As a result, most of the existing constitutive models are based on creep tests. They show considerable imperfections and rest on substantial restrictions. In particular, they are not able to describe relaxation behavior adequately because relaxation behavior in these models is completely determined by creep behavior.

Relaxation and creep are the two aspects of material viscosity. They hold, at least, the same importance in practice. The idea of using constitutive models based on creep tests to describe relaxation is based on the assumption that relaxation and creep are controlled by the same mechanism. This assumption is insufficient because it is not proved by experiments nor by field measurements. Recently, Haupt (1991) proposed a uniaxial constitutive law based on both relaxation and creep tests that was found to be able to describe the viscous behavior of rock salt more realistically compared to conventional equations.

The practical significance of relaxation tests lay in their ability to reveal certain material properties that could not be determined by creep tests. For example, the

existence of a creep limit can be proved much easier by relaxation tests than by creep tests (Haupt and Natau 1988). Figure 5.1 shows an idealized stress-strain diagram with an assumed creep limit and with curves of relaxation and creep tests. The creep limit represents a stress-strain curve along which both stress rate and strain rate are zero. As the relaxation curve is given by a zero strain rate and a continuously decreasing stress rate, it will always terminate on the creep limit. On the contrary, a creep test has a zero stress rate but not always a decreasing strain rate and therefore it may not reach the creep limit. With the creep test, at the best, only the existence of a creep limit can be proved, but never the non-existence. Another physical property that can be studied more readily by relaxation tests is the post-failure behavior and the comparison of viscous behavior at various stages of rock deformation in a single test.

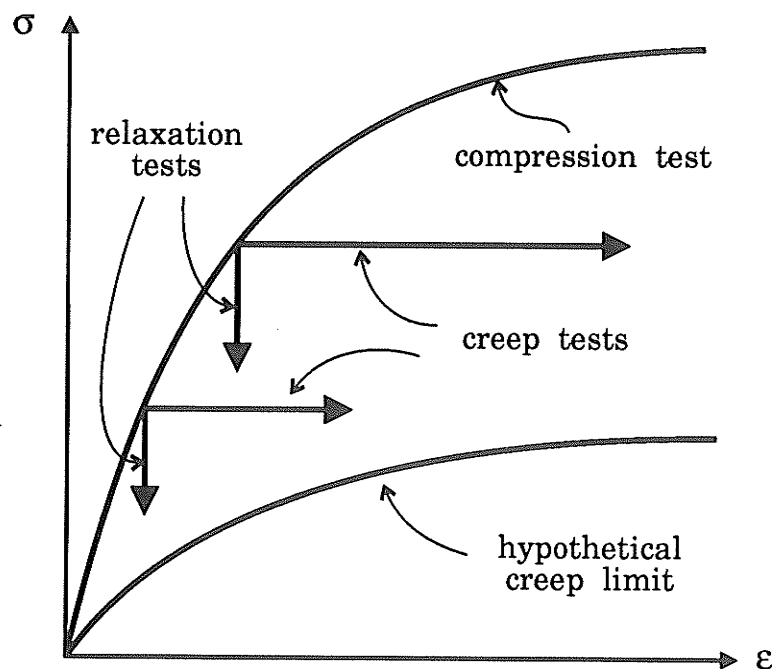


**Figure 5.1** Idealized stress-strain diagram with an assumed creep limit ( $\dot{\sigma}=0$ ,  $\dot{\epsilon}=0$ ) and with curves of relaxation and creep tests. A relaxation test will always terminate on the creep limit, but a creep test may not reach the creep limit (after Haupt and Natau 1988).

In this chapter, the general characteristics of time dependent behavior of potash before and near failure are investigated by performing reverse loading triaxial tests that simulate the *in-situ* loading path around underground cavities and by stress relaxation tests at various stages before and after yielding along the reversed loading path. Although, the obtained experimental results are insufficient to establish any explicit constitutive equations and to conduct precise quantitative analysis, it is possible to qualitatively discuss the existence of a creep limit and the relaxation behavior of potash before and near failure. In addition, attempts are made to extend Haupt's uniaxial constitutive model (Haupt 1991) to incorporate confining pressure and to fit the experimental data into the extended constitutive equation.

## **5.2 Testing Equipment, Data Acquisition and Sample Preparation**

### **5.2.1 Testing equipment**

The loading system was an Engineering Laboratory Equipment Ltd. (ELE) 100 kN constant displacement rate loading frame with 42 displacement rate settings. This system behaved as a *stiff* test frame compared to the relatively *soft* potash and enabled the investigation of the full stress-strain curves. The load cell was externally positioned (C92-20K-10P3 90 kN manufactured by Transducers Inc. of Cerritos, California). A standard NX core size Hoek cell was used with a pressure transducer for the measurement of confining pressure (GP-59F-10000 70 MPa pressure transducer from Transducers Inc. of Cerritos, California). The hydraulic unit used to supply the confining pressure was a model BP3308 (Power Qube) manufactured by Enerpac of Toronto, Ontario.

### 5.2.2 Data acquisition

In all the triaxial tests, 3 types of strain measuring devices were utilized: electrical resistance strain gauges, a Linear Variable Differential Transformer (LVDT) and calibrated resistance wires.

The strain gauges were 10 mm length foil (type PA06-500BA-350) manufactured by Micro Engineering II of Upland, California, with a resistance of  $350 \pm 0.5$  ohm and a strain limit of  $\pm 5\%$ . The strain gauges and other electrical equipments were wired in a Wheatstone quarter bridge circuit similar to the one described by Duncan (1990). Six strain gauges were used for each specimen, 3 oriented to measure the axial strain and the other 3 oriented to measure the lateral strain. All the gauges were positioned at the middle height of the specimen. The strain gauges were bonded to the potash specimen surface using M-Bond A15, a high strength epoxy adhesive manufactured by Micro Measurements, Measurement Group Ins. of Raleigh, North Carolina. Strain gauges were the principal strain measuring device in this study.

A Hewlett Packard model 7DCDT-250 LVDT was oriented to measure axial displacement between the loading platen and the load cell. The LVDT was used mainly as a backup system to keep track of total axial deformation in the specimen, especially when the axial gauges failed as specimen deformation increased.

A supplemental method for lateral strain measurement employed Evanohm resistance wires manufactured by Pelican Wire Company of Naples, Florida. The wire was of 0.0508 mm diameter,  $671.92 \text{ ohm.m}^{-1}$  resistance, and was insulated with an enamel lacquer. Four wraps of wire were placed around the specimen right above or

below the strain gauges, one wrap parallel to the other without any crisscross. The two ends of the wire were soldered to two terminals bonded to the specimen, roughly 2 cm apart. A voltage can pass through the wire in the same manner as if it were a strain gauge. During a test, voltage changes across the wire were recorded and calibrated to a strain measurement. More details of the wire application and calibration were described by Duncan (1990).

The data acquisition and servo-control systems used in this study included a Hewlett Packard (HP) 75 portable computer with an extended memory and I/O interface card, HP 9114B floppy drive, HP Think Jet printer, HP 822913A monitor, Amdek 300A monitor with video interface model MC00701A manufactured by Mountain Computer Inc., a HP 3421A 20 channel data acquisition/control unit with the interface of the Enerpac hydraulic unit, and 2 Skinner electrically operated air valves model V52LB2100 manufactured by Honeywell Ltd. for the adjustment of confining pressure. The computer program that was fully integrated with the stress and strain data collection was originally developed by Duncan (1990). The program was also modified to control the application and maintenance of the confining pressure and axial stress so as to achieve the designed stress paths.

### **5.2.3 Specimen preparation**

All potash rocks used in this chapter were from the PCS Lanigan Mine, Saskatchewan. The test specimens were cylindrical with standard NX core size (53.5 mm diameter), and were cored from potash blocks with the long axis normal to the

stratigraphic bedding. Kerosene was used as lubricating fluid for the diamond drill bit because potash is highly soluble in water. The cores were subsequently trimmed using a standard cutting saw with kerosene as the lubricating fluid and the ends were ground using a machinist's lap grinder. The finished specimen length was around 106 mm.

### 5.3 Reverse Loading Triaxial Tests

#### 5.3.1 Test procedure

Reverse loading triaxial tests conducted in this study are different from conventional triaxial tests in the way in which the deviatoric stress is applied to the specimens. In a conventional triaxial test, an isotropic stress state is applied to a specimen first to a value equal to the desired confining pressure, and then, a deviatoric stress ( $\sigma_1 - \sigma_3$ ) is applied to the specimen by increasing the axial stress ( $\sigma_1$ ) while maintaining the lateral stress ( $\sigma_3$ ) constant. In a reverse loading triaxial test, the specimen is loaded first under an isotropic compressive stress state to a desired reference stress (e.g. hydrostatic *in situ* stress in the deep underground environment), and then, a deviatoric stress ( $\sigma_1 - \sigma_3$ ) is applied to the specimen by reducing  $\sigma_3$  at a desired stress rate, while maintaining  $\sigma_1$  constant. Therefore, as its name implies, this is a reverse loading procedure compared to the conventional loading path. Reverse loading triaxial tests provide a loading path similar to that induced by underground rock excavations. Therefore, it is superior to the conventional triaxial tests for the investigation of mining induced deformation around underground openings and the response of drift walls to the passage of a mining machine.

In this study, each test specimen was loaded hydrostatically to an isotropic

compressive stress state of 30 MPa, a value slightly higher than the *in situ* stress in Saskatchewan potash mines. The specimens were then isotropically compressed for a period of 24 hours to return the potash specimens to a stress state similar to *in situ*. Finally, the deviatoric stress,  $q$ , was applied by unloading the confining pressure at a constant rate through time while keeping the axial stress at the original level (30 MPa).

### 5.3.2 Testing results

As described by Lajtai et al. (1991a) and illustrated in Figure 3.7, a general potash stress-strain curve under compression can be divided into several stages of deformation and fracturing: pre-fractured (pre-microfracture initiation), yielding, microfracture propagation (initiation to the onset of dilatancy), dilatancy (onset of dilatancy to failure), and the post failure stage. These stages are separated by the crack initiation stress, the yield stress, the crack damage stress, and the failure stress (peak strength), respectively. The crack initiation stress is marked on the stress-strain diagram by the point where the initial linearity of the lateral and volumetric strain curves ends; the yield stress is marked by the first deflection point on the axial stress-axial strain curve; the crack damage stress is close to the axial stress at which dilatancy begins (the point where the axial stress-volumetric strain curve reverses); and the failure stress is the axial stress corresponding to the highest point on the axial stress-axial strain curve. The general nature of the deformational processes in triaxial compression tests, at the relatively low  $\sigma_3$  values used, is similar to that obtained in uniaxial compression tests, except that the component of volumetric deformation is much smaller and the onset of

dilatant volumetric deformation is earlier. The effect of confining pressure on the crack initiation, yield, crack damage, and failure stresses was discussed by Lajtai et al. (1991a) and is illustrated in Figure 3.8.

Four specimens were tested under the reverse loading stress path. Table 5.1 lists the specimen number, time over which the confining pressure was unloaded to zero, and constant rate at which the deviatoric stress was loaded to the specimen. Three similar tests by Duncan (1990) are also listed for comparison. These tests cover the loading rate of deviatoric stress from 0.06 MPa/h to 60 MPa/h, corresponding to an unloading time of confining pressure from 500 hours to 0.5 hours, respectively.

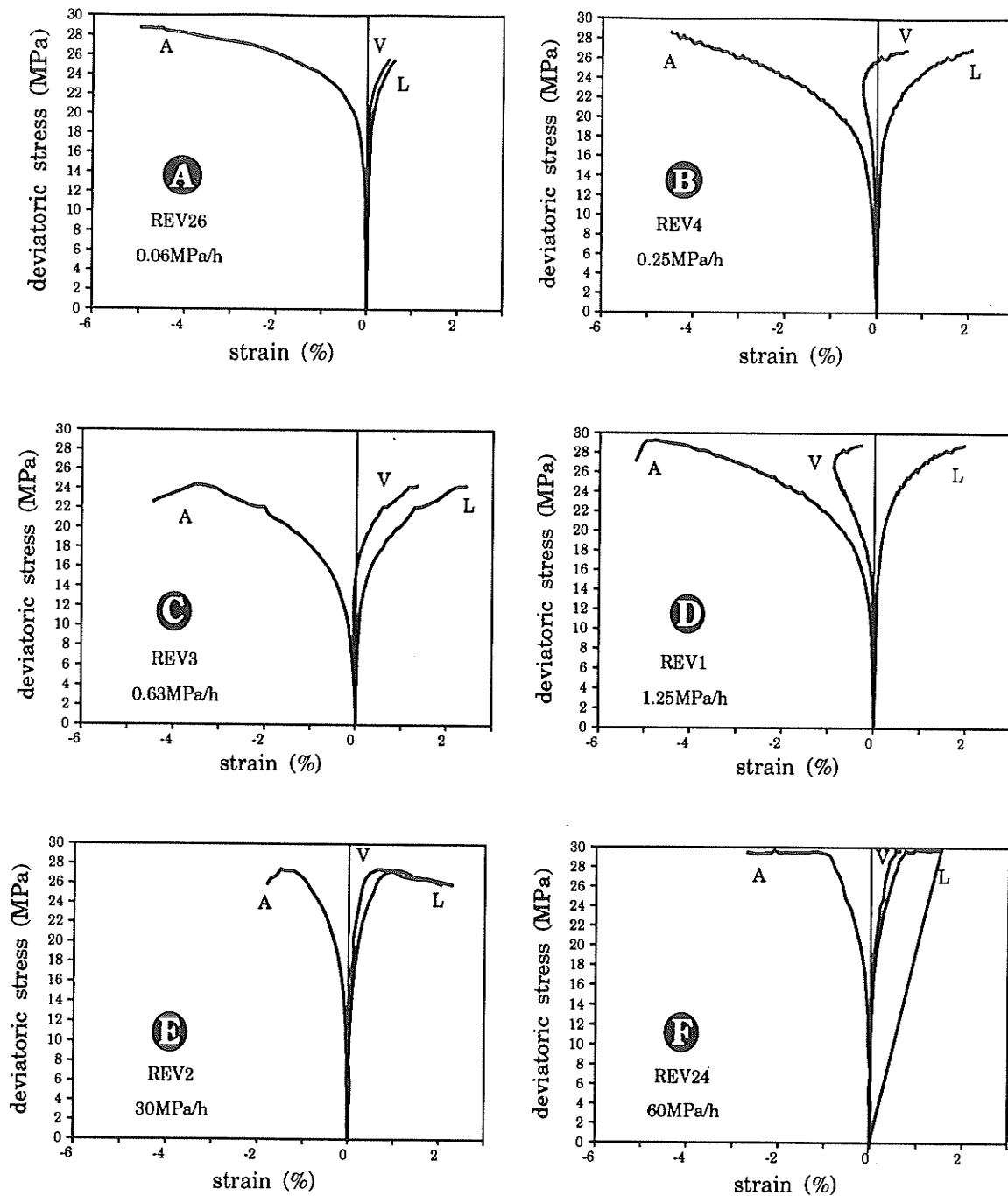
The deviatoric stress versus axial, lateral and volumetric strain at 6 different loading rates are shown in Figure 5.2. The general characteristics of the stress-strain curves in reverse loading tests are similar to those obtained in conventional compression

Table 5.1 Reverse loading triaxial tests

Specimen number	$\sigma_3$ unloading time (h)	$q$ loading rate (MPa/h)	$E_i$ (GPa)	$C_y^{**}$ (MPa)
REV4	120	0.25	11.72	2.3
REV3	48	0.63	13.03	2.7
REV1	24	1.25	19.89	3.2
REV2	1	30.0	29.08	7.6
REV26*	500	0.06	24.70	8.8
REV27*	24	1.25	31.10	9.0
REV24*	0.5	60.0	40.01	9.0

\* Tests by Duncan (1990) on Patience Lake potash.

\*\* Yield point, see Figure 3.7.



**Figure 5.2** Stress versus axial (A), lateral (L) and volumetric (V) strain curves at various stress rates from reverse loading triaxial tests on Saskatchewan potash. Tests REV26 and REV 24 were from Duncan (1990). The general characteristics of these curves are similar to those obtained from conventional compression tests (see Figure 3.7) and show a dependence on stress rate.

tests (Figure 3.7). For all applied stress rates, the behavior of potash is dominated by a quasi-elastic response up to the ductile yield point, with an initial linear elastic modulus ( $E_i$ ), a strain hardening, ductile behavior with decreasing deformational moduli above the yield point, and a strain softening response with a gradual failure process after the peak stress. The behavior is usually affected by the rate at which the deviatoric stress is applied to the specimen.

As noticed by Duncan (1990), the initial axial deformational moduli were found to have a strong dependence on the constant stress rate. For three different rates, Duncan found that the initial deformational moduli ranged from 40.1 GPa at the fastest stress rate, to 31.1 GPa at the intermediate stress rate, and to 24.7 GPa at the slowest stress rate. A similar effect was observed in this study at four different constant stress rates. The initial deformational moduli ranged from 29.08 GPa at the fastest stress rate, to 11.72 GPa at the slowest stress rate. However, the initial deformational moduli measured by Duncan are higher than those from this study (Figure 5.3 and Table 5.1), thus demonstrating significant specimen variation.

The conclusion by Duncan (1990) that the deviatoric stress at the ductile yield point remains unaffected by stress rate was not demonstrated in this study. Indeed, the initial linearity of the axial stress-axial strain curve is largely affected by stress rate. As a result, the deviatoric stress at the ductile yield point ( $C_y$ ) ranged from 7.6 MPa at the fastest stress rate to 2.3 MPa at the slowest stress rate (Figure 5.4).

The ductile behavior of potash after yield appears to be affected by stress rate as well. By comparing the stress-strain curves in Figure 5.2, one may conclude that at lower

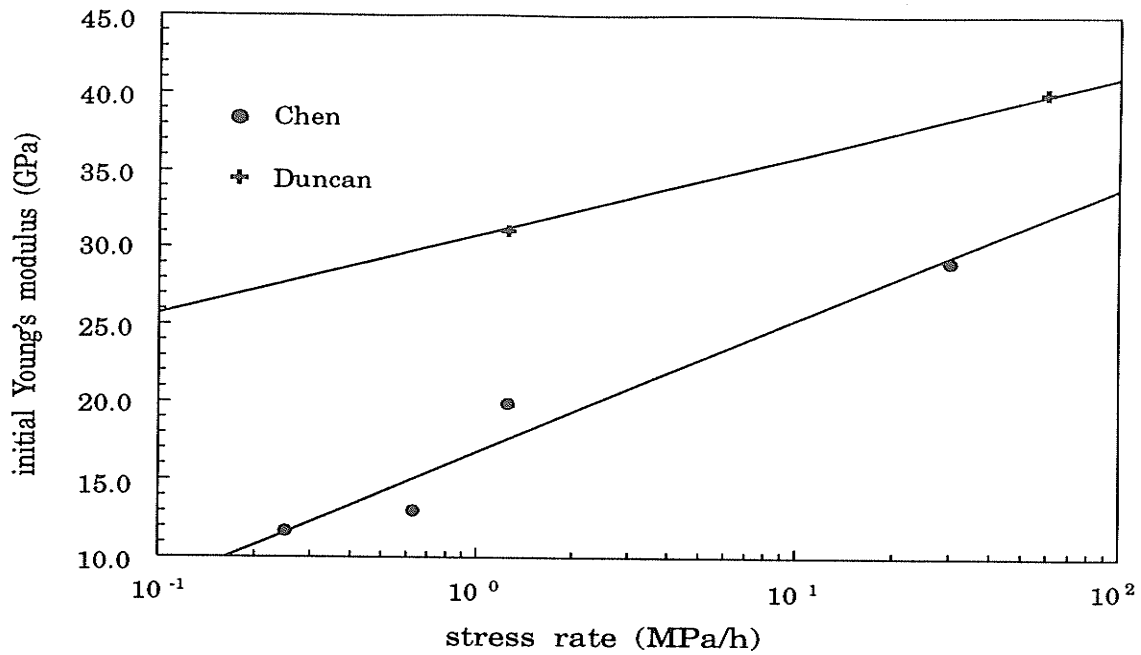


**Figure 5.3** Dependence of initial axial deformation moduli on stress rate at which deviatoric stress was applied to the specimen from the reverse loading tests on Saskatchewan potash.

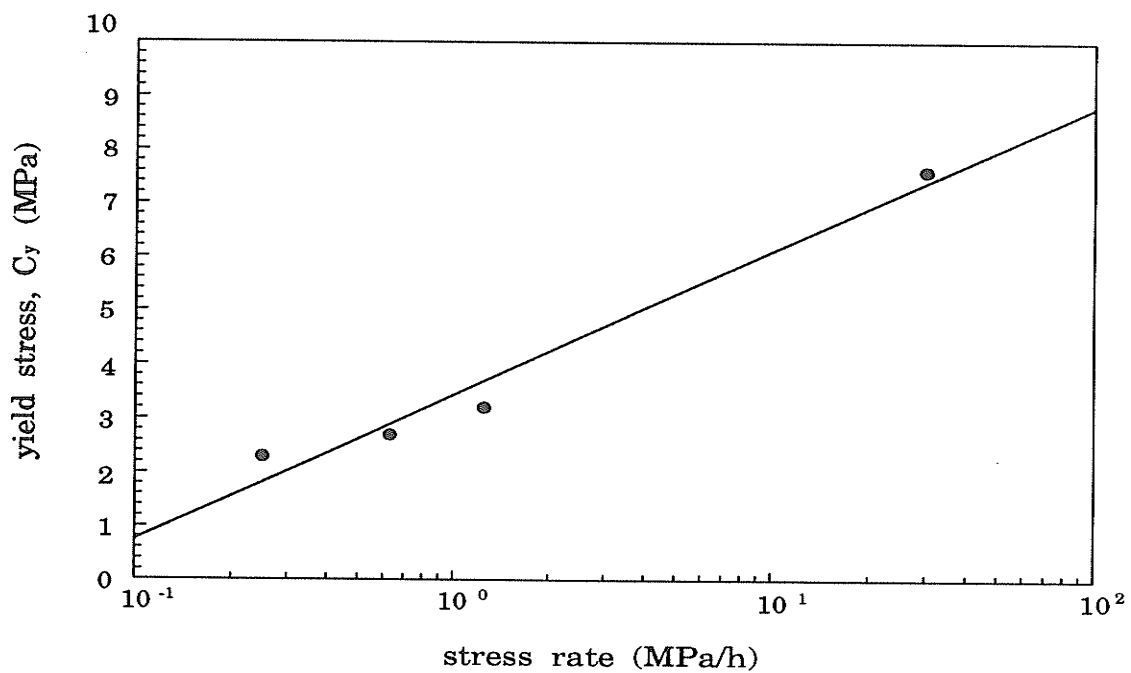


**Figure 5.4** Effect of stress rate on the deviatoric stress at the ductile yield point for Saskatchewan potash from reverse loading tests.

stress rates, the specimens undergo larger ductile deformation before reaching the peak stress than at higher stress rates.

## 5.4 Multiple-Stage Repeated Relaxation Test

### 5.4.1 Test procedure

Multiple-stage repeated relaxation tests were carried out in another series of reverse loading triaxial tests. Instead of unloading to zero at a constant rate through time, the confining pressure was reduced in increments (at a constant rate). After each increment of unloading of the confining pressure, a few axial stress relaxation cycles were performed.

In this study, each test specimen was loaded hydrostatically to an isotropic compressive stress state of 30 MPa. The specimens were then isotropically compressed for 24 hours. Finally, the deviatoric stress was applied to the specimen in a stepwise fashion by reducing the confining pressure incrementally. For each specimen, several relaxation cycles were performed at the deviatoric stress of 0 (i.e. the original hydrostatic stress state after isotropic compression), 6, 12, 18, 24 and 29 MPa. When a predetermined deviatoric stress level was reached, the confining pressure was held constant at that level, while the axial loading machine was turned off to allow the axial stress to relax. The axial stress drop  $\delta\sigma_l$ , together with the strain were recorded. After a certain relaxation period,  $t$ , the axial stress was reloaded to the original axial stress level  $\sigma_a$  ( $\sigma_a=30$  MPa in all the tests) and relaxation was repeated. Several relaxation cycles were performed at each stress level. A set of such repeated relaxation cycles at a

particular deviatoric stress stage is illustrated in Figure 5.5, where 5 relaxation cycles were performed over a period of 9 days. The first four cycles lasted for one day each, and the last one was prolonged for 5 days. After a number of reloading cycles, the axial stress was held constant again at the initial stress level of 30 MPa, while the deviatoric stress was increased at a constant rate to the next relaxation step by decreasing the confining pressure, and a new set of repeated relaxation cycles performed at the new level of deviatoric stress. Similar test procedures were used by Pushkarev and Afanesev (1973) and by Kaiser (1979) in conventional triaxial tests. The test was referred to as multiple-stage repeated relaxation test with the word *multiple* indicating stepwise loading, *stage* referring to a specific stress level and *repeated relaxation* indicating more than one relaxation cycles at each stage (Kaiser 1979). Such a testing procedure is unique in that it ensures the collection of the maximum amount of information and enables the comparison of relaxation characteristics at various stages of deformation from a single test.

Three multiple-stage repeated relaxation tests were performed. Table 5.2 lists the specimen number, constant rate at which the stepwise deviatoric stress was applied to the specimen, and number of relaxation cycles at each deviatoric stress level ( $q$ ). The time

Table 5.2 Multiple-stage repeated relaxation tests

Specimen number	(MPa/h)	Number of relaxation cycles at each stage					
		$q=0$	$q=6$	$q=12$	$q=18$	$q=24$	$q=29$
RLX3	1.25	3	3	3	3	3	-
RLX4	15.0	5	5	5	5	5	5
RLX5	30.0	5	5	5	5	5	5

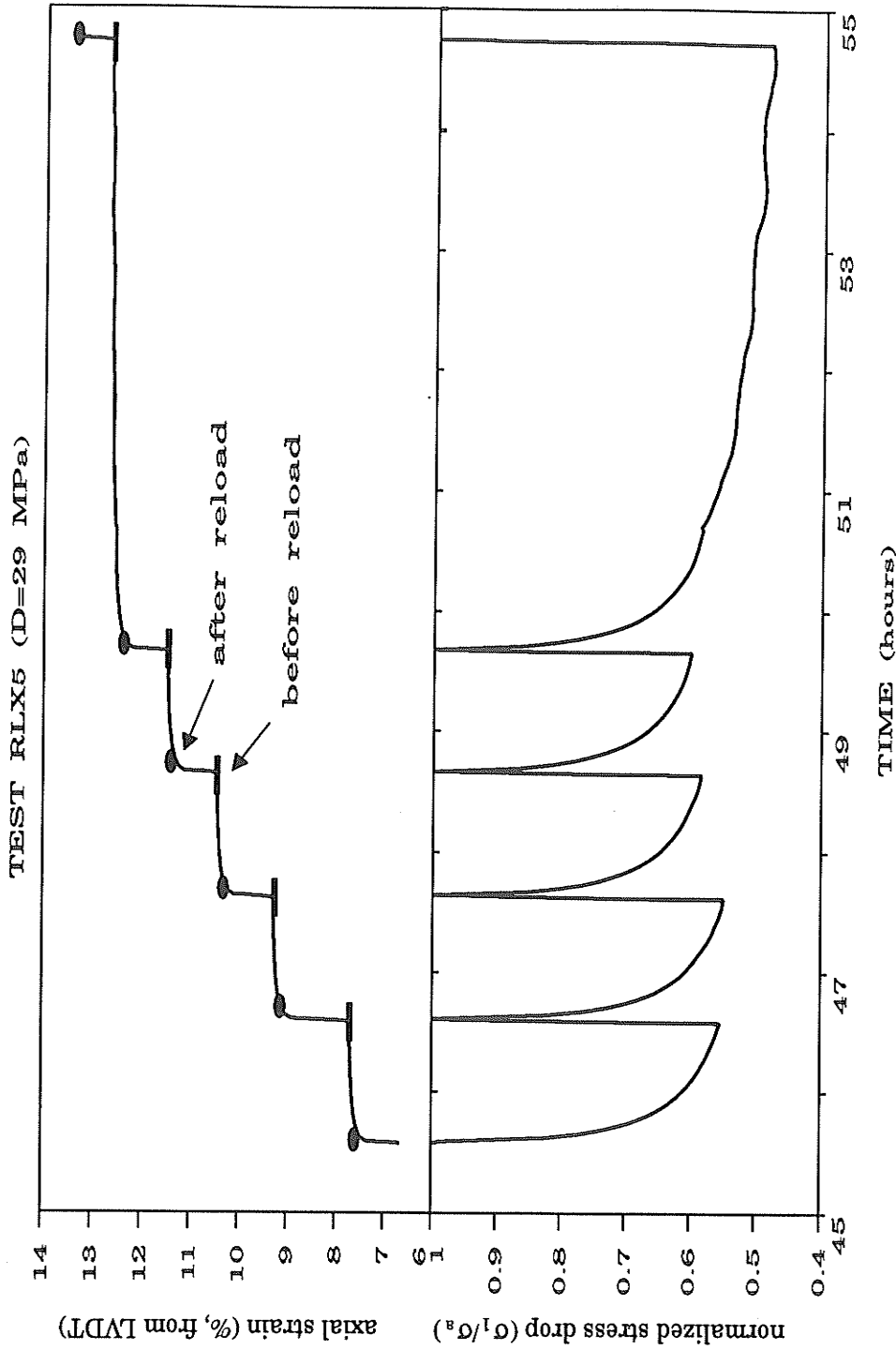


**Figure 5.5** Normalized stress drop ( $\sigma_1/\sigma_a$ , where  $\sigma_1$  is the axial stress at any time during relaxation and  $\sigma_a$  is the axial stress at the beginning of the relaxation cycle) and the total axial strain versus time for Test RLX5, Stage 6 ( $q=29$  MPa). The figure shows 5 relaxation cycles. The first four lasted for one day each and the last one was prolonged for 5 days.

period of each relaxation cycle was usually 24 hours, except the last cycle in tests RLX4 and RLX5, where it was prolonged for 5 days.

#### 5.4.2 Test results

To facilitate the discussion, the following notations are used:

- $\sigma_a$  axial stress at the beginning of a relaxation cycle.
- $\sigma_l$  axial stress at any time during relaxation (for creep tests,  $\sigma_l = \sigma_a$ ).
- $\sigma_e$  effective stress.
- $p$  confining pressure.
- $q$  deviatoric stress.
- $N_r$  sequence number of relaxation cycles at each stage.
- $\epsilon_a$  total vertical strain during relaxation. For the analysis of testing results from multiple-stage repeated relaxation tests, the vertical strain measured by LVDT was used because it provided a complete stress-strain curve, while strain gauges usually failed at earlier stages of the tests.
- $\epsilon_l$  total vertical strain at anytime (for stress relaxation tests,  $\epsilon_l \approx \epsilon_a$ ).
- $\epsilon_e$  effective strain.
- $q_{max}$  currently available strength, when, regardless of history, the rock is taken directly to failure by fast loading. In this study,  $q_{max}$  had not been reached after the confining pressure was completely unloaded from 30 MPa to zero.  $q_{max}$  for Lanigan potash in a reversed loading path is, therefore, larger than 30 MPa.
- $q_{min}$  Current long-term strength, when regardless of history, the rock is taken directly

to failure by infinitely slow loading. According to Bingham model,  $q_{min}$  is identical with the yield stress for a viscoplastic material (Kaiser 1979), which is around 2.3 MPa in the slowest reverse loading test, REV4. Therefore,  $q_{min}$  is lower than 2.3 MPa for Lanigan potash.

### Test RLX3

Testing of potash specimen RLX3 lasted for 9 days. The specimen was first loaded to an isotropic stress state of 30 MPa and left for isotropic compression at this stress state for 24 hours. Then, deviatoric stress was applied to the specimen by unloading  $\sigma_3$  from 30 MPa to zero in a stepwise fashion, at a constant rate of 1.25 MPa/h. Repeated relaxation tests were performed at deviatoric stress levels of 0, 6, 12, 18 and 24 MPa. At each stage, there were 3 relaxation cycles, each lasted for 24 hours. Figure 5.6 shows the deviatoric stress and axial strain curve with the axial strain determined by LVDT. Stage numbers of the inserted relaxation tests are also indicated. The general characteristics of this curve are similar to that of reverse loading triaxial tests without relaxation. The inserted relaxation phases do not have any effects on the stress-strain curve. Similar phenomena were observed by Haupt (1991) in conventional triaxial relaxation tests on salt. Figure 5.7 shows total vertical strain and normalized stress drop ( $\sigma_l/\sigma_a$ , where  $\sigma_l$  is the axial stress at any time during relaxation and  $\sigma_a$  is the initial axial stress at the beginning of a relaxation cycle) versus time for Test RLX3. The stress relaxation of potash increases significantly near failure and the deformation shows a transient stage with decreasing rate and a steady-state stage before failure. Figure 5.8

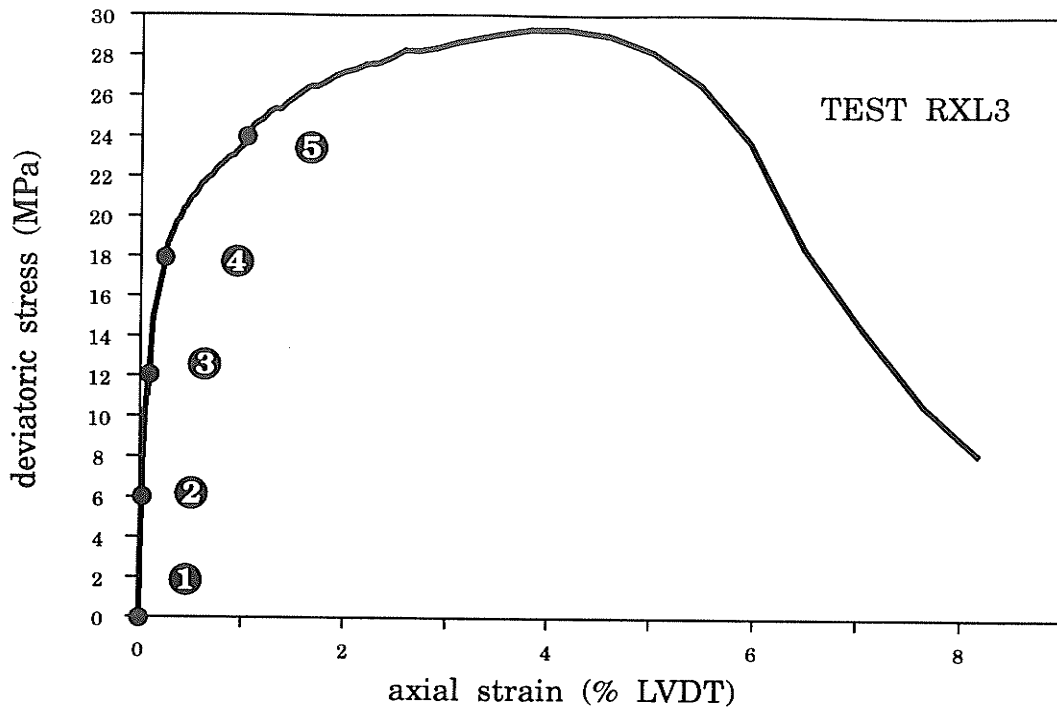


**Figure 5.6** Deviatoric stress versus axial strain curve for Test RLX3. The inserted relaxation tests are indicated by stage numbers. The axial strain was measured by LVDT. The inserted relaxation phases have no significant influence on the stress-strain curve.

shows that the normalized stress drop ( $\sigma_1/\sigma_a$ ) and logarithm of time have a linear relationship:

$$\sigma_1/\sigma_a = a + b(\log t) \quad (5.1)$$

The slope,  $b$ , increases with increasing deviatoric stress and has an approximately constant value at the same deviatoric stress level. At the same stress level, the intercept,  $a$ , decreases with increasing number of relaxation cycles ( $N_r$ ). As discussed in the introduction of this chapter and shown in Figure 5.1, relaxation tests allow a more definitive conclusion about the existence of a creep limit (defined by  $\dot{\sigma}=0$  and  $\dot{\epsilon}=0$ ) than creep tests. Since a relaxation test is defined by zero strain rate ( $\dot{\epsilon}=0$ ), the creep limit

### TEST RLX3

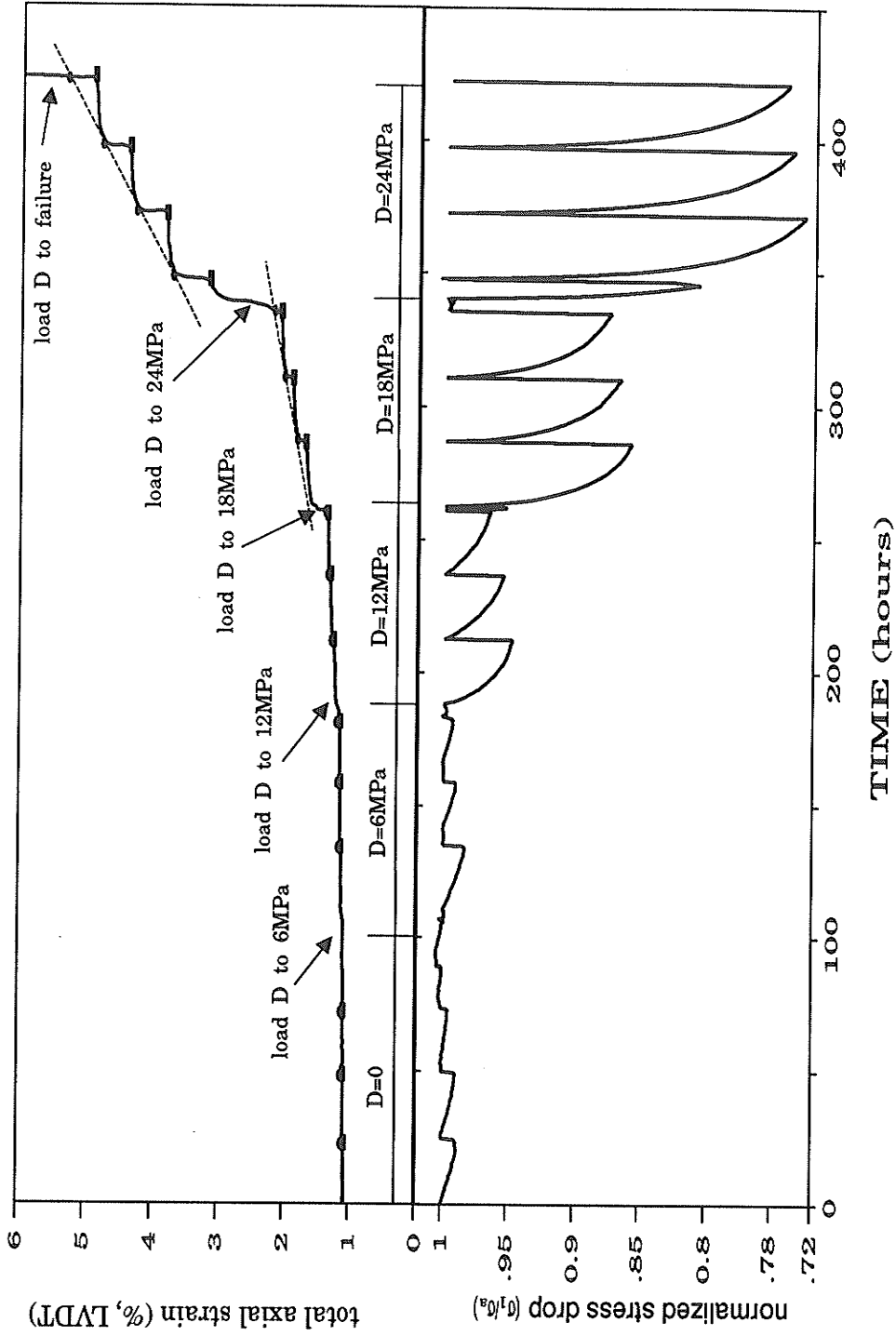


Figure 5.7 Total vertical strain and normalized stress drop versus time from Test RLX3. The stress relaxation of potash increases significantly as deviatoric stress increases and the deformation shows a steady-state stage prior to failure.

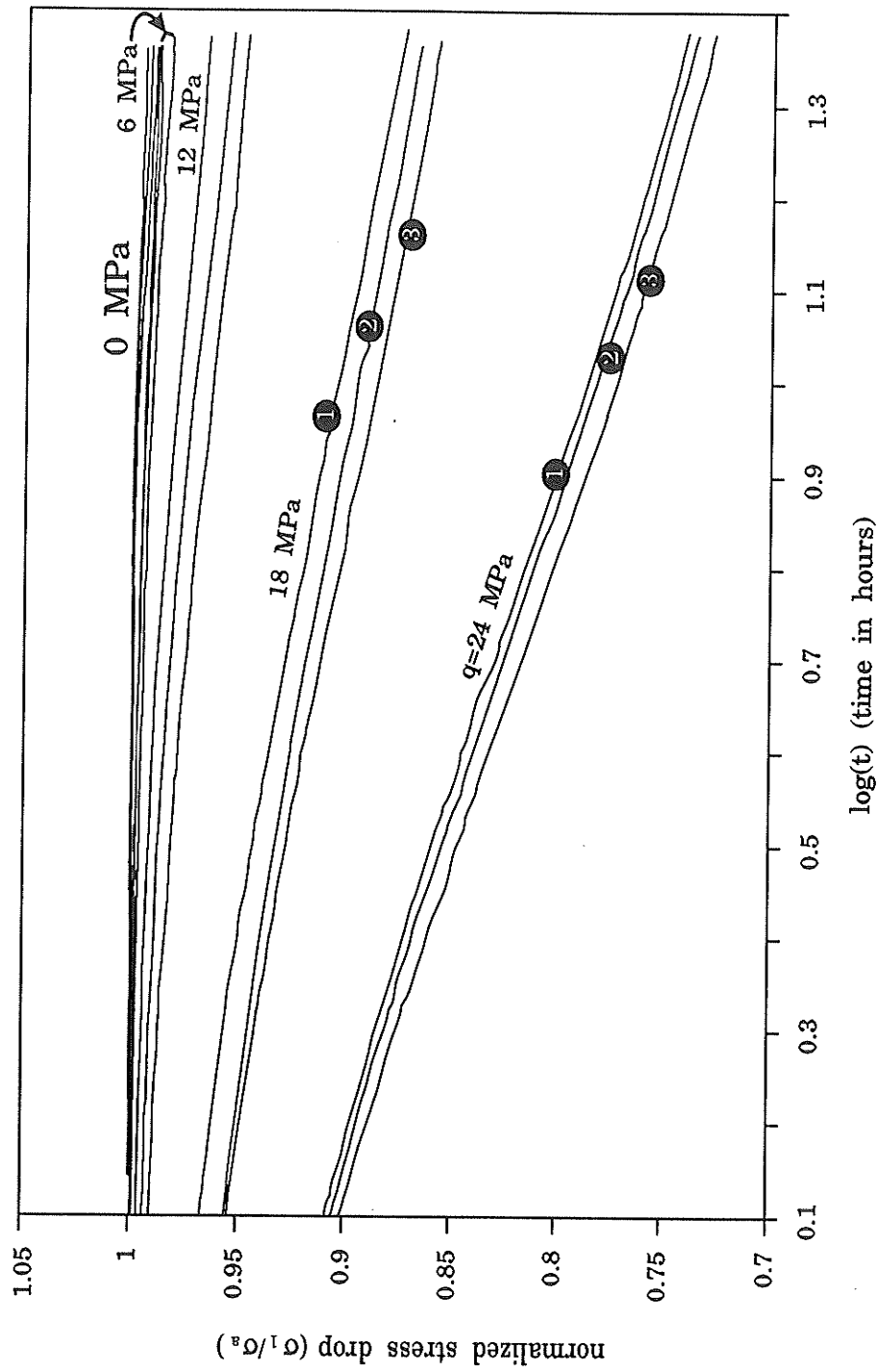
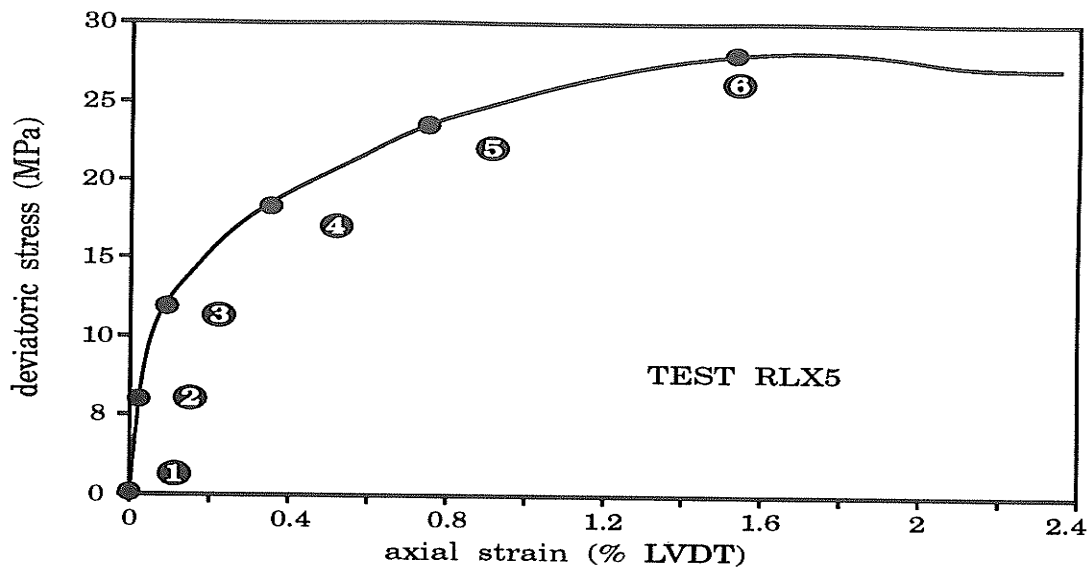


Figure 5.8 Linear relationship between normalized stress drop and logarithm of time at all stages from relaxation tests on Specimen RLX3, suggesting no creep limit exists for Lanigan potash.  $q$  is the deviatoric stress. Numbers indicate the sequence ( $N_r$ ) of repeated relaxation cycles at each deviatoric stress level.

is reached when the stress drop becomes zero (i.e. when  $\dot{\sigma}=0$ ). The linear relationship between normalized stress drop and the logarithm of time suggests that the stress rate will not become zero before the stress becomes zero. This might suggest that the potash investigated has no creep limit, i.e. it will creep at any load.

### Tests RLX5 and RLX4

Test on potash specimens RLX5 and RLX4 lasted for 56 days each. The specimens were first loaded to an isotropic stress state of 30 MPa and left for isotropic compression at this stress state for 24 hours. Then, deviatoric stress was applied to the specimen by unloading  $\sigma_3$  from 30 MPa to zero in a stepwise fashion. The stress rate at which deviatoric stress was applied to the specimen was 15 MPa/h for specimen RLX5 and 30 MPa/h for specimen RLX4. Repeated relaxation tests were performed at deviatoric stress levels of 0, 6, 12, 18, 24 and 29 MPa. At each stage, there were 5 relaxation cycles. The first 4 cycles lasted for 24 hours each and the last one was prolonged for 120 hours. Figure 5.9 shows the deviatoric stress and axial strain curve for Test RLX5. Stage numbers of the relaxation cycles are also indicated. The general characteristics of the curves are similar to those of reverse loading triaxial tests and of Test RLX3. Again, the inserted relaxation phases do not seem to influence the stress-strain curve. Figure 5.10 shows the total vertical strain ( $\epsilon$ ) and normalized stress drop ( $\sigma_1/\sigma_a$ ) versus time. The stress relaxation increases significantly near failure and the deformation shows a transient stage with decreasing rate and a steady-state stage before failure. Figure 5.11 shows, once again, the approximately linear relationship between



**Figure 5.9** Deviatoric stress versus axial strain curve for Test RLX5. The inserted relaxation tests are indicated by stage numbers. They have no significant influence on the stress-strain curve.

normalized stress drop ( $\sigma_1/\sigma_a$ ) and logarithm of time. The slope increases with increasing deviatoric stress and it is about a constant value for different relaxation cycles at the same stress level. The total stress drop after 24 hours of relaxation decreases with the increasing number of relaxation cycles at the same stress level and increases with increasing deviatoric stress.

#### 5.4.3 Discussion on potash behavior in multiple-stage repeated relaxation tests

The relaxation properties of potash are influenced by the stress rate at which the deviatoric stress is applied to the specimen. Figure 5.12 shows the relationship between normalized axial stress ( $\sigma_1/\sigma_a$ ) and logarithm of time for the elongated relaxation cycles (5 days) at the deviatoric stress levels of 0, 12, 18, 24, 29 MPa respectively for potash specimens RLX4 and RLX5. The stress rate is 30 MPa/h for specimen RLX4 and 15

TEST RLX5

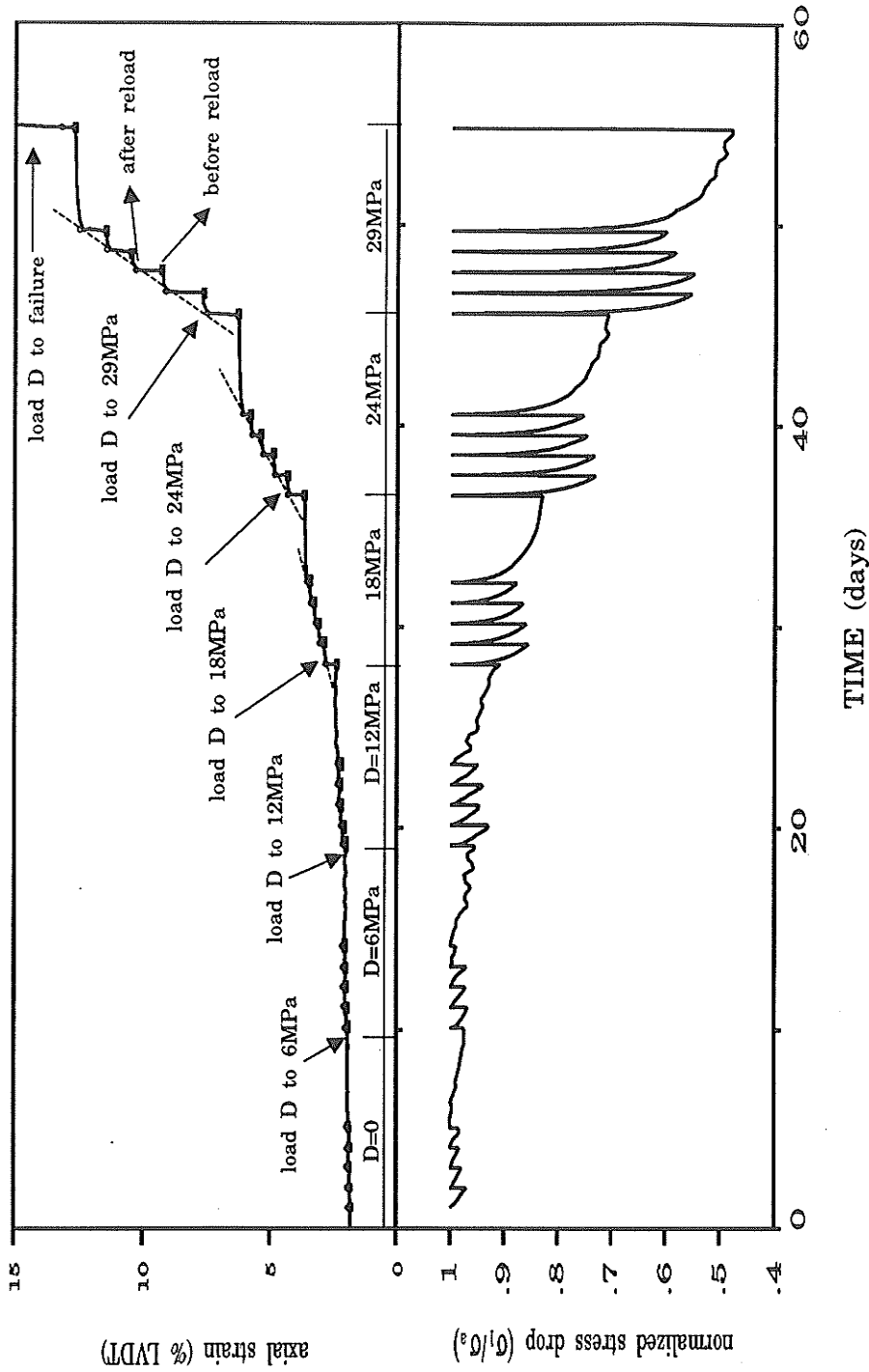


Figure 5.10 Total vertical strain and normalized stress drop versus time for Test RLX5. The stress relaxation increases significantly as deviatoric stress increases and the deformation shows a steady-state stage prior to failure.

TEST RLX5

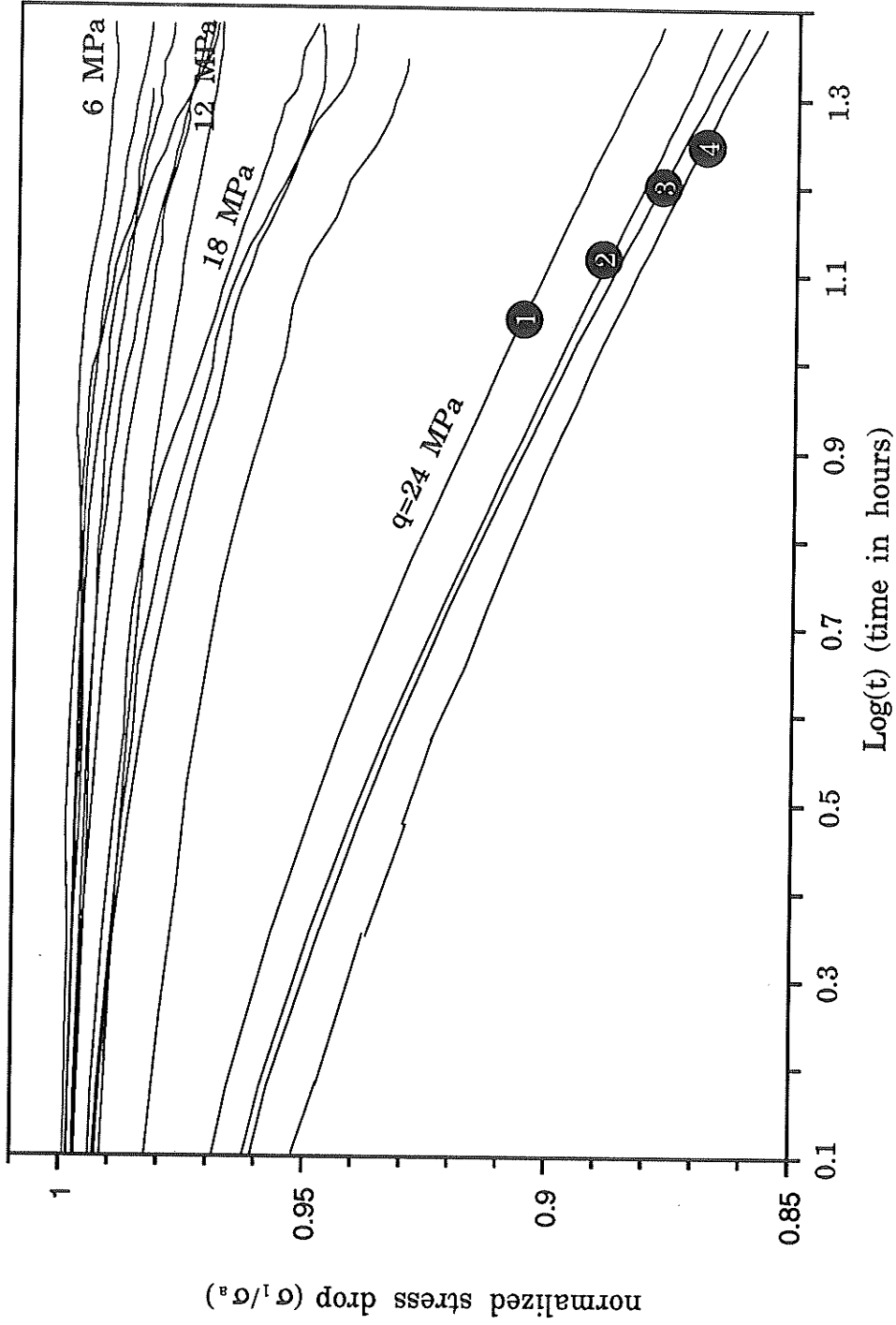


Figure 5.11 Linear relationship between normalized stress drop and logarithm of time for specimen RLX5.  $q$  is deviatoric stress level. Numbers indicate the sequence of repeated relaxation cycles at each deviatoric stress level.

Cycle 5 for tests RLX4 and RLX5

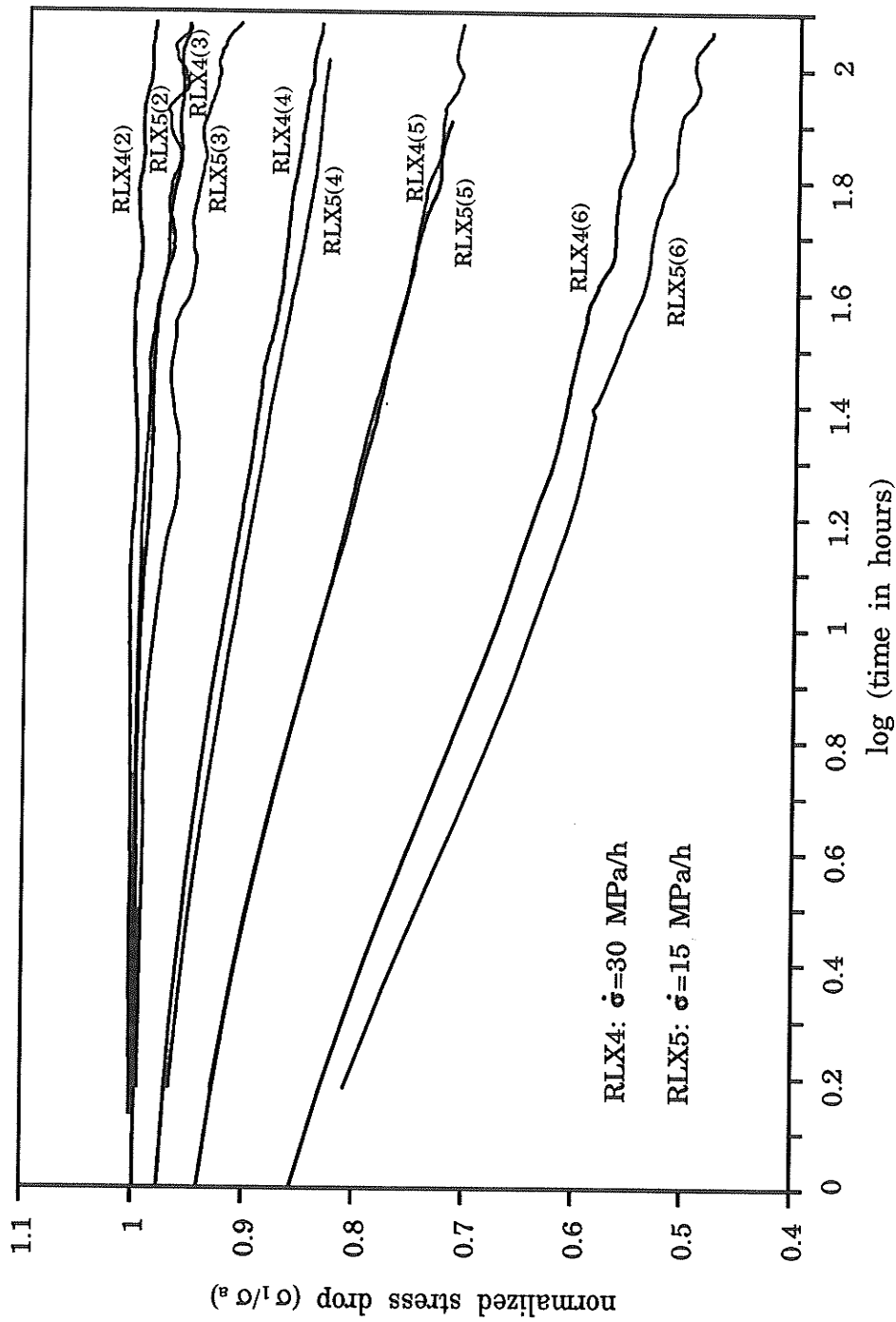


Figure 5.12 Relationship between normalized axial stress and logarithm of time for the elongated relaxation cycles (5 days) at various stages for Tests RLX4 and RLX5, showing the effect of stress rate on potash relaxation curves. Number in parentheses indicate stage numbers as shown in Figure 5.9.

MPa/h for specimen RLX5. The figure indicates that a linear relationship between stress drop and logarithm of time exists, with the slope of the relaxation curves increasing with increasing deviatoric stress. The figure also shows that at the same deviatoric stress level, the slope of the relaxation curve increases with the increasing stress rate. Figure 5.13 demonstrates that a higher stress rate induces a larger stress drop after a period of 5 days at all deviatoric stress levels.

At the same deviatoric stress level, the stress drop after a period of 24 hours decreases with the increasing number of relaxation cycles or the increasing total axial strain at low deviatoric stress. However, the stress drop is approximately the same for all the relaxation cycles at higher stress levels ( $q \geq 15$  MPa, Figure 5.14).

The general characteristics of relaxation curves at all deformational stages are identical. Potash rocks exhibit stress relaxation as soon as the deviatoric stress is developed. This may indicate that no long-term strength exists for potash in a reversed loading path. Since the relaxation phases gave no indication of reaching a constant stress level, it is assumed that the creep limit of the Lanigan potash might be zero. This means that the behavior is rate dependent even at very low stresses and consequently a relaxation test would terminate in a stress free state if continued for a sufficient length of time.

Relaxation curves are, therefore, influenced by the deviatoric stress ( $q$ ), stress rate ( $\dot{\sigma}$ ), and total or accumulated axial strain ( $\epsilon_a$ ) at which the relaxation test is conducted. The coefficients  $a$  and  $b$  in Equation (5.1) are, therefore, functions of  $q$ ,  $\dot{\sigma}$  and  $\epsilon_a$ :

$$a=f_1(q, \dot{\sigma}, \epsilon_a), \quad b=f_2(q, \dot{\sigma}, \epsilon_a) \quad (5.2)$$

where the explicit form of function  $f_1( )$  and  $f_2( )$  can be obtained by a curve fitting

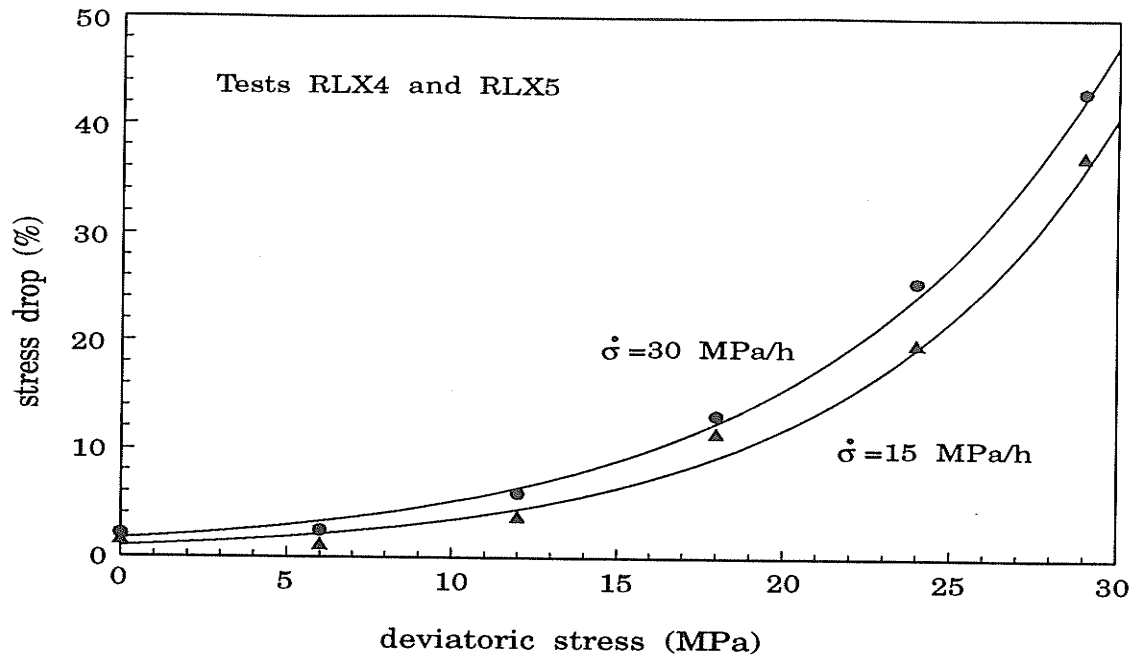


**Figure 5.13** The effect of stress rate on stress drop after 5 days of relaxation at various deviatoric stress level, showing that the higher stress rate induces a larger stress drop.

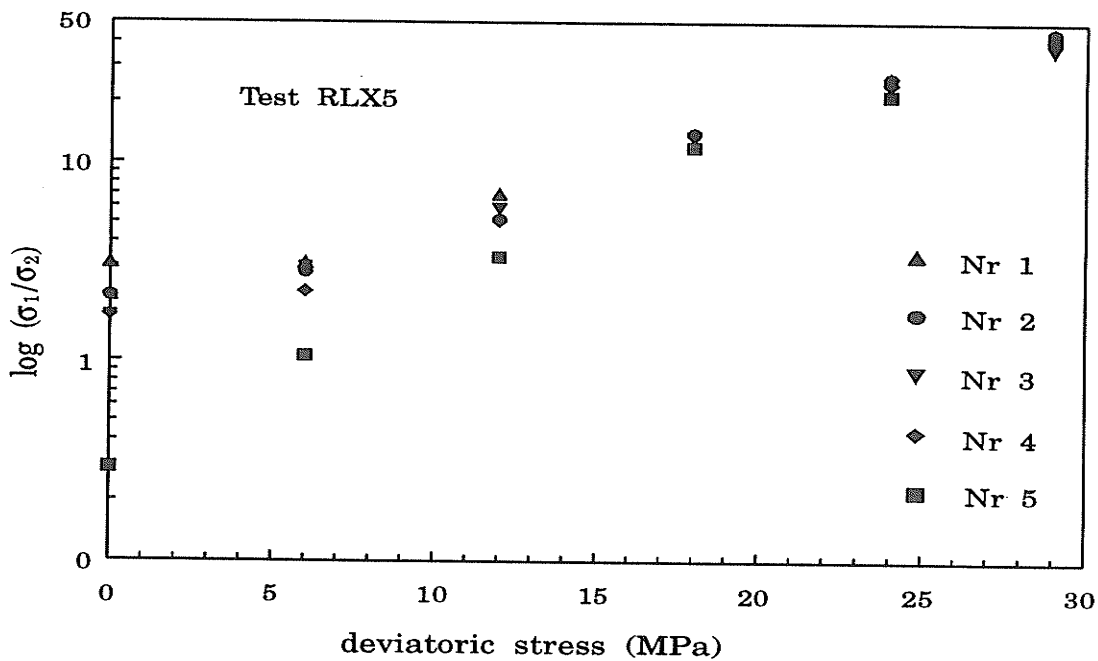


**Figure 5.14** Relationship between the stress drop after 24 hour of relaxation and the number of repeated relaxation cycles, showing a decreasing stress drop with increasing relaxation number at low deviatoric stress. However, stress drop is equivalent for all the relaxation cycles near failure at the higher stress level ( $q \geq 15$  MPa).

exercise from sufficient multiple-stage repeated relaxation tests.

## 5.5 Discussion on Stress-Strain Relationship and Material Parameters

### 5.5.1 Constitutive model based on Haupt (1991)

Haupt proposed the following uniaxial constitutive equation for salt, in which the relaxation function is independent of the creep function:

$$\frac{\dot{\epsilon}_{ij}}{c(\sigma_e, \epsilon_e)} = \frac{s_{ij}}{\sigma_0} + \frac{\dot{s}_{ij}}{r(\sigma_e, \epsilon_e)} \quad (5.3)$$

where

$$c(\sigma_e, \epsilon_e) = \frac{3}{2} \alpha \epsilon_e^{-\beta} \left( \frac{\sigma_e}{\sigma_0} \right)^{\delta-1} \quad (5.4)$$

is the creep function and

$$r(\sigma_e, \epsilon_e) = A \epsilon_e^{-B} \left( \frac{\sigma_e}{\sigma_0} \right)^{D-1} \quad (5.5)$$

is the relaxation function.  $\sigma_0$  is a reference value which is chosen as  $\sigma_0 = 1$  kPa.  $\alpha$ ,  $\beta$  and  $\delta$  are creep parameters and  $A$ ,  $B$  and  $D$  are relaxation parameters. They can be determined by appropriate creep and relaxation tests. The effective stress ( $\sigma_e$ ), the effective strain ( $\epsilon_e$ ) and the stress deviator ( $s_{ij}$ ) are defined by:

$$\sigma_e = \sqrt{\frac{1}{2}((\sigma_1 - \sigma_2)^2 + (\sigma_2 - \sigma_3)^2 + (\sigma_3 - \sigma_1)^2)}, \quad \epsilon_e = \sqrt{\frac{1}{2}((\epsilon_1 - \epsilon_2)^2 + (\epsilon_2 - \epsilon_3)^2 + (\epsilon_3 - \epsilon_1)^2)},$$

$$s_{ij} = \sigma_{ij} - \frac{1}{3} \sigma_{kk} \delta_{ij}$$

This constitutive law can be extended to include the confining pressure,  $p$ . In this case  $\sigma_e = (\sigma_1 - p)$ ,  $s_1 = 2/3(\sigma_1 - p)$ ,  $\dot{s}_1 = 2/3\dot{\sigma}_1$  and  $\epsilon_e = \epsilon_1$ , and the constitutive law becomes:

$$\frac{\epsilon_1^\beta \left( \frac{\sigma_1 - p}{\sigma_0} \right)^{-\delta}}{\alpha} \dot{\epsilon}_1 = 1 + \frac{\epsilon_1^\beta \left( \frac{\sigma_1 - p}{\sigma_0} \right)^{-D}}{A} \dot{\sigma}_1 \quad (5.6)$$

Creep behavior with  $\dot{\sigma}_1 = 0$  under confining pressure,  $p$ , is described by

$$\dot{\epsilon}_1 = \alpha \epsilon_1^{-\beta} \left( \frac{\sigma_1 - p}{\sigma_0} \right)^\delta \quad (5.7)$$

Using creep time

$$t_c = \left[ \frac{\alpha(\beta+1)}{\epsilon_a^{\beta+1}} \left( \frac{\sigma_1 - p}{\sigma_0} \right)^\delta \right]^{-1} \quad (5.8)$$

integration of (5.7) with respect to time and the initial condition,  $\epsilon_1(t_0) = \epsilon_a$ , yields the time dependent creep

$$\epsilon_1 = \epsilon_a \left[ \frac{(t-t_0)}{t_c} + 1 \right]^{\frac{1}{\beta+1}} \quad (5.9)$$

and the time dependent creep rate

$$\dot{\epsilon}_1 = \frac{\epsilon_a}{(\beta+1)t_c} \left[ \frac{(t-t_0)}{t_c} + 1 \right]^{-\frac{\beta}{\beta+1}} \quad (5.10)$$

Correspondingly, relaxation behavior with  $\dot{\epsilon}_1 = 0$  and the initial condition  $\sigma_1(t_0) = \sigma_a$  is described by (from Equation 5.6)

$$\dot{\sigma}_1 = -A \epsilon_1^{-B} \left( \frac{\sigma_1 - p}{\sigma_0} \right)^D \quad (5.11)$$

with relaxation time

$$t_r = \left[ (D-1) \frac{A}{(\sigma_a - p)} \varepsilon_1^{-B} \left( \frac{\sigma_a - p}{\sigma_0} \right)^D \right]^{-1} \quad (5.12)$$

The time dependent relaxation is obtained as

$$\sigma_1 = \sigma_a \left[ \frac{t - t_0}{t_r} + 1 \right]^{\frac{1}{1-D}} \quad (5.13)$$

and the relaxation rate becomes

$$\dot{\sigma}_1 = \frac{(\sigma_a - 1)}{(1-D)t_r} \left[ \frac{t - t_0}{t_r} + 1 \right]^{\frac{D}{1-D}} \quad (5.14)$$

where  $D > 1$ .

Since the relaxation rate as well as the stress decrease monotonously against time, a completely relaxing material without creep limit and with strain hardening is described by the constitutive law.

### 5.5.2 Determination of material parameters

To determine the relaxation parameters, Equation 5.11 is rewritten as

$$\log(-\dot{\sigma}_1) = \log(A \varepsilon_1^{-B}) + D \log \left( \frac{\sigma_1 - p}{\sigma_0} \right) \quad (5.15)$$

This represents a straight line in a bilogarithmic  $(-\dot{\sigma}_1) - ((\sigma_1 - p)/\sigma_0)$  diagram, from which parameter  $D$  can be derived as the gradient. Figure 5.15 shows the corresponding test results of 5 relaxation cycles at the confining pressure  $p = 6$  MPa, from potash specimen

RLX5. It can be ascertained that the gradients of the experimental curves behave rather homogeneously, whereas their position differs clearly depending on the number of relaxation cycles,  $N_r$ , or on the magnitude of the accumulated strain,  $\epsilon_a$ . Hence, at the same confining pressure level,  $D$  can be given fairly exactly. For the determination of  $A$  and  $B$ , first the intercepts of the coordinate at  $((\sigma_1-p)/\sigma_0)=0$  are determined for each relaxation curve depending on the total accumulated axial strain,  $\epsilon_a$ . Subsequently, these values are equated to  $A\epsilon_1^{-B}$  and plotted in dependency upon  $\epsilon_a$ . This relation, again, can be approximated by a straight line in a bilogarithmic graph (Figure 5.16), with  $B$  as the gradient and  $A$  as the intercept of the coordinate. For Lanigan potash  $A=1.59$  kPa/h,  $B=0.028122$  and  $D=10.13$  at a confining pressure of 6 MPa. By taking the same curve fitting procedures for relaxation curves at different stages, the dependence of  $A$ ,  $B$  and  $D$  on confining pressure,  $p$ , can be established.

The creep parameters  $\alpha$ ,  $\beta$  and  $\delta$  can be determined in a similar manner.

## 5.6 Chapter Summary

Results from the reverse loading triaxial tests and the multiple-stage repeated relaxation tests along the reverse loading path can be summarized as follows:

- (1) The general nature of potash deformation reflected by axial stress vs. axial, lateral and volumetric strain curves in a reverse loading tests is similar to that of conventional compression tests obtained by Lajtai et al. (1991a), i.e., composed of pre-fractured, yielding, microfracture propagation, dilatancy and post failure stages.
- (2) Potash behavior under a reverse loading path is strongly rate dependent, reflected by

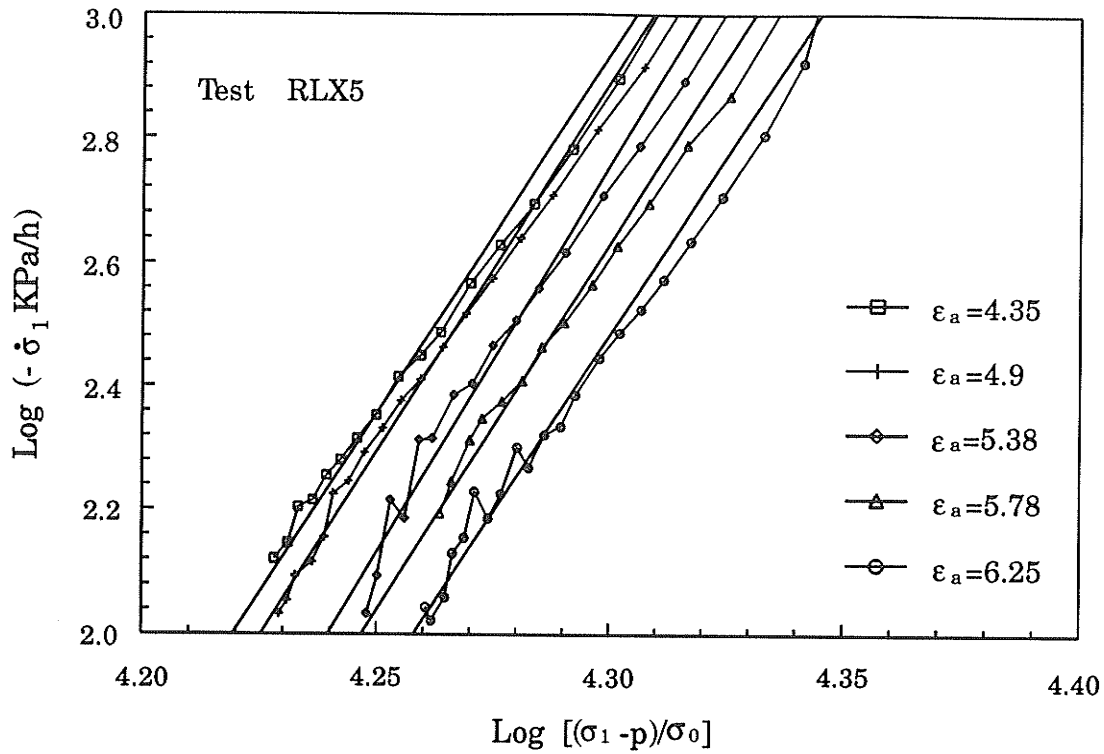


**Figure 5.15** Stress rate versus stress for determining relaxation parameters in Equation (5.15).

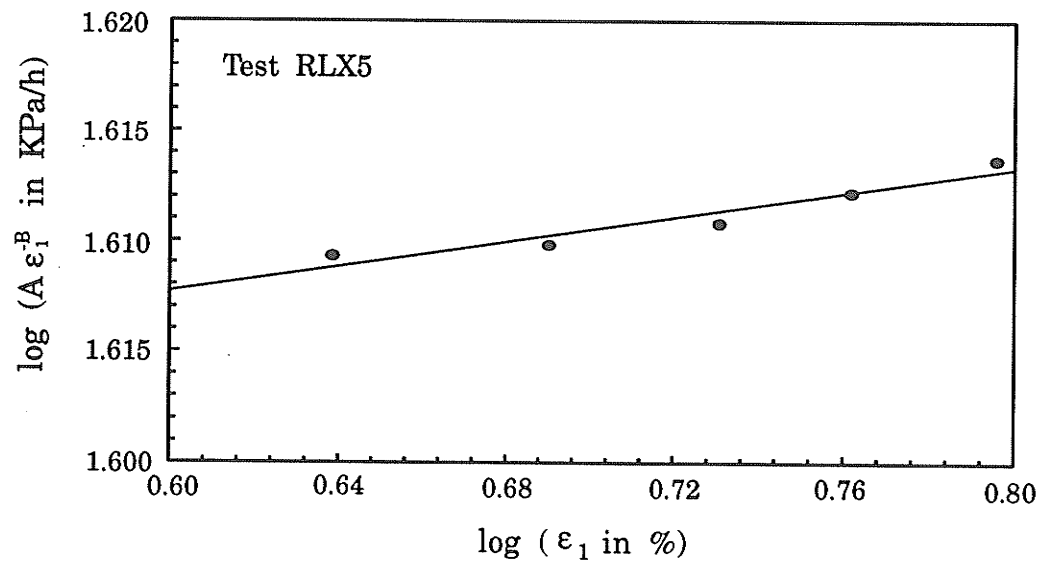


**Figure 5.16** Diagram for the determination of relaxation parameters  $A$  and  $B$ .

the dependence of the initial deformational moduli, the ductile yield point, and post-peak behavior on the rate at which the deviatoric stress was loaded to the specimen. The initial axial deformational moduli ranged from 29 GPa at the fastest stress rate to 12 GPa at the lowest stress rate. The deviatoric stress at the ductile yield point ranged from 7.6 MPa at the fastest stress rate to 2.3 MPa at the slowest stress rate. The lowest stress rate induces the largest amount of ductile deformation after yield, while the highest stress rate induces the smallest amount of ductile deformation before the ultimate failure point. In short, lower stress rate corresponds to higher ductility and higher stress rate corresponds to lower ductility and greater brittleness.

- (3) The general nature of the axial stress-axial strain curve from multiple-stage repeated relaxation tests is similar to those obtained from direct reverse loading tests. The inserted relaxation phases do not have significant effects on the stress-strain curves. This phenomenon provides a potential advantage in using inserted relaxation tests to investigate time dependent behavior at various stages of deformation during a single test. The same task by creep tests would be extremely time consuming and several tests would be required instead of one.
- (4) The relationship between normalized stress drop ( $\sigma_1/\sigma_a$ ) and logarithm of time is linear ( $\sigma_1/\sigma_a = a + b \log t$ ), suggesting that stress rate will not become zero before stress becomes zero. This might suggest that potash has no creep limit, and therefore its long-term strength,  $q_{min}$ , might be zero. If this is the case, then the Bingham model that has been well-accepted for salt rock analysis is not valid for Lanigan potash, since in this model the value of the long-term strength is equivalent to the yield stress.

- (5) The relaxation behavior of Lanigan potash before failure can be approximated by a strain-hardening constitutive law postulated by Haupt, with the effect of confining pressure incorporated.

## 6. BIMODULARITY OF EVAPORITES - Experimental Program II

### 6.1 Introduction

It is commonly assumed for the purpose of stress analysis and interpretation of certain rock tests (e.g. indirect tension tests) that the moduli of deformation are equal in tension and in compression. This assumption has been questioned at various times. Haimson and Tharp (1974) collected data for sandstone, marble, limestone and granite. They showed that these rocks are bimodular materials in which the elastic properties in tension are different from those in compression; the tensile modulus can be as little as 5% of the compressive modulus (Table 6.1). Wawersik (1968), Labuz (1985), and Khan and Irani (1988) further confirmed the bimodular behavior of granite. Similar behavior has also been found in other materials, such as bone (Simkin and Robin 1973), composites (Jeness and Kline 1974) and concrete (Guo and Zhang 1987).

Although the assumption of equal moduli in tension and in compression has been questioned, it is still commonly used in design and analysis in rock engineering. As long as the state of stress remains compressive, the assumption does not lead to erroneous results. However, in situations where the state of stress is tension or mixed tension and compression (i.e. at least one principal stress is of opposite sign to the others), the effects of different moduli in tension and in compression should be considered. Some examples of such situations are underground openings in massive rock (depending on shape, principal stress ratio, and the presence of adjacent openings), mine roofs in layered strata, hydraulic fracturing, rock cutting, and various indirect rock tensile tests. This

Table 6.1 Young's moduli in tension and compression collected by Haimson and Tharp (1974)

rock types	$E_t$ (GPa)	$E_c$ (GPa)	$E_t/E_c$
Westerly granite	17.24	72.39	0.24
Austin limestone	11.72	15.86	0.74
Carthage limestone	35.16	64.43	0.55
Indiana limestone	11.03	26.89	0.41
Georgia marble	23.44	42.06	0.56
Tennessee marble	53.09	76.53	0.69
Russian marble	8.96	20.68	0.43
Star Mine quartzite	75.84	75.84	1.00
Arizona sandstone	11.72	45.51	0.26
Berea sandstone	4.14	23.44	0.18
Millsap sandstone	0.69	14.00	0.05
Tennessee sandstone	1.38	16.55	0.08
Russian sandstone	11.72	57.23	0.21

requires the testing of rock specimens in tension and in compression. So far, both deformational properties are still unavailable for most rocks due to lack of proper measuring techniques.

In this chapter, a new testing technique is described that permits the direct determination of moduli of deformation both in compression and in tension at the same location on the same specimen and in the same compressive loading frame. The newly developed technique is used to measure moduli of halite, potash, granite and limestone. The standard direct tension and uniaxial compression tests are performed on halite and

potash to examine the validity of the new, combined compression-tension testing technique. Finally, the practical implications of rock bimodular property are discussed.

## 6.2 Development of Testing Technique

Traditionally, rock strength and moduli in tension and compression are measured by loading a right circular cylinder to failure in direct uniaxial tension and compression respectively and then determining the resulting axial stress, axial strain and failure load. Because of the difficulty in achieving true uniaxial tension in a direct tension test, this test is often avoided and various indirect tension tests such as the Brazilian test or the ring test are substituted (Lama and Vutukuri 1978). However, these indirect tension tests do not provide a state of uniaxial tensile stress throughout the specimen. Also, the interpretation of these tests is typically based on the assumption of linear elasticity and equal deformational moduli in tension and compression. Consequently, these methods cannot be used to measure deformational moduli or tensile strength without corrections being made for unequal moduli (Chen and Stimpson 1993a).

The new testing technique, described in this chapter, permits the direct determination of moduli of deformation in compression and in tension at the same location on the same specimen and in the same compressive loading frame. Therefore it is not necessary to have a machine with a tensile loading capability. This method also avoids the difficulties of interpreting the results of tensile properties determined on one specimen and the compressive properties determined on a different specimen. Also, the tensile and compressive strains required to derive the moduli of deformation are measured

at precisely the same point on the same rock specimen. This is a particularly important characteristic of the test when the rock specimens are highly heterogeneous.

### **6.2.1 Testing equipment and data acquisition**

The testing equipment and data acquisition for the new combined compression-tension tests and for the standard uniaxial compression tests were the same as the ones described in Chapter 5 for the triaxial tests. For the direct tension tests, the loading system was a 30,000# PTE Testing Machine with cable grips, manufactured by the A.H. Emery Company of New Canaan, Connecticut. The specimen was glued to steel loading grips with flexible cables attached. The data acquisition system for direct tension tests consisted of a Hewlett Packard (HP) 9816 Computer with a HP 9121 floppy drive, a HP 82905B printer and a HP 34379A 31 channel data acquisition/control unit. The computer code that managed this system was the one developed by HP, called Data Logger.

### **6.2.2 Specimen geometry and preparation**

The experimental technique is a modification of the method developed by Luong (1988) for the measurement of rock tensile strength on cylindrical specimens (Figure 6.1). It was found that Luong's method is unsuitable for measuring tensile strength due to stress concentrations around the notches at the ends of the drill slots which cause anomalous fractures. However, with a simple modification, the method can be applied to determine the deformational modulus. Figure 6.2 shows the modified specimen geometry that permits the attachment of electrical resistance strain gauges for the

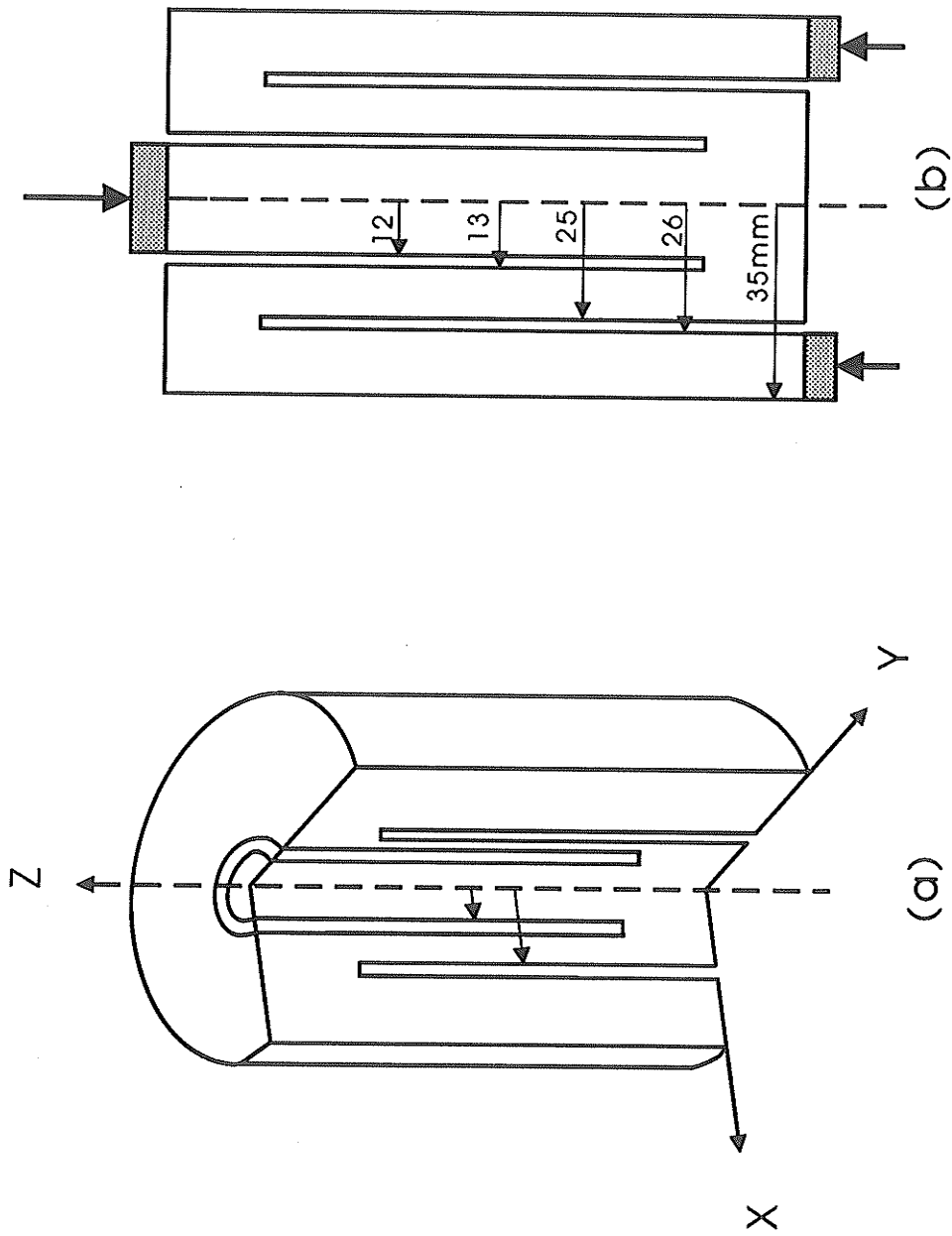
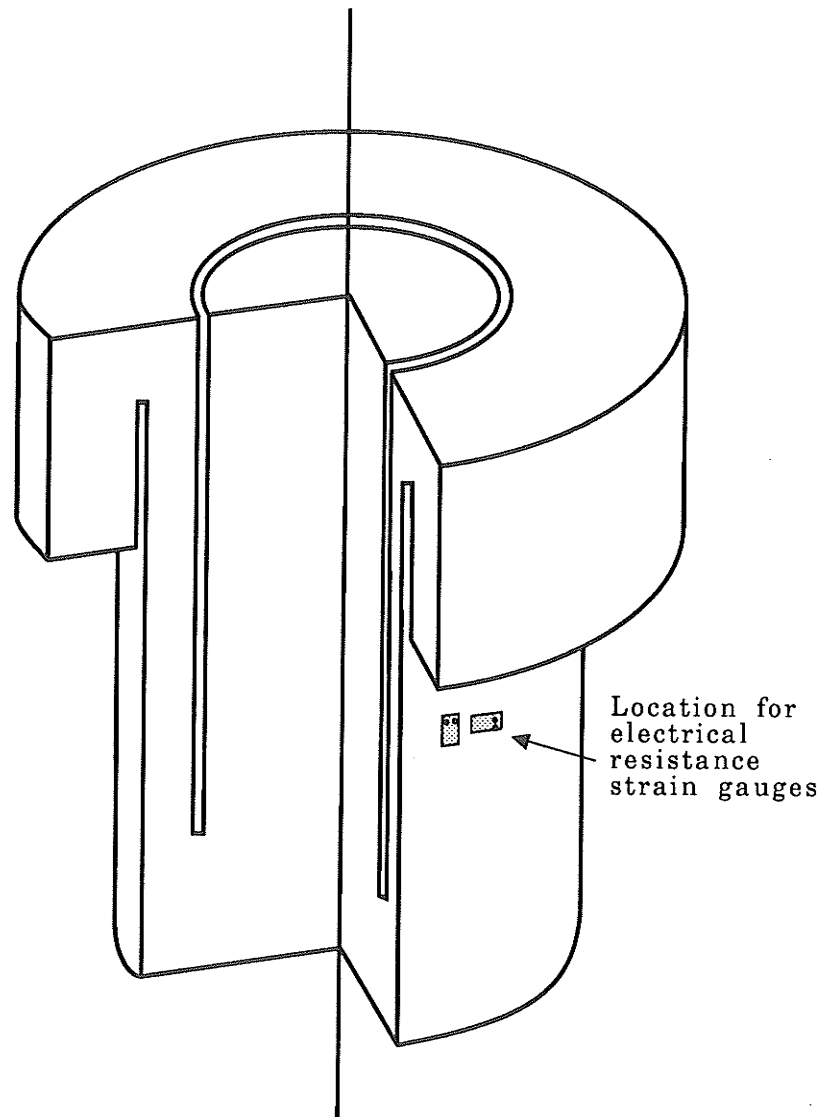


Figure 6.1 (a) Specimen geometry and (b) loading for tension test (after Luong 1988).



**Figure 6.2** Modified specimen geometry for the new, combined compression-tension test. The exposed surface of the middle rock annulus permits the attachment of axial and lateral electrical resistance strain gauges to measure deformation moduli.

measurement of axial and lateral strains and the determination of both the tensile and compressive moduli at the same point on the specimen.

The specimen was prepared by carefully drilling two coaxial annular slots from both ends with a water-flushed, thin walled, impregnated diamond bit, followed by removal of a section of the annulus between the outer cylindrical surface and the outer drill slot by cutting with a circular rock saw. This latter procedure exposed a surface (Figure 6.2) to which electrical resistance strain gauges were attached axially and laterally for the determination of the moduli of deformation and Poisson's ratios. Standard strain gauges used in regular uniaxial tension and uniaxial compression tests can be used in this new testing technique. Strain gauge selection is mainly based on specimen conditions, such as the type of material to be tested, grain size, homogeneity etc. The strain gauges used in this study were 350 ohm, 10 mm length bonded foil strain gauges manufactured by Micro Engineering II of Upland, California.

The optimum depths of the drill slots were determined using a linear elastic finite element program, SIMEX (Ayari 1991). The design objective was to select a specimen geometry that would provide a uniform stress distribution along the strain-gauged portion of the specimen and would keep stress concentrations around the notches at the ends of the drill slots to a minimum. The optimal drill bit diameters were determined from consideration of the results of stress analyses and the availability of diamond bits in certain standard diameters.

Development of tensile or compressive axial stresses in the strain-gauged portion of the specimen was achieved in the same compressive loading frame by a simple change

in the location and shape of metal loading platens. Figure 6.3 gives the specimen configuration for the tension test. A ring metal platen was used to support the outside rock annulus and a circular platen was used to transmit a compressive load to the inside core. With this arrangement, a tensile stress was induced in the middle rock annulus. Figure 6.4 shows the specimen configuration for the compression test, where the compressive load was applied directly to the middle rock annulus. Figures 6.5 and 6.6 show the set-up of tension and compression tests in the same compressive loading machine (ELE) by using appropriate loading platens. Figures 6.7 and 6.8 show the principal stress trajectories from finite element analyses and the uniform uniaxial tensile and compressive stress fields beneath the strain-gauged areas.

### 6.2.3 Experimental procedure

The new testing technique was used to measure tensile and compressive moduli of deformation of halite and potash from the Cominco Mine, Lac du Bonnet granite (Manitoba) and Tyndall limestone (Manitoba).

The experimental procedure was posited on two observations. Firstly, a rock specimen is much weaker in tension than in compression. Secondly, for most rock types damage leading to plastic deformation does not generally occur until after 25% of the ultimate load (e.g., 29% for Saskatchewan potash, 55% for Tyndall limestone, and 44% for Lac du Bonnet granite according to Lajtai et al. 1991a). Therefore, the first loading of the specimen was in compression to a point within the elastic range, followed by complete unloading, substitution of the compressive test platens with those for tensile

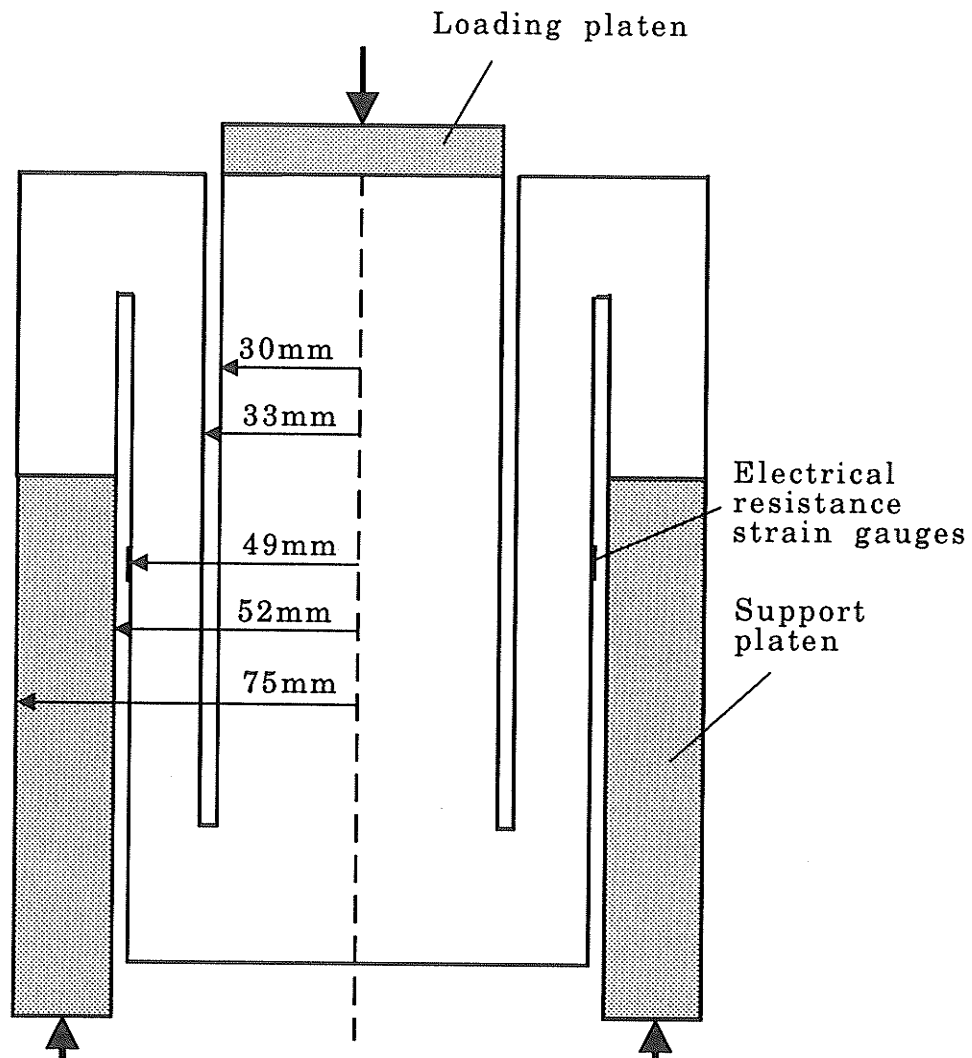


**Figure 6.3** Platen and loading configuration for tensile loading in the combined compression-tension test.

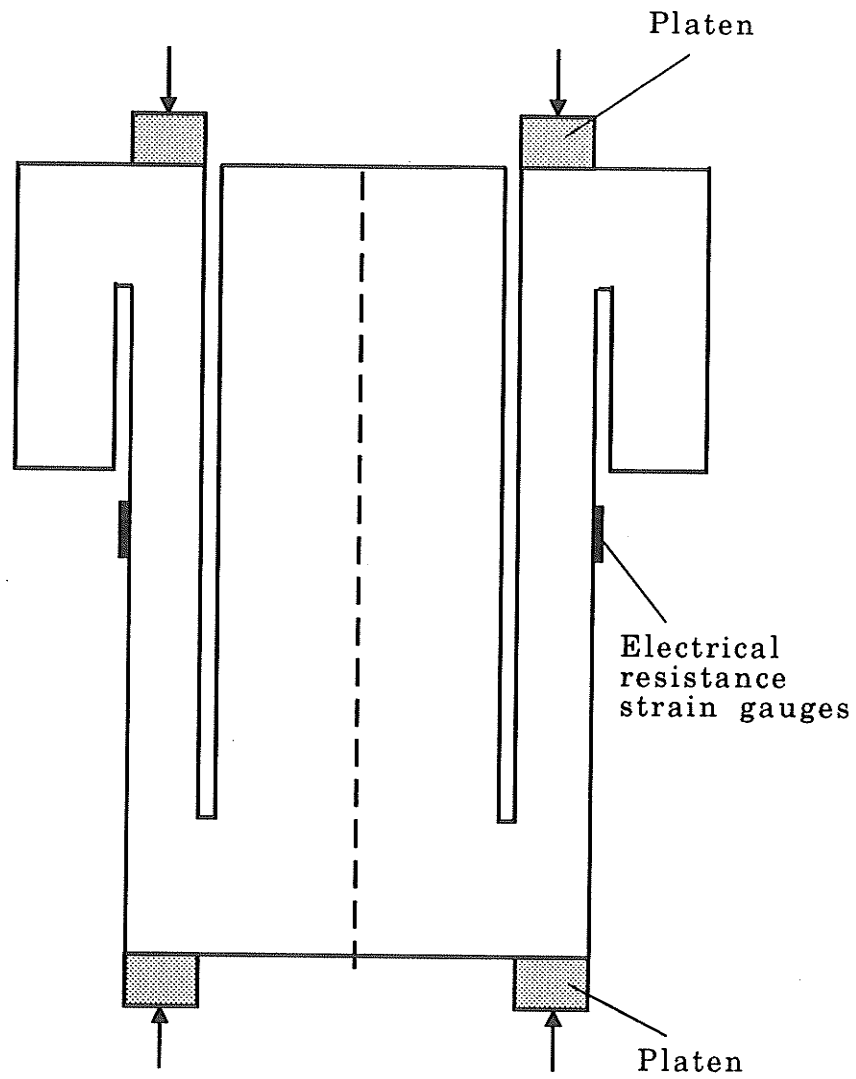


**Figure 6.4** Platen and loading configuration for compressive loading in the combined compression-tension test.

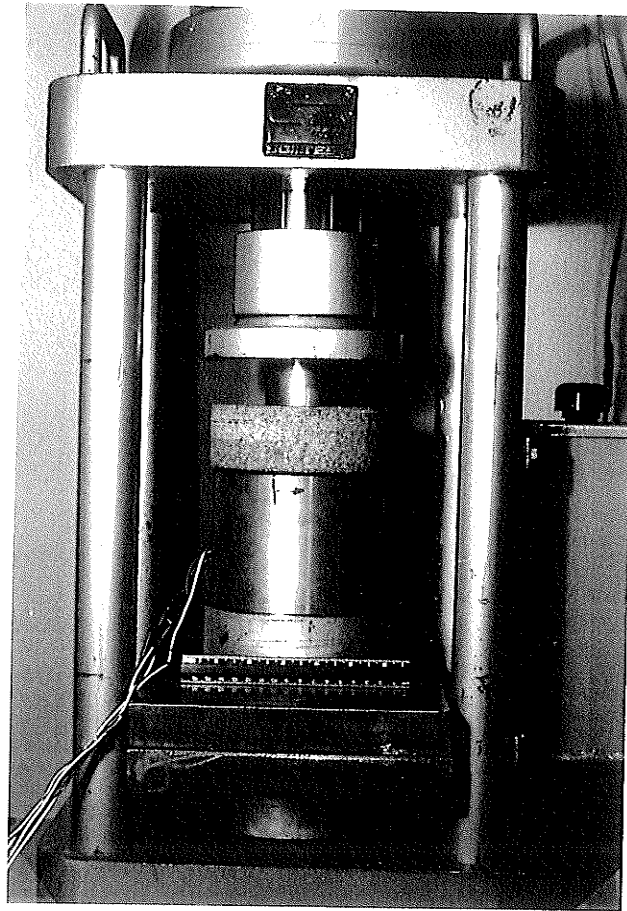


**Figure 6.5** Set-up of tension test in a compressive loading frame.

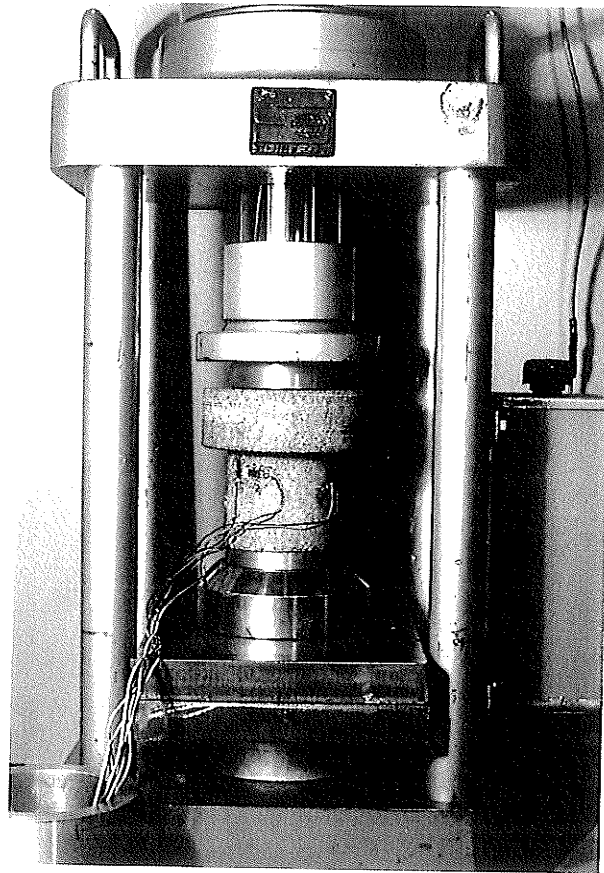


**Figure 6.6** Set-up of compression test in the same compressive loading frame as in tension test.

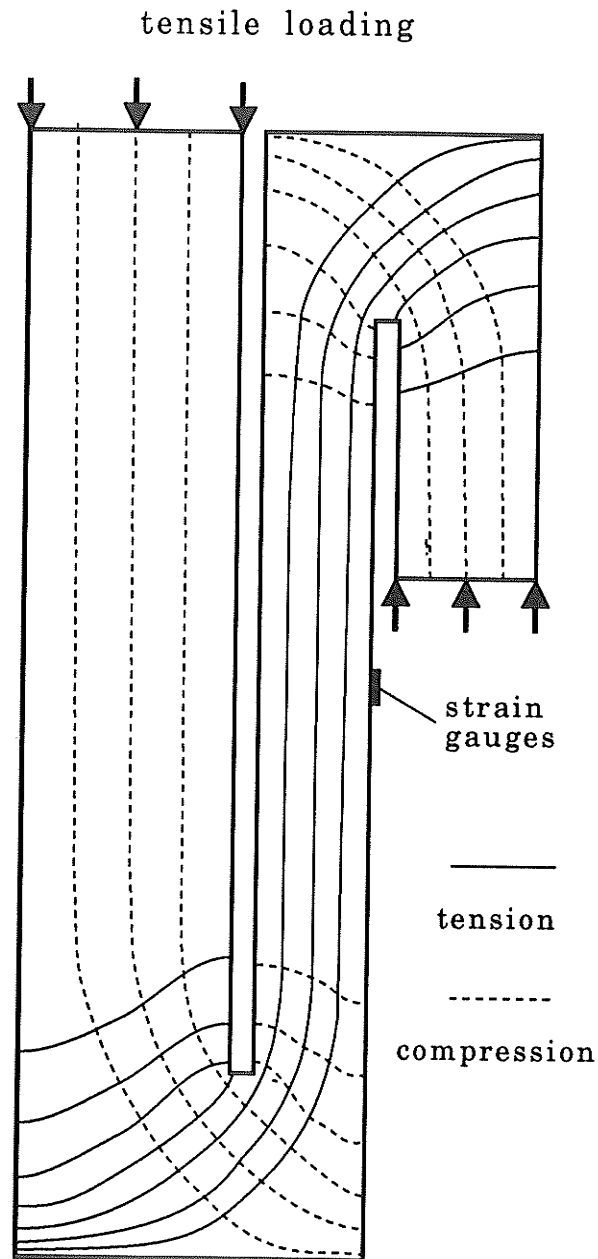


**Figure 6.7** Principal stress trajectories for tensile loading in the combined compression-tension test. The specimen configuration converts the applied compressive load on the specimen into a state of uniform tensile stress beneath the strain-gauged area.

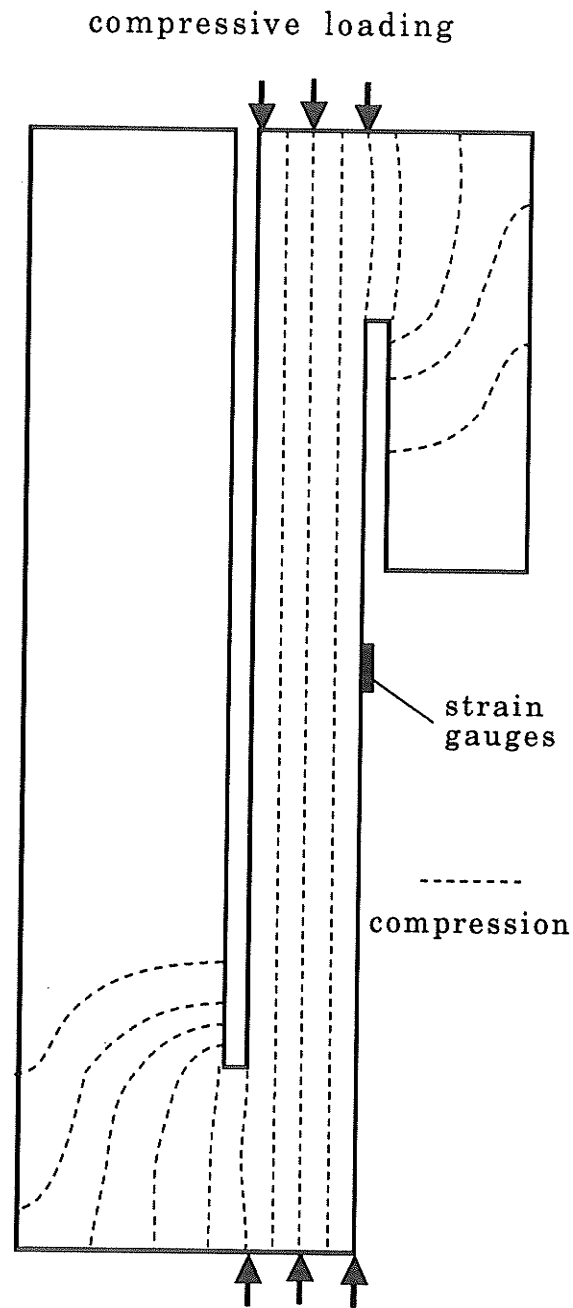


**Figure 6.8** Principal stress trajectories for compressive loading in the combined compression-tension test, showing a uniform compressive stress state beneath the strain-gauged area.

testing, and reloading in tension to about one third of the estimated uniaxial tensile strength. This loading sequence was repeated through increasing stress levels until the specimen fails, usually, in tension.

The uniform axial stress in the specimen was given by:  $\sigma = P/A$ , where  $P$  is the axial load and  $A$  is the cross sectional area of the rock annulus between the inner and outer drill slots normal to the axis of the cylindrical specimen. Axial and lateral strains for a given applied load were calculated from the change in resistance of the electrical resistance strain gauges and the gauge factor supplied by the manufacturer.

The potash and halite were obtained from the Middle Devonian Prairie Evaporite Formation (Holter 1969) at the Cominco Mine, 50 km southeast of Saskatoon, at a depth around 1100 metres, where potash has been mined extensively for the potassium content used as fertilizer. The potash is composed predominantly of medium to coarse grained sylvite (potassium chloride) and halite (sodium chloride), with some carnallite and interstitial clay. The grain size is 2 mm to 20 mm in diameter. Its mechanical properties depend on the loading rate and confining pressure (Lajtai et al. 1991b). The average uniaxial tensile strength is between 1-2 MPa and the average uniaxial compressive strength is around 25 MPa (Carter 1992b). The halite is composed mainly of pure halite crystals (sodium chloride) with grain size similar to that of potash. Its average uniaxial tensile strength is also 1-2 MPa and the average compressive strength is about 30 MPa.

The Lac du Bonnet (pink) granite was obtained from the Cold Spring Quarry near Lac du Bonnet, 90 km northeast of Winnipeg. It is part of the Lac du Bonnet batholith located on the edge of the Canadian Shield and consists of oligoclase, microcline feldspar,

quartz and biotite. It is relatively homogeneous with grain size from 0.5 mm to 20 mm (Lajtai 1982). The average uniaxial tensile strength is close to 14 MPa from Brazilian test data, around 10 MPa from uniaxial tension test data (Lajtai 1992), and the uniaxial compressive strength is 226 MPa (Carter 1992*b*).

The Tyndall limestone was obtained in the Ordovician Red River Formation from a local quarry near Garson, 40 km northeast of Winnipeg. It is partly dolomitized, contains numerous fossils and is much used for facing stone. The mechanical properties are highly variable throughout the quarry. Generally, the average uniaxial tensile strength is close to 4 MPa and the average uniaxial compressive strength is about 52 MPa (Carter 1992*b*; Carter et al. 1991*a*).

For potash and halite, both the new combined compression-tension test and the standard uniaxial compression and direct tension tests (Lama and Vutukuri 1978) on cylindrical specimens were performed. Specimens were carefully prepared for comparison of the new technique with the standard methods. Three halite blocks and three potash blocks were collected from the Cominco Mine. From each block, a combined compression-tension specimen with the dimensions indicated in Figure 6.3 was prepared and 2 core specimens of 2.03 cm diameter were drilled for each of the standard compression and tension tests. The axes of all the specimens were oriented perpendicular to the bedding. A displacement rate of 0.05 mm/minute was applied for the new combined compression-tension tests and for the uniaxial compression tests. For direct tension tests, the displacement rate was manually controlled to about 0.05 mm/minute.

For the new method, loading was cycled between compression and tension as noted above.

For all the tests, three axial and three lateral strain gauges were used to obtain Young's moduli and Poisson's ratios which were calculated from the initial linear portion of the stress-strain curves. The stress range of this initial linear portion of the stress-strain curve varies for different rock types, depending on the yield stress of each rock.

### 6.3 Experimental Results

#### 6.3.1 Results on Cominco halite

Tables 6.2 and 6.3 tabulate the results from the standard direct tension and uniaxial compression tests, respectively, including moduli of deformation in tension ( $E_t$ ) and in compression ( $E_c$ ), Poisson's ratio in compression ( $\nu_c$ ), the ultimate tensile strength ( $S_t$ ) and compressive strength ( $S_c$ ). The average Young's moduli are 25.8 GPa from the standard uniaxial compression tests and 14.6 GPa from the standard tension tests, which gives a ratio of Young's modulus in tension to that in compression of  $E_t/E_c=0.56$ . The average Poisson's ratio is 0.32 from the standard compression tests. Accurate estimation of Poisson's ratio in tension were not possible because lateral strain in tension is very small. The average compressive strength is 30 MPa and the average tensile strength is 1.4 MPa.

Table 6.4 presents the results from the combined compression-tension tests. The load-unload-reload cycles comprised an initial compressive loading to 3.5 MPa (load step 1), followed by complete unloading and reloading to 0.5 MPa in tension (load step 2).

Table 6.2 Results on halite in the uniaxial tension tests

specimen number	test number	$E_t$ (GPa)	$S_t$ (MPa)
S1	MODT05	13.8	1.2
	MODT06	14.7	1.3
S2	MODT07	12.5	1.6
	MODT08	11.9	1.7
S3	MODT09	17.2	1.2
	MODT10	17.4	1.3
Average	----	14.6	1.4

Table 6.3 Results on halite in the uniaxial compression tests

specimen number	test number	$E_c$ (GPa)	$\nu_c$	$S_c$ (MPa)
S1	MODC05	27.6	0.26	27.0
	MODC06	26.1	0.33	26.2
S2	MODC07	25.0	0.35	36.0
	MODC08	25.2	0.24	35.0
S3	MODC09	26,1	0.37	29.0
	MODC10	24.6	0.35	26.5
Average	----	25.8	0.32	29.9

Table 6.4 Results on halite from the new technique

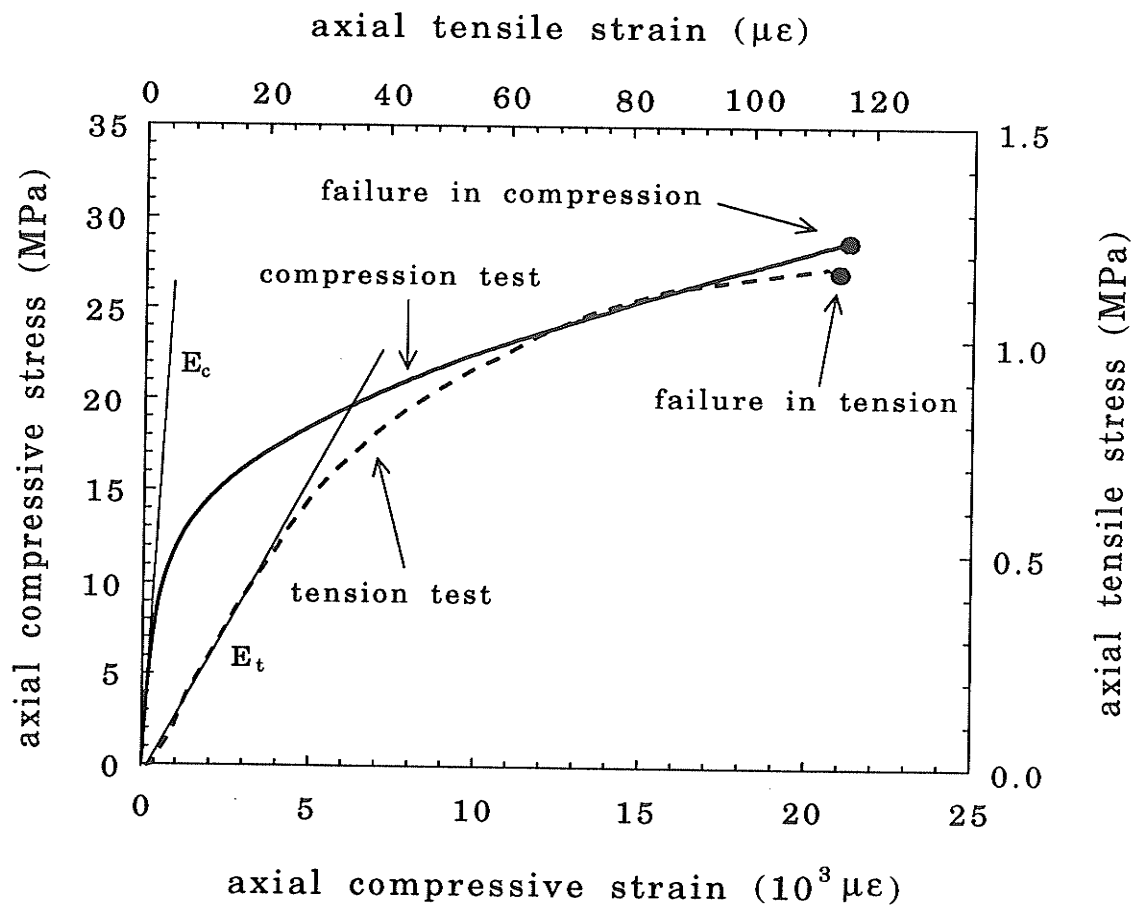
specimen number	stress state	load step	$P_{max}$ (MPa)	$E$ (GPa)	$\nu$
S1	Compression	1	3.5	32.2	0.30
		3	7.0	31.7	0.32
	Tension	2	0.5	18.3	----
		4	1.1*	17.1	----
S2	Compression	1	3.5	31.7	0.27
		3	7.0	29.6	0.24
	Tension	2	0.5	13.4	----
		4	1.0*	12.7	----
S3	Compression	1	3.5	22.4	0.25
		3	7.0	25.0	0.32
	Tension	2	0.5	12.7	----
		4	1.0*	10.0	----

\* Final failure

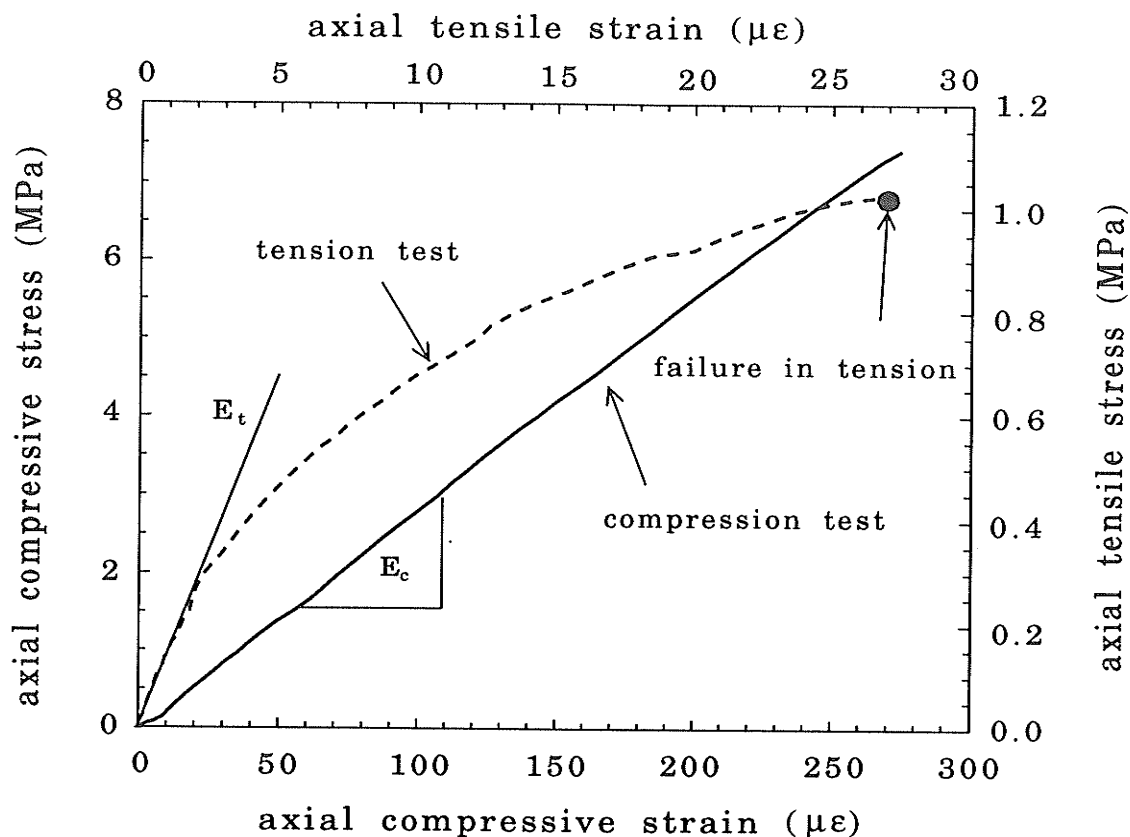
After unloading again, the specimen was loaded in compression to 7 MPa (load step 3) before a final unloading and reloading in tension until failure (load step 4). The average Young's moduli are 28.8 GPa in compression and 14.0 GPa in tension, which gives a ratio of Young's modulus in tension to that in compression of  $E_t/E_c=0.49$ . These data are comparable with those obtained from the standard uniaxial compression and uniaxial tension tests. The arithmetic mean of moduli ratio combining data from both tests is 0.5.

Figure 6.9 shows the axial stress-axial strain curves from the standard uniaxial compression and direct tension tests, where the specimens were loaded directly to failure. Figure 6.10 shows the axial stress-axial strain curves of the second compression cycle and the final tension test in the new technique, where the specimen was tested by two load-

unload-reload cycles as noted before. The compression curve, therefore, reflects only the initial portion of the whole stress-strain curve and shows an initial linear response up to 7.5 MPa. The elastic moduli in tension ( $E_t$ ) and compression ( $E_c$ ) are tangential moduli measured from the initial linear portion on the axial stress-axial strain curves from both the standard and the new tests. The initial linear portion usually covers a stress range of 0-0.3 MPa in tension and 0-7 MPa in compression.



**Figure 6.9** Halite axial stress-axial strain curves from the standard tension and compression tests. The specimen was loaded under tension or compression continuously to the final failure.  $E_t$  and  $E_c$  are Young's moduli in tension and in compression, respectively, measured as the slope of the linear portion of the stress strain curves.



**Figure 6.10** Halite axial stress-axial strain curves from the combined compression-tension test.  $E_t$  and  $E_c$  are Young's moduli in tension and in compression, respectively, measured as the slope of the linear portion of the stress strain curves.

### 6.3.2 Results on Cominco potash

Tables 6.5 and 6.6 tabulate the results from the standard uniaxial tension and compression tests, respectively, including moduli of deformation in tension ( $E_t$ ) and in compression ( $E_c$ ), Poisson's ratio in compression ( $\nu_c$ ) and the ultimate tensile strength ( $S_t$ ) and compressive strength ( $S_c$ ). The average Young's moduli are 21.5 GPa in compression and 25.4 GPa in tension, which gives a ratio of Young's modulus in tension to that in compression of  $E_t/E_c=1.18$ . The average Poisson's ratio is 0.31 in compression. The average compressive strength is 22.7 MPa and the average tensile strength is 1.6 MPa.

Table 6.5 Results on potash from uniaxial tension tests

specimen number	test number	$E_t$ (GPa)	$S_t$ (MPa)
S1	MODT01	20.8	1.4
	MODT02	24.5	1.8
S2	MODT03	26.9	1.3
	MODT04	27.4	1.6
S3	MODT11	28.1	1.9
	MODT12	24.9	1.8
Average	----	25.4	1.6

Table 6.6 Results on potash from uniaxial compression tests

specimen number	test number	$E_c$ (GPa)	$\nu_c$	$S_c$ (MPa)
P1	MODC01	20.0	0.31	20.5
	MODC02	20.4	0.44	21.2
P2	MODC03	20.8	----	21.5
	MODC04	25.2	0.37	23.0
P3	MODC11	21.7	0.21	24.5
	MODC12	20.9	0.20	25.5
average	----	21.5	0.31	22.7

Table 6.7 presents the results from the new combined compression-tension tests conducted in an identical fashion to the halite testing program. The average Young's moduli are 19.8 GPa in compression and 17.9 GPa in tension, which gives a ratio of Young's modulus in tension to that in compression of  $E_t/E_c=0.90$ . These data are comparable with those obtained by the standard uniaxial compression and uniaxial tension tests. The arithmetic mean of moduli ratio combining data from both tests is 1.0.

Figures 6.11 and 6.12 are the stress-strain curves from the standard tests and the new method respectively. Again, the compressive stress-strain curve from the new test (Figure 6.12) reflects only the initial portion of the whole stress-strain curve and shows a linear response up to 7.5 MPa. The elastic moduli in compression are tangential moduli

Table 6.7 Results on potash from the new technique

specimen number	stress state	load step	$P_{max}$ (MPa)	$E$ (GPa)	$\nu$
P1	Compression	1	3.5	18.2	0.20
		3	7.0	20.7	0.21
	Tension	2	0.5	19.7	----
		4	1.1*	16.5	----
P2	Compression	1	3.5	27.3	0.30
		3	7.0	28.3	0.31
	Tension	2	0.5	27.3	----
		4	1.0*	29.2	----
P3	Compression	1	3.5	14.2	0.25
		3	7.0	10.1	0.32
	Tension	2	0.5	7.2	----
		4	1.0*	----	----

\* Final failure.

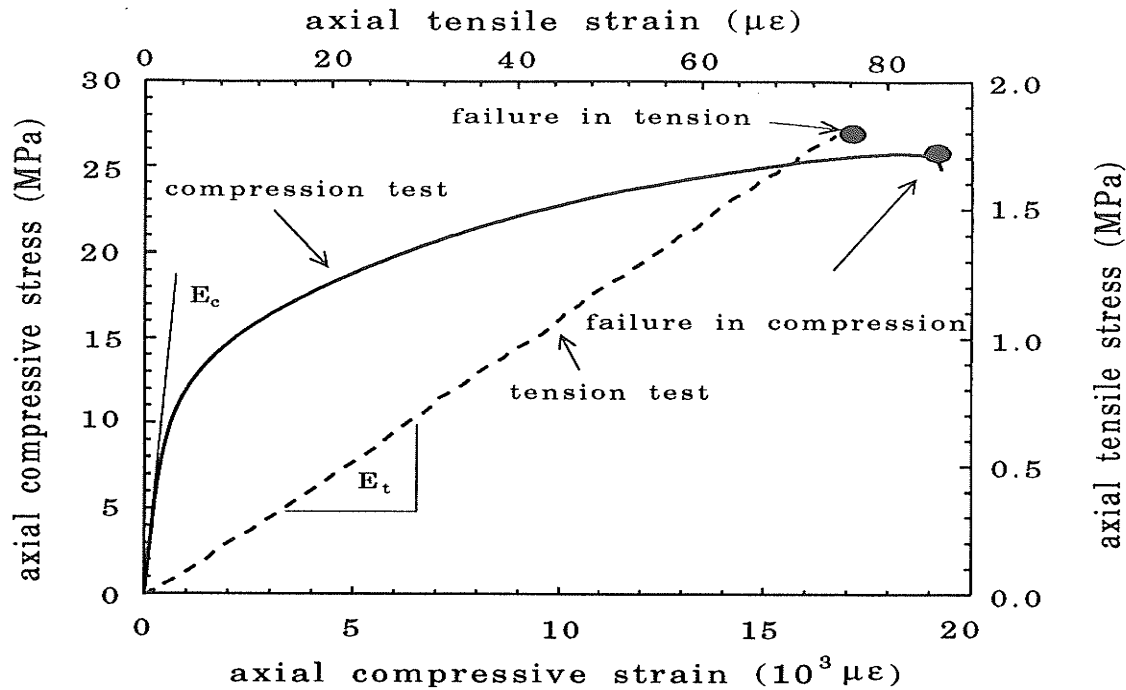


Figure 6.11 Potash axial stress-axial strain curves from the standard tension and compression tests.  $E_t$  and  $E_c$  are Young's moduli in tension and in compression, respectively, measured as the slope of the linear portion of the stress strain curves.

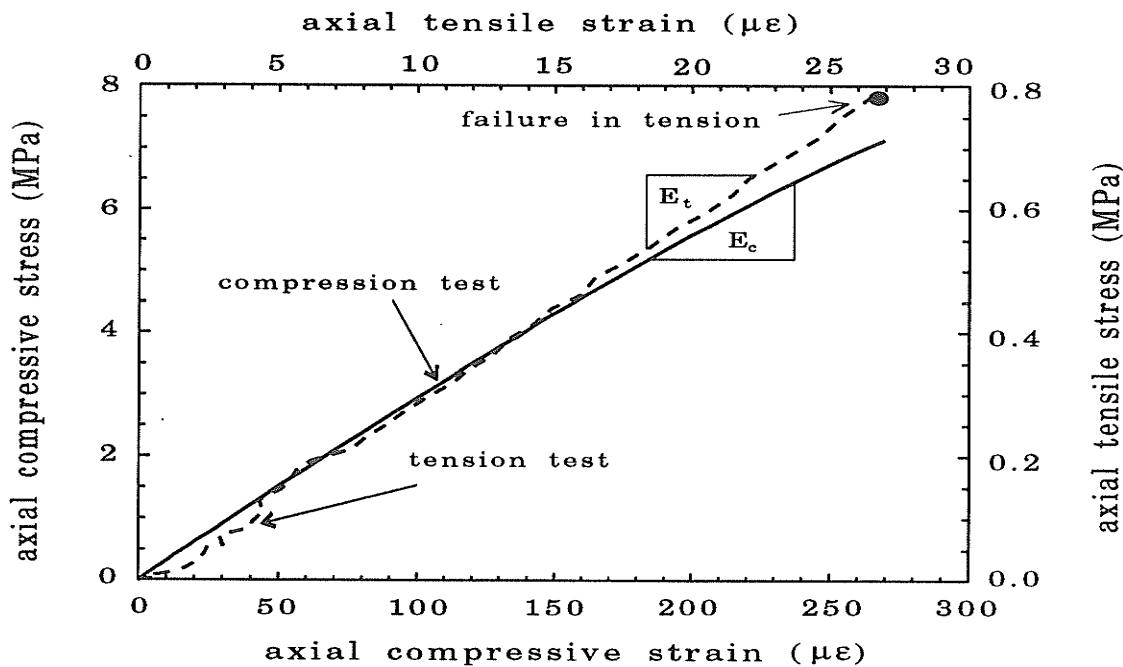


Figure 6.12 Potash axial stress-strain curves from the combined compression-tension test.  $E_t$  and  $E_c$  are Young's moduli in tension and in compression, respectively, measured as the slope of the linear portion of the stress strain curves.

measured at the initial linear portion in the stress range of 0-7 MPa. The tensile stress-strain curves of potash show an approximately linear response up to failure and its slope is taken as the tensile modulus.

### 6.3.3 Results on Lac du Bonnet granite

For comparison purposes, one combined compression-tension specimen was prepared from a block of Lac du Bonnet (pink) granite. The specimen was cycled in step loads as indicated in Table 6.8. The axial stress-axial strain curves in both tension and compression tests on the Lac du Bonnet granite show a short initial non-linear response, followed by an approximately linear portion that covers a stress range of 0.5-4 MPa in tension and 10-60 MPa in compression. The Young's modulus was measured as the slope of this linear portion of the stress-strain curves. The Young's modulus was not calculated

Table 6.8 Step loads and Young's moduli for Lac du Bonnet granite

stress state	load step	$P_{max}$ (MPa)	$E$ (GPa)	$\nu$	$E_a$ (GPa)	$\nu_a$ avg	$E_t/E_c$
compression	1	20.0	60.4	----	63.5	0.2	0.7
	3	30.0	62.5	----			
	5	40.0	64.3	0.17			
	7	50.0	66.7	0.22			
tension	2	1.0	----	----	44.3	0.2	
	4	2.0	43.1	0.17			
	6	4.0	43.6	0.21			
	8	4.4*	46.2	0.23			

\* Final failure

from the first tensile test due to the fact that the ultimate tensile stress is low and a large portion of the stress-strain curve is still in the initial non-linear portion. The average Young's moduli are 44.3 GPa in tension and 63.5 GPa in compression, respectively, giving a moduli ratio of 0.7. The Poisson's ratio in tension appears to be similar to that in compression for this specimen.

### 6.3.4 Results on Tyndall limestone

Three combined compression-tension specimens were tested. The loading steps are shown in Table 6.9. Specimen L1 failed in the third tensile cycle at a tensile stress of 0.7 MPa. The other two specimens, L2 and L3, failed at the first tensile cycle at tensile stresses of 0.66 MPa and 0.34 MPa, respectively. Results from Tyndall limestone appear

Table 6.9 Step loads and Young's moduli for Tyndall limestone

specimen number	stress state	load step	$P_{max}$ (MPa)	$E$ (GPa)	$\nu$
L1	Compression	1	10.0	26.2	0.21
		3	20.0	36.5	0.28
		5	30.0	39.0	0.24
	Tension	2	0.5	16.1	0.18
		4	1.0	12.7	0.16
		6	0.7*	16.8	0.13
L2	Compression	1	10.0	32.8	----
	Tension	2	0.66*	12.2	----
L3	Compression	1	10.0	27.2	----
	Tension	2	0.34*	7.5	----

\* Final failure.

to show some degree of variability between specimens. The Young's modulus in compression from three specimens ranges from 33.9 GPa (average of specimen L1) to 27.2 GPa. Young's modulus in tension ranges from 15.2 MPa (average of specimen L1) to 7.5 MPa. The ratio of tensile to compressive moduli is 0.3 to 0.4.

#### 6.4 Discussion of Experimental Results

For potash and halite direct comparisons were made between deformational moduli determined from the standard uniaxial compression and tension tests and those from the new procedure. In comparing the moduli ratios calculated from the two techniques, it must be recognized that different specimens were used for the standard uniaxial compression and uniaxial tension tests. Specimen variability may, therefore, have played a role in the results. However, the results from the two different tests are regarded as comparable and provide reasonable evidence for the validity of the new testing technique because the potash and halite blocks were quite uniform (crystal size and mineralogy). Testing results are also comparable with data from previous testing programs (Carter 1992*b*; Carter et al. 1991*b*; Duncan 1990).

A testing program on Lac du Bonnet granite yielded Young's moduli of 44 GPa in tension and 59 GPa in compression from a single cylindrical specimen that was tested in direct compression in a compressive loading machine first and then tested in direct tension in a tensile loading machine (Lajtai 1992), giving a moduli ratio of 0.7. The average Young's modulus in tension from a group of direct tension tests is 38 GPa (Lajtai 1992). The average Young's modulus in compression from various previous studies is 65-

70 GPa (Lajtai 1992; Carter 1992*b*; Martin and Christianson 1991; Katsube and Hume 1987). The moduli of Lac du Bonnet granite from the new combined compression-tension tests in this study are comparable with the above mentioned results.

Based on these comparisons, it can be suggested that the new technique is superior because it eliminates problems arising from specimen to specimen variability. For particularly non-uniform and/or heterogeneous materials, the specimen to specimen variation is considerable and makes any comparison of tensile and compressive moduli obtained from two different specimens by the conventional tests difficult.

Apart from potash, which has a moduli ratio of about 1.0, halite, granite and limestone have moduli ratios well below 1.0 (Table 6.10). Poisson's ratios in tension and in compression appear similar for all the rocks tested.

Luong's specimen configuration (Luong 1988) provided an excellent starting point for the development of the new testing technique presented in this chapter. However, Luong's idea of using the specimen configuration for measuring rock tensile strength appears to be flawed. Stress analyses by the finite element method indicated high stress

Table 6.10 Summary of Young's moduli in tension and in compression

rock type	$E_t$ (GPa)	$E_c$ (GPa)	$E_t/E_c$
Cominco halite	14.3	27.3	0.5
Cominco potash	22.7	20.7	1.1
Lac du Bonnet granite	44.3	63.5	0.7
Tyndall limestone	11.9	28.7	0.4

concentrations around the notches at the ends of the drilling slots (Figure 6.13). Moreover, all the specimens taken to failure invariably ruptured at or close to the blind end of the inner slot (Figures 6.14), instead of in the area where uniform tensile stress is induced. This method is, therefore, unsuitable for the measurement of tensile strength, since it yields a strength much lower than the actual rock tensile strength.

In the final section of this chapter, some practical implications of bimodular behavior of rock are briefly discussed.

### **6.5 Implications of Bimodular Behavior of Rock**

Bimodular behavior is of significance in situations where the state of stress is tension or mixed compression and tension. These conditions arise in a number of situations in rock engineering (underground openings in massive and layered strata, fragmentation or cutting by blasting, drilling, TBM's and roadheaders, allowable mud pressures in well bores, well bore stability, hydraulic fracturing, internally pressurized openings (hydro-power tunnels, underground gas/compressed air storage)), and in rock testing (Brazilian, hydraulic extension, ring, and beam bending tests for tensile strength). States of mixed stress may also arise in weathering of rock surfaces, thermal stressing of rock, and from residual stresses.

Bimodularity is of practical significance because it influences stress distribution, strains, displacements, and fracture propagation. For example, a simply supported, uniformly loaded beam with a moduli ratio of 0.5 will suffer maximum deflections some 50% larger than a beam with a moduli ratio of 1.0 (Chen et al. 1991). The analysis of

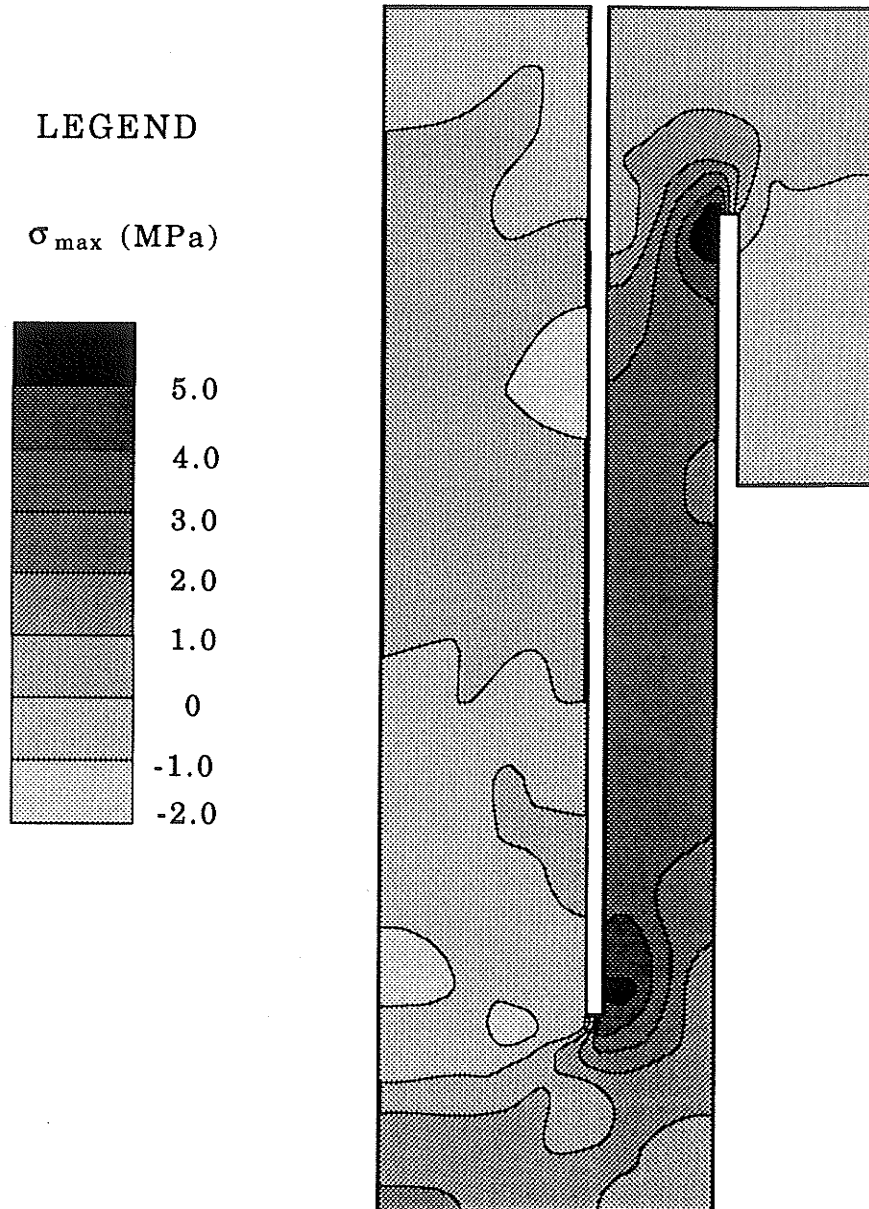


**Figure 6.13** Contour map of the maximum tensile principal stress in tensile loading test by the combined compression-tension technique, indicating high stress concentrations around the notches at the ends of the drilling slots.

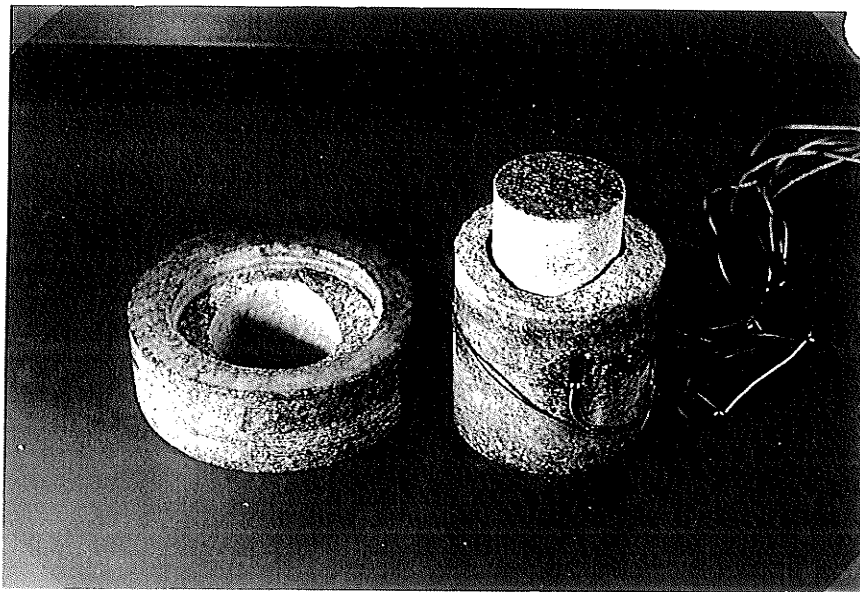
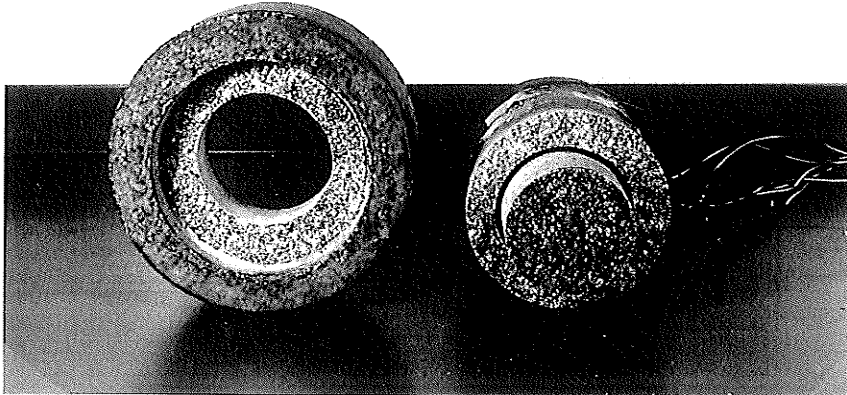


**Figure 6.14** Photo of specimen G1 after testing. The specimen was taken to failure by rupturing at the blind end of the inner slot.

roof behavior and fracture in rock should therefore take into account any bimodular behavior, e.g. in the potash mines in Saskatchewan, the roof or back of underground excavations is typically a layer of halite whose moduli ratio was determined to be about 0.5.

Hydraulic fracturing from boreholes for *in situ* stress determination and reservoir stimulation (for production of oil/hydrothermal power) places the rock in a state of mixed stress. Haimson and Tharp (1974) examined the stresses around a borehole in bimodular rock and found the hydraulic pressures required for fracturing to be higher than those predicted from the assumption of equal moduli in tension and compression.

Wilson (1988) obtained a moduli ratio of 0.4 for Athabasca oil sands and concluded that the propagation of hydraulic fractures to provide paths for steam injection and oil flow would require more energy than if the material was unimodular.

The three-point beam bending, hydraulic extension, Brazilian and ring tests are the most commonly utilized indirect tension tests and for their interpretation it is generally assumed that the moduli in tension and in compression are equal. A recent investigation (Chen and Stimpson 1993*a* and 1993*b*) shows that this assumption leads to erroneously high estimates of tensile strength. For example, for a material with a moduli ratio of 0.5, the tensile strength is overestimated by 25% for a hydraulic extension test, and by 15% for the beam bending, Brazilian and ring tests. The influence of bimodularity on indirect tension tests is treated in greater detail in the following chapter.

## 6.6 Chapter Summary

The new testing technique allows the measurement of deformational moduli in tension and in compression of rock from one specimen in a single compression frame. Using this test, bimodularity has been demonstrated in halite, granite, and limestone.

The bimodularity of rock should be taken into account when the state of stress is mixed (tension and compression). Failure to do so may lead to significant errors in design and interpretation of indirect tensile strength test data.

## 7. IMPLICATIONS OF ROCK BIMODULAR BEHAVIOR

### 7.1 Introduction

Chapter 6 provided evidence for the bimodular properties of several rocks. Although recognition of material bimodularity dates back as far as Saint-Venant (1864), the determination of the constitutive relations for bimodular materials has been undertaken only within the last few decades, starting with Ambartsumyan (1966). Since the 1970's, numerous attempts have been made to establish bimodular elastic stress-strain relationships and their analytical solutions for simple engineering structures. One of the leading contributions, which brought out an extensive body of literature, is the work of Bert and coworkers (Bert 1985). For more than 10 years, they have been investigating bimodular composite structures, such as beams (Bert and Tran 1982; Bert 1983*a* and 1983*b*; Gordaninejad and Bert 1989), plates (Bert et al. 1981; Gordaninejad 1989), cylindrical shells (Bert and Reddy 1980; Bert and Kumer 1981) and columns (Bert and Ko 1985).

In rock mechanics, research on material bimodularity has been sporadic. Fairhurst (1961) and Burshtein (1967) derived stress formulae for rectangular beams in flexure, while Adler (1970) developed formulae for beams of circular, as well as, more general cross-sections. These studies were based on the *transformed section* concept of mechanics of materials. Later works were mainly based on a simplified bilinear, elastic constitutive relation originally developed by Ambartsumyan (1966), e.g., Haimson and Tharp, and Passaris' stress solutions around boreholes (Haimson and Tharp 1974; Passaris 1977),

Sundaram and Corrales' discussion on the Brazilian test (Sundaram and Corrales 1980), and Khan and Yuan's attempt to develop a three-dimensional finite element program for brittle, bimodular, rock-like materials (Khan and Yuan 1988). Ambartsumyan's relation utilizes the assumption that  $\nu_t/E_t = \nu_c/E_c$ , where  $\nu_t$  and  $E_t$  are the Poisson's ratio and Young's modulus in tension, and  $\nu_c$  and  $E_c$  are the Poisson's ratio and Young's modulus in compression, respectively. Since this assumption has no experimental verification, the validity of Ambartsumyan's model has been questioned (Jones 1977; El-Tahan et al. 1989).

In rock tensile testing and rock excavation, bimodularity has been ignored largely although its influence may be significant due to the occurrence of mixed compression and tension stress states in various situations as discussed in the final section of Chapter 6.

In this chapter, the practical implications of rock bimodularity are discussed further and the existing constitutive models for bimodular materials for plane problems are reviewed briefly. The analytical solutions for simple structures such as beams and thick-walled cylinders are derived and a finite element program is developed to incorporate a bimodular constitutive model proposed by El-Tahan et al. (1989). Finally, the effects of bimodularity on four of the commonly utilized indirect rock tensile tests (three-point beam bending, hydraulic extension, Brazilian and ring tests) and on roof failure in a simulated rectangular underground opening in potash are investigated either analytically or numerically.

## 7.2 Review of Constitutive Equations for Bimodular Materials

### 7.2.1 General constitutive relationships in plane problems

From the following general constitutive equations:

$$\varepsilon_{ij} = \frac{(1+\nu)}{E} \sigma_{ij} - \frac{\nu}{E} \delta_{ij} \sigma_{kk}$$

One can obtain the matrix form of the constitutive relation in plane problems as:

$$\begin{Bmatrix} \varepsilon_1 \\ \varepsilon_2 \\ \gamma_{12} \end{Bmatrix} = \begin{bmatrix} C_{11} & C_{12} & 0 \\ C_{12} & C_{22} & 0 \\ 0 & 0 & C_{33} \end{bmatrix} \begin{Bmatrix} \sigma_1 \\ \sigma_2 \\ \tau_{12} \end{Bmatrix} \quad (7.1)$$

where  $C_{22} = C_{11}$ ,  $C_{33} = 2(C_{11} - C_{12})$ . For general linear, elastic, homogeneous, and isotropic materials, the elastic compliances in this stress-strain relation are constants:  $C_{11} = 1/E$  and  $C_{12} = -\nu/E$  for plane stress,  $C_{11} = \frac{1}{E}(1-\nu^2)$  and  $C_{12} = -\frac{1}{E}\nu(1+\nu)$  for plane strain, where  $E$

is Young's modulus and  $\nu$  is Poison's ratio.

### 7.2.2 Constitutive relation for bimodular materials

For bimodular materials, constitutive equations have to be established according to the sign of the principal stresses. Throughout this study, a negative stress value denotes compression and a positive stress value denotes tension. There are two stress regions:

**Region of the first kind** All the principal stresses are either positive or negative ( $\sigma_1 > 0$ ,  $\sigma_2 > 0$  or  $\sigma_1 < 0$ ,  $\sigma_2 < 0$ ). The material can be treated as isotropic. The general constitutive relation is described by Equation 7.1, with the corresponding elastic constants equal to  $E_t$ ,  $\nu_t$  for  $\sigma_1 > 0$  and  $\sigma_2 > 0$  and  $E_c$ ,  $\nu_c$  for  $\sigma_1 < 0$  and  $\sigma_2 < 0$ .

**Region of the second kind** One of the principal stresses has a different sign than the other two ( $\sigma_1 > 0, \sigma_2 < 0$  or  $\sigma_1 < 0, \sigma_2 > 0$ ). The material behavior is similar to that of an orthotropic medium. The general constitutive relation can still be described by Equation 7.1. However, the elastic compliances ( $C_{11}, C_{12}, C_{22}$  and  $C_{33}$ ) are not constants but depend on the signs of the principal stresses. Their determination hinges on a proper material bimodular model.

### 7.2.3 Review of material bimodular models

Several material bimodular models exist in the literature, all using Equation 7.1 as a basic constitutive relation. The primary difference among these models is in the way in which the symmetry of compliances is imposed. An earlier model, introduced by Ambartsumyan (1966), is known as the bilinear model. The model imposes symmetry of the compliance matrix by forcing an artificial reciprocal relation between the elastic constants in tension and compression (i.e.,  $\nu_t/E_t = \nu_c/E_c$ ). This assumption was questioned for real materials experimentally (Jortner 1972; Neelamegan et al. 1984; Novak and Bert 1968). The model yields a cross compliance,  $C_{12}$ , that is not continuous in the principal stress space (Figure 7.1a). Jones (1977) proposed the Weighted Compliance Matrix material model (WCM) to impose symmetry of compliances by introducing weighting factors that are functions of the principal stresses. However, the slope of the cross compliance in the WCM model is not continuous, indeed, it changes dramatically at the  $\sigma_2$  principal stress axis (Figure 7.1b). Recently, El-Tahan et al (1989) proposed MWCM model which is a modification of the WCM model by eliminating the slope discontinuity

by connecting the circular arcs in quadrants I and III (each having a different radius) with an ellipse as indicated in Figure 7.2. The parametric representation of the ellipse is:

$$x = a \cos \theta, \quad y = b \sin \theta, \quad r = \sqrt{x^2 + y^2} \quad (7.2)$$

In principal stress space, these parameters are identified as:

$$a = C_{12}^t, \quad b = C_{12}^c, \quad r = C_{12} \quad (7.3)$$

$$\tan \theta = \frac{\sigma_2}{\sigma_1}, \quad \sin \theta = \frac{\sigma_2}{\sqrt{\sigma_1^2 + \sigma_2^2}}, \quad \cos \theta = \frac{\sigma_1}{\sqrt{\sigma_1^2 + \sigma_2^2}}$$

Substituting (7.3) into (7.2) and performing the same exercise in the  $\sigma_2$ - $\sigma_3$  and  $\sigma_3$ - $\sigma_1$  planes, equations for  $C_{12}$ ,  $C_{13}$  and  $C_{23}$  are obtained (El-Tahan et al 1989):

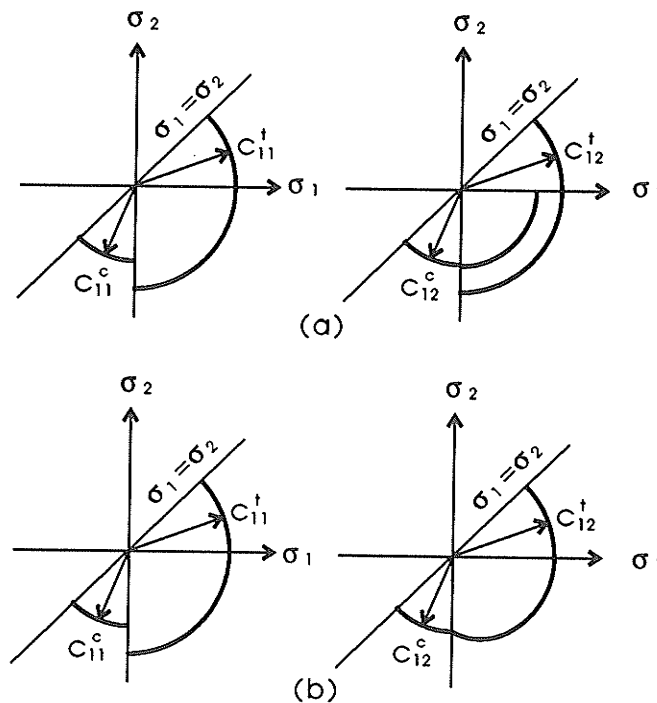


**Figure 7.1** Compliances of bimodular constitutive relation (after El-Tahan et al. 1989). (a) Ambartsumyan model, the cross compliance,  $C_{12}$ , is not continuous in the principal stress space; (b) WCM model, the cross compliance is continuous, but its slope is not continuous.

$$\left. \begin{aligned} C_{12}^2 &= K_1 \left(\frac{\nu_t}{E_t}\right)^2 + K_2 \left(\frac{\nu_c}{E_c}\right)^2 \\ C_{13}^2 &= K_3 \left(\frac{\nu_t}{E_t}\right)^2 + K_4 \left(\frac{\nu_c}{E_c}\right)^2 \\ C_{23}^2 &= K_5 \left(\frac{\nu_t}{E_t}\right)^2 + K_6 \left(\frac{\nu_c}{E_c}\right)^2 \end{aligned} \right\} \quad (7.4)$$

where

$$\begin{aligned} K_1 &= \frac{\sigma_1^2}{(\sigma_1^2 + \sigma_2^2)}, & K_2 &= \frac{\sigma_2^2}{(\sigma_1^2 + \sigma_2^2)}, & K_3 &= \frac{\sigma_1^2}{(\sigma_1^2 + \sigma_3^2)} \\ K_4 &= \frac{\sigma_3^2}{(\sigma_1^2 + \sigma_3^2)}, & K_5 &= \frac{\sigma_3^2}{(\sigma_2^2 + \sigma_3^2)}, & K_6 &= \frac{\sigma_2^2}{(\sigma_2^2 + \sigma_3^2)} \end{aligned} \quad (7.5)$$

With these cross compliances, all the coefficients in the constitutive relations for plane problems (Equation 7.1) can then be expressed explicitly.

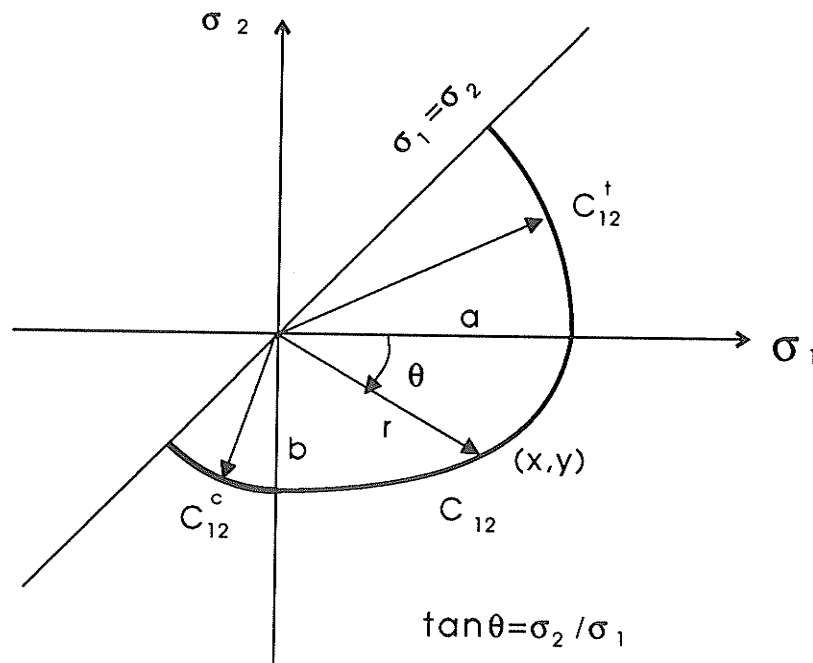


**Figure 7.2** Cross compliance in MWCM bimodular material model, both the cross compliance and its slope are continuous (after El-Tahan et al. 1989).

**Plane stress:** Assuming that  $\sigma_1$  is the maximum principal stress and  $\sigma_1 > \sigma_2$ , all the stress states lie below the  $\sigma_2 - \sigma_1 = 0$  line as shown in Figure 7.3a. There are three cases associated with a plane stress problem:

Case 1:  $\sigma_1 \geq 0, \sigma_2 \geq 0$ , region of the first kind

$$C_{11} = C_{22} = \frac{1}{E_t}, \quad C_{12} = -\frac{\nu_t}{E_t} \quad (7.6)$$

Case 2:  $\sigma_1 \geq 0, \sigma_2 < 0$ , region of the second kind

$$C_{11} = \frac{1}{E_t}, \quad C_{22} = \frac{1}{E_c}, \quad C_{12}^2 = K_1 \left(\frac{\nu_t}{E_t}\right)^2 + K_2 \left(\frac{\nu_c}{E_c}\right)^2 \quad (7.7)$$

Case 3:  $\sigma_1 < 0, \sigma_2 < 0$ , region of the first kind

$$C_{11} = C_{22} = \frac{1}{E_c}, \quad C_{12} = -\frac{\nu_c}{E_c} \quad (7.8)$$

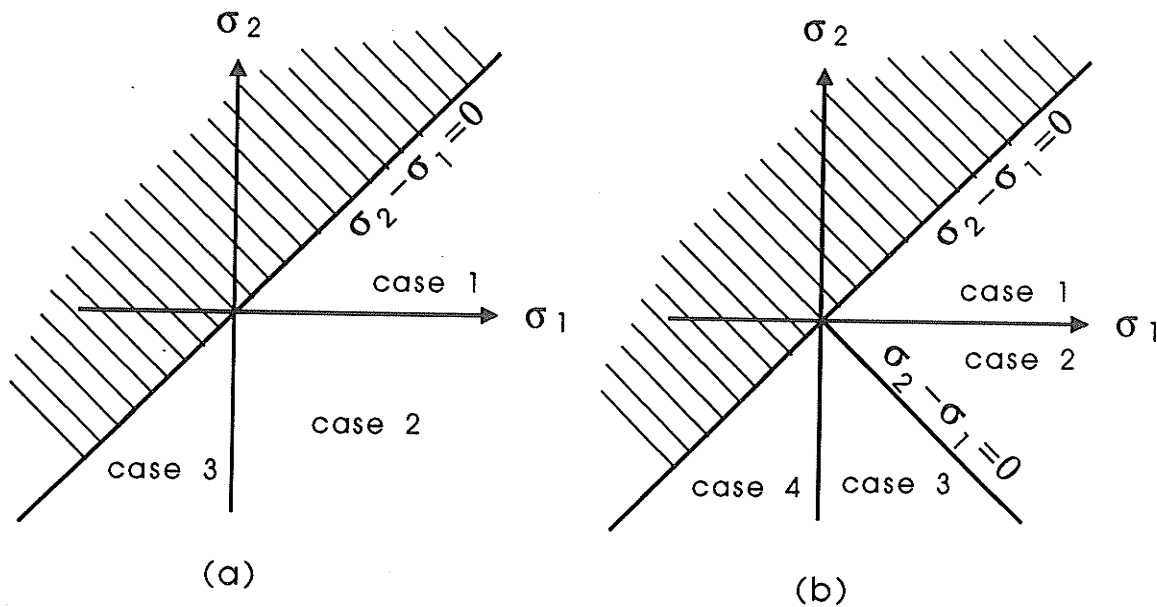


**Figure 7.3** The principal stress-space representation of various cases of (a) plane stress, and (b) plane strain. There are three cases for a plane stress problem and four cases for a plane strain problem according to the signs of the principal stresses.

**Plane strain:** Using  $\hat{C}$  replaces corresponding  $C$  in Equation 7.1. There are four distinct cases for plane strain problem (Figure 7.3b)

Case 1:  $\sigma_1 \geq 0, \sigma_2 \geq 0$ , region of the first kind

$$\hat{C}_{11} = \hat{C}_{22} = \frac{1}{E_t}(1 - \nu_t^2), \quad \hat{C}_{12} = -\frac{1}{E_t}\nu_t(1 + \nu_t) \quad (7.9)$$

Case 2:  $\sigma_1 \geq 0, \sigma_2 < 0, \sigma_1 + \sigma_2 \geq 0$ , region of the second kind

$$\hat{C}_{11} = C_{11}^t - \frac{C_{13}^2}{C_{33}^t}, \quad \hat{C}_{22} = C_{22}^c - \frac{C_{23}^2}{C_{33}^t}, \quad \hat{C}_{12} = C_{12} - \frac{C_{13}C_{23}}{C_{33}^t} \quad (7.10)$$

where  $C_{11}^t = C_{33}^t = 1/E_t$ ,  $C_{22}^c = 1/E_c$ ,  $C_{13} = -\nu_t/E_t$ ,  $C_{12}$  and  $C_{23}$  are defined in Equation 7.4.

Case 3:  $\sigma_1 \geq 0, \sigma_2 < 0, \sigma_1 + \sigma_2 < 0$ , region of the second kind

$$\hat{C}_{11} = C_{11}^t - \frac{C_{13}^2}{C_{33}^c}, \quad \hat{C}_{22} = C_{22}^c - \frac{C_{23}^2}{C_{33}^c}, \quad \hat{C}_{12} = C_{12} - \frac{C_{13}C_{23}}{C_{33}^c} \quad (7.11)$$

where  $C_{11}^t = 1/E_t$ ,  $C_{22}^c = C_{33}^c = 1/E_c$ ,  $C_{23} = -\nu_c/E_c$ ,  $C_{12}$  and  $C_{13}$  are defined in Equation 7.4.

Case 4:  $\sigma_1 < 0, \sigma_2 < 0$ , region of the first kind

$$\hat{C}_{11} = \hat{C}_{22} = \frac{1}{E_c}(1 - \nu_c^2), \quad \hat{C}_{12} = -\frac{1}{E_c}\nu_c(1 + \nu_c) \quad (7.12)$$

By applying stress and strain transformations and after algebraic and trigonometric manipulations, the strain-stress relationship in Cartesian coordinates (x-y) can be written as:

$$\begin{Bmatrix} \epsilon_x \\ \epsilon_y \\ \gamma_{xy} \end{Bmatrix} = [S] \begin{Bmatrix} \sigma_x \\ \sigma_y \\ \tau_{xy} \end{Bmatrix} \quad (7.13)$$

where

$$[S] = \begin{bmatrix} C_{11} & C_{12} & 0 \\ C_{12} & C_{11} & 0 \\ 0 & 0 & C_{33} \end{bmatrix} + A \begin{bmatrix} n^4 & m^2 n^2 & -2mn^3 \\ m^2 n^2 & m^4 & -2m^3 n \\ -2mn^3 & -2m^3 n & 4m^2 n^2 \end{bmatrix} \quad (7.14)$$

where  $m = \cos\theta$ ,  $n = \sin\theta$ ,  $\theta$  is the angle between the x-axis and the maximum principal stress axis and  $A = C_{22} - C_{11}$ . The magnitude of  $A$  reduces to zero in regions of the first kind. The stiffness matrix is then:

$$[D] = [S]^{-1}$$

Due to the nonlinearity and dependency of  $[D]$  on the sign and the magnitude of the principal stresses, an iterative technique is usually necessary for solving any bimodular constitutive relations. However, for very simple problems, an analytical solution is possible based on certain assumptions. Usually, these simple problems are plane stress problems where the principal axes are identical with the reference coordinates and the sign of a specific principal stress remains unchanged throughout the region, or the problem has well defined compression and tension areas and their boundary conditions can be easily defined.

### 7.3 Analytical Solutions for Simple Structures

Whenever available, analytical solutions are essential for investigating the practical significance of bimodularity. In addition, analytical solutions on simple structures can be used to check the validity of numerical solutions. Therefore, in this section analytical solutions are derived incorporating bimodularity for two simple structures: a prismatic beam and a thick-walled cylinder. The beam is an elastic, simply supported beam with a uniformly distributed load,  $q$ , rectangular cross section (height  $h$  and width  $b$ ), span  $l$ ,

and Young's moduli  $E_t$  in tension and  $E_c$  in compression (Figure 7.4). The equations for the calculation of the neutral axis, beam deflection and stress components are derived based on the classical beam theory. The cylinder is a thick-walled cylinder with an internal radius  $r_i$ , an external radius  $r_o$ , and an internal pressure  $P_i$  and an external pressure  $P_o$  (Figure 7.5). Stresses are analyzed based on the solution proposed by

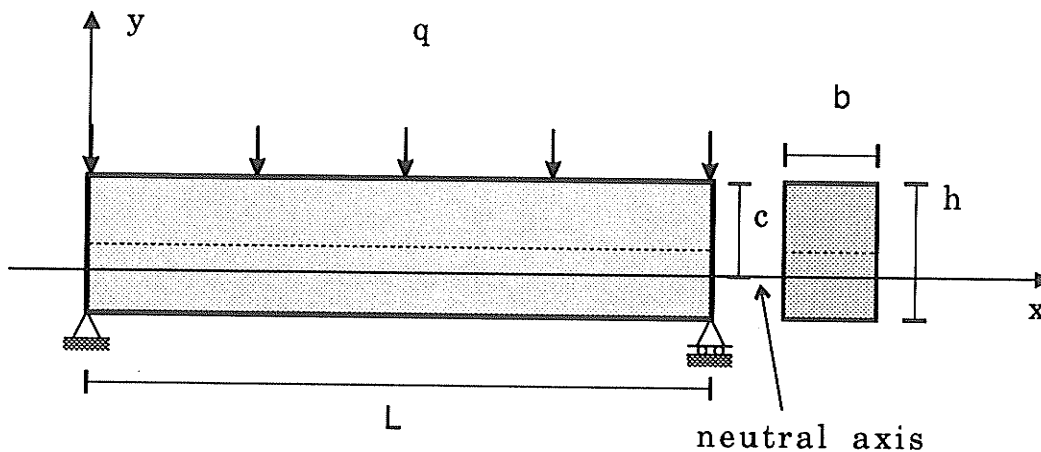


**Figure 7.4** Simply supported beam with uniformly distributed load  $q$ , a rectangular cross section (height  $h$ , width  $b$ ), and span  $L$ .

Haimson and Tharp (1974). Both problems have significant bearing in underground rock engineering. The beam problem is an approximation to the behavior of roof and floor and the cylinder is typically used for predicting the stress distribution around deep underground circular openings.

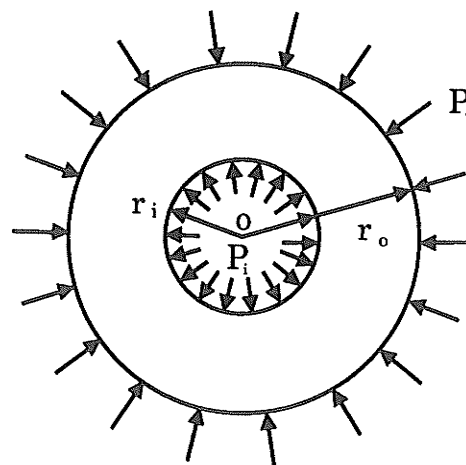


**Figure 7.5** Cross section of the thick-walled cylinder.

### 7.3.1 Solution of bimodular beam

In a simple beam bending problem, the principal stresses act along the  $x$  and  $y$  axes and  $\sigma_x$  is positive below the neutral axis (in tension) and negative above the neutral axis (in compression). Bimodular solution can be obtained using classical beam theory, provided that similar basic assumptions are maintained (Beer and Johnston 1981).

**Normal stress  $\sigma_x$ :** The longitudinal strain for a beam under pure bending is:

$$\epsilon_x = -\frac{y}{\rho} \quad (7.15)$$

where  $y$  is the vertical coordinate starting from the neutral axis and  $\rho$  is the curvature of a deformed neutral axis (Figure 7.6). The absolute values of the maximum compressive strain (on the top of the beam,  $y=c$ ) and the maximum tensile strain (on the bottom of the beam,  $y=-(h-c)$ ) are:

$$\epsilon_{mc} = \frac{c}{\rho}, \quad \epsilon_{mt} = \frac{h-c}{\rho} \quad (7.16)$$

where  $h$  is the beam height and  $c$  is the distance of the neutral axis from the top of the beam. Solving (7.16) for  $\rho$  for  $y \geq 0$  and  $y < 0$ , respectively and substituting the results into (7.15) yields:

$$\epsilon_x = \begin{cases} -\frac{y}{c} \epsilon_{mc} & y \geq 0 \\ -\frac{y}{(h-c)} \epsilon_{mt} & y < 0 \end{cases}$$

In the elastic range, Hook's law for uniaxial stress applies, i.e.  $\sigma = E\epsilon$ , therefore:

$$\sigma_x = \begin{cases} -\frac{y}{c} \sigma_{mc} & y \geq 0 \\ -\frac{y}{(h-c)} \sigma_{mt} & y < 0 \end{cases} \quad (7.17)$$

where  $\sigma_{mc} = E_c \varepsilon_{mc}$  and  $\sigma_{mt} = E_t \varepsilon_{mt}$  are the absolute values of the maximum compressive stress and the maximum tensile stress.

At this moment the location of the neutral axis ( $c$ ), the maximum stresses  $\sigma_{mc}$  and  $\sigma_{mt}$  are unknown. Three equations are required to solve these three unknowns. From the following static equilibrium equations:

$$\int \sigma_x dA = 0$$

$$\int (-y \sigma_x dA) = M$$

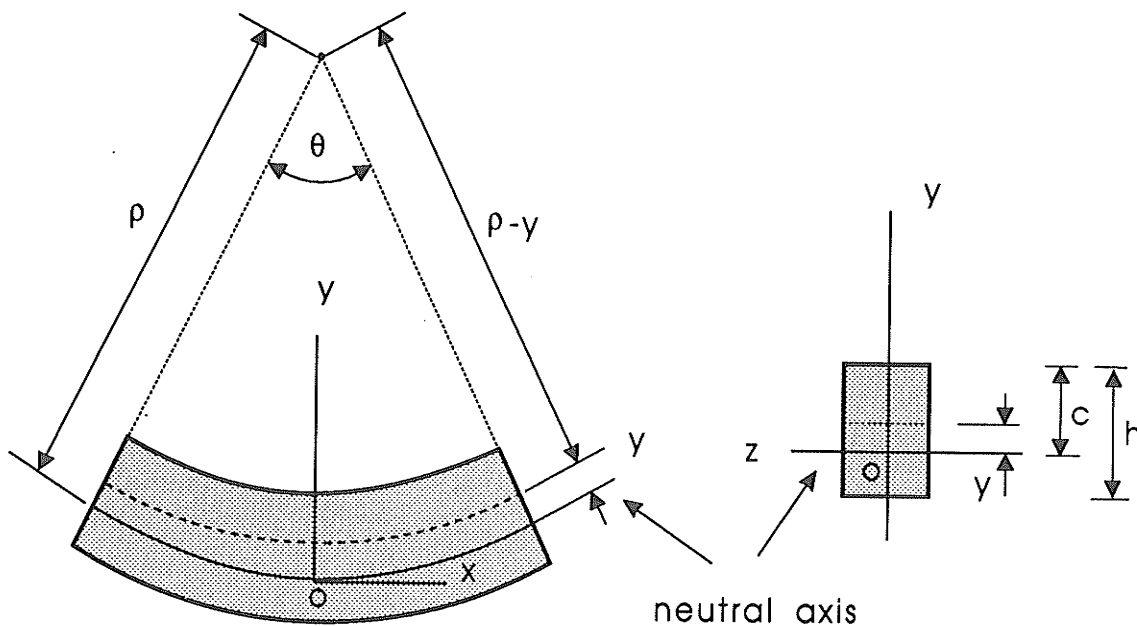


**Figure 7.6** A beam under pure bending: (a) longitudinal, vertical section (plane of symmetry), and (b) transverse section.  $c$  is the distance of the neutral axis from the top of the beam,  $\rho$  is the curvature of the deformed neutral axis, and  $y$  is the vertical coordinate starting from the neutral axis.

it can be shown that

$$c = \left( \frac{\sigma_{mt}}{\sigma_{mc} + \sigma_{mt}} \right) h \quad (7.18)$$

and that

$$\frac{\sigma_{mc}}{c} I_1 + \frac{\sigma_{mt}}{(h-c)} I_2 = M$$

where  $A$  is the cross sectional area of the beam,  $M$  is the total moment applied to the section, and  $I_1$  and  $I_2$  are the moments of inertia of the section area above and below the neutral axis respectively. For the case of a rectangular cross section shown in Figure 7.4,

$I_1 = \frac{1}{3}bc^3$ ,  $I_2 = \frac{1}{3}b(h-c)^3$ . The last equation becomes:

$$\frac{1}{3}bc^2\sigma_{mc} + \frac{1}{3}b(h-c)^2\sigma_{mt} = M \quad (7.19)$$

Recalling Equation (7.16)

$$\sigma_{mc} = E_c \frac{c}{\rho}, \quad \sigma_{mt} = E_t \frac{h-c}{\rho}$$

Therefore

$$\frac{\sigma_{mt}}{\sigma_{mc}} = \frac{E_t}{E_c} \left( \frac{h-c}{c} \right) = k \left( \frac{h-c}{c} \right) \quad (7.20)$$

where  $k$  is the moduli ratio ( $k = E_t/E_c$ ). By solving equations (7.18), (7.19) and (7.20) simultaneously, we obtain the location of the neutral axis,  $c$ , and the absolute values of the maximum stresses  $\sigma_{mt}$  and  $\sigma_{mc}$ :

$$c = \frac{h}{(1+k^{-1/2})} \quad (7.21)$$

$$\sigma_{mc} = (1+k^{-1/2}) \frac{3M}{bh^2}, \quad \sigma_{mi} = (1+k^{1/2}) \frac{3M}{bh^2} \quad (7.22)$$

For  $k < 1$ ,  $c < 0.5h$  and the neutral axis lies above the centre line of the beam; for  $k > 1$ ,  $c > 0.5h$  and the neutral axis lies below the centre line of the beam; and for  $k = 1$ ,  $c = 0.5h$ , the neutral axis and the centre line coincide. Substituting (7.22) and (7.21) back into (7.17) yields:

$$\sigma_x = \begin{cases} -(1+k^{-1/2})^2 \frac{3M}{bh^3} y & y \geq 0 \\ -(1+k^{1/2})^2 \frac{3M}{bh^3} y & y < 0 \end{cases} \quad (7.23)$$

**Shearing stress  $\tau_{xy}$ :** The shearing stress can be derived by considering a cantilever beam,  $AB$ , subjected to a load,  $P$ , at its free end (Figure 7.7). We detach a portion  $ACC'A'$  from the beam by passing a horizontal section  $A'C'$  at a distance  $y$  above the neutral axis, and a vertical section  $CC'$  at a distance  $x$  from free end. The forces acting on the free body  $ACC'A'$  are shown in Figure 7.8. Recalling equation 7.23 and

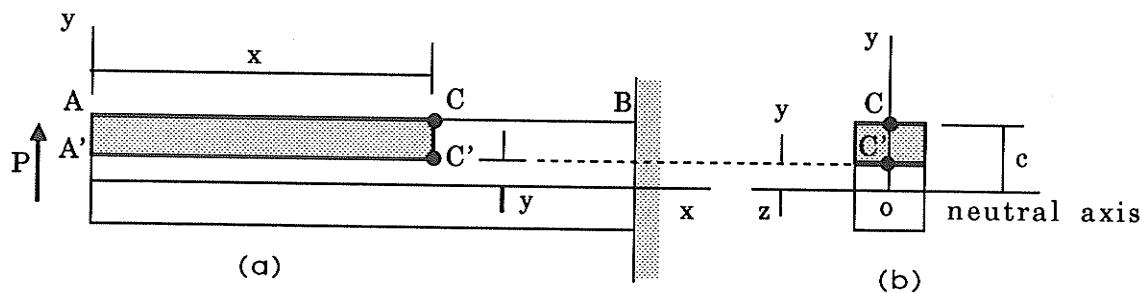


Figure 7.7 Portion  $ACC'A'$  in a cantilever beam for deriving shearing stress  $\tau_{xy}$ .

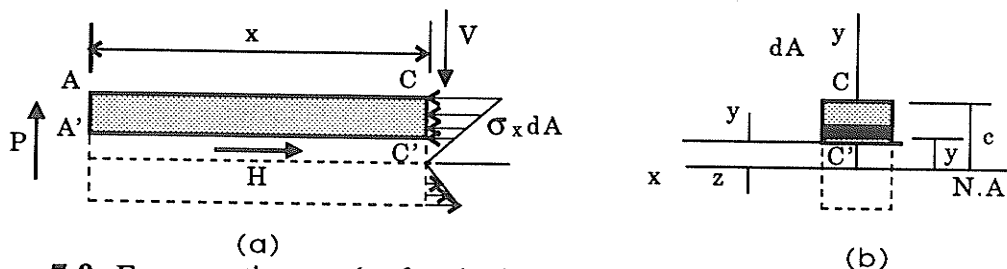


Figure 7.8 Forces acting on the free body  $ACC'A'$  for deriving shear stress  $\tau_{xy}$ .

because  $\sum F_x = 0$ :

$$H = \begin{cases} \frac{3M}{bh^3} (1+k^{-1/2})^2 \int_{y=y}^{y=c} y dA_1 & y \geq 0 \\ \frac{3M}{bh^3} (1+k^{1/2})^2 \int_{y=h-c}^{y=y} y dA_2 & y < 0 \end{cases}$$

where

$$\int_{y=y}^{y=c} y dA_1 = Q_1$$

$$\int_{y=h-c}^{y=y} y dA_2 = Q_2$$

are the first moment with respect to the neutral axis of the area located above  $y$  for  $y \geq 0$  and of the area located below  $y$  for  $y < 0$  respectively. Considering the moment  $M = Vx$  ( $x$  coordinate starts from the left end of the beam as shown in Figure 7.4), where  $V$  is the vertical shear in a section, we get shear flow:

$$q = \frac{H}{x} = \begin{cases} \frac{3V}{bh^3} (1+k^{-1/2})^2 Q_1 & y \geq 0 \\ \frac{3V}{bh^3} (1+k^{1/2})^2 Q_2 & y < 0 \end{cases} \quad (7.24)$$

Since  $\Delta H = q \Delta x$  (Figure 7.9), the average shear stress is:

$$\tau_{ave} = \frac{\Delta H}{\Delta A} = \frac{q \Delta x}{b \Delta x} = \frac{q}{b}$$

For a narrow rectangular beam ( $b \leq 0.25h$ ) (Figure 7.4), the variation of the shear stress,  $\tau_{xy}$ , across the width of the beam is less than 0.8% of  $\tau_{ave}$  (Beer and

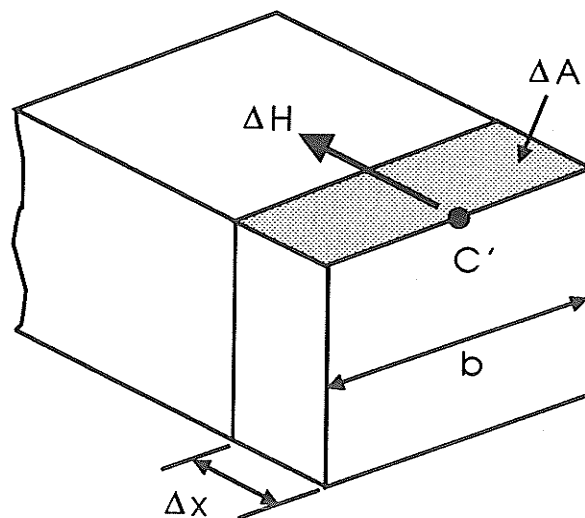


Figure 7.9 The shear force  $\Delta H$  exerts on a portion of length  $\Delta x$  of the horizontal cut through  $C'$ .

Johnston 1981), therefore:

$$\tau_{xy} \approx \tau_{ave} = \frac{q}{b}$$

For a beam with a rectangular cross section

$$Q_1 = \frac{1}{2}b (c^2 - y^2), \quad Q_2 = \frac{1}{2}b[(h-c)^2 - y^2]$$

Substituting  $Q_1$ ,  $Q_2$  into (7.24), substituting the obtained results into  $\tau_{xy}$ , and recalling (7.21):

$$\tau_{xy} = \begin{cases} \frac{3V}{2bh^3} [h^2 - (1+k^{-1/2})^2 y^2] & y \geq 0 \\ \frac{3V}{2bh^3} [h^2 - (1+k^{1/2})^2 y^2] & y < 0 \end{cases} \quad (7.25)$$

So far we have derived the equations for calculating the normal stresses  $\sigma_x$  (equation 7.23) and the shear stresses  $\tau_{xy}$  (equation 7.25). It should also be noted that in portions of the beam located under a concentrated or distributed load, the normal stress,  $\sigma_y$ , will be exerted on the horizontal faces of a cubic element in addition to  $\tau_{xy}$ . In this case, equations (7.23) and (7.25) may still be used to determine the values of  $\sigma_x$  and  $\tau_{xy}$ , since the error involved is small for the values of the span-depth ratio encountered in practice (i.e.  $L/h \geq 10$ , Beer and Johnston 1981).

**Normal stress  $\sigma_y$ :** For the case of a simply supported beam subject to a distributed load,  $q$ , along the upper surface,  $\sigma_y$  varies from  $\sigma_y = -q$  at the upper surface to  $\sigma_y = 0$  at the lower surface. Considering the equilibrium condition of a cubic element above and below the neutral axis respectively and recalling  $V = q(0.5l - x)$  and  $M = 0.5q(lx - x^2)$ , we obtain:

$$\sigma_y = \begin{cases} -q + \frac{3q}{2h^3} [h^2(c-y) - \frac{1}{3}(1+k^{-1/2})^2(c^3-y^3)] & y \geq 0 \\ -\frac{3q}{2h^3} [h^2(y+h-c) - \frac{1}{3}(1+k^{1/2})^2(y^3+(h-c)^3)] & y < 0 \end{cases} \quad (7.26)$$

**Deflection of beam by integration:** According to Equation (7.15), considering Hook's law, substitute  $\sigma_{mc}$  and  $\sigma_{mt}$  from equation (7.22). Recalling  $M=0.5q(lx-x^2)$ , will yield:

$$\frac{1}{\rho} = \frac{3q}{2bh^3} \frac{1}{E_c} (1+k^{-1/2})^2 (lx-x^2) = \frac{3q}{2bh^3} \frac{1}{E_t} (1+k^{1/2})^2 (lx-x^2) \quad (7.27)$$

The curvature of a curve at a point  $Q(x,y)$  may be expressed as (elementary calculus):

$$\frac{1}{\rho} = \frac{\frac{d^2y}{dx^2}}{[1+(\frac{dy}{dx})^2]^{3/2}}$$

where  $d^2y/dx^2$  and  $dy/dx$  are the second and the first derivatives of the function  $y(x)$  of that curve. In the case of a deformed beam,  $dy/dx$  (the slope) is very small, and its square is negligible compared to unity, hence:

$$\frac{1}{\rho} \approx \frac{d^2y}{dx^2} \quad (7.28)$$

Let  $\bar{k} = \frac{1}{E_c} (1+k^{-1/2})^2 = \frac{1}{E_t} (1+k^{1/2})^2$ , substitute  $\bar{k}$  back into equation (7.27), then equate it

with equation (7.28). This yields:

$$\frac{d^2y}{dx^2} = \frac{3q\bar{k}}{2bh^3} (lx-x^2) \quad (7.29)$$

Solving this equation with the boundary conditions, we obtain:

$$y(x) = \frac{3q\bar{k}}{2bh^3} \left[ \frac{1}{6}lx^3 - \frac{1}{12}x^4 - \frac{1}{12}l^3x \right]$$

$$\theta(x) = \frac{3q\bar{k}}{2bh^3} \left[ \frac{1}{2}lx^2 - \frac{1}{3}x^3 - \frac{1}{12}l^3 \right]$$
(7.30)

where  $y(x)$  is the deflection of elastic curve and  $\theta(x)$  is the angle of deflected beam.

For  $k = E_t/E_c = 1$ , the beam equations derived in this study reduce to the ones in the classic beam theory (Beer and Johnston, 1981). Figures 7.10-7.13 illustrate the influence of the moduli ratio,  $k$ , on beam deflection and stress distribution. To simplify plotting, the origin of the  $x$  and  $y$  coordinates in these figures is at the bottom left corner of the beam. The beam deflection and  $x$ ,  $y$  coordinates are normalized by the

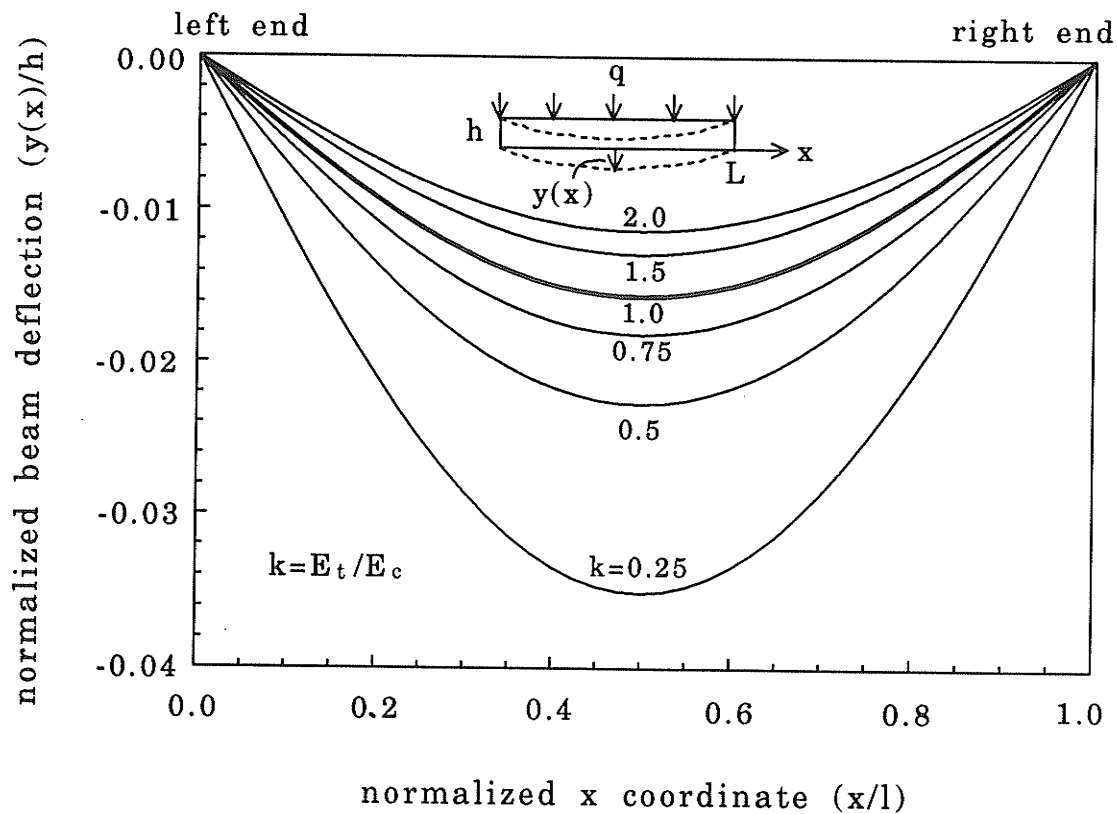


**Figure 7.10** Analytical results showing the influence of moduli ratio,  $k$ , on beam deflection,  $y(x)$  (normalized by beam height,  $h$ ). Negative sign denotes downward displacement. Beam deflection increases significantly as  $k$  decreases.

corresponding beam dimension and the stresses are normalized by the applied load,  $q$ . The beam deflection,  $y(x)$ , along the beam central line increases significantly as moduli ratio,  $k$ , decreases. Such effects are significant when  $k < 1$ , which is the case for most rocks (Figure 7.10). For  $k=1$ , the neutral axis of the beam is at the beam central line, therefore the horizontal normal stress,  $\sigma_x$ , along the beam central line is zero. For bimodular materials, the beam central line is in tension (positive stress) for  $k < 1$ , in compression (negative stress) for  $k > 1$ , and the magnitude of  $\sigma_x$  increases as the deviation of  $k$  from unity increases (Figure 7.11). For a unimodular material ( $k=1$ ),  $\sigma_x$  shows a

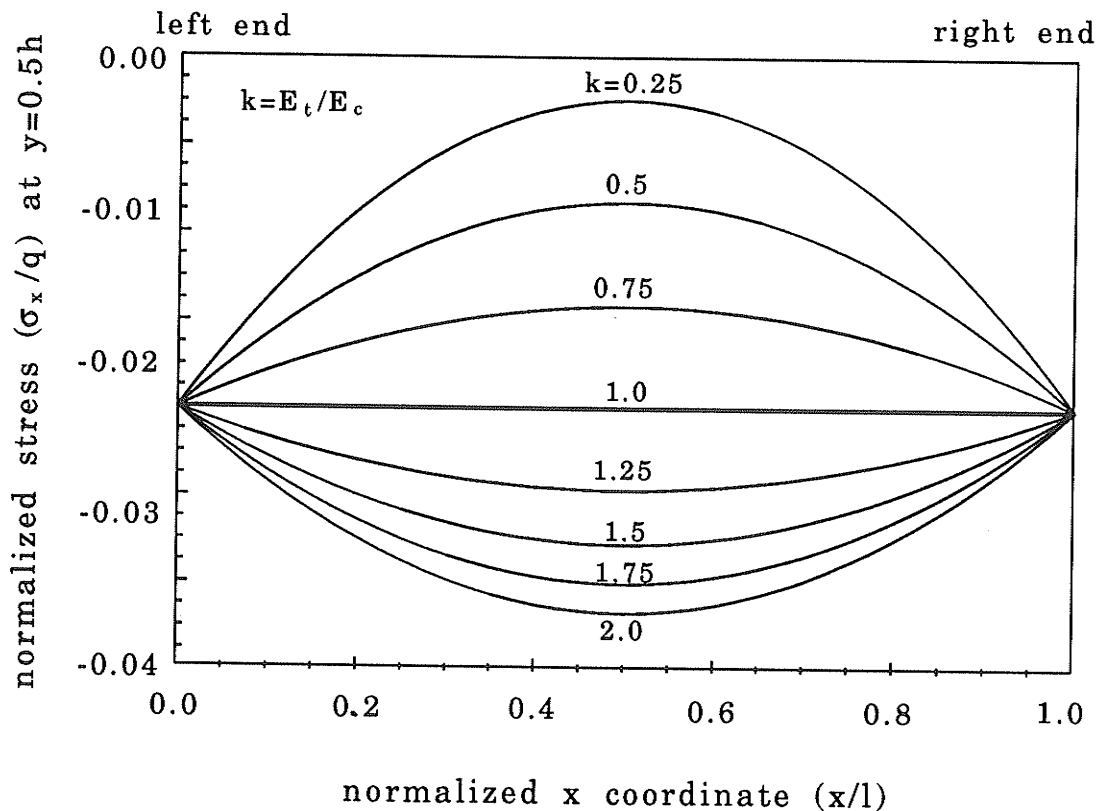


**Figure 7.11** Analytical solution showing the distribution of  $\sigma_x$  at the central height of the beam along the beam span with various deformation moduli ratio,  $k$ .  $L$  is beam span,  $h$  is beam height,  $q$  is applied load/unit length on the top surface. The origin of  $x$  and  $y$  is at the left bottom corner of the beam.

linear distribution over beam height at central beam span. For bimodular materials,  $\sigma_x$  is bilinear with the change in gradient at the neutral axis. The maximum tensile stress at the bottom surface decreases as  $k$  decreases and the maximum compressive stress at the top surface increases as  $k$  decreases (Figure 7.12). For  $k=1$ , the shear stress,  $\sigma_{xy}$ , along the beam height at the right end of the beam shows a parabolic distribution with the axis of symmetry coinciding with the neutral axis at the beam central line and the maximum shear stress locates at the middle height of the beam. For a bimodular material, the maximum shear stress is not at the middle height of the beam, but depends on the location of the neutral axis (Figure 7.13).

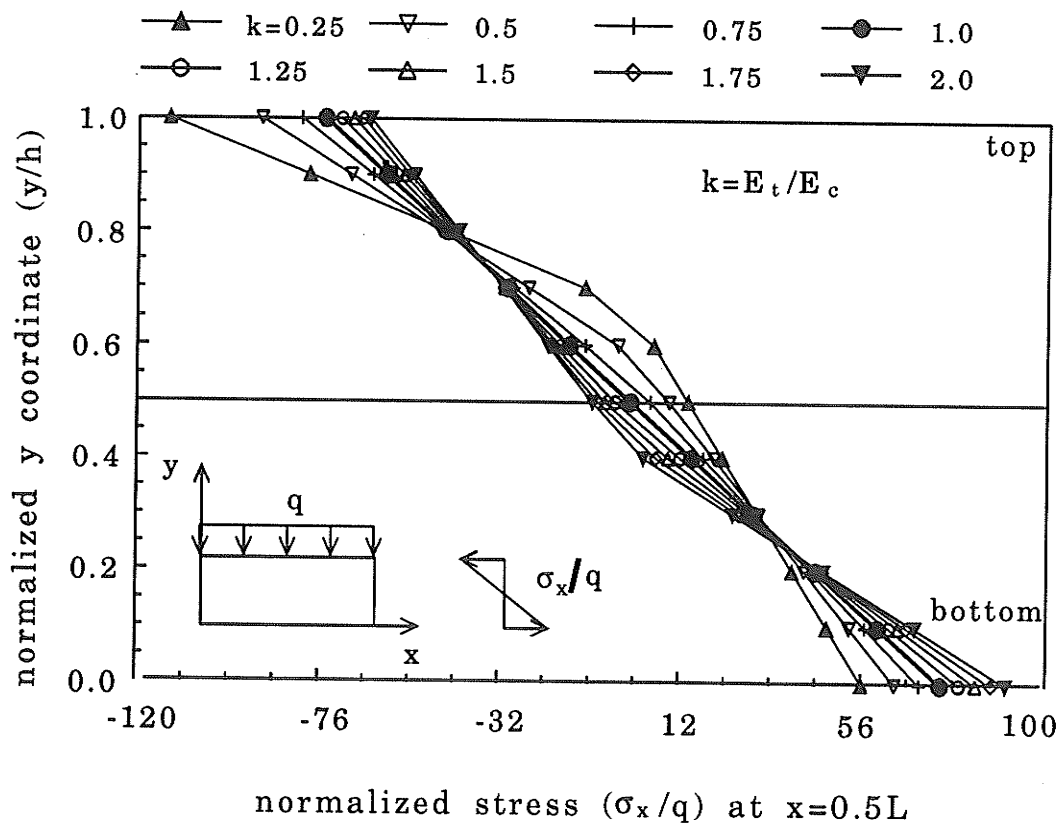


**Figure 7.12** Analytical solution showing the distribution of  $\sigma_x$  at the centre span of the beam along the beam height as moduli ratio,  $k$ , varies.  $h$  is beam height and  $L$  is beam span.

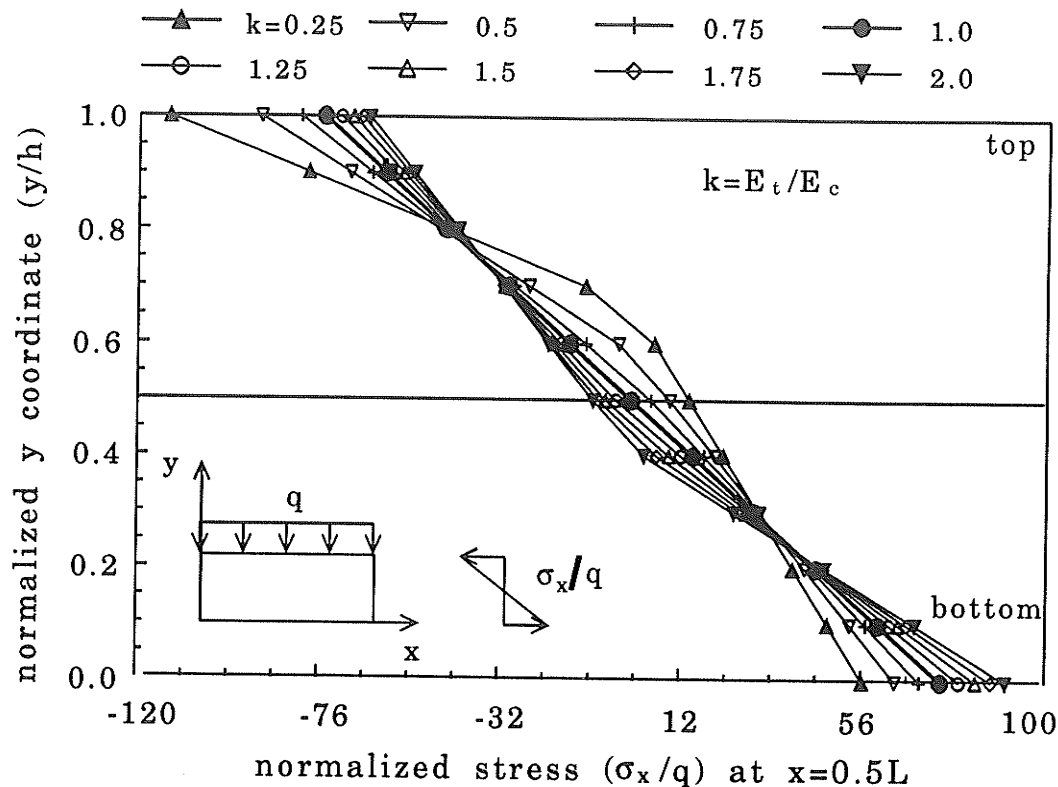


**Figure 7.13** Analytical solution showing the distribution of  $\sigma_{xy}$  at the right end of the beam along the beam height as moduli ratio,  $k$ , varies.

### 7.3.2 Hydraulic extension of bimodular, thick-walled cylinder

Haimson and Tharp (1974) analyzed stresses around boreholes in a bimodular elastic rock medium, using the simplified bi-linear elastic constitutive relation introduced by Ambartsumyan (1966). The effect of bimodularity on the stresses, especially on the tangential stresses, was found to be significant. As an example, Figure 7.14 shows the distribution of stresses for both linear and bimodular cases in a cylinder of finite thickness ( $r_o/r_i=5$ ). At  $r=r_i$  the bimodular tangential stress is lower than the value predicted by linear theory. Figure 7.15 is for a circular hole in an infinite medium. The drop in  $\sigma_\theta$  at  $r=r_i$  as a result of rock bimodularity is most severe. In the particular case shown

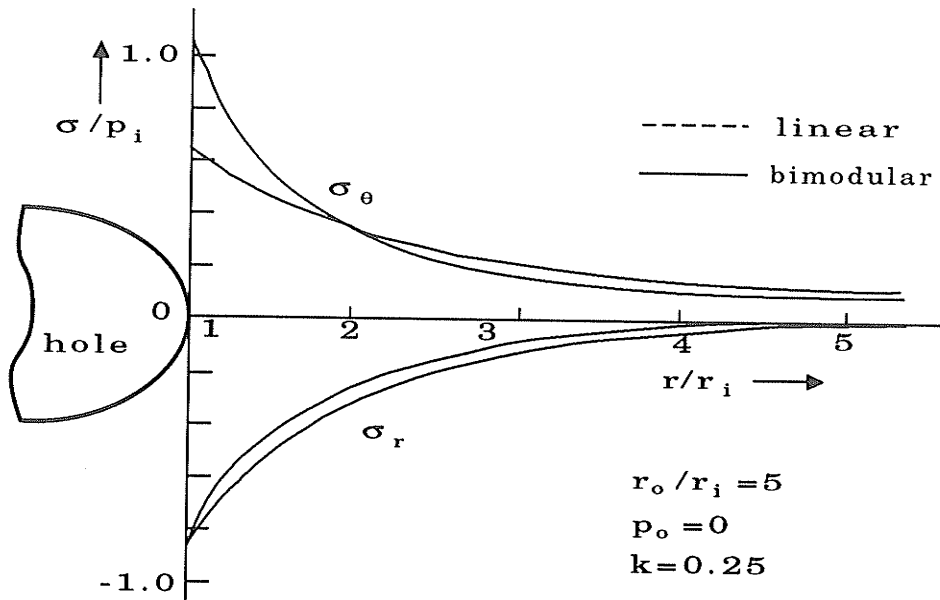


**Figure 7.14** Radial and tangential stress distribution in a thick hollow cylinder.  $\sigma_\theta$  is the tangential stress,  $\sigma_r$  is the normal stress,  $P_i$  is the internal pressure,  $P_o$  is the external pressure,  $r_i$  is the internal radius,  $r_o$  is the external radius, and  $k$  is moduli ratio.

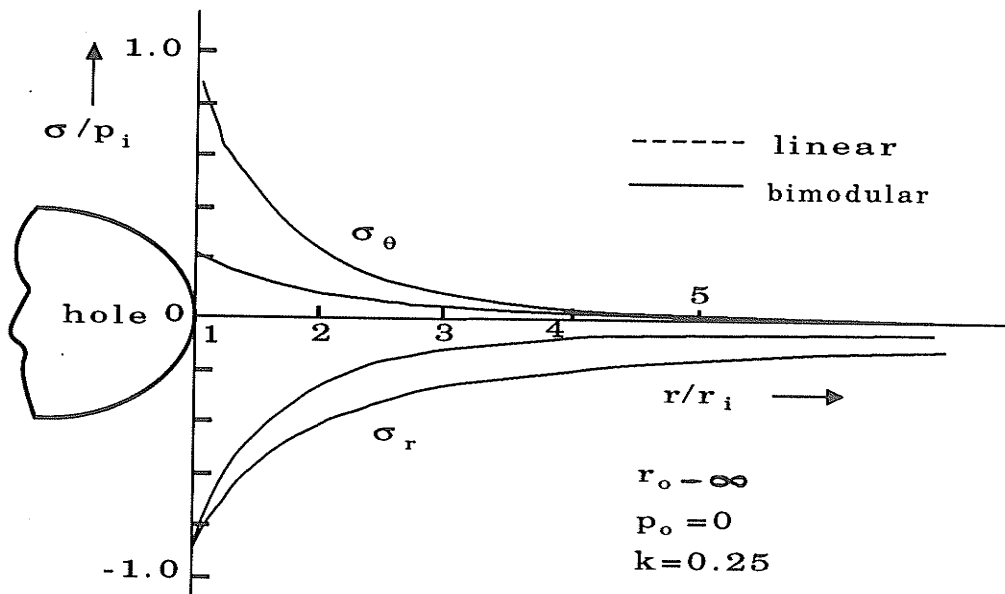


**Figure 7.15** Radial and tangential stress around a wellbore.  $\sigma_\theta$  is the tangential stress,  $\sigma_r$  is the normal stress,  $P_i$  is the internal pressure,  $P_o$  is the external pressure,  $r_i$  is the internal radius,  $r_o$  is the external radius, and  $k$  is moduli ratio.

( $k=1/4$ ), the tangential stress is only one quarter of that expected from linear theory.

In Haimson and Tharp's solution, the condition of  $\nu_r/E_r = \nu_c/E_c$  was assumed, which, as mentioned before, has been questioned experimentally for real materials. However, it is only under this assumption that the analytical solution for a thick-walled cylinder is obtainable. For both Jones' and El-Tahan's models, an iterative scheme is required to solve the problem due to nonlinearity. Actually, even under certain simplified assumptions, there are only a few simple cases where analytical solutions are obtainable. Therefore, a numerical scheme needs to be developed.

#### 7.4 Finite Element Implementation of Bimodularity

The Modified Weighted Compliance Matrix (MWCM) material constitutive model (El-Tahan et al. 1989, described in section 7.2) has been incorporated into a user-friendly, menu-driven, finite element program, SIMEX (Ayari 1991). The MWCM model is superior to the bilinear (Ambartsumyan 1966) and WCM models (Jones 1977) because it ensures the continuity of both cross-compliance in the elastic matrix and the slope of the cross-compliance while the signs of the principal stresses vary. In this model:

$$\{\epsilon\} = [S(\sigma_p)]\{\sigma\} \quad (7.31)$$

where  $\{\epsilon\}$  is the strain tensor,  $\{\sigma\}$  is the stress tensor, and  $[S(\sigma_p)]$  is the elasticity matrix defined by Equation 7.14 which is a function of the principal stresses and their orientation. This formulation leads to a set of non-linear equilibrium equations:

$$[K(\sigma_p)]\{a\}=\{R\} \quad (7.32)$$

where  $\{a\}$  is the node displacement vector,  $\{R\}$  is the total load vector, and  $[K(\sigma_p)]$  is the global stiffness matrix.

The analysis starts in the principal stress coordinate system and then uses a transformation from the principal to the Cartesian coordinates. Since the global stiffness matrix,  $[K(\sigma_p)]$ , is a function of the principal stresses, the non-linearity of the problem is resolved through an iterative scheme which predicts fictitious equilibrium states as the basis for a reliable solution process. Moreover, having a problem of stress-induced anisotropy in nature, the numerical algorithm starts by assuming a common isotropic continuum and subsequently adjusts the material properties in a gradual fashion, eliminating spurious solutions commonly found for such problems. Figure 7.16 illustrates the flow-chart of this numerical scheme.

Figure 7.17 compares the analytical results with the FEM solutions for the deflection of a beam with  $E_c=40 \times 10^6$  KPa,  $k=0.67$  and a distributed load  $q=400$  MPa at the upper surface. The influence of moduli ratio,  $k$ , on the maximum deflection of the same beam is presented in Figure 7.18 for both analytical and FEM solutions. The maximum deflection increases as  $k$  increases. These two figures demonstrate that the finite element results are in a good agreement with the analytical solutions.

In the following sections, analytical solutions and the finite element program will be utilized to discuss the effects of bimodularity on the interpretation of indirect rock tensile strength tests and roof behavior in a simulated underground opening.

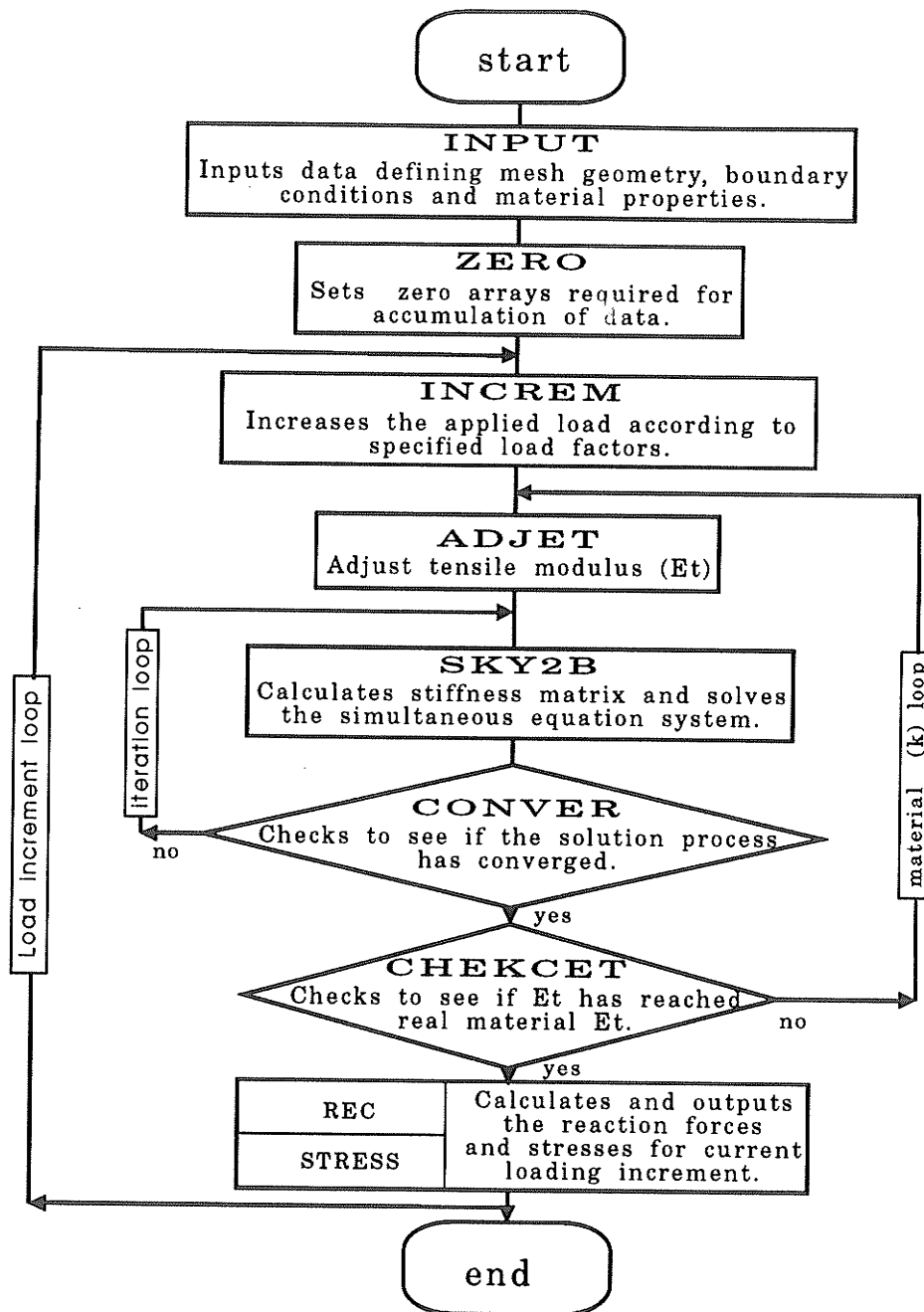


**Figure 7.16** Flow-chart of the finite element program for bimodular materials. Names in capital form are names of subroutines in the FEM code.

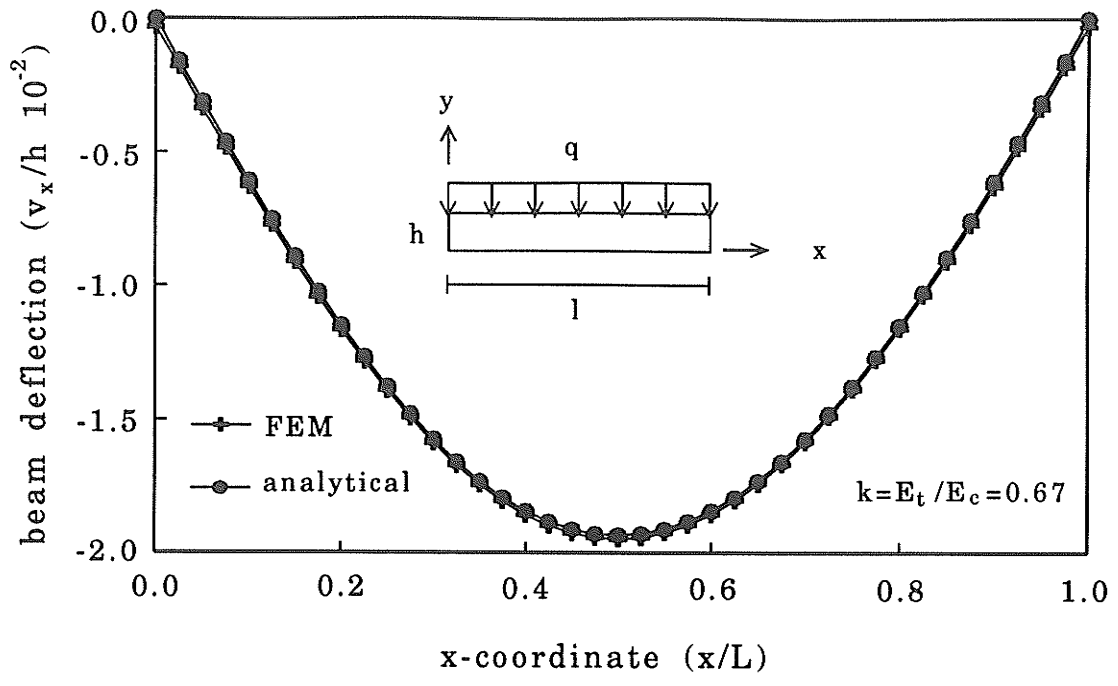


Figure 7.17 Comparison of beam deflection from FEM and analytical solutions for a simply supported beam with uniformly distributed load.

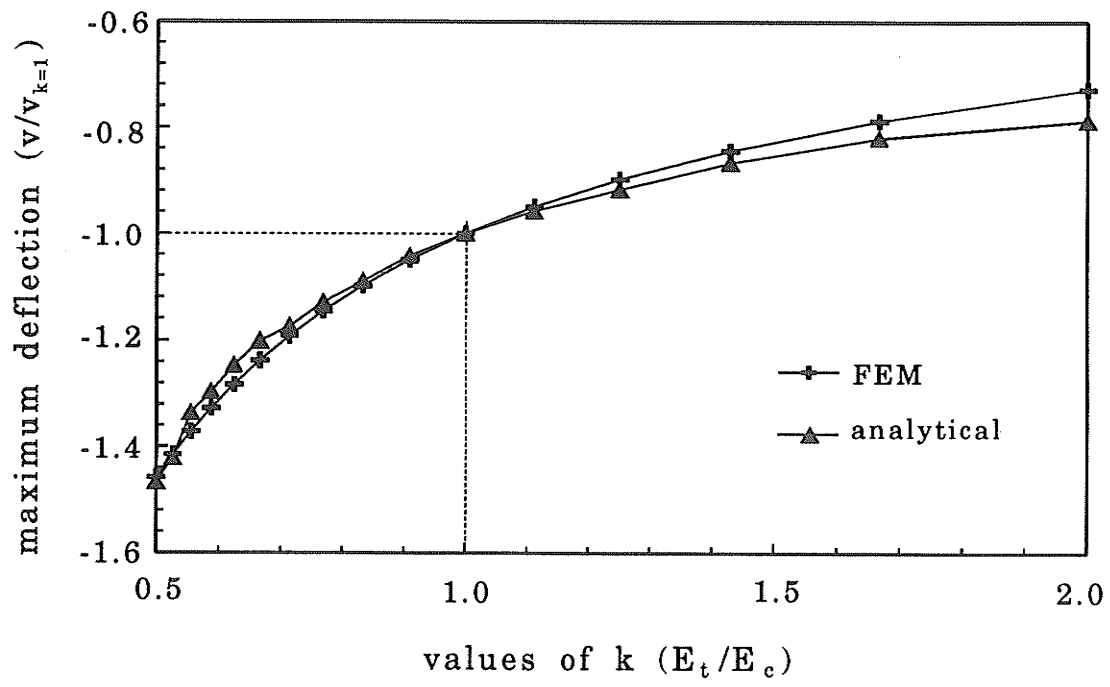


Figure 7.18 Comparison of FEM and analytical solutions of the maximum beam deflection with various deformation moduli ratio ( $k$ ).

### **7.5 Effect of Bimodularity on Indirect Measurement of Rock Tensile Strength**

Tensile failure is an important and common aspect in many rock engineering problems and therefore the tensile strength of rock has long been of interest. Its measurement is important in hydraulic fracturing, underground stability, machine cutting of rock, drilling and blasting, borehole stability, core discing and comminution.

The direct tension test is widely accepted to be the most accurate of available techniques for determining the tensile strength of rock (Hardy and Jayaraman 1970). However, when brittle rocks are tested in direct tension, there are difficulties associated with loading the specimen to avoid the introduction of bending and torsion-related stresses, and local stress concentrations. As a result, a number of indirect methods have been developed whereby the tensile strength is measured by inducing a tensile principal stress in specially shaped and loaded specimens (see Section 7.5.1). Because they are usually easier to perform, indirect tension tests have been widely adopted as alternatives to the direct tension test. However, the results from indirect tension tests have been shown to vary within wide limits and to yield higher values than those derived from direct tension testing (Hardy and Jayaraman 1970; Vutukuri et al. 1974). The validity of these methods for measuring uniaxial rock tensile strength is therefore debatable. Assumptions about stress-strain behavior that are required to interpret results from these tests must also be questioned, including anisotropy and material bimodularity.

In this section, the effects of bimodularity on four of the most commonly utilized indirect rock tensile tests - three-point beam bending, hydraulic extension, Brazilian, and ring - are investigated. The specimen configuration and stress analysis for each method

are briefly reviewed for the case of equal moduli in tension and compression. The effects of bimodularity on the simple beam bending and hydraulic extension tests are discussed according to the analytical solutions obtained in Section 7.3. The Brazilian and ring tests are investigated by the finite element program developed in Section 7.4. Finally, the applicability of these indirect tensile tests to brittle rocks with bimodular properties is discussed and corrections to tensile strength to accommodate the influence of bimodularity are presented for each test method.

#### **7.5.1 Indirect determination of rock tensile strength**

According to Vutukuri et al. (1974), the indirect methods for determining the tensile strength of rock can be grouped into bending tests (bending of prismatic or cylindrical specimens and bending of discs), hydraulic extension tests, diametrical compression of discs (Brazilian test and ring test), and miscellaneous methods, e.g. diametrical compression of cylinders, diametrical compression of spheres, compression of square plates and centrifugal tension.

##### **Bending of prismatic specimens**

When a homogeneous and isotropic beam is subjected to three-point bending, tensile stresses develop on the convex side of the beam (Figure 7.19). The maximum tensile stress is at the extreme-most fibre and is given by (Vutukuri et al. 1974):

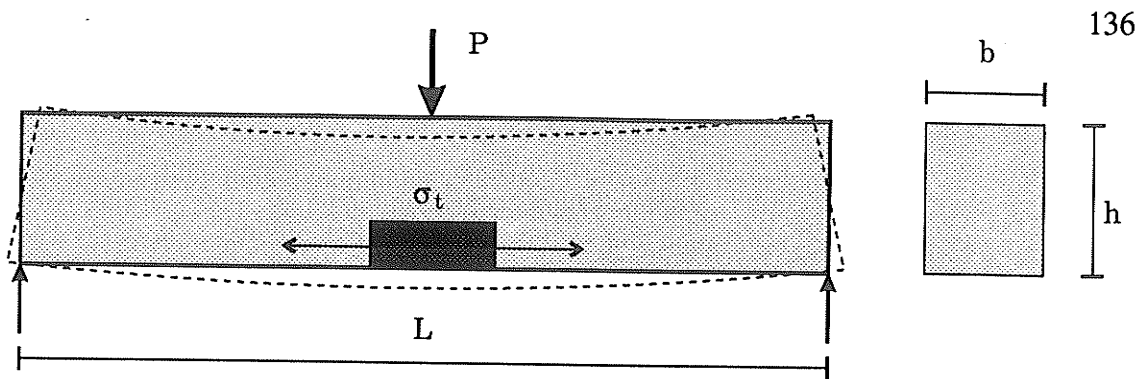


**Figure 7.19** Three point bending test of a beam with rectangular cross section. The maximum tensile stress,  $\sigma_t$ , is developed at the extreme-most fibre on the convex side of the beam. Dashed lines show deformed shape of the beam.

(7.33)

$$\sigma_t = -\frac{Mc}{I}$$

where  $\sigma_t$  at failure is taken as the material tensile strength (or modulus of rupture),  $M$  is bending moment,  $c$  is distance from the neutral axis, and  $I$  is the moment of inertia of the cross-section of the beam about the neutral axis.

### Hydraulic extension test

When a thick-walled cylinder or a ring is subjected to an internal hydrostatic pressure, failure occurs due to an induced tangential tensile stress,  $\sigma_t$ , whose value is maximum at the inner surface (Figure 7.20) and is given by (Vutukuri et al. 1974):

$$\sigma_t = -P_i \frac{(r_o^2 + r_i^2)}{(r_o^2 - r_i^2)} \quad (7.34)$$

where  $\sigma_t$  at failure is taken as the material tensile strength,  $P_i$  is the applied hydrostatic pressure at the inner surface, and  $r_i$  and  $r_o$  are the internal and external radii of the cylinder, respectively.

### Brazilian test

The Brazilian test was introduced by Carneiro (1947). The test makes use of a circular solid disc which is loaded in compression to failure across a diameter. Frocet (1948) analyzed the stress distribution in a thin disc under the action of two diametrically opposite concentrated loads (Figure 7.21). For linear elasticity, the stresses along the loaded diameter ( $x=0$ ) are (Jaeger and Cook 1979):

$$\sigma_x = -\frac{P}{\pi t R}, \quad \sigma_y = \frac{P}{\pi t R} \left[ \frac{3R^2 + y^2}{R^2 - y^2} \right] \quad (7.35)$$

where  $\sigma_x$  and  $\sigma_y$  are the normal stress components along the  $x$  and  $y$  directions, respectively,  $P$  is the applied force,  $t$  is the thickness of the disc, and  $R$  is the radius of the disc. The normal stress,  $\sigma_x$ , is tensile. This stress is equated to the uniaxial tensile strength, providing failure of the disc is by the development of a vertical crack that initiates at the centre of the specimen and propagates towards the

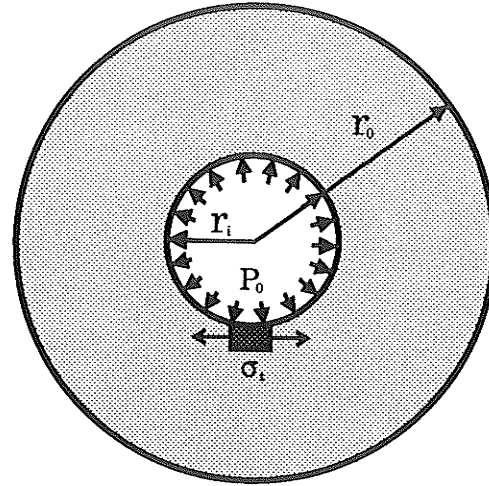


Figure 7.20 Hydraulic extension of a ring. Tensile stress,  $\sigma_t$ , is developed in the tangential direction and is the maximum at the inner surface.

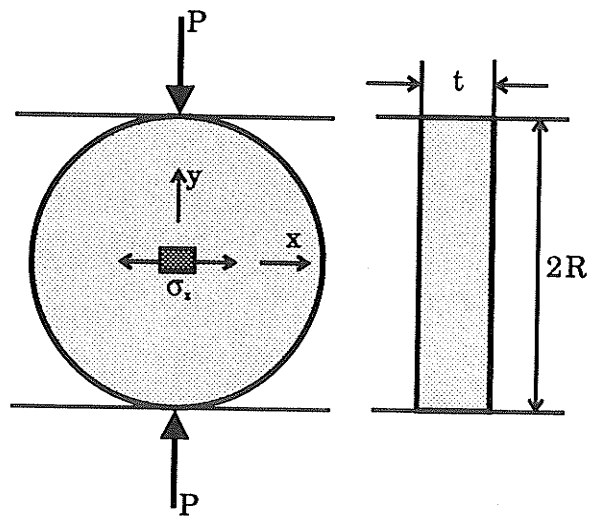


Figure 7.21 Brazilian test. A constant tensile stress,  $\sigma_t$ , is developed in the central portion of the disc along the loaded diameter.

loading points. However, the specimen does not actually fail in uniaxial tension. The compressive stress,  $\sigma_y$ , varies along the loaded diameter from  $(3P)/(\pi tR)$  at the centre of the disc to infinity (theoretically) at the loading points, and therefore, failure at the centre of the disc is actually under bi-axial stress conditions. For hard, brittle rocks obeying the Griffith fracture criterion, the Brazilian test is considered widely as a good measure of uniaxial tensile strength. This criterion states that failure occurs when  $\sigma_1 = \sigma_f$ , if  $3\sigma_1 + \sigma_3 \geq 0$ , where  $\sigma_f$  is the uniaxial tensile strength and  $\sigma_1$  and  $\sigma_3$  are the tensile and compressive principal stresses at the point of fracture. This criterion is satisfied at the central point of a solid Brazilian disc where  $\sigma_x$  and  $\sigma_y$  are identical with  $\sigma_1$  and  $\sigma_3$ , respectively, and therefore  $\sigma_x$  at failure is taken as the uniaxial tensile strength (Mellor and Hawkes 1971).

### Ring test

The Brazilian test suffers from the disadvantage that not only tensile stresses are developed in the disc but compressive stresses as well. The latter may induce failure around the loading platens. The ring test has been developed to reduce the possibility of such extraneous failures. In this procedure, a disc with a central hole is subjected to diametrical compression (Figure 7.22). The tangential tensile stress,  $\sigma_t$ , at the inner surface along the loaded diameter is given by (Hobbs 1964):

$$\sigma_t = -\frac{P}{\pi t r_o} \left[ 6 + 38 \left( \frac{r_i^2}{r_o^2} \right) \right] \quad (7.36)$$

where  $\sigma_t$  at failure is taken as the material tensile strength,  $P$  is the applied force,  $r_i$  and

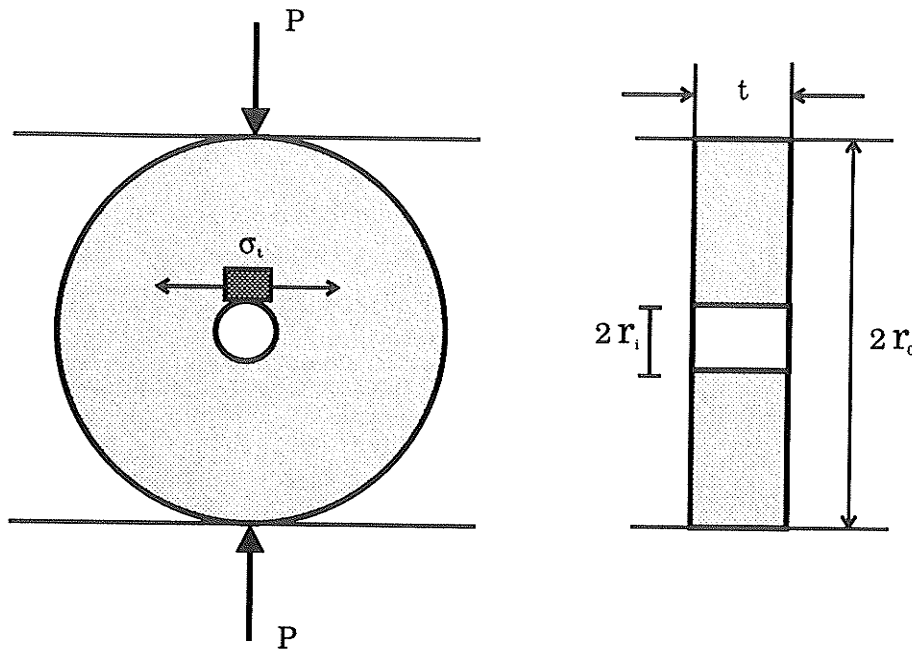


**Figure 7.22** Ring test. A maximum tensile stress is developed at the intersection of the central hole and the loaded diameter.

$r_o$  are the internal and external radii respectively, and  $t$  is the specimen thickness. It can be shown by comparing Equations 7.35 and 7.36 that the maximum tensile stress in a disc with a central hole is at least 6 times larger than the maximum tensile stress in a solid disc when subjected to the same load. This condition ensures that tensile failure will occur rather than compressive failure at the loading points. Furthermore, the stress state at which failure occurs is uniaxial tension at the point of fracture. Therefore, the ring test should give a tensile strength value that is closer to the uniaxial tensile strength as determined by the direct pull tensile test than the Brazilian test (neglecting possible size and stress gradient effects).

One of the basic assumptions in deriving Equations 7.33 to 7.36 is that the

material is homogeneous, isotropic, linear elastic, and unimodular. However, brittle rocks usually show a bimodular property. For example, the new test procedure described in Chapter 6 has demonstrated that the moduli in compression and tension are different for at least three of the four materials tested. Moduli ratios,  $k$ , varied from 0.3 to 1 ( $k=E_t/E_c$ , where  $E_t$  is Young's modulus in tension and  $E_c$  is Young's modulus in compression). Specifically, the moduli ratio is 0.5 for halite from the Cominco Mine, 0.7 for Lac du Bonnet granite, and 0.3-0.4 for Tyndall limestone.

The effect of this bimodularity on the interpretation of indirect tension tests will be considered in the following section.

## 7.5.2 Influence of rock bimodularity

### Bending of a prismatic beam

Stress equations that incorporate the effect of the moduli ratio,  $k$ , for a prismatic beam have been derived using the classical beam theory in Section 7.3. For a bimodular beam in pure bending, the location of the neutral axis is no longer at the centre line of the beam, but depends on the ratio of Young's moduli in tension and compression and is given by Equation 7.21. The maximum tensile stress,  $\sigma_t$ , at the extreme-most fibre is given by Equation 7.22 ( $\sigma_m$ ). This stress at failure is equated to the tensile strength. For a beam with a arbitrary cross section,  $\sigma_t$  is given by:

$$\sigma_t = -\frac{Mh}{(k^{-\frac{1}{2}} + k^{-1})I_1 + (k^{\frac{1}{2}} + 1)I_2} \quad (7.37)$$

where  $I_1$  and  $I_2$  are the moment of inertia of the portions of the beam above and below

the neutral axis, respectively.

Figure 7.23 illustrates the relationship between the normalized maximum tensile stress,  $\sigma_t/\sigma_{t(k=1)}$ , and the moduli ratio,  $k$ , for a beam of rectangular cross section, where  $\sigma_{t(k=1)}$  is the tensile stress for  $k=1$ . It may be noted that the maximum tensile stress in a beam increases as  $k$  increases. For many rocks  $k < 1$  and, therefore, for these materials the tensile strength computed using the normal assumption of  $k=1$  is overestimated. For bimodular materials, test results should be interpreted according to Equation 7.22 ( $\sigma_{mi}$ ) instead of Equation 7.33.

### Hydraulic extension test

Haimson and Tharp (1974) analyzed stresses around boreholes in a bimodular, elastic rock, using a simplified bi-linear, elastic constitutive relation. For the thick-walled cylinder in a hydraulic extension test, the maximum tensile stress is given by:

$$\sigma_t = -k^{\frac{1}{2}} P_i \frac{(r_o^{2k^2} + r_i^{2k^2})^{\frac{1}{2}}}{(r_o^{2k^2} - r_i^{2k^2})^{\frac{1}{2}}} \quad (7.38)$$

where  $k$  is the moduli ratio,  $P_i$  is the applied hydraulic pressure at the inner surface, and  $r_o$  and  $r_i$  are the external and internal radii, respectively. At failure,  $\sigma_t$  is equated to the material tensile strength. Figure 7.24 shows the influence of  $k$  on the normalized maximum tensile stress. Again, ignoring the bimodularity of rock results in an overestimation of tensile strength, which increases in magnitude as the ratio of external and internal radii,  $m=r_o/r_i$ , increases.

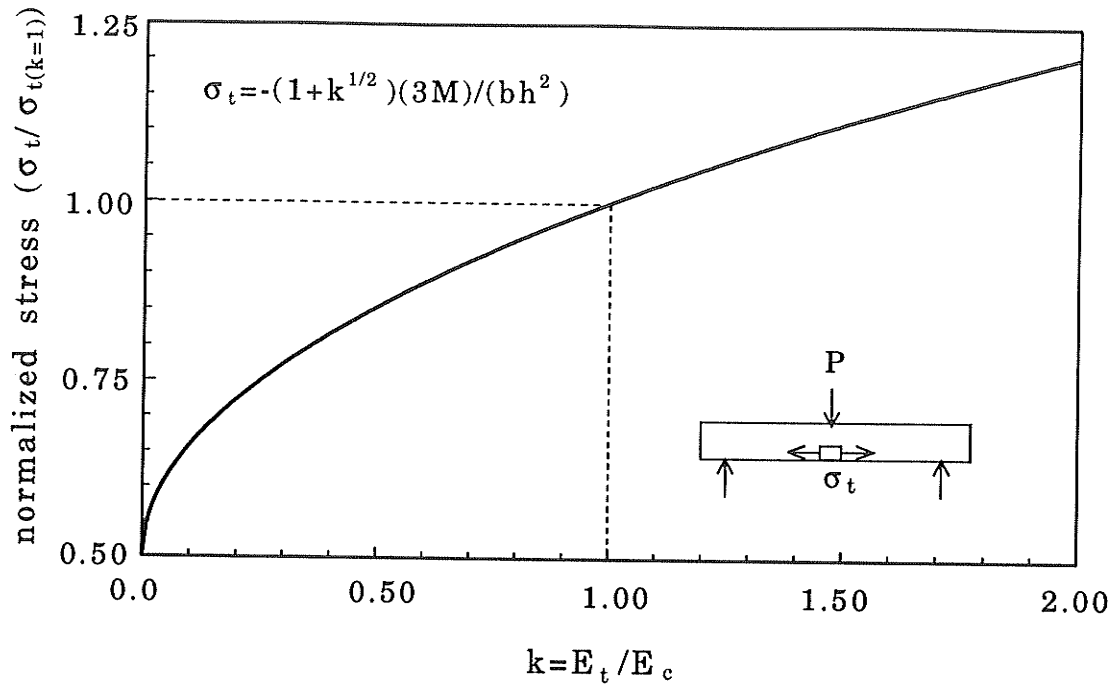


**Figure 7.23** Analytical results showing the influence of moduli ratio,  $k$ , on the normalized maximum tensile stress,  $\sigma_t/\sigma_{t(k=1)}$ , for a beam bending test.

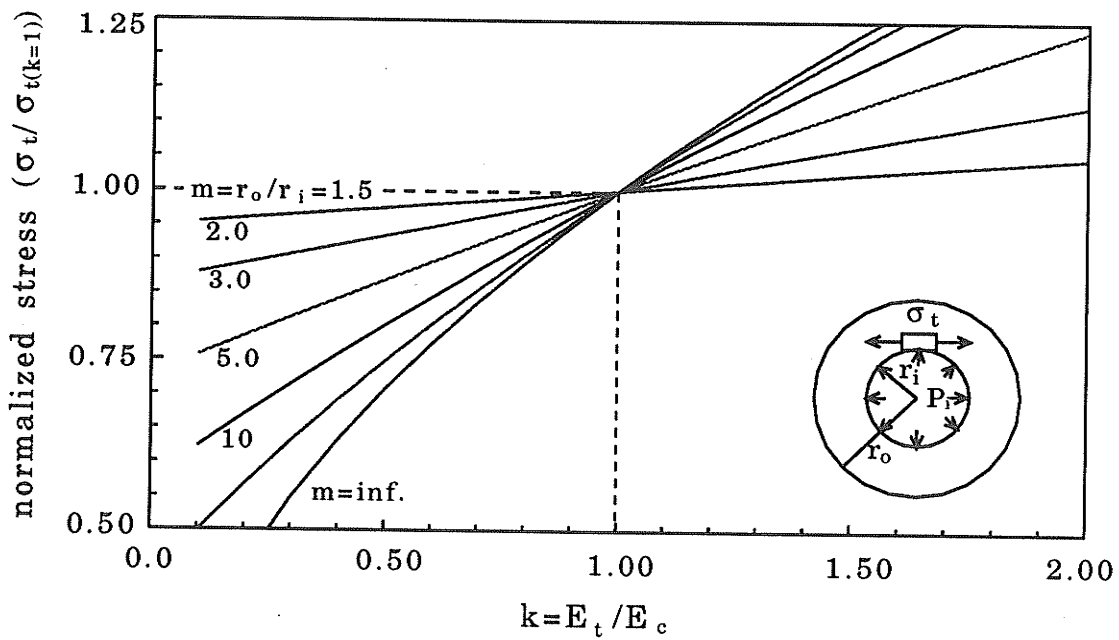


**Figure 7.24** Analytical solution of the relationship between moduli ratio,  $k$ , and the normalized maximum tensile stress,  $\sigma_t/\sigma_{t(k=1)}$ , in a hydraulic extension test.  $m$  is the ratio of the external and internal radii.

### Brazilian test

The effect of the moduli ratio,  $k$ , on the results of the Brazilian test was examined numerically using the finite element program developed in Section 7.4. The finite element mesh (Figure 7.25) was constructed so that the edges of each element coincided with the trajectories of the principal stresses (Frochet 1948), except in the area near the applied load where a set of finer elements was designed to obtain better dimensional ratios. Eight-noded isoparametric serendipity elements were utilized. One quarter of a Brazilian disc was analyzed using symmetry about the horizontal and vertical axes. Roller supports were used along symmetric axes and a pin support was used in the centre of the disc. Figure 7.26 shows the influence of  $k$  on the normalized maximum tensile stress at the centre of the disc. The solid line was derived from data obtained during this study using a curve-fitting technique. For  $k < 1$ , the tensile stress is less than predicted by the standard equation (Equation 7.35). The correct tensile stress can be approximated by the following power function obtained from a curve-fitting procedure:

$$\sigma_x = -1.023k^{0.252} \frac{P}{\pi tR} \quad (7.39)$$

This stress at failure is assumed to be the material tensile strength.

As mentioned previously, the MWCM model is more rigorous mathematically than other bimodular constitutive models because it ensures the continuity of both cross-compliance and the slope of the cross-compliance. However, similar to other models, a high degree of non-linearity related to sudden changes in material constants (from  $E_t, \nu_t$  to  $E_c, \nu_c$  or vice versa) leads to algorithmic difficulties numerically (numerical instability) and results in spurious stresses for low  $k$  values (e.g.  $k < 0.3$ ). This can be remedied by

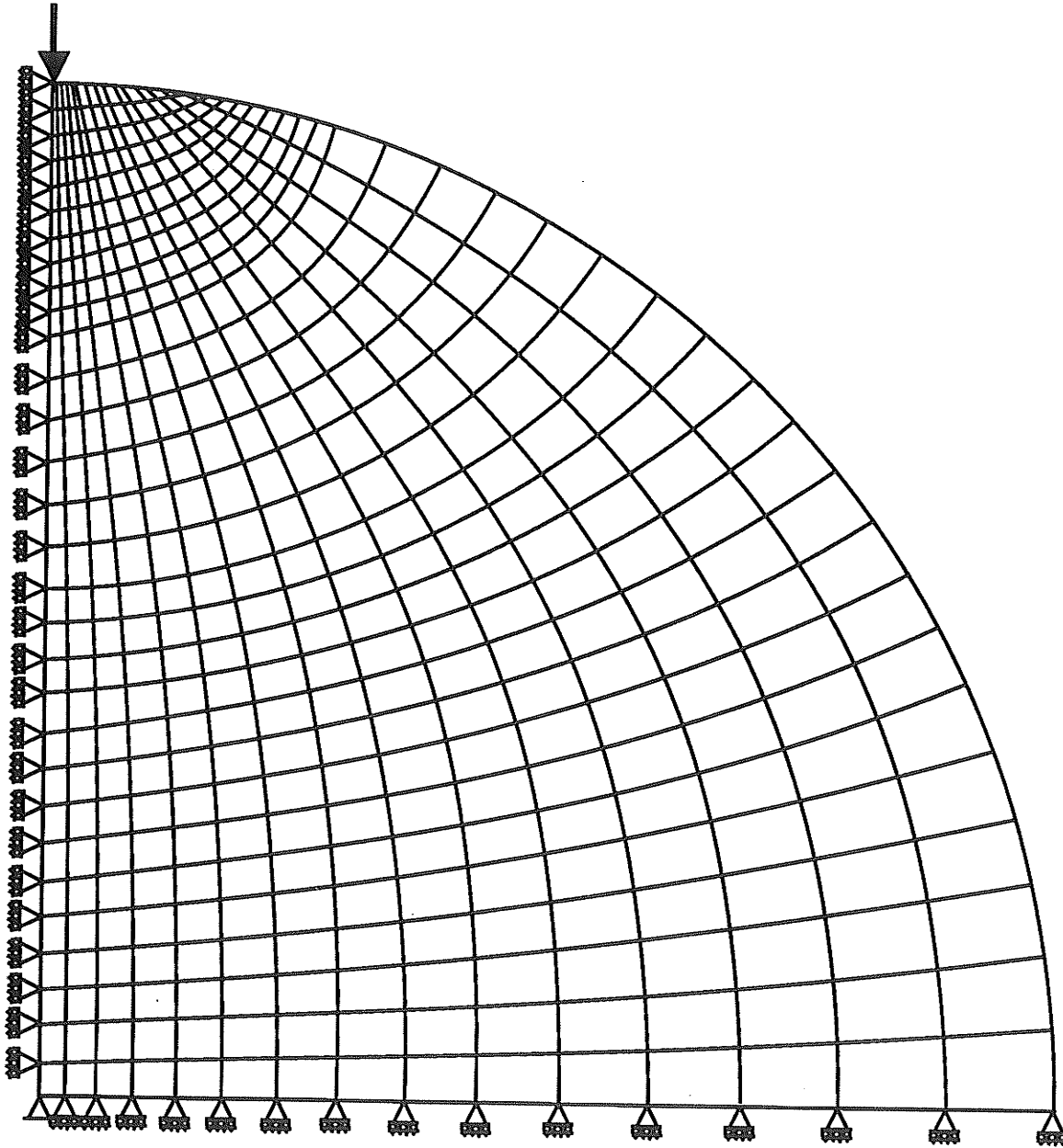


Figure 7.25 Finite element mesh for the Brazilian test.

adjusting material properties in a gradual fashion. However, incorporating such adjustments in the model is not efficient. In any case, the MWCM model and the finite element code developed during this study provide a good estimation for most rocks, because most rocks have  $k$  values between 0.4 and 1.0. Also, extrapolation to the lower  $k$  values using Equation 7.39 agrees reasonably well with Sundaram and Corrales' data (Sundaram and Corrales 1980) (Figure 7.26) (Note: the curve has been fitted through data points from this study only).

### Ring test

The effect of the moduli ratio on the normalized maximum tensile stress calculated for a ring test is similar to that for the Brazilian test. Finite element analyses provided the points in Figure 7.27 which were used to develop the following corrected stress relation:

$$\sigma_t = -1.0056k^{0.219} \frac{P}{\pi t r_o} \left[ 6 + 38 \left( \frac{r_i}{r_o} \right)^2 \right] \quad (7.40)$$

where  $\sigma_t$  at failure is assumed to be the material tensile strength.

The absence of data for  $k < 0.35$  in Figure 7.27 is, again, due to numerical instabilities associated with the constitutive model. However, considering the similarity of trend to those for the Brazilian and the beam tests, the effect of bimodularity at low  $k$  values can be estimated with some confidence using Equation 7.40.

### 7.5.3 Application of indirect tensile tests

Analytical and numerical analyses indicate that material bimodularity significantly

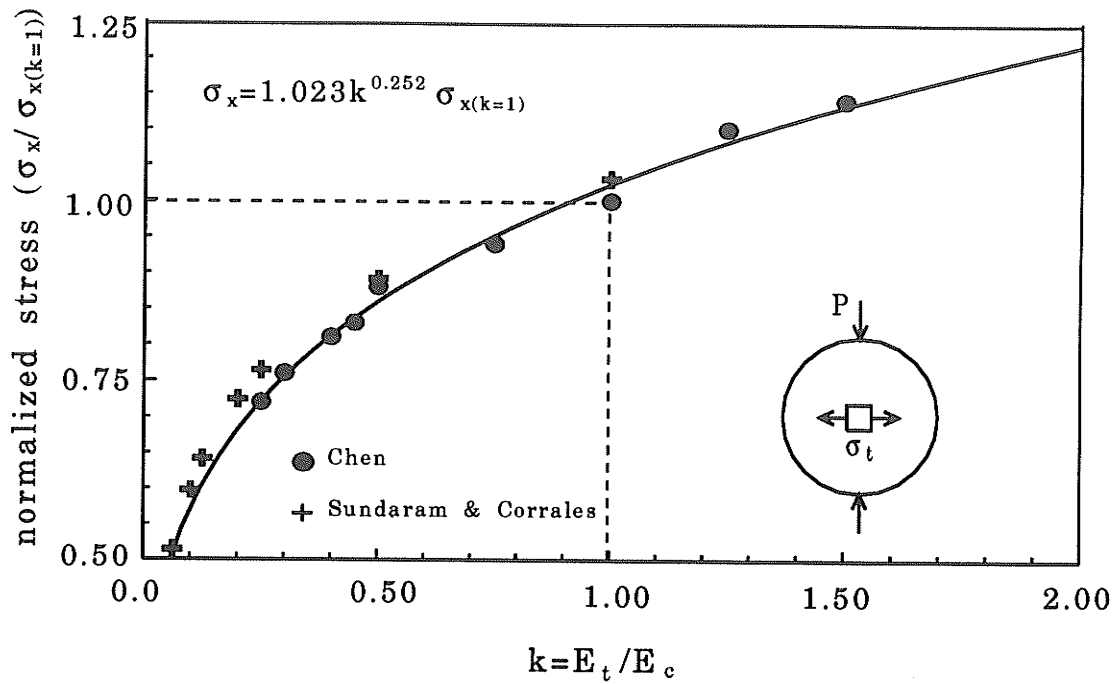


Figure 7.26 Finite element results showing the influence of moduli ratio,  $k$ , on the normalized maximum tensile stress,  $\sigma_x/\sigma_{x(k=1)}$ , in a Brazilian disc.

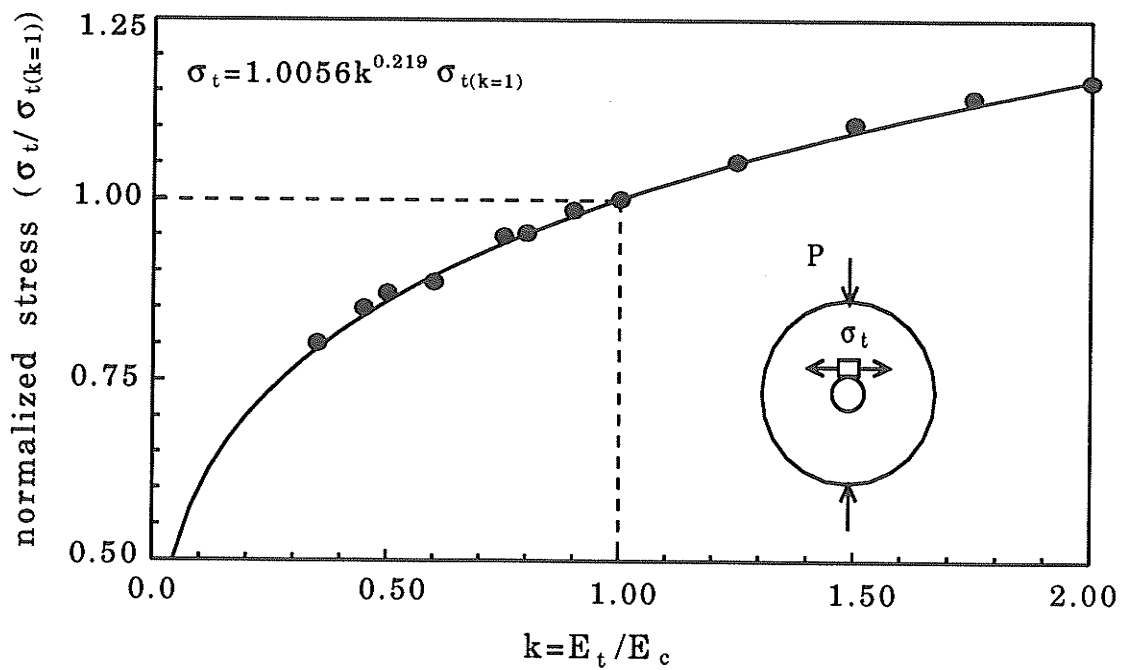


Figure 7.27 Finite element results showing the influence of moduli ratio,  $k$ , on the normalized maximum tensile stress,  $\sigma_t/\sigma_{t(k=1)}$ , in the ring test.

influences the interpretation of indirect tensile strength tests. For materials with a moduli ratio  $k$  larger than 1, current formulae underestimate the material tensile strength. For materials with moduli ratio less than 1, which includes most rocks, the uniaxial tensile strength is overestimated. For  $k=0.5$ , the error is 15% for the Brazilian, ring and beam bending tests and 25% for the hydraulic extension test with a ratio of external and internal radii of 10. The error grows as the deviation of  $k$  from unity increases.

For the four tests, the corrected tensile strengths,  $\sigma_t$  ( $\sigma_x$  for the Brazilian test), can be estimated from:

$$\sigma_t = a(1 + bk^c)\sigma_{t(k=1)} \quad (7.41)$$

where  $a$ ,  $b$  and  $c$  are constants for the specific test. The constants can be obtained either analytically for simple configurations or numerically for more complicated geometric and loading conditions. The  $k$  value can be determined in a single test using the newly developed testing technique in Chapter 6.

## 7.6 Influence of Material Bimodularity on Roof Behavior

Influence of material bimodularity on the roof behavior of a wide, rectangular opening is investigated by the finite element program for varying boundary stresses. Figure 7.28 shows model configuration and finite element mesh. Eight noded isoparametric serendipity elements were used. One quarter of the model was calculated using symmetry. Roller supports were placed on the symmetric axes. Stresses were applied as distributed edge load on the far-field boundaries. Figure 7.29 shows that the maximum roof deflection increases with decreasing  $k$  value. Solid lines in this figure are

obtained from a curve fitting approach. The effect is most pronounced at low values of  $m$  ( $\sigma_h/\sigma_v$ ) and is negligible for the hydrostatic stress condition ( $m=1.0$ ). For example, when  $m=\sigma_h/\sigma_v=0$ , the maximum roof deflection for a material with a  $k$  value of 0.5 is at least 30% larger than that of a material with equal moduli in tension and in compression. Maximum roof deflection can be determined from the following equation:

$$\ln y = (a + bm + cm^2) \ln k \quad (7.42)$$

where  $y$  is the maximum roof deflection,  $k = E_t/E_c$ , is the moduli ratio,  $m$  is the ratio of far field horizontal principal stress and vertical principal stress, and  $a$ ,  $b$ , and  $c$  are

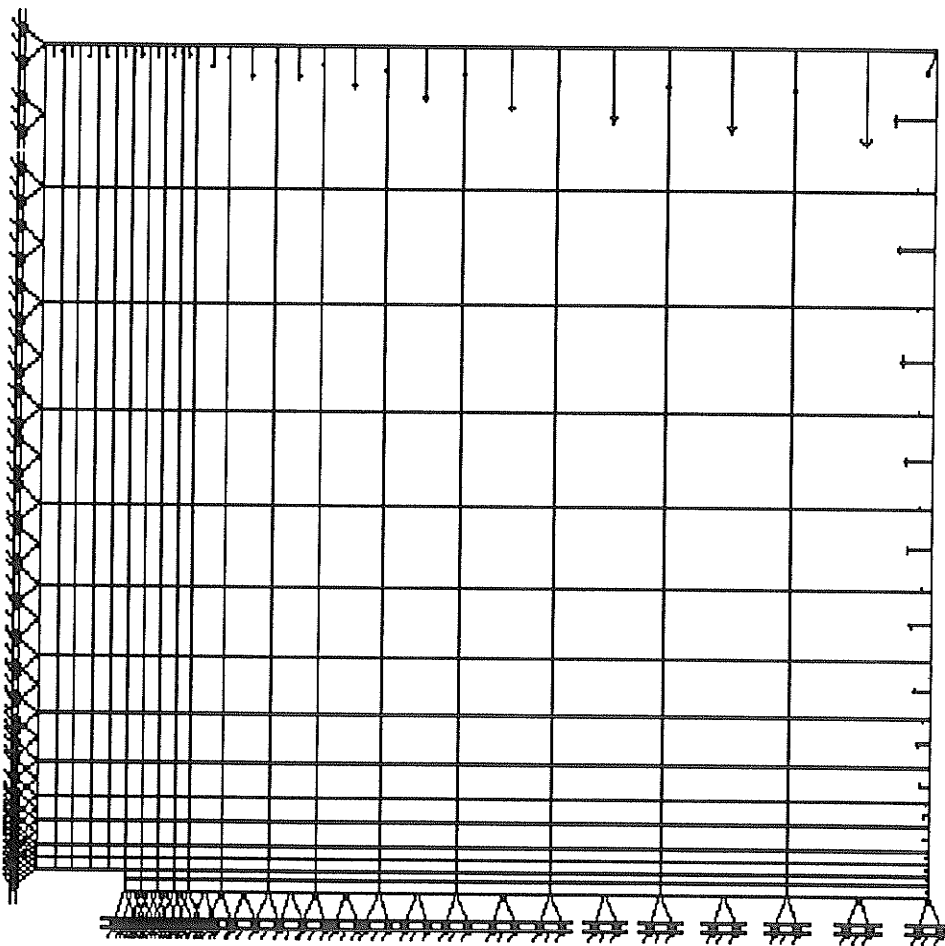


**Figure 7.28** Finite element mesh of a single rectangular opening ( $25 \times 5 \text{ m}^2$ ). Arrows represent applied load.

constants depending on the opening geometry ( $a$ ,  $b$  and  $c$  are -0.38, 1.19 and -0.81 respectively for the particular geometry presented in this paper).

The influence of bimodularity on roof failure was evaluated by assessing the influences of  $k$  on the maximum tensile stress at the middle span and the load required to initiate cracks. Only a particular case of  $m=0$  (uniaxial load) was analyzed. Figure 7.30 shows that the maximum tensile stress at middle span decreases slightly as  $k$  decreases. For a material with  $k=0.5$ , the maximum tensile stress is about 95% of the stress when  $k=1$ . For a material with  $k=2.0$ , the maximum tensile stress is about 110% of the stress when  $k=1$ .

For crack initiation, a recently developed criterion, USR, was utilized (Lajtai et al. 1991a; Yuan and Lajtai 1991). USR is simply a new form of *safety factor*. A USR value of unity represents the equilibrium condition and USR less than unity signifies the initiation of cracks. An increasing load was applied to the finite element model shown in Figure 7.28. The USR values were checked after each loading step by plotting USR contours. Once  $USR < 1$  at a point, crack would initiate. The applied loads at which crack initiation was predicted were recorded and plotted in Figure 7.30 for various  $k$  values. This figure shows that a low  $k$  value implies a higher applied load to initiate cracks.

These analyses indicate that, as a result of bimodularity and for a given geometry and loading, the maximum roof deflection and the factor of safety against crack initiation increase. The effect of bimodularity is most significant under low horizontal stress states and negligible for a hydrostatic stress condition ( $m=1$ ).

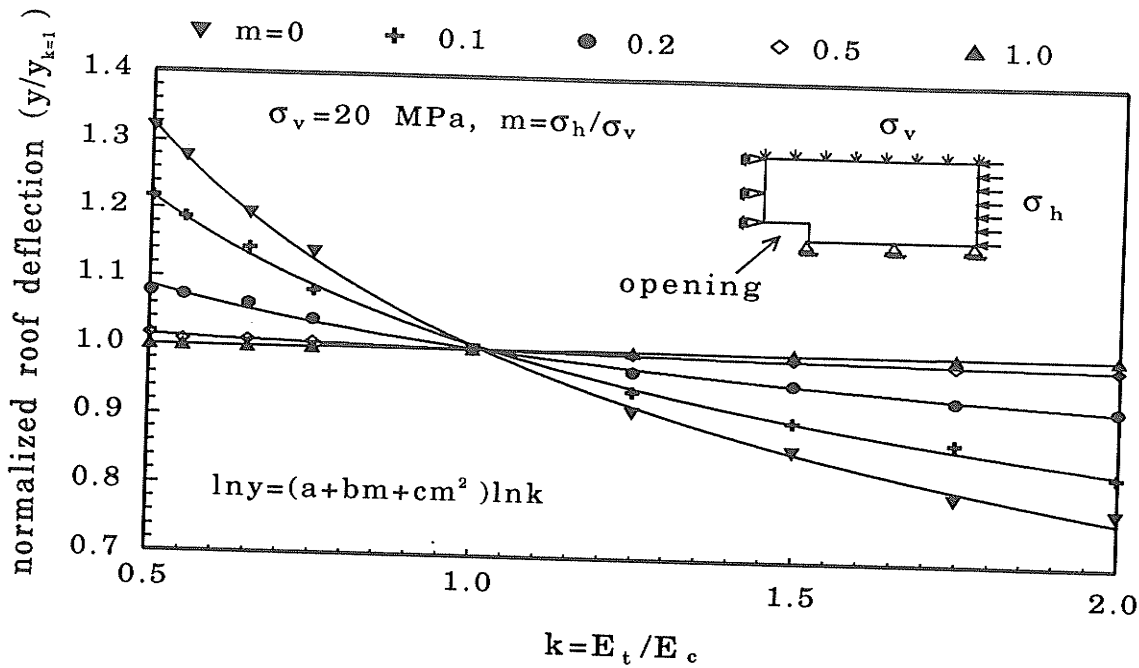


Figure 7.29 Finite element solution showing the influence of moduli ratio,  $k$ , on the maximum roof deflection at various horizontal to vertical principal stress ratios,  $m$ .

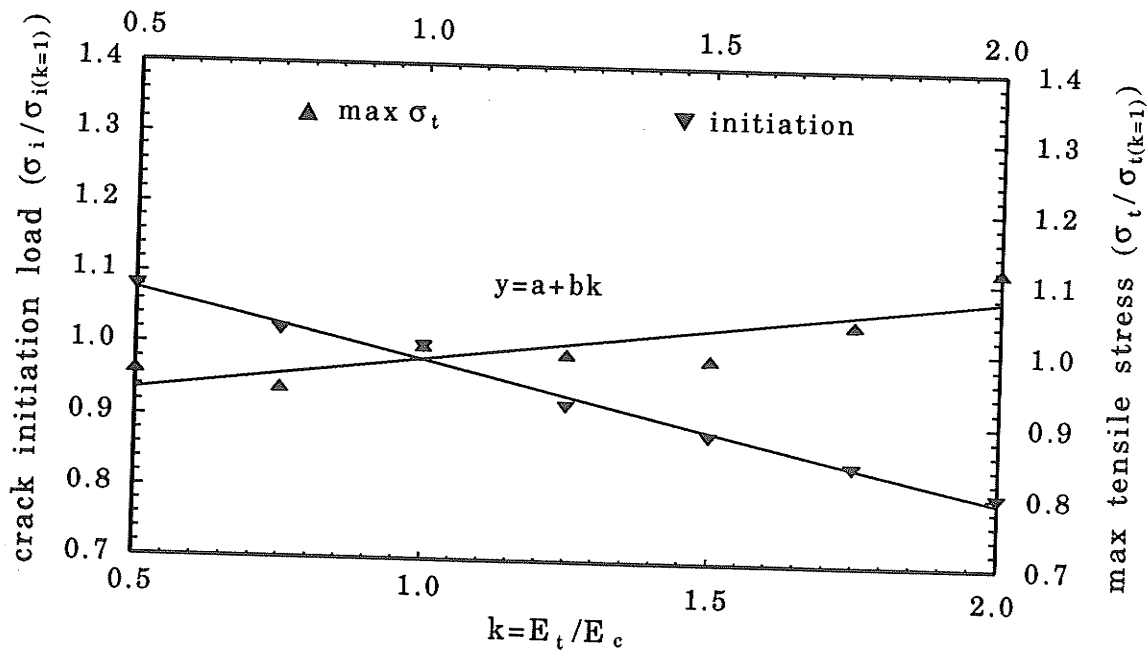


Figure 7.30 Finite element solution showing the influence of moduli ratio,  $k$ , on the maximum tensile stress at the middle span of the opening and on crack initiation load ( $m=0$ ).

## 7.7 Chapter Summary

The bimodular constitutive model, MWCM (Modified Weighted Compliance Matrix material model), has been incorporated into the finite element program SIMEX. The program's accuracy has been validated against analytical solutions. The program also incorporates fracture mechanics capabilities that enable the investigation of the effect of material bimodularity on fracturing around mine openings.

It has been shown that for rocks in which Young's modulus in tension is less than that in compression, the tensile strengths derived from beam bending, hydraulic extension, Brazilian and ring tests are overestimated if bimodularity is ignored. The actual tensile strength can be estimated only if the ratio of deformational moduli in tension and in compression is known. Rock bimodularity also has significant influence on roof deflection under low horizontal stresses.

## 8. DEFORMATION AND FRACTURE OF POTASH YIELD PILLARS

### 8.1 Introduction

As reviewed in Chapters 2 and 3, due to the complex time and stress history dependent deformational properties of potash and salt, mining in such rocks usually utilizes the stress-control techniques, in which the *yield pillar* is one of the principal tools for strata control. Differing from traditional pillar design that is based on the ultimate strength theory, yield pillar design uses the rock material's progressive deformational properties during and after yield. As a result, a yield pillar deforms progressively at a designed rate during its service life and transfers its load to adjacent stiff pillars or abutments and controls the stress redistribution around openings. Serata (1983) illustrated the applications of yield pillars in various stress-control mining techniques (e.g., Figures 2.2, 3.4, 3.5 and 3.6). Yield pillar techniques have been used successfully in potash mining in Saskatchewan and have proven to be the most suitable methods for stabilizing backs, minimizing floor heave, prolonging mine life and maximizing extraction.

Yield pillar design derives from calculations of stress distribution based upon various simplifying assumptions for material properties and mechanical models. Questions have been raised about these methods with respect to proper failure criteria, strength, strain rate, and transient stresses and strains (Hambley 1989). Moreover, the actual nature of deformation within yield pillars is still poorly understood. Efforts to address yield pillar deformational mechanisms have been limited to numerical and physical model simulations, without or with only poor, field observations for calibration (Kripakov 1981;

Chen and Karmis 1988; Tsang and Peng 1989; Kicher and Park 1986). This is because most of the observations are of measured room closure at the initial stages of pillar deformation during mining excavation. Long-term pillar deformation has not been documented.

The phenomenon of long-term deformation in potash yield pillars is addressed in this chapter through the examination of yield pillars in which 8 years of deformation has taken place. The objectives of this study are: 1. Documentation and interpretation of mesoscopic deformational features observed within yield pillars; 2. Documentation and interpretation of microfabric anisotropy as an indicator of ductile strain in the yield pillars; and 3. Development of a hypothesis of progressive pillar failure.

## 8.2 Background

In the Cominco Mine at Vanscoy, Saskatchewan, a series of potash openings was completed in 1977 as 5-entry mining systems, with an original yield pillar width of 6.7 metres and height of 3.35 metres. Eight years later, in 1985, a cross-cut was excavated at right angles to the original openings (Figure 8.1), revealing the details of deformation in the upper parts of the original yield pillars and the halite back (Figure 3.3), providing

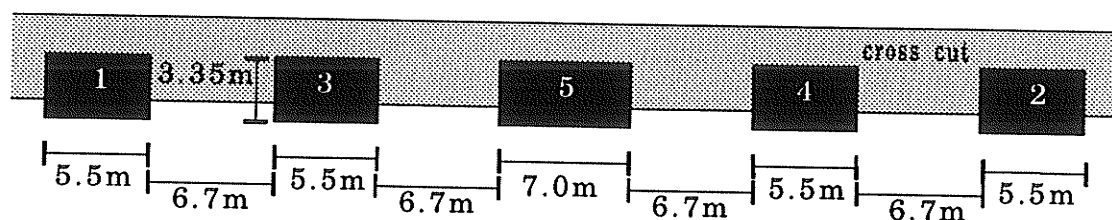


**Figure 8.1** Cross section showing the original 5-entry potash openings and the later cross cut. Mining sequence of the original openings is shown by numbers.

a rare opportunity to study highly deformed yield pillars. Detailed investigations were carried out on three representative yield pillars in 1990.

Although 5 years had passed since the excavation of the new cross-cut to the time when this study was carried out, the deformation observed is believed to be mainly due to the original opening. The effect of making the new cross-cut is negligible. In fact, the maximum stress concentration around underground openings is inside the wall. Near the pillar surface, stress is relieved and the pillar rock forms *slabs* ruptured by successive extensional failure parallel to the wall or *blocks* isolated by diagonal shear zones. These slabs or blocks behave in a rather elastic manner and do not undergo large amount of internal ductile deformation. This has been observed *in situ* (Kaiser 1987, 1988), by physical modelling (Ewy and Cook 1990), by stress analysis (Hoek and Brown 1980) and through numerical simulations (Pietruszczak and Mroz 1980). It is demonstrated further in this study by the existence of *shear wedges* at pillar margins.

### 8.3 Study Methods

The study methods included photography, mapping and determination of microfabric anisotropy. Pillar sections were photographed first and then mapped in detail with an emphasis on macroscopic structural features. Oriented samples were collected from key locations in the pillar walls and prepared for microfabric studies. These samples were collected from the walls of the new crosscut where extensional fractures and diagonal shear zones parallel to the new opening isolate the wall from longer term ductile deformation related to the new cross-cut.

Visual inspection of the fabric anisotropy within oriented samples from the interior of the pillars was the basis for specifying two perpendicular surfaces used in the analyses of microfibrils; both surfaces were vertical, one parallel to the original mine openings and the other perpendicular to the openings. These two surfaces were cut and polished in all samples, and were subjected to microscopic mapping of grain location and grain shapes, and digitization of grain boundaries. Fabric anisotropy was determined using INSTRAIN (Erslev 1989), a computer program for integrated fabric analysis. The program evaluates fabric anisotropy according to two methods, the centre-to-centre method and the object shape method (Erslev 1988). The former measures fabric anisotropy based on grain position of multiple grains, and the latter determines the shape and orientation of individual grains. INSTRAIN determines and evaluates the best fitting shape ellipses, computes ellipticity and determines the inclination of the major axis of the ellipses with respect to the horizontal. The ellipses from the two surfaces were combined to produce a three dimensional fabric anisotropy ellipsoid.

Fabric anisotropies are a consequence of ductile pillar deformation. Consequently, the magnitudes of fabric anisotropies can be used as an estimation of the accumulated finite strains and the fabric anisotropy ellipsoid axes can be used to mark the orientations of the principal strains. In modern structural geology, various techniques and procedures have been developed to help visualize strain and to permit direct measurement of strains in rock using certain naturally occurring objects, such as pebbles and fossils (Ramsay 1983). The object shape and centre-to-centre methods used in this study are most powerful among strain measuring techniques for two dimensional strain analyses.

### 8.3.1 Object shape method

The object shape method determines fabric anisotropy using objects that had initially circular, sub-circular, sub-elliptical or elliptical shapes, by measuring the elliptical shape ( $R_f$ ) and the orientation ( $\phi$ ) of the long axis of the deformed objects and by constructing a  $R_f/\phi$  data graph (Ramsay, 1983).

On a two-dimensional cut through the rock, the initial shape factor,  $R_i$ , is changed to the finally observed axial ratio,  $R_f$ . The orientation of the long axis of the ellipse is changed from  $\theta$  in undeformed state to  $\phi$  after deformation. Cloos (1947) used the arithmetic mean of  $R_f$  to determine the shape of the finite strain ellipse ( $R_s$ ) from deformed oolites that had an initial spherical shape ( $R_i=1$ ):

$$A = \frac{1}{n} \sum_1^n R_f \quad (8.1)$$

where  $n$  is the number of markers. The arithmetic mean was found to be a satisfactory estimation of  $R_s$ . For markers with initially elliptical shapes, Lisle (1977) examined the accuracy of various means of  $R_f$  in determining  $R_s$  and found that the following harmonic mean gave a closer approximation to  $R_s$ :

$$H = \frac{n}{\sum_1^n \frac{1}{R_f}} \quad (8.2)$$

Generally, various means gave values that are larger than  $R_s$  and  $A > G > H$ , where  $A$  is the arithmetic mean defined by Equation 8.1,  $H$  is the harmonic mean given by Equation 8.2, and  $G$  is the geometric mean defined by:

$$G = \sqrt[n]{R_{f_1} \times R_{f_2} \times R_{f_3} \times \dots \times R_{f_n}} \quad (8.3)$$

Lisle (1977) found that as  $R_s$  increases, the percentage error in the mean values decreases,

especially for  $H$  (Figure 8.2). If  $R_s$  is greater than 2, there is generally less than 10 percent error in strain estimates using the harmonic mean. If  $R_s$  is greater than 3, errors are very small. Thus the harmonic mean should provide good strain estimates where initial axial ratios are small to moderate and where  $R_s$  is reasonably large. The method, however, also requires that the strain was homogeneous and that there was no preferred orientation of long axes of markers prior to deformation. Lisle (1977) applied the harmonic mean to pebbles in a deformed conglomerate and further compared the results to those obtained by  $R_f/\phi$  techniques for strain analysis using *theta-curves* (Lisle 1977). He found that at high strains, the harmonic mean would seem to be a more definitive and simpler method for obtaining valuable strain estimates.

In INSTRAIN, a new method - the *mean object ellipse* method is implemented and is utilized in the object strain analysis in this study. It gave better estimates of object strain than simple arithmetic mean or harmonic mean of all the objects. The method determines the least-squares best-fit ellipse defined by the shape of any selected number ( $n$ ) of neighboring objects. This best-fit ellipse is then plotted in a  $R_f/\phi$  diagram and the harmonic mean of ellipticity ( $R_f$ ) and the orientation ( $\phi$ ) are calculated. In addition, an ASCII file

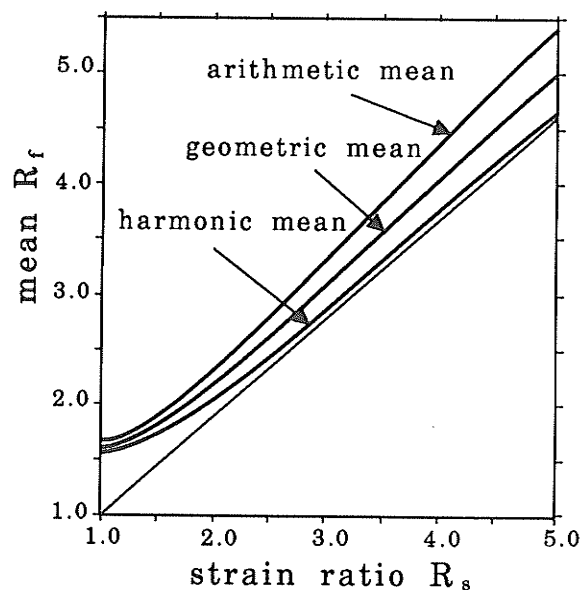


**Figure 8.2** The mean axial ratio of deformed elliptical markers as determined using  $A$ ,  $G$  and  $H$  compared to the tectonic strain ratio (after Lisle 1977).

containing the centre location of object, object volume, object dimensions and mean object ellipse (the least-squares best-fit ellipse determined by neighboring objects) can be written to disk. This data file can then be used to evaluate strain variation versus location and mineral types, etc.

### 8.3.2 Centre-to-centre method

When a body of rock containing uniformly distributed particles is strained, the particle centres are displaced relative to one another such that the centres of particles that are adjacent in the undeformed rock come to lie closer together in the shortened direction of the deformed rock and farther apart in the extended direction.

Ramsay (1967) utilized this phenomenon to determine the shape and orientation of the finite strain ellipse. The method, which has become known as the *centre-to-centre method*, is applied by measuring the distance between initially adjacent particle centres ( $d$ ) and the orientation of a line joining the two centres with respect to a reference direction ( $\alpha$ ), and then plotting  $d$  vs.  $\alpha$  for many pairs of measurements. The strain ratio and the orientation of the maximum and minimum principal strain can then be determined from the  $d$  vs.  $\alpha$  plot for the deformed rock.

Ramsay developed the centre-to-centre method for rocks in which pressure solution is evident. Grain shape analysis is unsuitable in such rocks due to the dissolution of parts of grains along pressure solution surfaces (Figure 8.3). In addition, the centre-to-centre method provides a more realistic estimate of rock strain than grain shape measurements in situations where dispersed particles in a matrix have not deformed

homogeneously with their matrix since both the strain of grains and the matrix between grains is taken into account by the grain centre-to-centre measurements.

The method, however, is limited to aggregates with uniformly distributed particles in the undeformed state and where the nearest neighboring grains of the undeformed rock can be identified easily in the deformed state. Fry (1979) proposed the all object-to-object separation method based on the same principle as the centre-to-centre method. Fry's method eliminates the problem of identifying objects which were nearest neighbors before deformation. The centre-to-centre distances separating every object from every other object define the shape of the finite strain ellipse. The relative positions of grains are directly plotted by sequentially putting the origin of an overlay on each grain centre and recording the position of other grain centres as points. As a result, a point vacant area or a very low point density area will occur around the central overlay reference point. The vacancy arises from the fact that any two original particles cannot come to lie closer than the sum of their radii. Around the vacancy high concentration of points will occur.

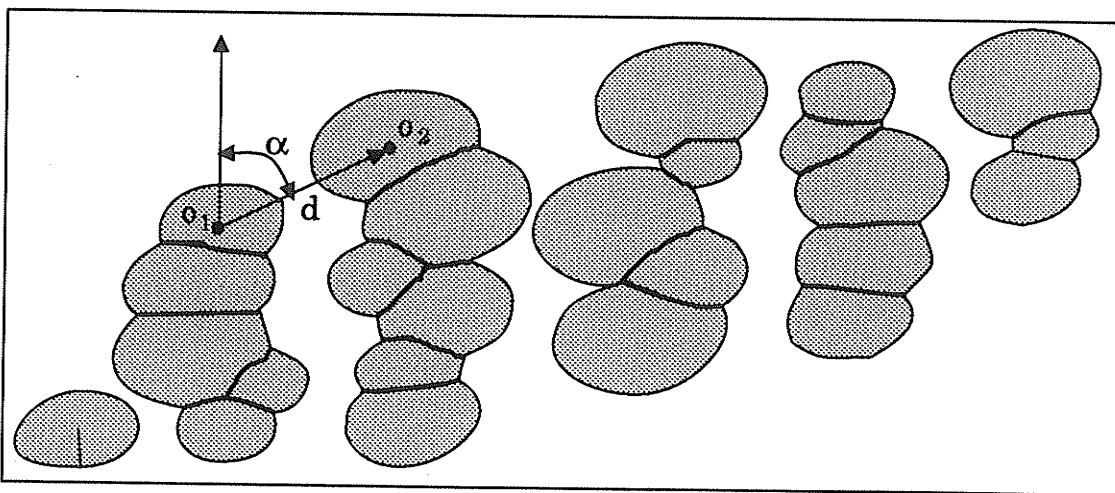


**Figure 8.3** Section through a deformed aggregate. The partially deformed spheres have undergone partial pressure solution along their mutual contacts (after Ramsay 1967).

This concentration has either a circular or an elliptical form like that of the central vacancy that reflects the shape of the strain ellipse.

The method requires that the strain is homogeneous and that the objects originally have an isotropic and homogeneous distribution. In addition, the method is severely affected by three dimensional clustering of object centres and the size variations. The definition of strain ellipse is often weak and ambiguous. Erslev (1988) normalized the Fry diagram by dividing the centre-to-centre distance between two objects by the sum of their average radii, which eliminates variations due to object size and sorting. Therefore, normalized Fry diagrams form much better defined vacant fields and sharper rims of maximum point density regardless of the original sorting and anti-clustering in the aggregate. Figure 8.4 provides an example of Fry centre-to-centre plot (a) and normalized Fry centre-to-centre plot (b).

The normalized Fry method does not correct for initial ellipticity or preferred orientation any better than the Fry method. It does not improve the accuracy of centre-to-

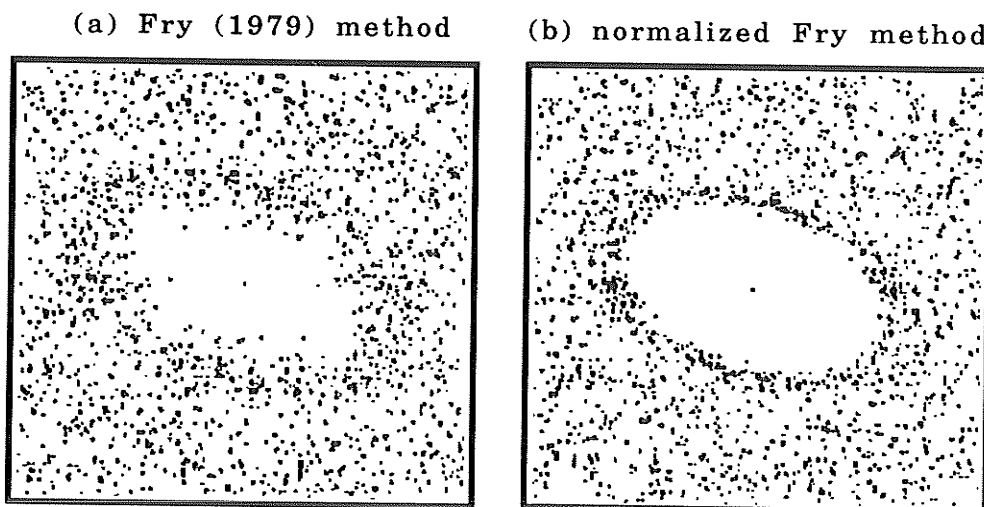


**Figure 8.4** Examples of Fry centre-to-centre plot (a) and normalized Fry centre-to-centre plot (b).

centre analyses in unpacked aggregates. The assumption of homogeneous strain holds effective for the normalized Fry method. The three main constraints of the Fry methods are: edge effects, sample size and visual interpretation. The normalized Fry method overcomes the constraint due to sample size variation and improves visual interpretation by increased resolution. However, it does not improve the constraint associated with edge effects, resulting from the limited size of the original plot. As each point of the original plot is to be used as the centre of the derived plot, a problem may arise whereby apparent point density on the plot falls away with distance.

### 8.3.3 Evaluation of three-dimensional strain

Both the object shape method and the centre-to-centre method evaluate two dimensional strains. By combining strains measured from two surfaces that are perpendicular to each other, three dimensional strains can be calculated based on the assumption of no volume changes.

The coordinate system in Figure 8.5 is selected in such a way that the  $x$ -axis is

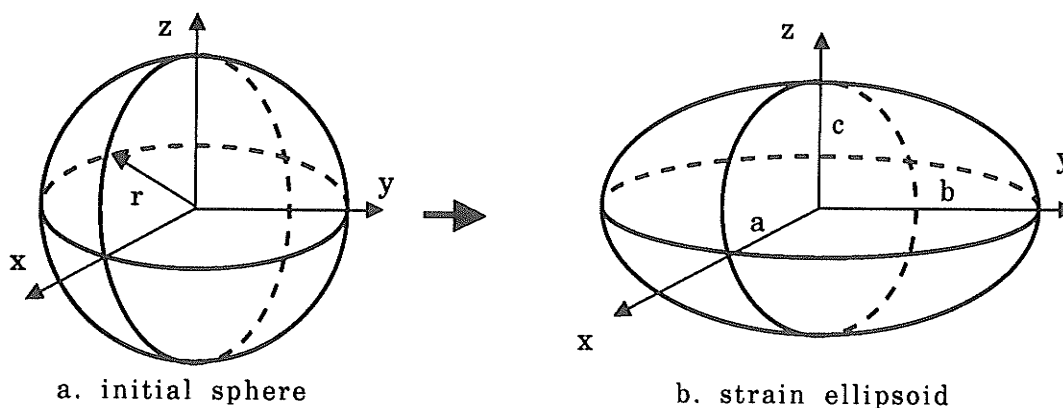


**Figure 8.5** Geometry of the original sphere and the deformed ellipsoid for deriving three dimensional strains.

perpendicular to the original opening,  $y$ -axis is parallel the original opening and the  $z$ -axis represents the vertical direction, i.e.,  $x$ - $z$  plane represents sample surface perpendicular to the original openings and  $y$ - $z$  plane represents surface parallel to the original openings. An initial sphere with the radius of  $r$  is deformed to an ellipsoid with semi-axis  $a$ ,  $b$  and  $c$ . Hence, strains along  $x$ ,  $y$  and  $z$  directions ( $\epsilon_a$ ,  $\epsilon_b$  and  $\epsilon_c$ ) can be defined as:

$$\left. \begin{aligned} \epsilon_a &= \frac{(a-r)}{r} = \frac{a}{r} - 1 \\ \epsilon_b &= \frac{(b-r)}{r} = \frac{b}{r} - 1 \\ \epsilon_c &= \frac{(c-r)}{r} = \frac{c}{r} - 1 \end{aligned} \right\} \quad (8.4)$$

therefore,

$$\left. \begin{aligned} a &= r(1 + \epsilon_a) \\ b &= r(1 + \epsilon_b) \\ c &= r(1 + \epsilon_c) \end{aligned} \right\} \quad (8.5)$$

Let  $e_1$  and  $e_2$  represent the ellipticity ( $R_f$ ) of the strain ellipse obtained from sample surfaces perpendicular to and parallel to the original openings respectively, by definition,

$$\left. \begin{aligned} e_1 &= \frac{a}{c} \quad \text{ellipticity in } x\text{-}z \text{ plane} \\ e_2 &= \frac{b}{c} \quad \text{ellipticity in } y\text{-}z \text{ plane} \end{aligned} \right\} \quad (8.6)$$

Since the volume of the initial sphere equals:

$$V_0 = \frac{4}{3} \pi r^3$$

and the volume of the strain ellipsoid equals:

$$V = \frac{4}{3} \pi abc = \frac{4}{3} \pi r^3 (1 + \epsilon_a)(1 + \epsilon_b)(1 + \epsilon_c)$$

letting  $V_0 = V$ , yields:

$$(1+\varepsilon_a)(1+\varepsilon_b)(1+\varepsilon_c)=1 \quad (8.7)$$

Compare (8.5) and (8.6):

$$\left. \begin{aligned} \frac{a}{c} &= \frac{(1+\varepsilon_a)}{(1+\varepsilon_c)} = e_1 \\ \frac{b}{c} &= \frac{(1+\varepsilon_b)}{(1+\varepsilon_c)} = e_2 \end{aligned} \right\} \quad (8.8)$$

Solving equations (8.7) and (8.8),  $\varepsilon_a$ ,  $\varepsilon_b$  and  $\varepsilon_c$  can be obtained as:

$$\left. \begin{aligned} \varepsilon_a &= \frac{(e_1-k)}{k} \\ \varepsilon_b &= \frac{(e_2-k)}{k} \\ \varepsilon_c &= \frac{(1-k)}{k} \end{aligned} \right\} \quad (8.9)$$

Where

$$k=(e_1e_2)^{\frac{1}{3}}$$

## 8.4 Results from Pillar 1

Figure 8.6 is the photograph of the cross section of Pillar 1. There is one metre between every two black dots. Black circles are sample locations. Figure 8.7 is the mapped section of the same pillar. It also shows fabric anisotropy ellipsoids based on both sylvite shape method (a) and centre-to-centre method (b). The ellipsoids were drawn to scale according to the magnitude of fabric anisotropy and centred at sample locations.

### 8.4.1 Dimensional changes and mesoscopic structures

The deformation in this pillar is manifest by a change in dimensions and

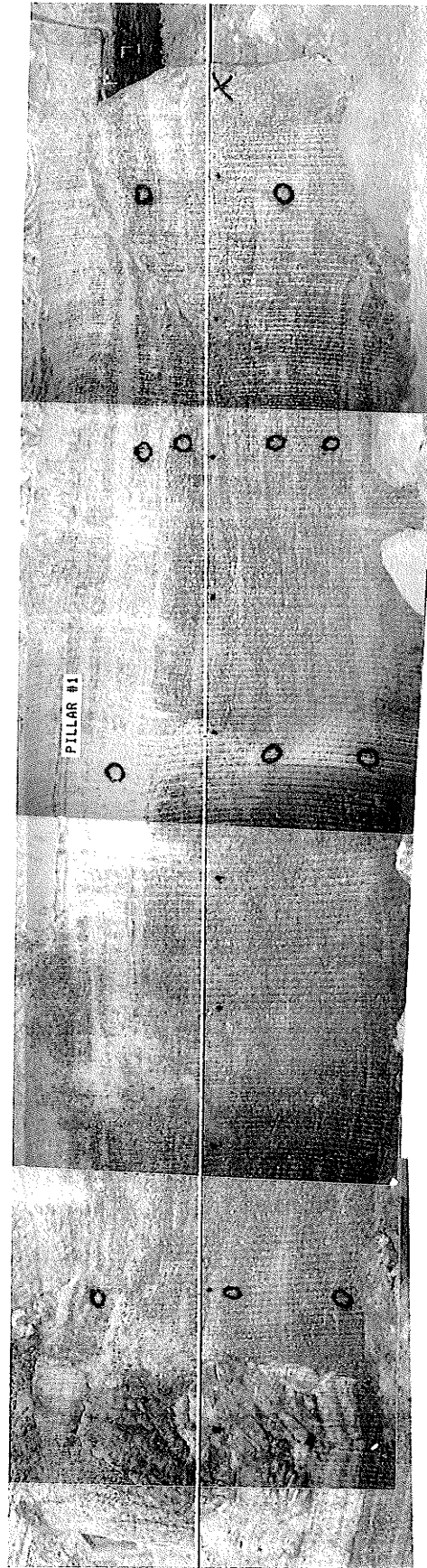
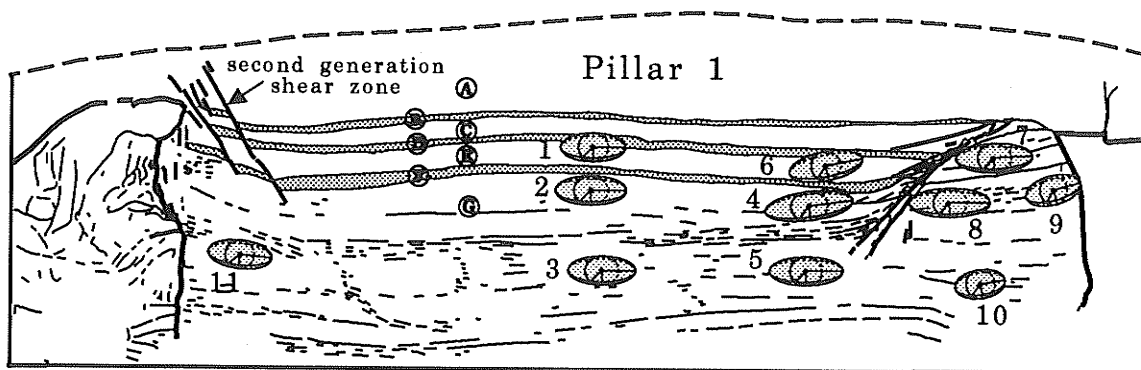
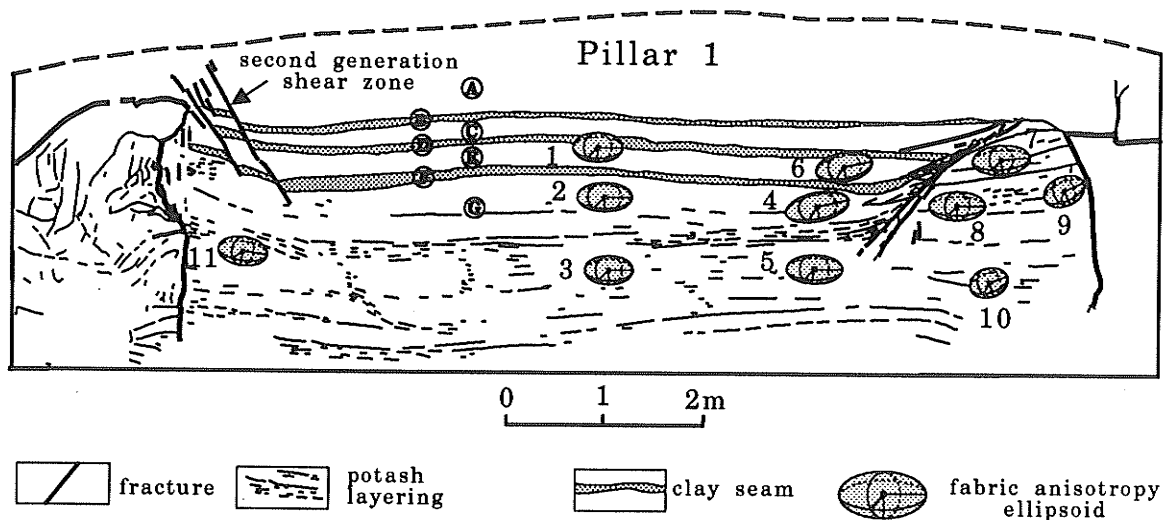


Figure 8.6 Photograph of the cross section of Pillar 1. There is one metre between every two black dots. Black circles are sample locations. The revealed pillar section is about two thirds of the upper part of the original pillar.

(a) shape method (sylvite)



(b) centre-to-centre method

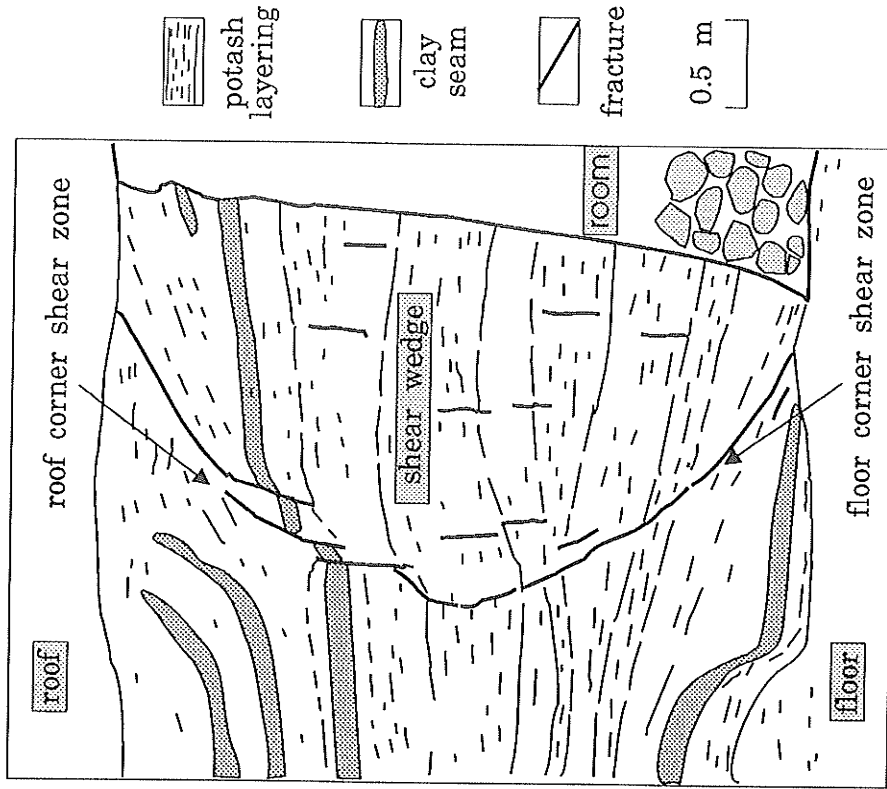


**Figure 8.7** Mapped cross section of Pillar 1. A-halite unit; B-first clay layer; C-potash; D-second clay layer; E-potash; F-third clay layer; G-potash. (a) Fabric anisotropy ellipsoids from the shape method for sylvite grains. (b) Fabric anisotropy ellipsoids from the centre-to-centre method. All the ellipsoids are centred at sample locations. See Table 1 for the ellipsoid dimensions.

development of structures that overall, indicate horizontal extension and vertical shortening. The magnitude of horizontal extension can be determined by the difference between the current pillar width (9 metres) and the original pillar width (6.7 metres). Determination of the magnitude of any vertical shortening, based on original and deformed thicknesses, is more problematic because spatial variations in original thicknesses of clay seams and interbedded potash layers are not well understood. However, the fabric study presented below confirms the presence of vertical shortening in the interbedded potash and provides some idea of its magnitude. Small shear zones have developed in the corner areas of the pillar. These shear zones are characterized primarily by ductile effects, although discrete dislocations and other brittle phenomena occur also.

The room to the right of Pillar 1 (Figure 8.7) is still stable. The shear zone that extends from the upper corner of the room into the pillar contains several small fractures parallel to the zone on which normal displacements of rock layers have occurred. Also present are sigmoidal tension fissures and drag flexures of clay seams. The details of the structures suggest that the shear zone initiated at the roof corner, propagated diagonally downward into the middle height of the pillar, and that the displacement was hangingwall down. Although the base of the pillar is not revealed, it can be suggested that a similar shear zone was also initiated at the floor corner, propagated diagonally up into the middle height of the pillar, and had a similar sense of movement. Such shear zones have been revealed in some other yield pillars at the Cominco Mine (Figure 8.8).

The corner shear zones may extend sufficiently to isolate a wedge area at the pillar



(a)

(b)

Figure 8.8 Development of shear zones and shear wedge in another pillar at the Vanscoy Mine. (a) Photo; (b) Sketch.

margin - *shear wedge* (Figure 8.8). Shear wedges may be detached from the pillar and pushed into the adjacent openings as pillar deformation increases. Similar effects have been noticed by Feder (1978) in tunnel walls and have been referred to as the *cherry stone* effect.

Broken potash and salt in the room to the left of Pillar 1 (Figure 8.7) indicates that the shear wedge on the left side of the pillar has moved out into this room and disintegrated, and that the resulting increase in roof span has caused the salt unit to collapse to some degree. Furthermore, a subsequent set of shears with normal displacement has developed, extending down from the salt unit above the pillar into the central area of the pillar, indicating the possible development of a second-generation shear wedge (Figure 8.7).

From the foregoing discussion, it can be concluded that, on a mesoscopic scale, pillar deformation involves both bulk rock flattening and repeated development of localized shear wedges at pillar margins.

#### 8.4.2 Microfabric

Study of microfabric anisotropies from selected locations within this pillar provide additional insight into the characteristics of the induced deformation. The ellipsoids shown in Figures 8.7(a) and 8.7(b) are based on sylvite shape analysis and centre-to-centre analysis, respectively. Table 8.1 presents ellipsoid axial dimensions with the dimension in the vertical direction ( $Z$ ) being normalized to unity. Table 8.2 shows the evaluation of the corresponding three dimensional strains. The ellipsoids have axes which coincide with

Table 8.1 Ellipsoid dimensions of Pillar 1 with Z normalized to unity

	Sample Number	X	Y	Z	$\phi$ (degree)
shape method (sylvite)	1	2.26	2.07	1	0
	2	2.47	2.09	1	0
	3	2.35	2.29	1	0
	4	3.02	2.85	1	+8
	5	2.52	2.28	1	0
	6	2.55	2.38	1	+14
	7	2.61	2.57	1	+3
	8	2.75	2.18	1	0
	9	1.94	1.90	1	+15
	10	1.73	1.61	1	+10
	11	2.20	2.05	1	+5
centre-to- centre method	1	1.71	1.31	1	0
	2	1.89	1.69	1	0
	3	1.67	1.52	1	0
	4	2.18	1.93	1	+13
	5	1.91	1.66	1	0
	6	1.93	1.66	1	+12
	7	1.96	1.59	1	+5
	8	1.91	1.83	1	0
	9	1.46	1.33	1	+23
	10	1.32	1.27	1	+20
	11	1.68	1.65	1	+8

Note: X-long axis; Y-intermediate axis; Z-short axis;  $\phi$ -inclination of X from the horizontal, positive for plunging down towards the pillar.

Table 8.2 Three dimensional strain of Pillar 1

	Sample Number	$\epsilon_a$ (%)	$\epsilon_b$ (%)	$\epsilon_c$ (%)
shape method (sylvite)	1	35	24	-40
	2	43	21	-42
	3	34	31	-43
	4	49	38	-51
	5	41	27	-44
	6	40	30	-45
	7	38	36	-47
	8	51	20	-45
	9	25	23	-35
	10	23	14	-29
	11	33	24	-39
centre-to-centre method	1	31	1	-24
	2	28	15	-32
	3	22	12	-27
	4	35	20	-38
	5	30	13	-32
	6	31	12	-32
	7	34	9	-32
	8	26	21	-34
	9	17	7	-20
	10	11	7	-16
	11	19	17	-29

Note:  $\epsilon_a$  - sub-horizontal strain perpendicular to the original openings (X direction);  
 $\epsilon_b$  - sub-horizontal strain parallel to the original openings (Y direction);  
 $\epsilon_c$  - sub-vertical strain (Z direction).

the principal strains in the pillar, namely vertical to subvertical shortening and horizontal to subhorizontal extension in the other two directions. Horizontal extension perpendicular to the original openings exceeds that parallel to the original openings. Fabric ellipsoids with the highest dimensional ratios are located near the upper-corner shear zones, and those with the lowest dimensional ratios are in the middle of the isolated shear wedge adjacent to the room to the right. Intermediate ratios characterize the central portion of the pillar.

Further understanding of the nature of the deformation is obtained by plotting the fabric anisotropies on a standard Flinn diagram (Figure 8.9). The ratio of the major axis

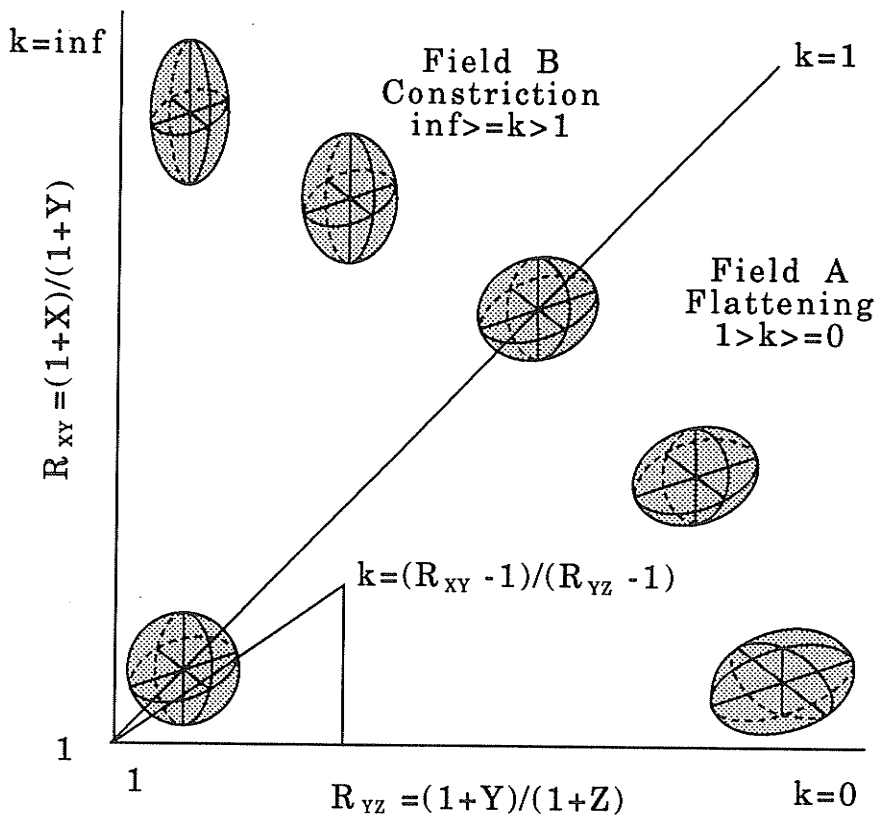


**Figure 8.9** The Flinn diagram for representing the shape of strain ellipsoids (after Ramsay 1983).  $inf$ =infinite.

to intermediate axis of the strain ellipsoid ( $R_{XY}$ ) is plotted against the ratio of the intermediate axis to minor axis ( $R_{YZ}$ ). A parameter  $k$  is used to describe the position of an ellipsoid on the Flinn diagram.  $k$  is equal to  $(R_{XY}-1)$  over  $(R_{YZ}-1)$ . Ellipsoids with  $k$  values between zero and unity have oblate forms and the strain producing them is referred to as flattening. One principal strain axis has been shortened and the other two elongated. Ellipsoids with  $k$  values between unity and infinity have prolate forms and the strain is referred to as constriction. One principal strain axis has been elongated and the other two shortened. The distance from the origin on the Flinn diagram represents the fabric anisotropy magnitude.

Figure 8.10 shows the Flinn plot for both the centre-to-centre method and sylvite grain shapes (shape method) for Pillar 1. Most of the ellipsoids of Pillar 1 on the Flinn plot are located close to the horizontal axis, signifying flattening. The results from sylvite grains show larger dimensional ratios than the centre-to-centre method, indicating that the fabric anisotropies, as determined by the two methods, may be revealing different components of deformation. This will be discussed further in Section 8.7 later in this chapter.

### 8.5 Results from Pillar 2

Figure 8.11 is the photograph of the cross section of Pillar 2. Figure 8.12 shows the results of mapping, microfabric analyses and the interpretation of deformation for the upper part of Pillar 2. Tables 8.3 and 8.4 present axial dimensions of ellipsoids and the corresponding three dimensional strains, respectively.

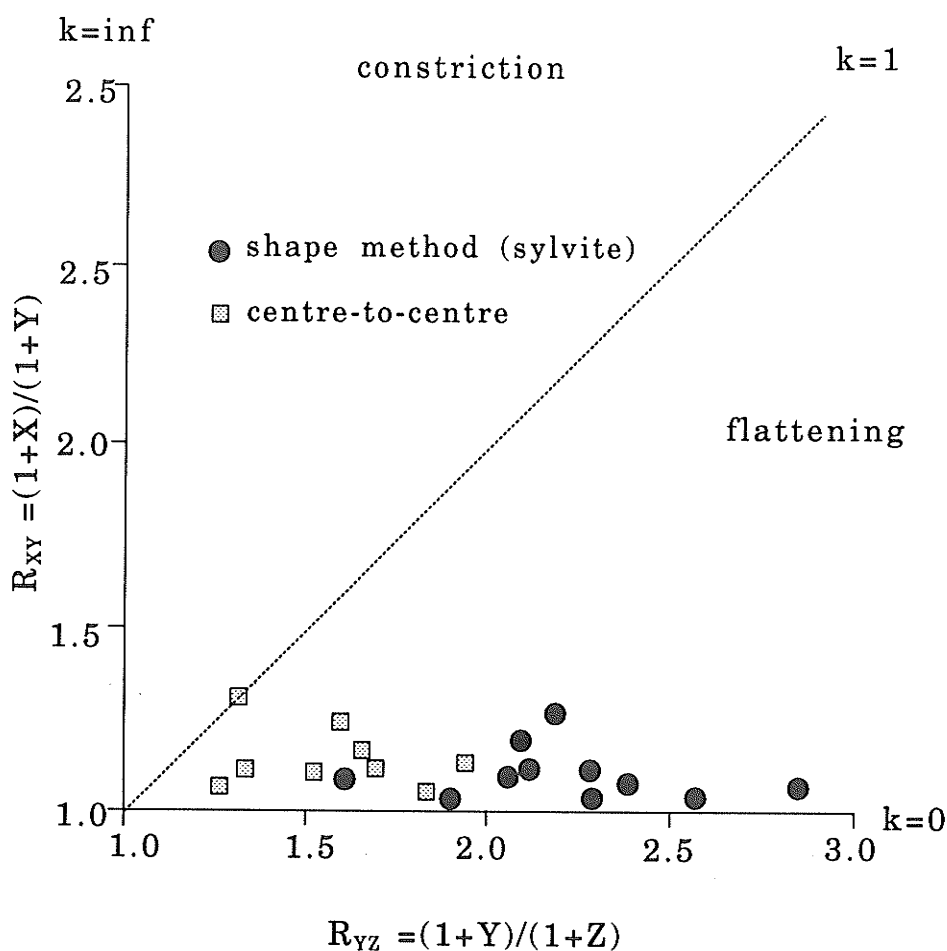


**Figure 8.10** Flinn diagram for strain measured in Pillar 1. Most ellipsoids are located very close to the horizontal axis, signifying apparent flattening. inf=infinite.

### 8.5.1 Dimensional changes and mesoscopic structures

The current width of this pillar is 6.5 m, a value slightly less than the original pillar width (6.7 m), in spite of the fact that ductile horizontal extension of the pillar has taken place (as illustrated below). Rooms on both sides of this pillar have collapsed and contain fragmented potash and salt. The salt roof has deformed and sagged into the

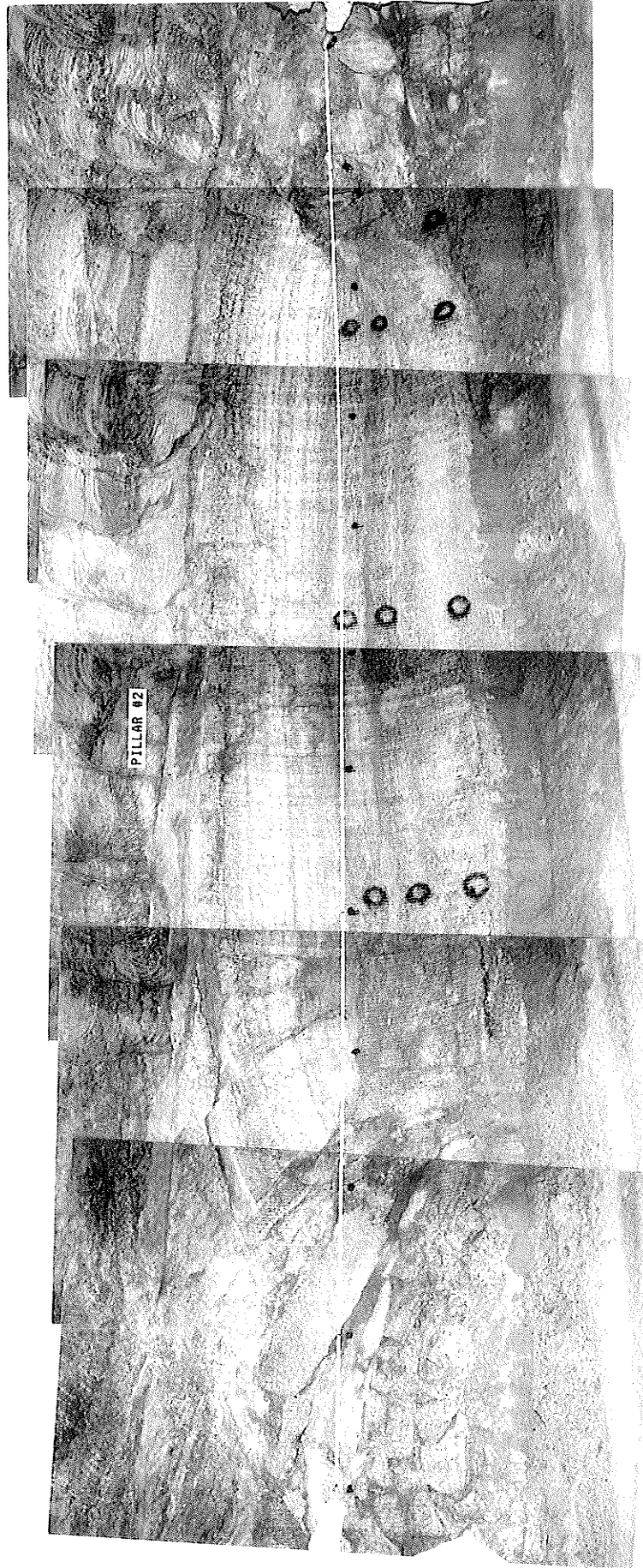
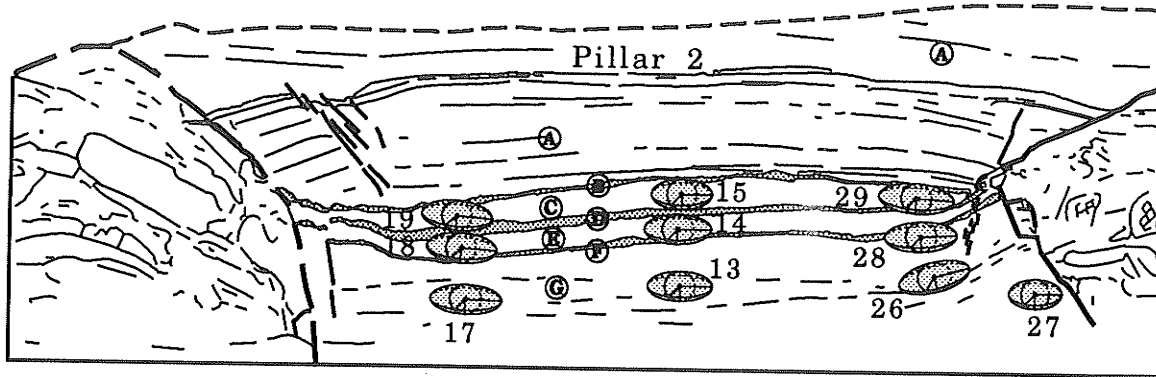
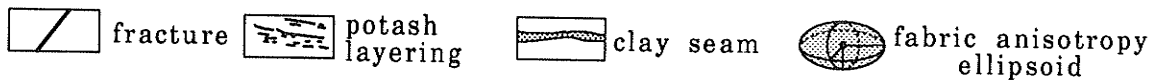
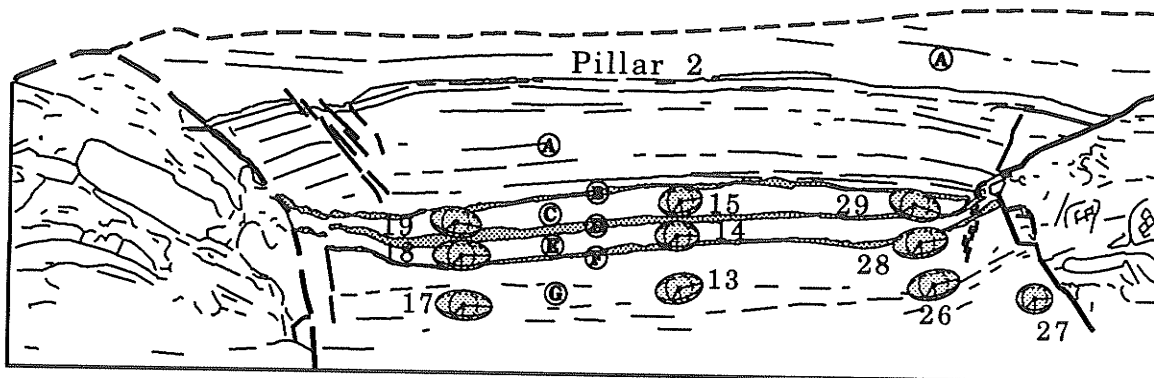


Figure 8.11 Photograph of the cross section of Pillar 2. There is one metre between every two black dots. Black circles are sample locations. The revealed pillar section is about two thirds of the upper part of the original pillar.

(a) shape method (sylvite)



(b) centre-to-centre method



**Figure 8.12** Mapped cross section of Pillar 2. A-halite unit; B-first clay layer; C-potash; D-second clay layer; E-potash; F-third clay layer; G-potash. (a) Fabric anisotropy ellipsoids from the shape method for sylvite grains. (b) Fabric anisotropy ellipsoids from the centre-to-centre method. All the ellipsoids are centred at sample locations. See Table 3 for the ellipsoid dimensions.

Table 8.3 Ellipsoid dimensions of Pillar 2 with Z normalized to unity

	Sample Number	X	Y	Z	$\phi$ (degree)
shape method (sylvite)	13	2.17	2.01	1	+3
	14	2.25	2.11	1	+2
	15	2.04	2.09	1	+2
	17	2.41	2.43	1	+2
	18	2.37	2.18	1	+4
	19	2.38	2.34	1	+5
	26	2.38	2.08	1	+15
	27	1.76	1.65	1	+1
	28	2.38	2.34	1	+2
	29	2.48	2.55	1	-4
centre-to- centre method	13	1.60	1.44	1	+14
	14	1.46	1.40	1	0
	15	1.47	1.43	1	+10
	17	1.90	1.73	1	+3
	18	1.93	1.62	1	0
	19	1.73	1.61	1	+10
	26	1.75	1.74	1	+14
	27	1.21	1.19	1	0
	28	1.81	1.59	1	+8
	29	1.73	1.65	1	-19

Note: X-long axis; Y-intermediate axis; Z-short axis;  $\phi$ -inclination of X from the horizontal, positive for plunging down towards the pillar.

Table 8.4 Three dimensional strain of Pillar 2

	Sample Number	$\epsilon_a$ (%)	$\epsilon_b$ (%)	$\epsilon_c$ (%)
shape method (sylvite)	13	33	23	-39
	14	34	25	-40
	15	26	29	-38
	17	34	35	-44
	18	37	26	-42
	19	34	32	-44
	26	40	22	-41
	27	23	16	-30
	28	34	32	-44
	29	33	39	-46
centre-to-centre method	13	21	9	-24
	14	15	10	-21
	15	15	12	-22
	17	30	16	-33
	18	32	11	-32
	19	23	14	-29
	26	21	20	-31
	27	7	5	-11
	28	27	12	-30
	29	22	16	-29

Note:  $\epsilon_a$  - sub-horizontal strain perpendicular to the original openings (X direction);  
 $\epsilon_b$  - sub-horizontal strain parallel to the original openings (Y direction);  
 $\epsilon_c$  - sub-vertical strain (Z direction).

rooms. In the yield pillar, the three clay seams have been pinched together near the upper corner areas. In the upper left portion of Figure 8.12, a series of diagonal fractures has developed in the salt unit above the pillar and extended diagonally downward towards the pillar. Some of these show normal displacement of salt layers. In the upper right portion, a single diagonal fracture has developed in the salt unit. This merges with the zone of clay layer pinching and extends downward into the pillar as a series of small, indistinct and discontinuous fractures.

These structures and pillar dimensions suggest that initial shear wedges on either side of Pillar 2 have collapsed into adjacent rooms, that some roof collapse has occurred as well, and that second generation shear wedges have developed subsequently.

### **8.5.2 Microfabric**

The pattern of microfabric anisotropy in Pillar 2 is similar to that observed in Pillar 1. The greatest anisotropy is close to where shear zones have developed; intermediate values characterize the central part of the pillar, and the lowest value is isolated in the shear wedge close to the room on the right. The Flinn diagram for this pillar (Figure 8.13) shows that the fabric anisotropies indicate flattening, and that again there is a significant difference between the results from the centre-to-centre method and the sylvite grain shapes.

### **8.6 Results from Pillar 3**

Only one side of Pillar 3 was studied. Figure 8.14 is the photograph of the pillar

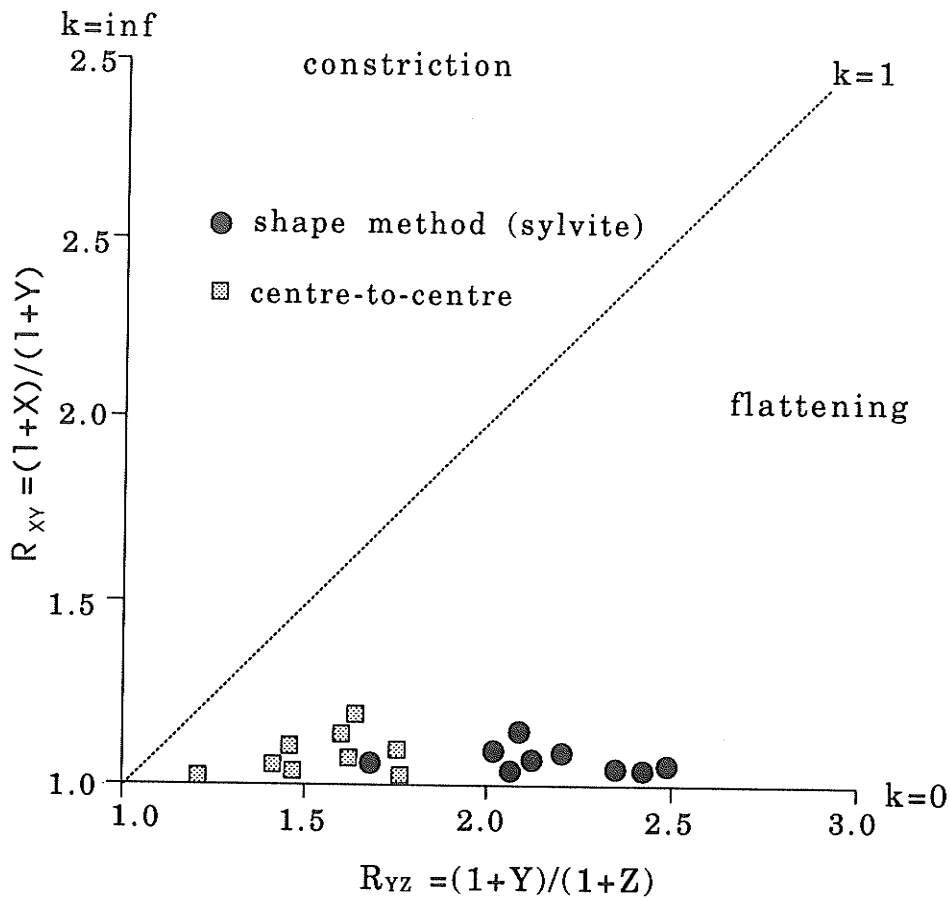


**Figure 8.13** Flinn diagram for Pillar 2. Most of the strain ellipsoids are located very close to the horizontal axis, signifying apparent flattening. inf=infinite.

section. Figure 8.15 shows the mapped pillar section together with fabric anisotropy ellipsoids at each sample location. Tables 8.5 and 8.6 present ellipsoid axial dimensions and the corresponding three dimensional strains.

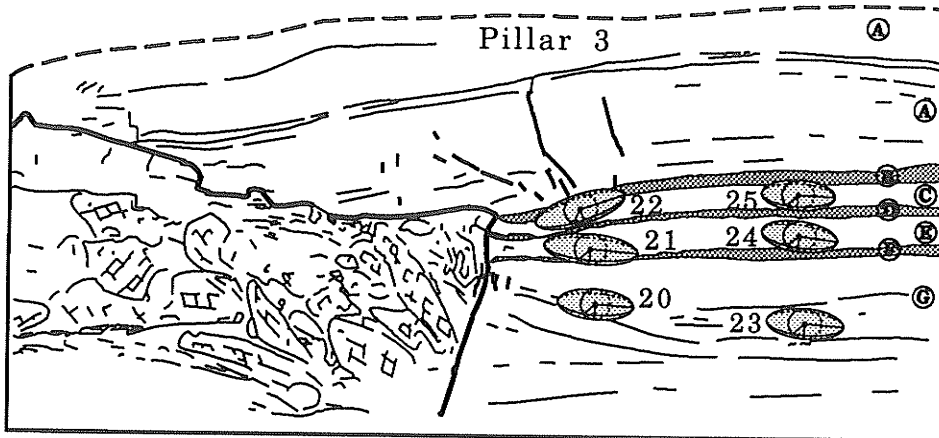
### 8.6.1 Dimensional changes and mesoscopic structures

Fragments of potash and salt in the room to the left indicate collapse of at least one shear wedge and roof. Brittle fractures have developed in the salt unit above the pillar and extended diagonally downward towards the pillar. The clay seams and interbedded



**Figure 8.14** Photograph of the cross section of Pillar 3. There is one metre between every two black dots. Black circles are sample locations. The revealed pillar section is about two thirds of the upper part of the original pillar.

(a) shape method (sylvite)



(b) centre-to-centre method

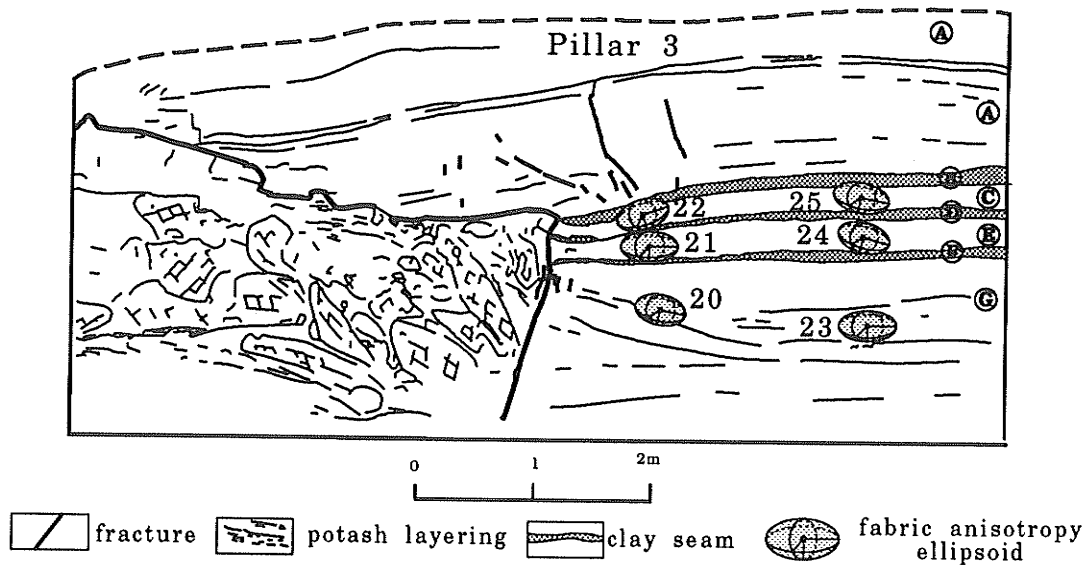


**Figure 8.15** Mapped cross section of Pillar 3. A-halite unit; B-first clay layer; C-potash; D-second clay layer; E-potash; F-third clay layer; G-potash. (a) Fabric anisotropy ellipsoids from the shape method for sylvite grains. (b) Fabric anisotropy ellipsoids from the centre-to-centre method. All the ellipsoids are centred at sample locations. See Table 5 for the ellipsoid dimensions.

Table 8.5 Ellipsoid dimensions of Pillar 3 with Z normalized to unity

	Sample Number	X	Y	Z	$\phi$ (degree)
shape method (sylvite)	20	2.51	2.49	1	+5
	21	3.09	2.80	1	+5
	22	3.08	2.71	1	-20
	23	2.50	2.52	1	+6
	24	2.47	2.54	1	+9
	25	2.38	2.35	1	+3
centre-to- centre method	20	1.68	1.64	1	+12
	21	1.88	1.78	1	0
	22	1.75	1.68	1	-18
	23	1.87	1.82	1	+2
	24	1.70	1.68	1	+18
	25	1.83	1.69	1	+12

Note: X-long axis; Y-intermediate axis; Z-short axis;  $\phi$ -inclination of X from the horizontal, positive for plunging down towards the pillar.

potash units show severe pinching near the upper pillar corner. These features may indicate the initial development of another shear wedge.

### 8.6.2 Microfabric

The Flinn diagram for this pillar (Figure 8.16) indicates a fabric anisotropy distribution similar to the other two pillars. Once again the results from the centre-to-centre method are lower than those based on sylvite shapes (shape method).

Table 8.6 Three dimensional strain of Pillar 3

	Sample Number	$\epsilon_a$ (%)	$\epsilon_b$ (%)	$\epsilon_c$ (%)
shape method (sylvite)	20	36	35	-46
	21	51	36	-51
	22	52	33	-51
	23	35	36	-46
	24	34	38	-46
	25	34	33	-44
centre-to-centre method	20	20	17	-29
	21	23	23	-34
	22	22	17	-30
	23	24	21	-33
	24	20	18	-29
	25	26	16	-31

Note:  $\epsilon_a$  - sub-horizontal strain perpendicular to the original openings (X direction);  
 $\epsilon_b$  -sub-horizontal strain parallel to the original openings (Y direction);  
 $\epsilon_c$  - sub-vertical strain (Z direction).

## 8.7 Strain Partitioning, Deformational Mechanisms and Finite Strain Measurement

### 8.7.1 Mineral components and strain partitioning

By mapping the magnitude of fabric anisotropy based on the shape changes of individual sylvite and halite grains with respect to grain types, it can be shown that the magnitude of shape change has been partitioned according to mineral types. Figures 8.17, 8.18 and 8.19 illustrate this partitioning for three rock samples from Pillar 1 by comparing spatial variations in the magnitude of shape anisotropy on a grain by grain basis. Figure 8.17 represents a sample from near the upper right corner ductile shear

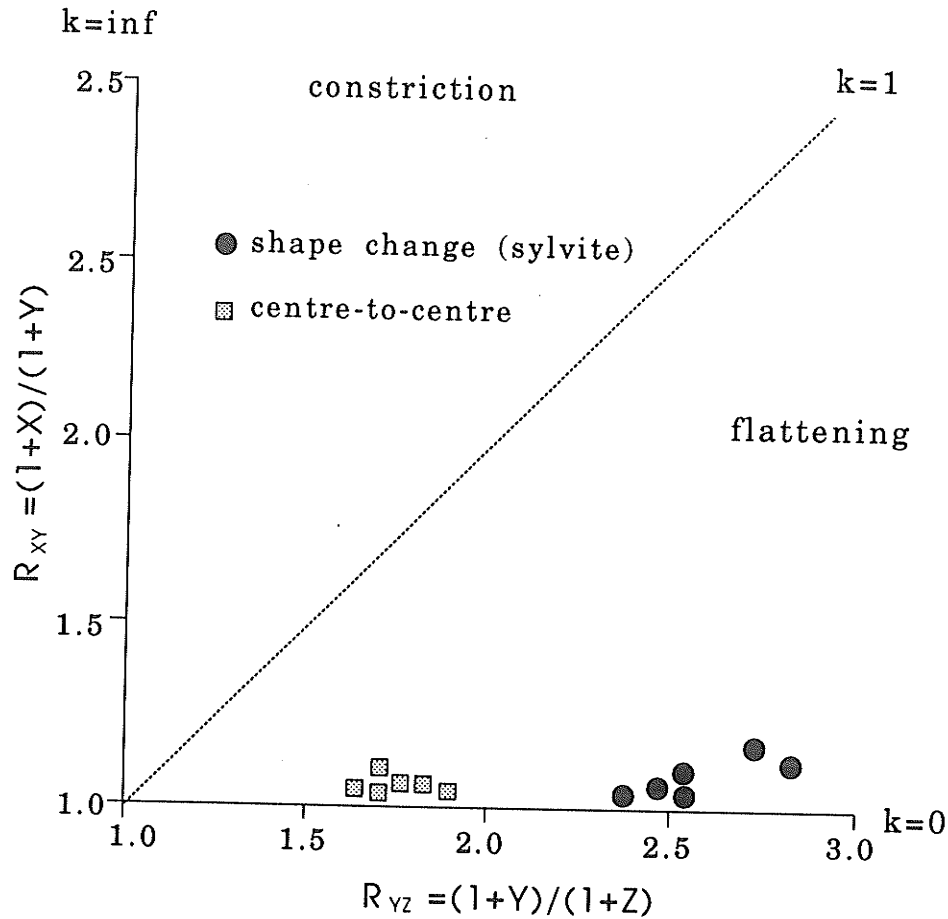


**Figure 8.16** Flinn diagram for Pillar 3. Most strain ellipsoids are located very close to the horizontal axis, signifying apparent flattening of rock. inf=infinite.

zone, Figure 8.18 is a sample from the central part of the pillar, and Figure 8.19 is a sample from the middle of the shear wedge at the right end of Pillar 1. Each of these figures represents three images of a vertical polished surface perpendicular to the original openings: (a) shows a tracing of grain shapes and locations, (b) plots contours showing the variation of dimensional ratio based on both sylvite and halite grains, and (c) is a relief diagram showing the variation of dimensional ratios. These figures illustrate that low dimensional ratio (lower ductile deformation in individual grain) coincide with

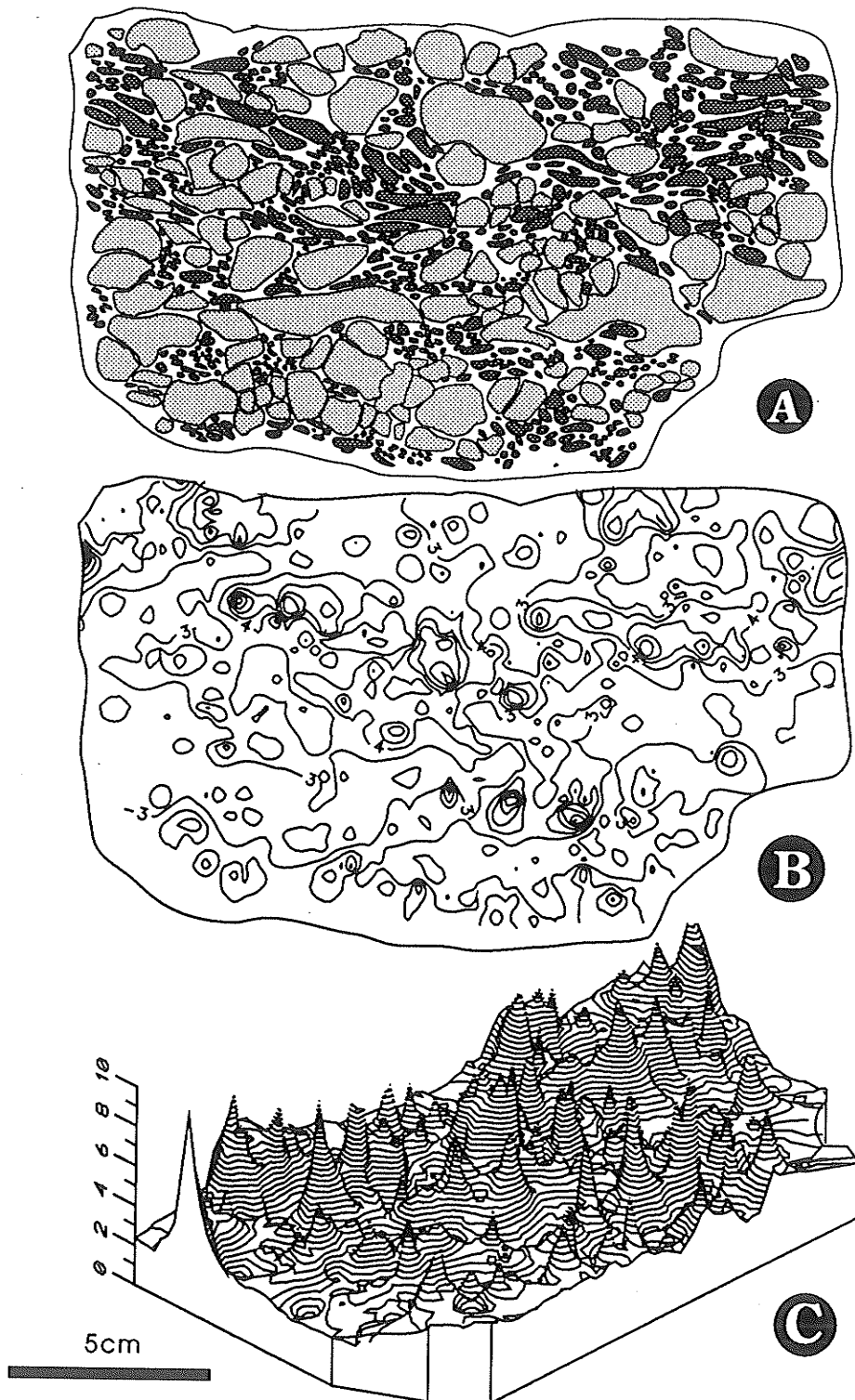


**Figure 8.17** Strain partitioning results from Sample 4, from near corner ductile shear zone in Pillar 1. (a) Tracing of grain shapes, darker grains are sylvite, lighter grains are halite; (b) Contour map of dimensional ratios of grains, contour interval equals 1; (c) Relief map of dimensional ratios of grains. Peaks correspond to areas of sylvite concentration, valleys correspond to areas of halite grains.

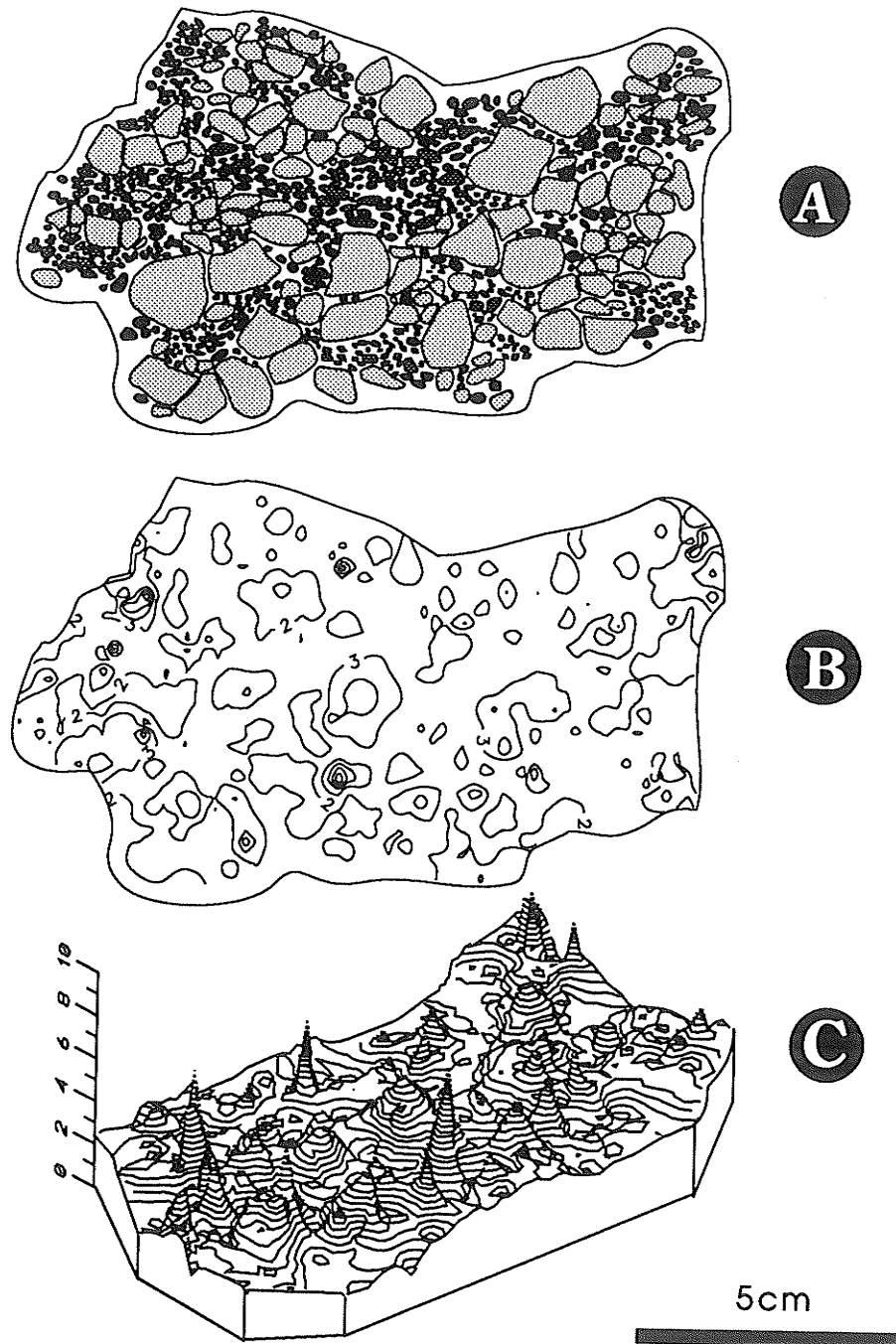


**Figure 8.18** Strain partitioning results from Sample 3, This sample is located in the central part of pillar 1. (a) Tracing of grain shapes, darker grains are sylvite, lighter grains are halite; (b) Contour map of dimensional ratios of grains, contour interval equals 1; (c) Relief map of dimensional ratios of grains. Peaks correspond to areas of sylvite concentration, valleys correspond to areas of halite grains.

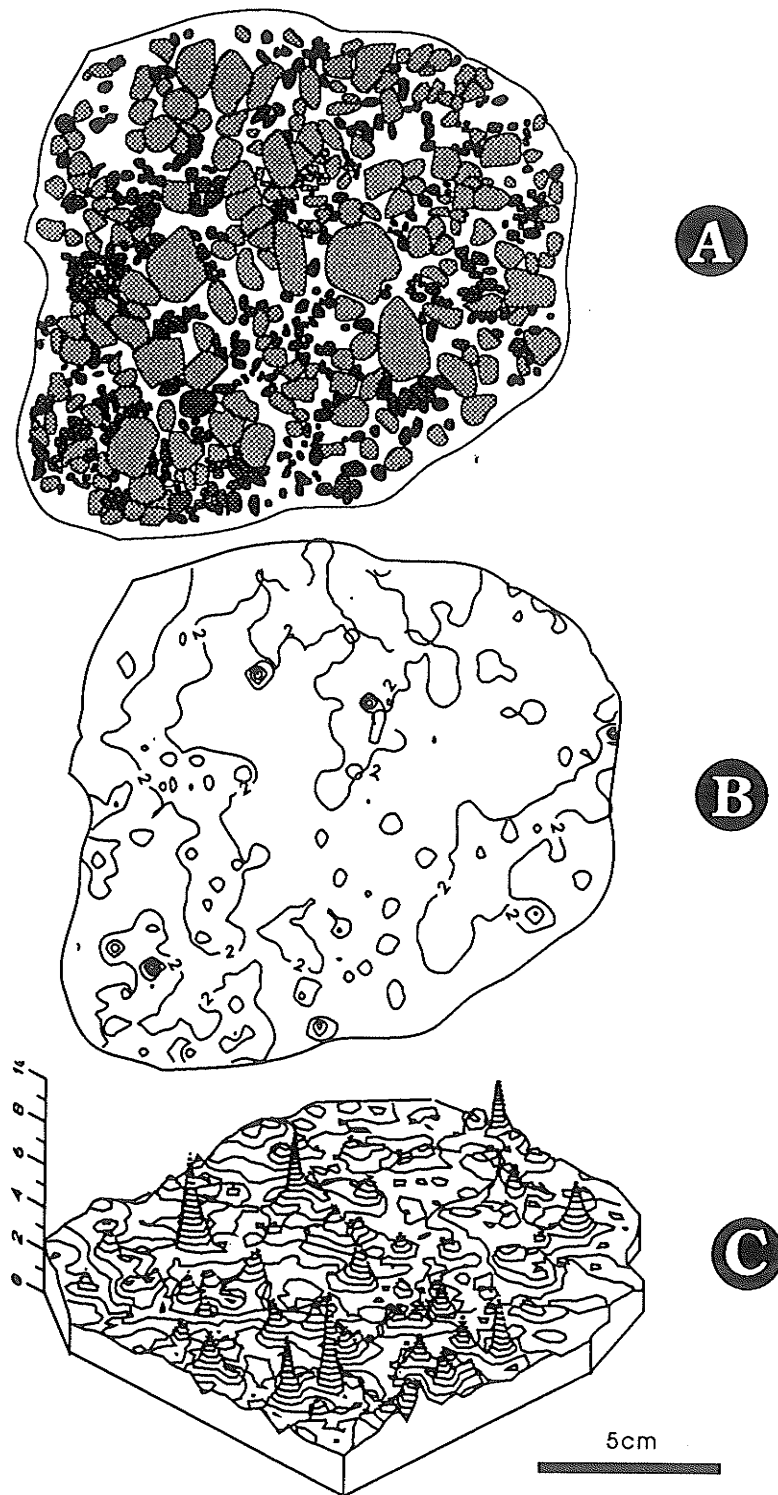


**Figure 8.19** Strain partitioning results from Sample 10, locating at the centre of shear wedge in Pillar 1. (a) Tracing of grain shapes, darker grains are sylvite, lighter grains are halite; (b) Contour map of dimensional ratios of grains, contour interval equals 1; (c) Relief map of dimensional ratios of grains. Peaks correspond to areas of sylvite concentration, valleys correspond to areas of halite grains.

aggregation of halite grains and higher dimensional ratios (higher ductile deformation) coincide with sylvite grains. This phenomenon is due to the fact that sylvite grains and halite grains have behaved in quite different mechanisms during deformation and have resulted in different manifestation of deformation.

### **8.7.2 Fabric anisotropy, deformational mechanisms and finite strain measurement**

The different deformational mechanisms of sylvite grains and halite grains can be illustrated by comparing Figures 8.20 and 8.21. Figure 8.20 shows an undeformed potash sample taken from a fresh mining surface. Grains of sylvite and halite are equant in shape and show an interlocking crystalline texture. Halite has a grain size slightly coarser than sylvite. Grain boundaries are characterized by thin coatings of clay. The fabric of the undeformed potash is isotropic at this scale.

In contrast, Figure 8.21 shows two samples from yield pillars that have undergone 8 years of deformation. The sylvite grains are lenticular and are aligned. They have been flattened without visible loss of continuity. Halite grains, on the other hand, have deformed in a brittle fashion by fracturing. Rotation and displacement of the broken halite fragments are consistent with the direction of flattening observed in the sylvite. In total, the deformed potash ore has some of the properties of an augen mylonite, wherein the halite constitutes the augen. The fabric anisotropy in these rocks is clearly a consequence of the deformation produced in the yield pillar after mining the initial rooms.

Deformational mechanisms in halite include fracturing and the displacement and rotation of fragments. Original halite grains are reduced to fractured aggregates. The

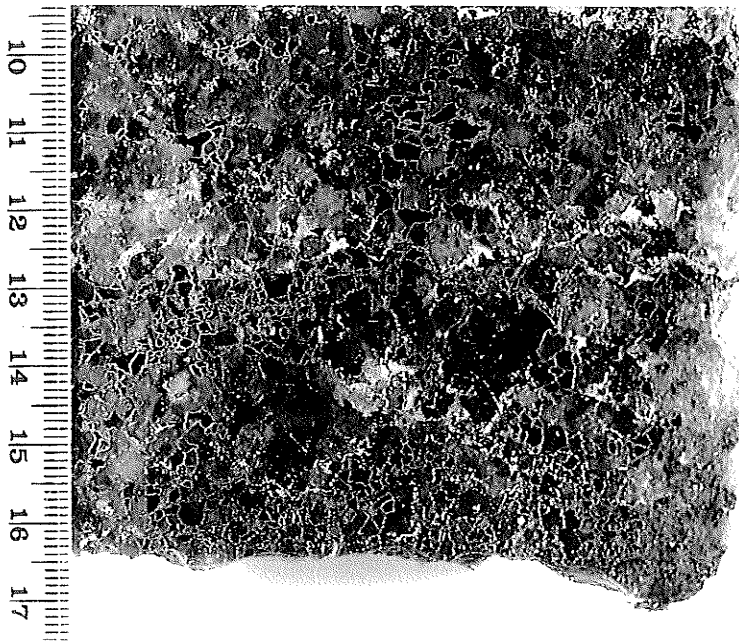


**Figure 8.20** A sample of undeformed potash collected from a fresh mining surface. The scale is centimetres.

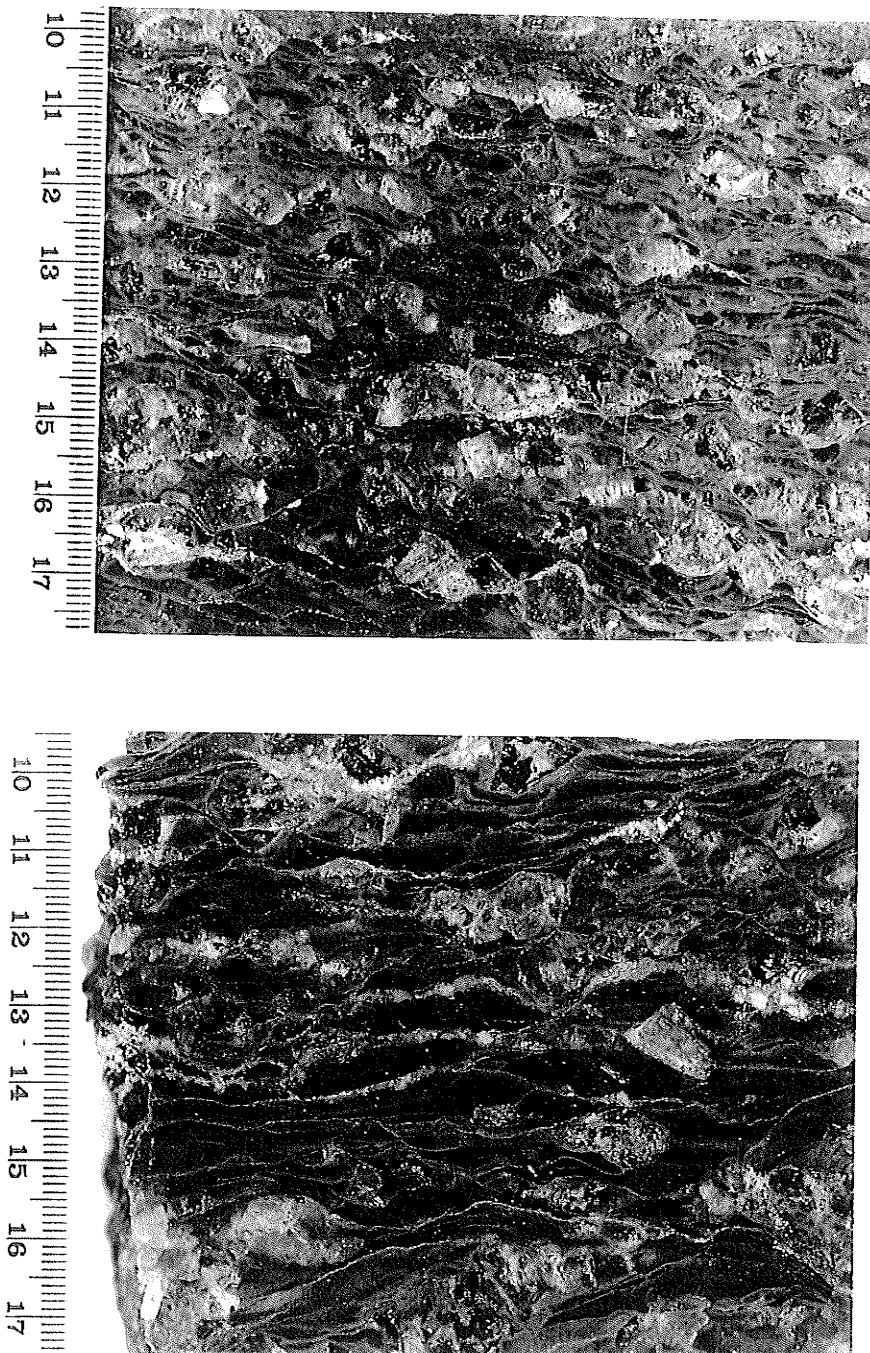


**Figure 8.21** Samples of deformed potash collected from yield pillars after 8 years of deformation. Sylvite is dark and flattened; halite occurs as light and broken aggregates in the shape of augen. The scale is centimetres. (a) Deformed potash equivalent in grain size to Figure 8.20; (b) Deformed potash coarser grained than Figure 8.20.

sylvite is not fractured, but undergoes shape change without loss of continuity. Deformational mechanisms within sylvite are problematic although some that could apply have been discussed by Hansen and Senseny (1983) and Senseny (1992). These include polygonization and recrystallization. The fact that sylvite is optically isotropic means that a methodology such as TEM is required to identify specific mechanisms. An alternative mechanism for sylvite strain is pressure solution, although no positive evidence to this effect has been observed. Finally, grain boundary sliding has occurred between halite and sylvite grains, between halite fragments, and along contacts between neighboring sylvite grains. The last type of grain boundary sliding is indicated by the accentuated curvilinear distribution of sheared clay around flattened sylvite.

Although there is clear evidence that the fabric anisotropies are a consequence of deformation, and that the fabric anisotropy ellipsoid axes mark the orientations of the principal strain axes, it is equally clear that the fabric ellipsoids, as determined by the two methods, indicate different components of the strain experienced by the potash pillars. The total strain at this scale is a complex mixture of several components, including the brittle deformation of halite, the ductile grain shape changes of sylvite and grain boundary sliding. The centre-to-centre anisotropy appears to register the combined deformational responses of both halite and sylvite. The shape method measures the shape changes in sylvite alone. Neither method measures the grain boundary sliding component. Consequently, neither method provides a measure of total or bulk rock strain.

Nevertheless it is possible to track the progress of one of the components of strain, namely the ductile deformation of sylvite grains, during progressive pillar deformation.

In the following interpretation of pillar failure, the shape anisotropy ellipsoids based on the sylvite shape method have been equated to finite strain ellipsoids.

### **8.8 Interpretation of Progressive Pillar Failure**

Pillar dimensional changes, mesoscopic structures and fabric anisotropies indicate that pillar deformation involves ductile flattening of pillar interiors, development of shear zones and shear wedges at pillar margins, and the detachment or collapse of shear wedges and salt roof into rooms. Furthermore, the study suggests that these effects are sequential and may be repetitive. Figure 8.22 presents an interpretation of progressive pillar failure based on these processes; four stages of deformation are postulated, starting with an original pillar width of 6.7 metres and height of 3.35 metres.

#### **a) Stage 1**

This stage of pillar deformation is characterized by ductile strain and the initial development of the fabric anisotropy throughout the pillar. We interpret the central pillar sylvite strain in this stage as represented by values in the shear wedge at the right end of pillar 1, i.e., approximately 29% shortening in the subvertical direction, 23% subhorizontal elongation perpendicular to the original openings, and 14% horizontal elongation parallel to the original openings.

#### **b) Stage 2**

With further flattening of the pillar, ductile shear zones develop at the pillar

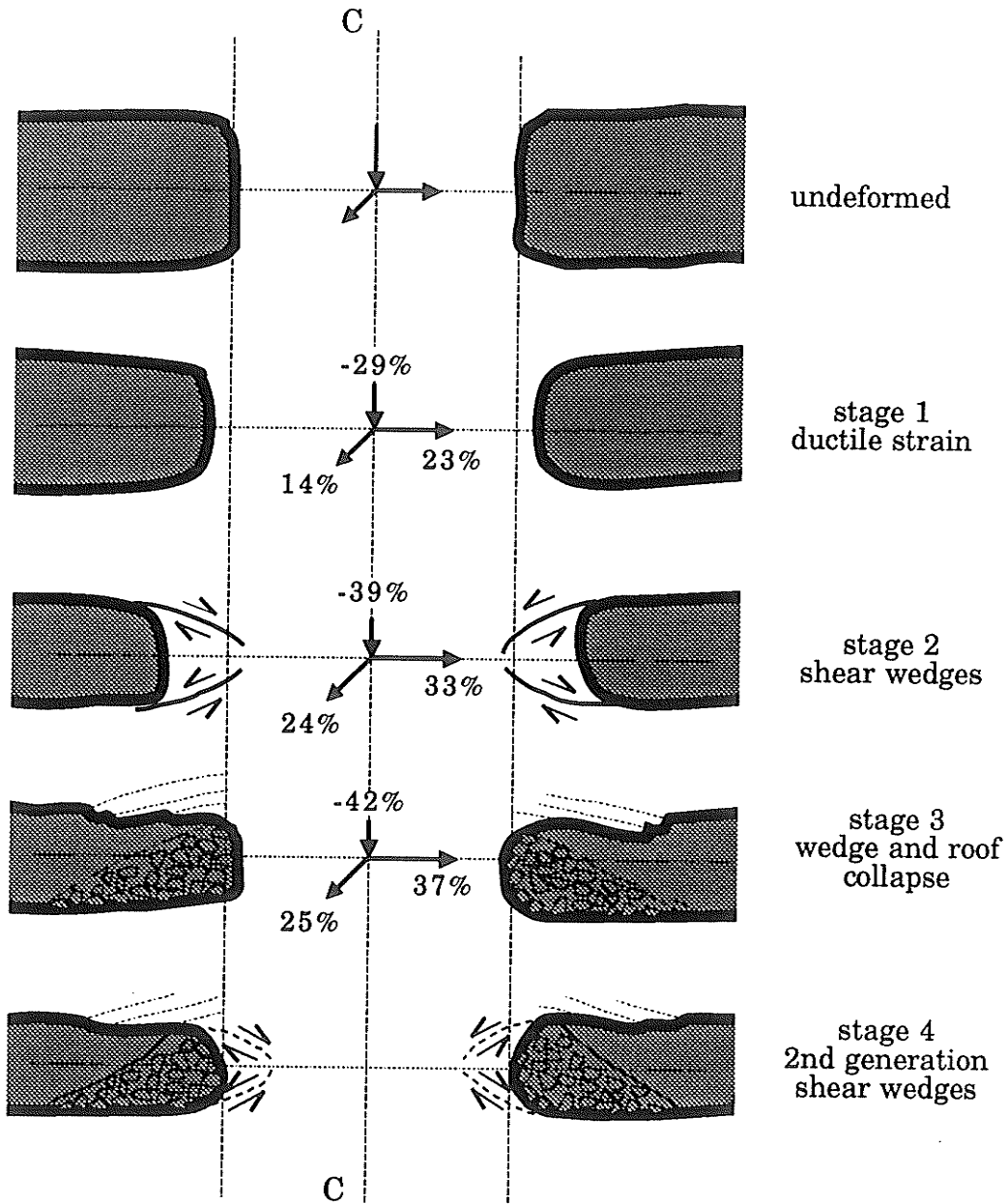


**Figure 8.22** Proposed model of progressive pillar deformation. C marks the centre line of the pillar and parallel vertical lines mark the position of the original pillar width. The principal strain values are based on shape changes in sylvite and represent interpretation of sylvite strain in the centre of the pillars.

corners. As the shear zones propagate diagonally into the pillar and meet, they form a shear wedge which becomes isolated from further significant flattening. Sylvite strain in the centre of the pillar during this stage appears to have been approximately 39% shortening in the subvertical direction, 33% subhorizontal elongation perpendicular to the original openings, and 24% horizontal elongation parallel to the original openings. During this stage, the pillar width increases due to bulk rock flattening and due to outward movement of the shear wedges into the adjacent rooms.

### **c) Stage 3**

As the shear wedges move progressively into adjacent rooms, they collapse or disintegrate. This stage may be accompanied by failure of the salt roof and by floor heave. The latter was not observed because the base of the pillar was not exposed, however, it is a reasonable supposition, given that 80% of room convergence in mining entries is derived from upward floor movement (Cominco Ltd. 1985). Although flattening continues to increase pillar width, the loss of the shear wedges may lead to a pillar width less than the original. Pillar 2 represents the beginning of this stage. The sylvite strain values in the centre of the pillar during this stage are estimated as 42% shortening in the subvertical direction, 37% subhorizontal elongation perpendicular to the original openings and 25% horizontal elongation parallel to the original openings.

### **d) Stage 4**

With further flattening of the pillar, a second generation of shear zones may

develop. The second generation shears may be initiated by diagonal cracks in the salt unit above the pillar due to collapse and bending of roof strata related to the earlier shear wedge fragmentation. The shear zones at the left end of Pillar 1, at both ends of Pillar 2 and at the left end of Pillar 3, may be examples of developing second generation shear zones. The pillar width at this stage may increase slightly over that in Stage 3, until the second generation shear wedges collapse.

### 8.9 Chapter Summary

1. Pillar deformation at the Vanscoy Mine over a period of 8 years has been shown to involve bulk rock flattening, the development of shear zones at pillar corners, the development of shear wedges at pillar margins, and the detachment of those shear wedges into adjacent rooms. Furthermore, these effects appear to be sequential and repetitive.
2. Bulk rock strain in pillars has been achieved through a combination of brittle deformation of halite, plastic deformation of sylvite and grain boundary sliding.
3. Deformational mechanisms in halite include fracturing and displacement and rotation of fragments. Sylvite deforms continuously through mechanisms yet to be determined.
4. The bulk rock strain has led to the development of a fabric anisotropy that can be detected by the centre-to-centre method or by the grain shape method. The fabric anisotropy ellipsoids determined by the two methods have similar orientations but different dimensional ratios.

5. Both types of ellipsoids indicate flattening according to the Flinn classification system. Shortening has occurred in the vertical to subvertical orientation, greatest elongation has taken place in the horizontal to subhorizontal direction normal to the original openings, and lesser elongation has taken place parallel to the original openings.
6. Neither type of fabric anisotropy ellipsoid is fully sensitive to strains produced by grain boundary sliding, consequently neither registers bulk rock strain. However, the shape ellipsoids are useful in tracking sylvite strain variations during progressive pillar failure.

## 9. NUMERICAL SIMULATION OF DEFORMATION AND FRACTURE IN POTASH YIELD PILLARS

### 9.1 Introduction

Due to complicated boundary conditions, loading histories, and inelastic and time-dependent deformational properties, rock behavior in the underground mining environment is usually analyzed numerically. In fact, as stated by Zienkiewicz (1992), "Computational mechanics is today the base on which most of the achievements of engineering and physics are built". Without numerical tools, the translation of complex mathematical theories that describe the mechanics of deformation into practical artifacts would be impossible. The first steps were taken early this century by the pioneering work of Richardson (1910), who introduced finite difference approximations. Subsequently, the escalation of the power of electronic digital computers marked a turning point and allowed the rapid development of various numerical approaches. With this development, the focus of attention in rock mechanics has shifted from laboratory and field measurements to computation. Traditional field and laboratory measurements and experiments on rock, especially in rock masses, are usually costly and difficult to perform. It follows that modelling, as an alternative form of experimentation, becomes an essential ingredient of both the science of rock mechanics and rock engineering design. A proper numerical modelling procedure would provide valuable information more economically and more reliably if "the modelling exercise is performed in the same way as one would perform a laboratory experiment" (Starfield and Cundall 1988).

Zienkiewicz (1992) summarized five apparently distinct approximation methodologies as: finite differences, finite elements, finite volumes, spectral methods and boundary solutions. Although each has its proponents and real and imaginary benefits, and each has its legitimate field of application, there is a common thread that runs through all the approximation procedures and the reason for choosing a method for a particular problem is often dictated by availability of computer software and personal preference. All the approximation procedures can be regarded as particular cases of the weighted residual (or generalized Galerkin) method (Zienkiewicz 1992).

In studying progressive deformation within yield pillars and around deep underground openings, numerical modelling techniques have been used extensively. Several approaches have been suggested by various authors. For example, Kripakov's analyses on the stability of coal yield pillars (Kripakov 1981); Kripakov and Melvin's discussion on rock failure around coal mines (Kripakov and Melvin 1983); and Park and Ash's studies on the stability of deep coal mines (Park and Ash 1985). In most of these works, the finite element method was used and non-linear behavior was simulated by gradually altering the elastic modulus of the yielding materials, i.e., using a *quasi-elastic* approach. Later studies, such as Dawson and Munson (1983), Yu et al. (1988), and Chen and Karmis (1988), incorporated viscoelastic and/or viscoplastic solutions. However, the application of numerical modelling with long term field and laboratory documentation as calibration is still sporadic.

In this chapter, a finite element program, **SIMEX** (Ayari 1991, 1992) is used to simulate potash yield pillar deformation and failure as described in Chapter 8. First, the

initiation and propagation of corner shear zones are modeled based on the theory of linear elastic fracture mechanics. Then, a viscoplastic approach is used to model progressive potash yield pillar deformation and failure processes, including the initiation and extension of corner ductile shear zones in terms of *strain localization bands* (or shear bands, Papanastasiou and Vardoulakis 1992). A brief introduction of the computer code, **SIMEX**, is given. The relevant concepts and formulae in linear elastic fracture mechanics (LEFM), elasto-plasticity, elasto-viscoplasticity, and strain localization are reviewed. Simulation procedures and results are presented. Finally, long-term pillar stability is discussed.

## 9.2 Introduction to **SIMEX** (Simulation of Mining EXcavation)

**SIMEX** is a user-friendly, menu-driven, finite element program developed by Dr. M.L. Ayari (1991, 1992). The program is written in NDP Fortran. It employs the PHAR LAP tools for extended memory management, uses the HALO graphics package for graphical displays, and runs on 386 or 486 IBM compatible personal computers. The program includes an elastic version and a viscoplastic version. In the elastic version of the program, a discrete crack propagation model is incorporated based on the theory of LEFM. With its remeshing ability, **SIMEX** can be used to nucleate and propagate fractures without exiting the modelling procedure. Later extensions to the elastic part of **SIMEX** include a new fracture and failure criterion, stress averaging, and local solutions (Yuan and Lajtai 1991). The viscoplastic part of **SIMEX**, in its present form, is a continuous model based on general elasto-viscoplastic theory (Ayari 1992). It incorporates

yield functions such as Von-Mises, Mohr-Coulomb, Drucker-Prager, Tresca, and a user-defined failure function. **SIMEX** can also model strain hardening/softening behavior by fitting a non-linear, experimental stress-strain curve with a piece-wise linear approximation. Although the viscoplastic version of **SIMEX** includes only a basic, continuous viscoplastic model, bands of highly localized strains often occur during progressive simulation, depending on the nature of the problem simulated, its boundary conditions, and mesh geometry (size and orientation). Such strain localization phenomenon is a result of progressive failure of ductile materials (Needleman and Tvergaard 1984; Papanastasiou and Vardoulakis 1992) and can be used as an indication of failure history and failure pattern.

### **9.3 Basic Concepts**

Most of the fracture related numerical models are based on the theory of linear elastic fracture mechanics. For elasto-plastic and elasto-viscoplastic problems, considerable discussion still exists on appropriate fracture criteria although some commonly accepted numerical solutions do exist, such as the J-integral approach (Owen and Fawkes 1983). The phenomenon of strain localization in progressively deformed viscoplastic materials is, probably, an alternative way of describing failure behavior. In this section, some basic concepts and formulae in linear elastic fracture mechanics, elasto-plasticity, elasto-viscoplasticity, and strain localization are briefly reviewed.

### 9.3.1 Basic concepts in Linear Elastic Fracture Mechanics (LEFM)

In linear elastic fracture mechanics, the stability of an existing fracture is characterized by *stress intensity factors* that are defined in 2D as:

$$\begin{Bmatrix} K_I \\ K_{II} \end{Bmatrix} = \lim_{r \rightarrow 0} \sqrt{2\pi r} \begin{Bmatrix} \sigma_{22} \\ \sigma_{12} \end{Bmatrix}_{\theta=0} \quad (9.1)$$

where  $\sigma_{ij}$  are the stresses near the crack tip, and  $K_I$ ,  $K_{II}$  are the stress intensity factors in mode I and mode II respectively (Figure 9.1).

In **SIMEX**,  $K_I$  and  $K_{II}$  are calculated using nodal displacements near the crack tip from a special quarter-point triangular crack-tip element (Barsoum 1978; Ingraffea 1983) (Figure 9.2):

$$\begin{Bmatrix} K_I \\ K_{II} \end{Bmatrix} = \begin{Bmatrix} \left(\frac{2G}{1+\kappa}\right) \sqrt{\frac{2\pi}{L}} [4(v_5-v_4)-(v_2-v_3)] \\ \left(\frac{2G}{1+\kappa}\right) \sqrt{\frac{2\pi}{L}} [4(u_5-u_4)-(u_2-u_3)] \end{Bmatrix} \quad (9.2)$$

where  $L$  is the radial length of the special crack tip element,  $u_i$  and  $v_i$  are the displacements in  $x$  and  $y$  directions at node  $i$  ( $i=2,3,4$  or  $5$ , as shown by the numbers in Figure 9.2),  $G$  is the shear modulus, and  $\kappa$  is a measure of Poisson's ratio ( $\nu$ ) and depends on the conditions of plane strain or plane stress:

$$\kappa = \begin{cases} 3-4\nu & \text{plane strain} \\ \frac{3-\nu}{1+\nu} & \text{plane stress} \end{cases}$$

Once the stress intensity factors ( $K_I$  and  $K_{II}$ ) are numerically computed and the

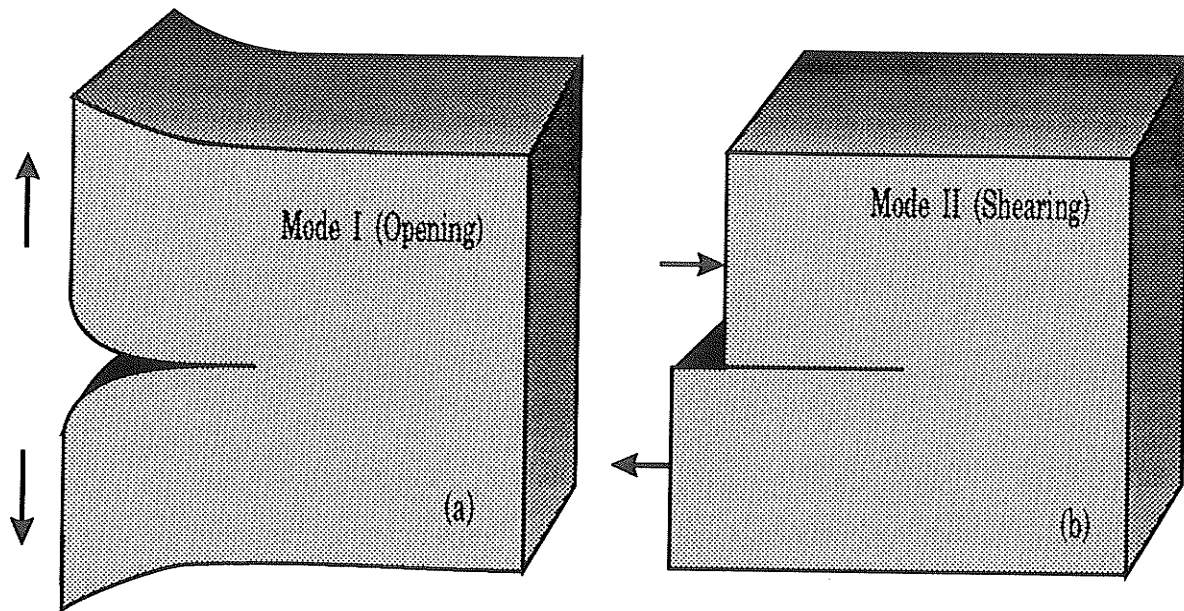


**Figure 9.1** Fundamental modes of fracture in 2D, (a) Mode I (Opening Mode), (b) Mode II (Shearing Mode).

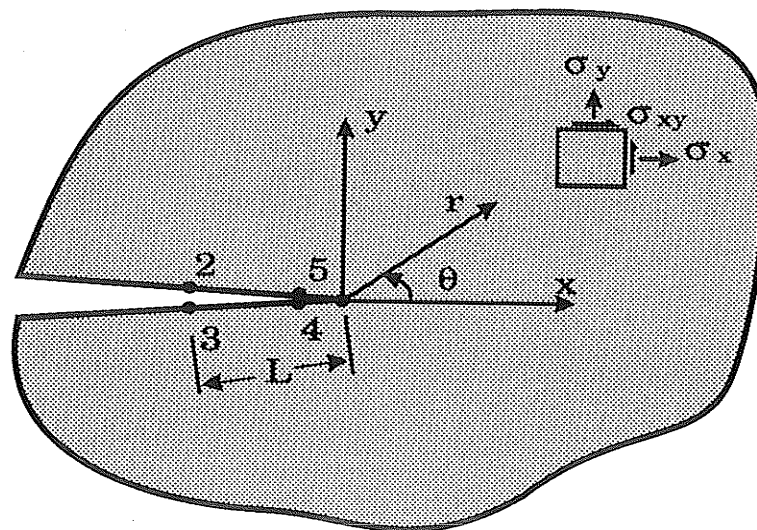


**Figure 9.2** Crack tip coordinates, stresses, and node numbers.

material fracture toughness ( $K_{Ic}$ ) is experimentally determined ( $K_{Ic} \approx 0.34$  MPa  $\sqrt{m}$  for potash, Carter et al. 1991a), fracture propagation criteria can be formulated encompassing these variables, which will determine (a) the angle of incipient crack propagation with respect to the crack axis, and (b) whether the stress intensity factors are in such a critical combination as to cause the crack to propagate.

In the case of mode I, fracture extension occurs when

$$K_I \geq K_{Ic} \quad (9.3)$$

and the crack will extend along its own direction.

For mixed mode fractures (combination of modes I and II), crack propagation criteria have not yet been well developed. There exist three major criteria for the mixed mode fractures: maximum circumferential tensile stress criterion (Erdogan and Sih 1963), maximum energy release rate criterion (Hussian et al. 1974), and minimum strain energy density criterion (Sih 1973). Among them, the maximum circumferential tensile stress criterion is most widely used. According to this criterion, the angle of crack propagation ( $\theta$ ) measured anti-clockwise from the crack direction (Figure 9.2) is:

$$\tan\theta = \frac{1}{4} \frac{K_I}{K_{II}} + \frac{1}{4} \left[ \left( \frac{K_I}{K_{II}} \right)^2 + 8 \right]^{1/2} \quad (9.4)$$

and crack propagates when the following combination of  $K_I$ ,  $K_{II}$  and  $K_{Ic}$  is reached:

$$\frac{K_I}{K_{II}} \cos^3\left(\frac{\theta}{2}\right) - \frac{3}{2} \frac{K_{II}}{K_{Ic}} \cos\left(\frac{\theta}{2}\right) - \sin\theta = 1 \quad (9.5)$$

In case of pure mode II ( $K_I = 0$ ), crack propagation occurs when  $K_{II} \geq 0.87K_{Ic}$  and the angle of crack propagation is  $70^\circ 32'$  to the initial axis of the crack according to Equations 9.4 and 9.5.

### 9.3.2 Basic concepts of elasto-plasticity

In practice, beyond a certain stress level, material behavior is inelastic. If time dependency is absent, this inelastic property is called *elasto-plasticity* and is represented by the rheological analogue of a spring and a slider in series as shown in Figure 9.3. The spring represents elastic behavior. The slider represents plastic behavior as it does not move unless the stress on it exceeds a threshold limit and it does not return to its original position after stress is removed. This rheological model suggests that total strains in the material are composed of elastic strains in the spring and plastic strains in the slider:

$$\boldsymbol{\varepsilon} = \boldsymbol{\varepsilon}^e + \boldsymbol{\varepsilon}^p \quad (9.6)$$

where  $\boldsymbol{\varepsilon} = [\varepsilon_x, \varepsilon_y, \varepsilon_z, \gamma_{xy}, \gamma_{yz}, \gamma_{zx}]^T$ , the vector of strain components.  $T$  represents the transpose and superscripts  $e$  and  $p$  denote elastic and plastic components, respectively. The elastic component of strain is related to stress by

$$\sigma_{ij} = D_{ijkl}^e \varepsilon_{kl}^e \quad (9.7)$$

where  $D_{ijkl}^e$  is the elastic matrix defined by Young's modulus and Poisson's ratio. The initiation of the plastic strain component is defined by a *yield criterion* in the form of

$$F(\sigma_{ij}) = 0 \quad (9.8)$$

Some of the commonly utilized yield criteria are Tresca, Von-Mises, Huber-Hencky, Mohr-Coulomb, Drucker-Prager, and Hoek-Brown.

The plastic strain is related to stress by a *flow rule*:

$$d\boldsymbol{\varepsilon}^p = d\lambda \frac{\partial Q(\boldsymbol{\sigma})}{\partial \boldsymbol{\sigma}} \quad (9.9)$$

where  $d\boldsymbol{\varepsilon}_p$  is the vector of plastic strain increments,  $d\lambda$  is a positive scalar and  $Q(\boldsymbol{\sigma}) = \text{constant}$  is the *plastic potential function* that defines the direction of the plastic

strain increment. When  $Q \equiv F$ , the plastic strain increment vector is normal to the yield surface and the flow rule is called an *associated* flow rule. Otherwise it is called a *non-associated* flow rule. The post-yield behavior is defined by the dependence of the yield surface ( $F$ ) on the accumulated plastic strain ( $\epsilon^p$ , referred to as *strain hardening*), or plastic work done ( $W^p$ , referred to as *work hardening*) and is usually described by a function of the yield function ( $F$ ):

$$\dot{\phi} = \dot{\phi}(F) \begin{cases} > 0 & \text{when } F = 0 \text{ plastic strain change} \\ = 0 & \text{when } F < 0 \text{ no plastic strain change} \end{cases} \quad (9.10)$$

$F=0$  represents a closed surface (*yield surface*) in stress space. If the yield surface expands as the accumulated plastic strain increases, the material behavior is called *hardening*; if the yield surface shrinks as the accumulated strain increases, the behavior is called *softening*; and if the yield surface remains unchanged during plastic deformation, it is called *perfectly plastic*.  $F < 0$  corresponds to elastic deformation and  $F > 0$  has no meaning in elasto-plasticity.

### 9.3.3 Basic concepts of elasto-viscoplasticity

The theory of elasto-plasticity does not consider time effect. In the theory of elasto-viscoplasticity, plastic strains are called viscoplastic strains and are assumed to accrue with time. The rheological analogue of an elasto-viscoplastic material consists of a spring in series with a viscoplastic unit formed by a slider and a viscous dashpot in parallel (Figure 9.4). When the slider fails, the plastic strains will take place with time as the viscous dashpot does not respond instantaneously. The concepts of yield function,

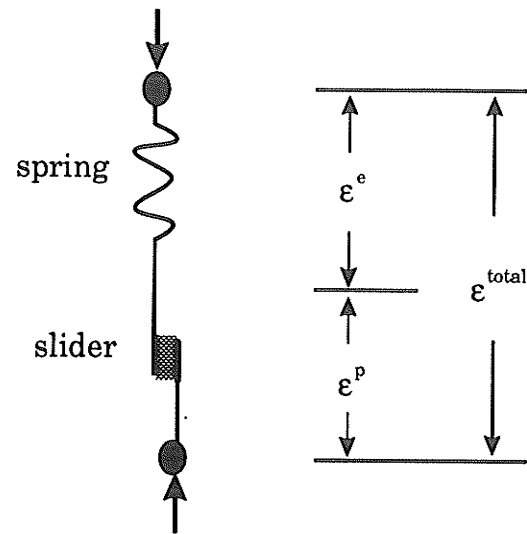


Figure 9.3 Rheological analogue of elasto-plastic material.

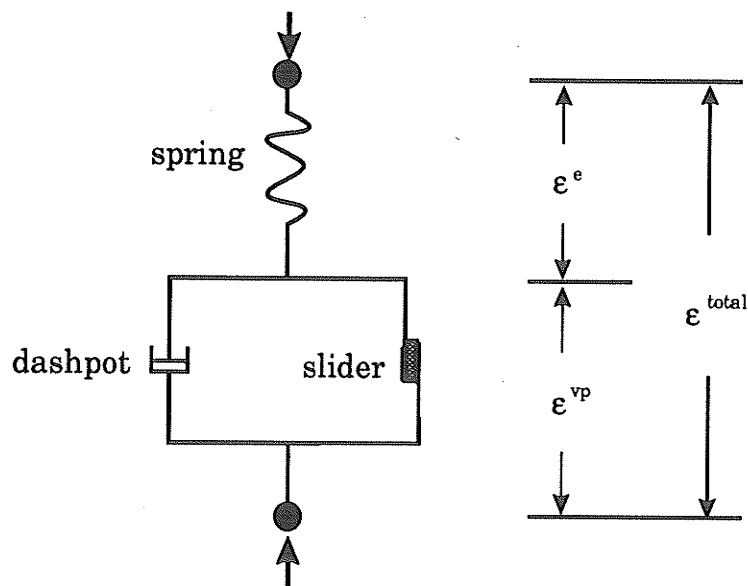


Figure 9.4 Rheological analogue of elasto-viscoplastic material.

flow rule and hardening/softening developed for the theory of elasto-plasticity are valid for the theory of elasto-viscoplasticity as well, except that the plastic strain is time dependent and is described as the plastic strain rate with respect to the true time as

$$\dot{\epsilon}^{vp} = \gamma \langle \phi(F) \rangle \frac{\partial Q}{\partial \sigma} \quad (9.11)$$

where  $\gamma$  is called the *fluidity parameter*. It is a material constant involving units of 1/time and is usually obtained from experimental tests.  $\phi(F)$  is defined as

$$\phi = \phi(F) \begin{cases} > 0 & \text{when } F > 0 & \text{plastic strain change} \\ \leq 0 & \text{when } F \leq 0 & \text{no plastic strain} \end{cases} \quad (9.12)$$

In elasto-viscoplasticity,  $F \leq 0$  represents elastic deformation and  $F > 0$  is admissible and corresponds to time dependent plastic strain change.

**SIMEX** follows an associated flow rule:

$$\dot{\epsilon}_{vp} = \gamma \langle \phi(F) \rangle \frac{\partial F}{\partial \sigma} \quad (9.13)$$

where  $\phi(F)$  can be either an exponential law

$$\phi(F) = \exp\left(M\left(\frac{F-F_0}{F_0}\right)\right) - 1 \quad (9.14)$$

or a power law:

$$\phi(F) = \left(\frac{F-F_0}{F_0}\right)^N \quad (9.15)$$

where  $M$  and  $N$  are constants that should be determined from laboratory or field testing results.  $F_0$  is the initial failure surface that indicates the initiation of plastic deformation. Post-yield hardening and/or softening behavior is described through a hardening parameter,  $H^n$ , defined by:

$$H^n = \left( \frac{\partial \dot{\epsilon}_{vp}}{\partial \sigma} \right)^n \quad (9.16)$$

where  $n$  represents the number of the current time step. SIMEX incorporates  $H^n$  by inputting an experimental stress-strain curve consisting of a set of linear segments. Since the number of such linear segments is unlimited as long as the computer memory is sufficient, such approximation could be accurate. In this study, a complete potash stress-strain curve shown in Figure 9.5 is used to calibrate the post-yield hardening and softening behavior.

### 9.3.4 Strain localization and instability

A phenomenon that frequently accompanies large plastic deformations is the concentration of shear strain into one or more narrow bands. This process is called *strain*

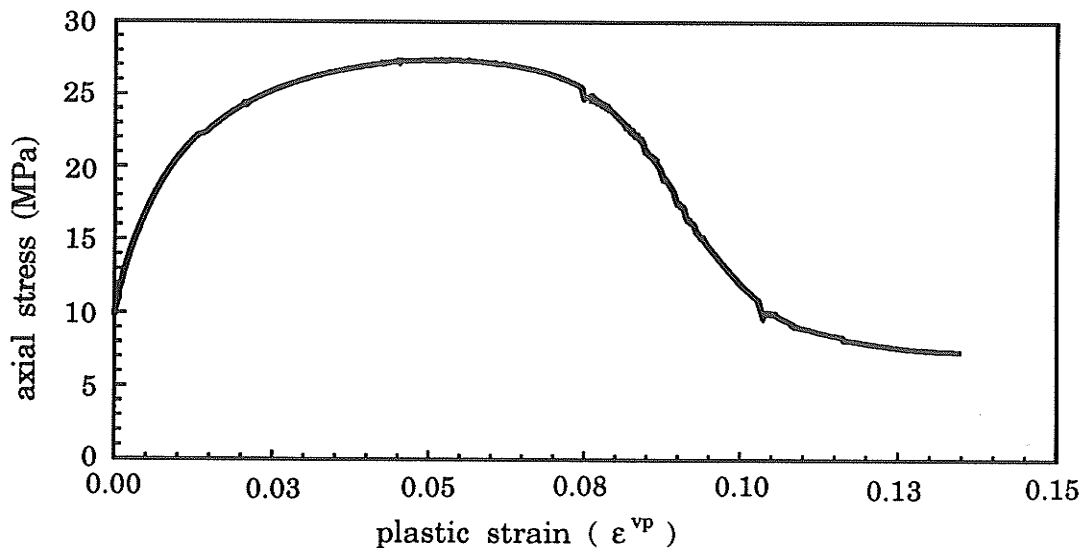


**Figure 9.5** Axial stress-axial plastic strain curve of Saskatchewan potash for calibrating post yield hardening and softening behavior. It is from a conventional triaxial compression test with 0.5 MPa confining pressure and a strain rate of  $1.75 \mu\epsilon \cdot s^{-1}$ . The specimen was cylindrical with diameter of 5 cm and height of 10 cm (after Duncan 1990).

*localization*. Although the physical mechanisms triggering such localization vary widely, the localized strains in shear bands often precipitate shear fractures and lead to instability. In other circumstances, shear bands do not lead to fractures, but localized shearing becomes an important mechanism for subsequent plastic deformation. Hence, shear bands have a dual significance as a precursor to fracture and as a mechanism of large plastic strain. Consequently, numerous efforts have been made to study localization phenomena during the last two decades. Major theoretical contributions that enhanced the understanding of shear bands are due to the theory of *equilibrium bifurcation*, following the work of Thomas (1961), Hill (1962), Mandel (1966), Rudnicki and Rice (1975), Rice (1976), Vardoulakis et al. (1978), Vardoulakis (1980, 1981, 1984), and Vermeer (1982). The experiments by Vardoulakis et al. (1978) and Arthur et al. (1977) provided detailed information about the inclination angle of shear bands in biaxial testing devices.

For infinite-domain problems, analytical expressions for the critical hardening modulus and the orientation of localization bands at bifurcation have been derived. A comprehensive review can be found in Molenkamp (1985).

For more complicated boundary problems and post-localization studies, the analyses of shear bands can only be done numerically. In this case, a few approaches can be identified from the available publications. Needleman and Tvergaard (1984) triggered localized necking and shear banding through initial imperfections in the form of strategically placed weak elements. Prevost (1984), Griffiths (1981), Bardet and Mortazavi (1987), Shuttle and Smith (1988) and Cundall (1989) followed the same approach to trigger localization in soil plasticity problems. In the study of Ortiz et al.

(1986), the onset of localization was detected by the failure of Mandel's material stability criterion (existence of zero eigenvalues of the acoustic tensor) carried out at the element level; the element interpolation is extended by adding suitably defined base functions that reproduce the localized deformational modes. De Borst (1988) analyzed the formation of shear-bands in materials obeying a non-associated flow rule by implementing eigenvalue analysis of the global stiffness matrix to determine the load at which bifurcations are possible. Papanastasiou and Vardoulakis (1992) achieved robust post-localization computations by introducing internal length (grain size) in a strain-softening material model and analyzed progressive localization in relation to borehole stability.

Even without any special treatment, as an objective phenomenon of large plastic deformation observed in many laboratory tests and geological processes, shear bands occur naturally in many strain hardening/softening related numerical simulations. However in numerical modelling, their formation and development are influenced to a large extent by the artificial conditions imposed by the numerical grids - both the orientation and the element size.

In many circumstances, shear strains are so concentrated that they develop into true discontinuities or fractures. Therefore, shear band theory is also an alternative way of studying fracture mechanics in elasto-plastic or elasto-viscoplastic problems, where the theory of linear elastic fracture mechanics can hardly be applied.

#### **9.4 LEFM Simulation of Corner Shear Zones**

Finite element analyses of initiation and propagation of corner shear zones have

been carried out with the elastic version of SIMEX based on the general assumptions of the Linear Elastic Fracture Mechanics (LEFM). However, the direction of fracture propagation predicted by LEFM is erroneous in a compression dominated stress field. Consequently, the assumption that fracture propagates along the direction of the maximum compressive stress was adopted (Carter 1992*b*).

Since fracture intensity factors only provide a critical value for fracture propagation from existing flaws, a criterion that predicts fracture initiation in a continuous medium is required before applying the theory of LEFM. In this study, the Mohr-Coulomb yield criterion is adapted to predict fracture initiation ( $c=10$  MPa and  $\phi=15^\circ$ ) and then the theory of LEFM is followed to propagate fractures.

In SIMEX, the process of nucleating and propagating a crack is accomplished by a build-in fracture propagator that can be invoked by simply clicking the mouse on the pull-down menu. A crack path must first be traced along element boundaries and crack tips must be specified. Mesh at the crack tips can then be refined and singularity can be imposed by changing crack tip elements to special quarter-point triangular elements. The new mesh can then be reanalyzed. Stress intensity factors at the existing crack tips and stress state at various nodes can be viewed to check the possibility of further cracking at the current load, or otherwise, the load can be increased to produce new cracks or to propagate the existing cracks.

Figure 9.6 shows the mesh geometry, supports and loading conditions. One quarter of a  $5\text{m}\times 5\text{m}$  opening was assumed to be excavated in an isotropic elastic potash medium with Young's modulus  $E=20$  GPa, Poisson's ratio  $\nu=0.32$ , and fracture

toughness  $K_{Ic}=0.34$  MPa $\sqrt{m}$ . The corner fracture simulated was, therefore, in an abutment pillar. Roller supports were placed along the axes of symmetry and on the right side, far-field boundary. A uniformly distributed edge load was gradually applied on the top boundary to nucleate and propagate cracks. As load increased, a stress concentration occurred at the pillar corner (Figure 9.7). When the load increased to 16 MPa, combination of the maximum and minimum principal stresses reached the Mohr-Coulomb yield criterion at the pillar corner ( $\sigma_1=56.56$  MPa,  $\sigma_2=11.84$  MPa) with the maximum compressive stress oriented at 120 degrees from the horizontal direction. Consequently, a corner crack was nucleated from the corner along this direction down into the pillar based on the field observations (Figure 9.8). The mesh was refined at the crack tip and singularity was imposed. Under the same load, the crack propagated in mode II ( $K_I=0$ ,  $K_{II}=15.5$ ), indicating a shear effect as shown by the arrows along the crack path in Figure 9.8. The corner fracture continued to propagate as the load increased. At a load of 25 MPa, the corner fracture almost extended to the middle height of the pillar (Figure 9.9). A zone on the pillar edge was isolated by the fracture and stresses in this area were relieved (Figure 9.10). By symmetry, a similar crack also initiated at the lower corner of the pillar and propagated upward into the pillar. When the roof corner fracture and the floor corner fracture met, a shear wedge formed that was isolated from further deformation, similar to the *shear wedge* or *Cherry Stone* described in Chapter 8.

Although the above described simulation reproduced the initiation and propagation of corner shear zones, various assumptions in linear elastic fracture mechanics do not describe the mechanical behavior of potash. First of all, potash behaves in a highly non-

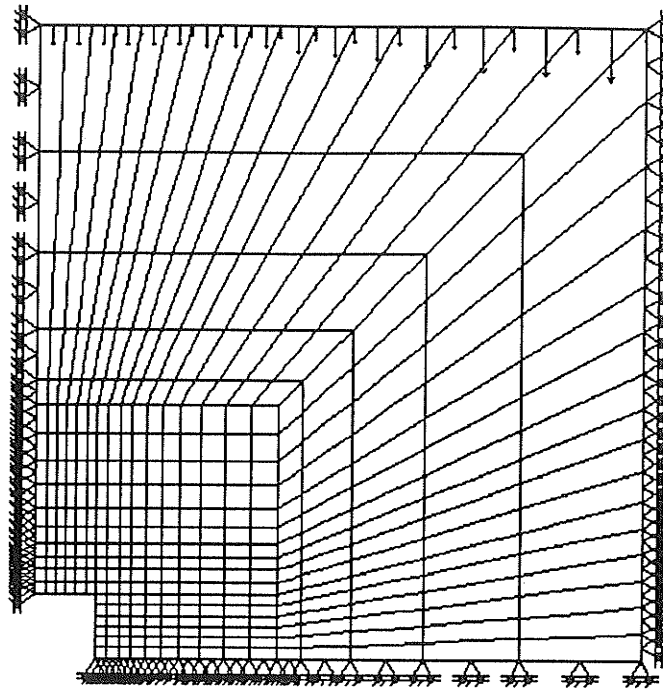


**Figure 9.6** Finite element mesh geometry, supports and loading conditions of pillar model for simulating corner shear zones based on the theory of linear elastic fracture mechanics. Load was applied as distributed edge load shown by the arrows at the top.

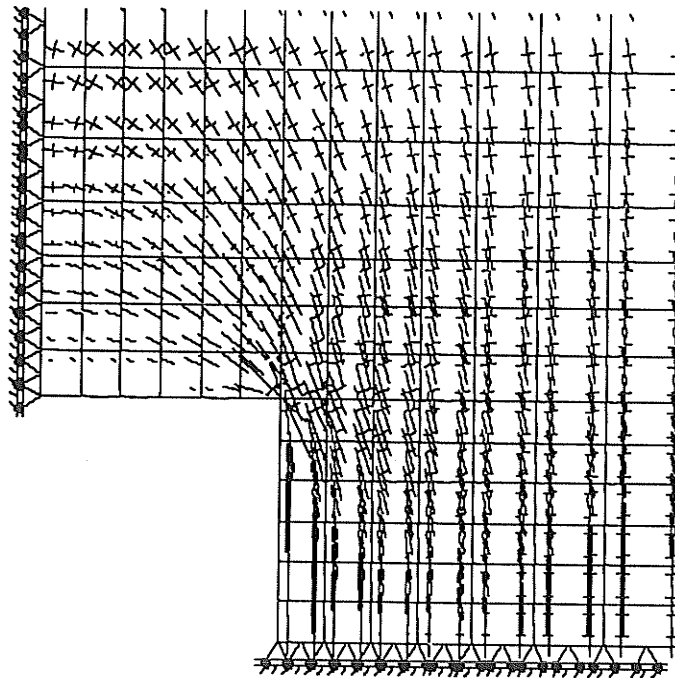


**Figure 9.7** Principal stress distribution showing stress concentration at room corner.

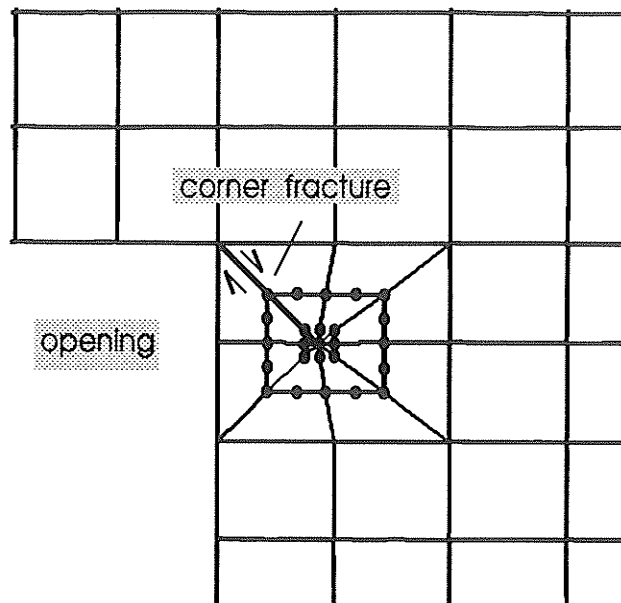


**Figure 9.8** Generation of corner diagonal crack with refined mesh and imposed singularity elements (special quarter point triangular elements, their nodes are shown by black dots).

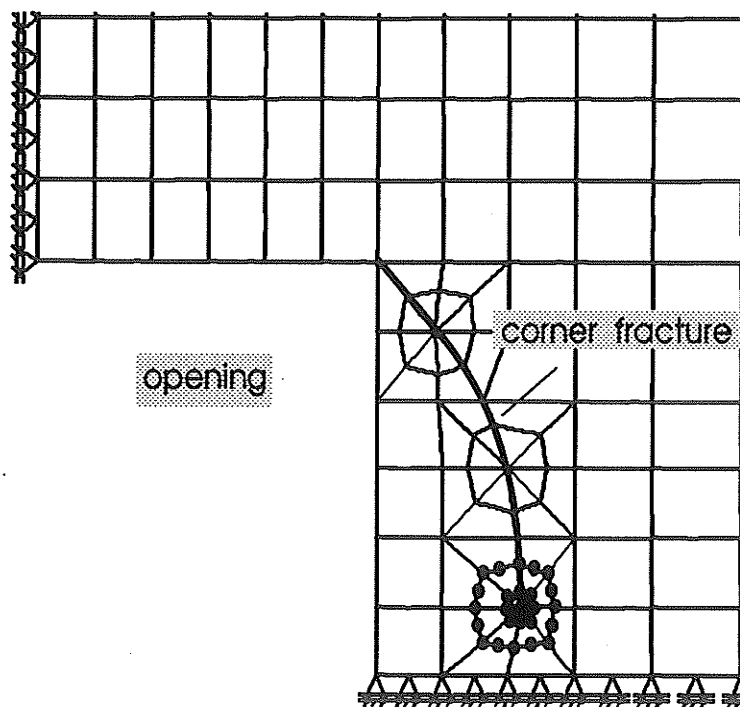


**Figure 9.9** At a load of 25 MPa, the corner fracture extended to the middle height of the pillar.

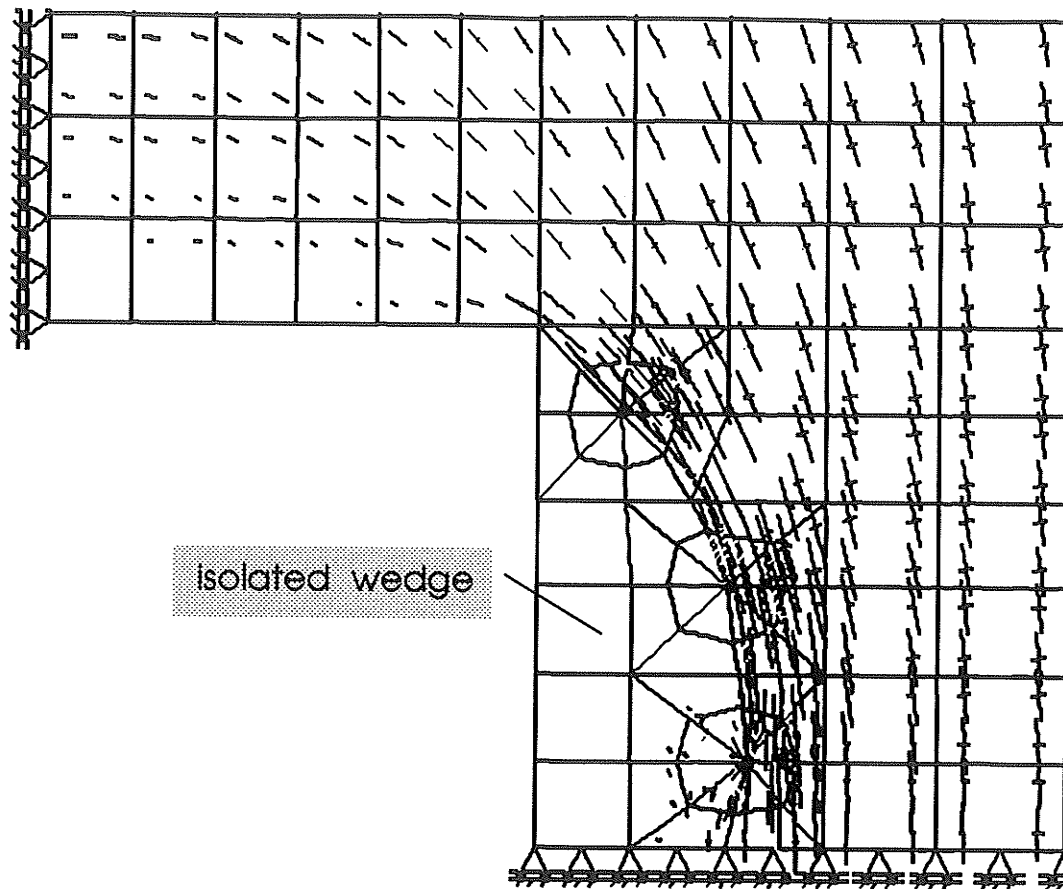


**Figure 9.10** Principal stress distribution after corner diagonal crack extended to the middle height of the pillar. A zone was isolated by the corner fracture and stresses in this isolated area were relieved.

linear and inelastic way that cannot be described by linear elastic theory. Secondly, shear zones at pillar corners show considerable ductile effects and appear as a complex zone of ductile strain, which cannot be described by a simple mathematical fracture. Finally, corner ductile shear zones are a consequence of progressive deformation of the potash yield pillar and their formation, in turn, affects the subsequent pillar deformation and stability. This process cannot be considered using elastic analysis. Therefore, in the following sections, pillar behavior is modeled based on viscoplastic theory.

### 9.5 Viscoplastic Modelling Procedure with SIMEX

A simple conceptual yield pillar model was constructed based on the three-entry mining system of the parallel room mining technique shown in Figure 3.5. The model was analyzed with the viscoplastic version of SIMEX. The opening and pillar dimensions were selected according to the opening geometry at the Cominco Mine (Figure 8.1). Figure 9.11 shows the finite element model configuration, including dimensions, supports and loading conditions. Plane strain was assumed. The model was simplified to include only two materials. The overlying and underlying strata were assumed to be a weak, elastic material (A in Figure 9.11) with Young's modulus  $E_1=30$  MPa and Poisson's ratio  $\nu_1=0.3$ . The potash ore zone was modeled as a weaker, viscoplastic layer that obeyed the Mohr-Coulomb failure criterion, with a Young's modulus  $E_2=20$  MPa, Poisson's ratio  $\nu_2=0.32$ , cohesion  $c=2$  MPa, angle of internal friction  $\phi=15^\circ$  and a fluidity parameter  $\gamma=5.5 \times 10^{-2}$ . These parameters were chosen on the basis of previously published data and experimental results from earlier Chapters in this thesis. The hardening parameter was calibrated according to the experimental axial stress-axial plastic strain curve shown in Figure 9.5. The initial time increment,  $\Delta t_0$ , was 10 days. Only half of the 3-entry model was analyzed due to symmetry. Roller supports were used along the symmetric axis and on the bottom far-boundary. A uniformly distributed edge load (25 MPa) was applied to the top boundary and to the right-hand side, far-boundary, placing the opening panel in a hydrostatic stress state similar to the *in situ* stress state in Saskatchewan potash mines.

Generation of the finite element mesh in SIMEX is achieved by using a few

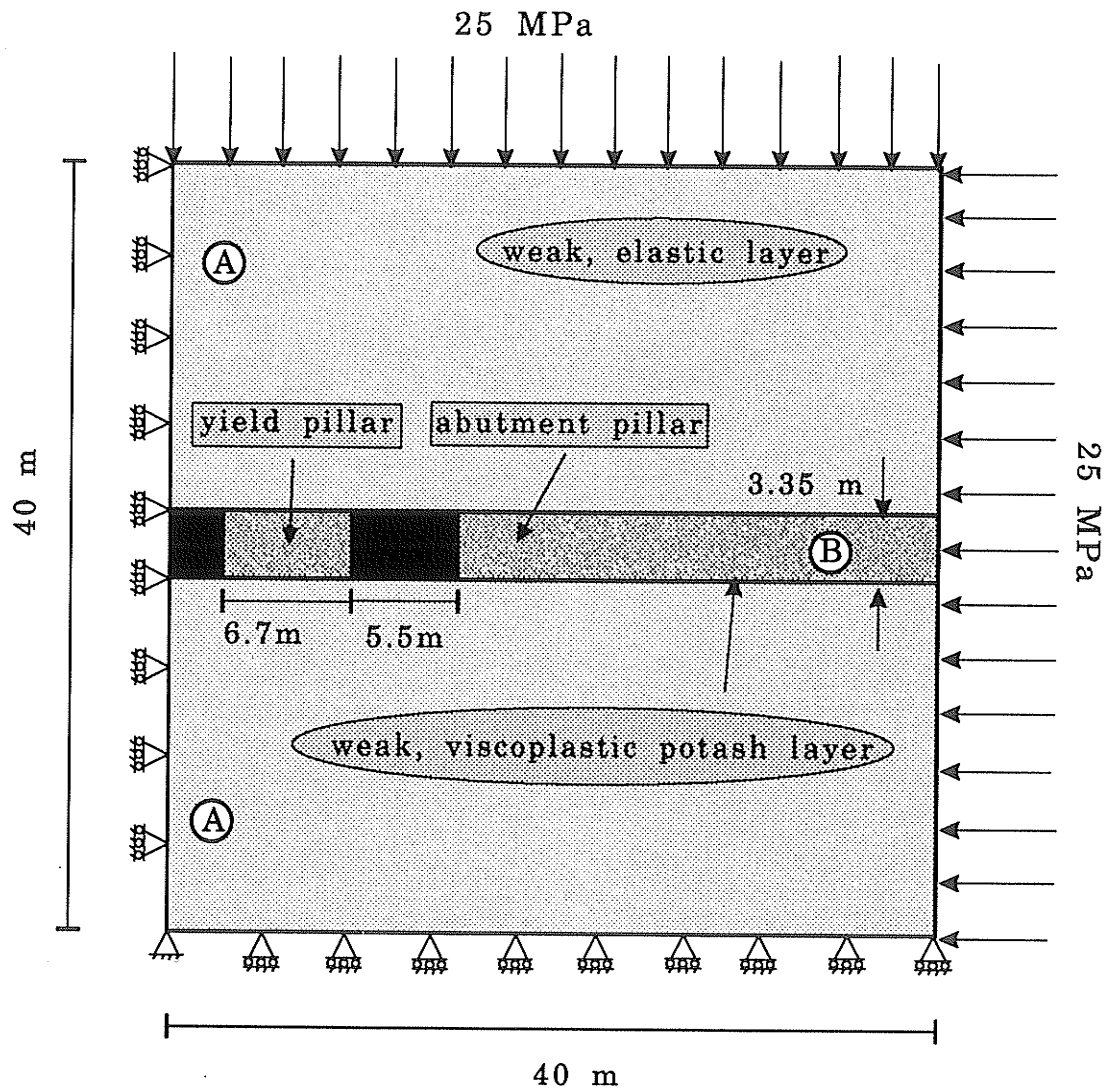


**Figure 9.11** Finite element model configuration for simulating viscoplastic pillar deformation and fracturing, including dimensions, supports and loading conditions. (A) Weak, elastic layer representing overlying and underlying strata. (B) Weak, viscoplastic potash layer.

super-elements. Once the element mesh is generated, the required material parameters, yield surfaces, post-yield characteristics, solving algorithms and loading curves can then be inputted. Details of these steps are described by Ayari (1992).

Excavation of openings or removal of failed elements during analysis is a simple process with **SIMEX**, using its mouse-controlled excavation feature. The code also allows a fully user-controlled analyzing process. Output results can be checked at any time during the analysis. Opening geometry can then be adjusted accordingly and analysis can continue. In this study, each time incremental step is defined as 10 days. However, due to the complex interaction between viscous and gradual plastic deformation and the lack of time related measurements for calibrations, the time given in days in the following presentation should be considered as a relative or reference time only. Another limitation of this simplified finite element model is the assumption that the roof and floor materials are elastic. The effects of plastic roof and floor will be discussed later.

## **9.6 Results of Viscoplastic Simulation**

The analysis started by performing an initial step prior to excavation to achieve an *in situ* stress state. Openings were then excavated. Figure 9.12 shows the finite element mesh of the yield pillar, abutment pillar and surrounding rocks.

### **9.6.1 Fracture pattern**

Plastic strain occurred immediately after room excavation, initiating at room corners and extending into both yield pillar and abutment (Figure 9.13). 60 days after the

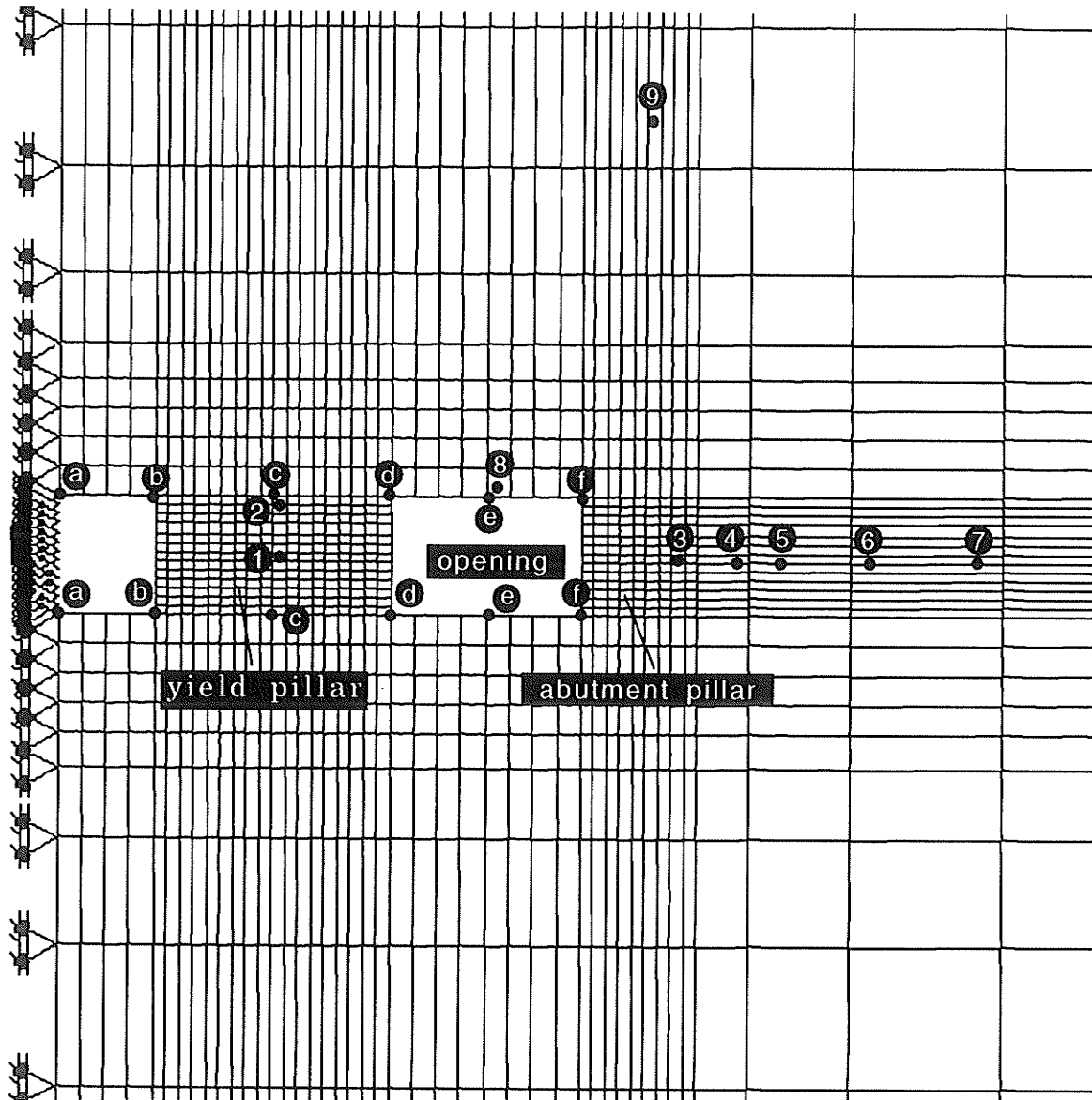


**Figure 9.12** Finite element mesh showing opening, yield pillar, abutment pillar and surrounding strata. Numbers and letters show the locations of stress and convergence histories in Figures 9.20 and 9.26, respectively.

excavation, the entire pillar yielded and the area of plastic deformation extended further into the abutment. Plastic strain did not uniformly distribute, but localized along diagonal directions near pillar edges (Figure 9.14), similar to the fracture pattern observed from field mapping (corner-ductile shear zones) in Chapter 8. As strain localization bands (or shear bands) developed from the roof and floor corners extended towards each other, a wedge of rock formed in which stresses were relieved, particularly in a zone adjacent to the strain localization bands (Figure 9.15), signifying complete failure at these locations. Besides strain localization zones along diagonal directions that symbolize corner ductile shear zones, zones of highly localized plastic strain also occurred at pillar edges in the vertical direction, parallel to the opening walls. As tensile cracks are usually observed *in situ* parallel to opening walls, the nature of failure in these areas could be similar to the tensile cracking or buckling in uniaxial tests. Once formed, the cracked material in these areas would fall into the openings and should not contribute to further ductile pillar deformation. Diagonal strain localization bands isolated shear wedges mechanically from further ductile deformation and physically from the rest of the pillar. As pillar deformation continued and the lateral displacement towards the openings increased, the isolated wedges could detach from the pillar and be squeezed into the openings. Therefore the isolated wedges on both sides of the yield pillar and on the abutment were removed after 60 days and the analysis continued. Figure 9.16 shows the plastic strain distribution 70 days after room excavation. Strain localization occurred near the collapsed opening walls in both the yield pillar and abutment, as well as at the top and bottom of the yield pillar. The newly isolated wedges on both sides of the yield pillar and at the abutment

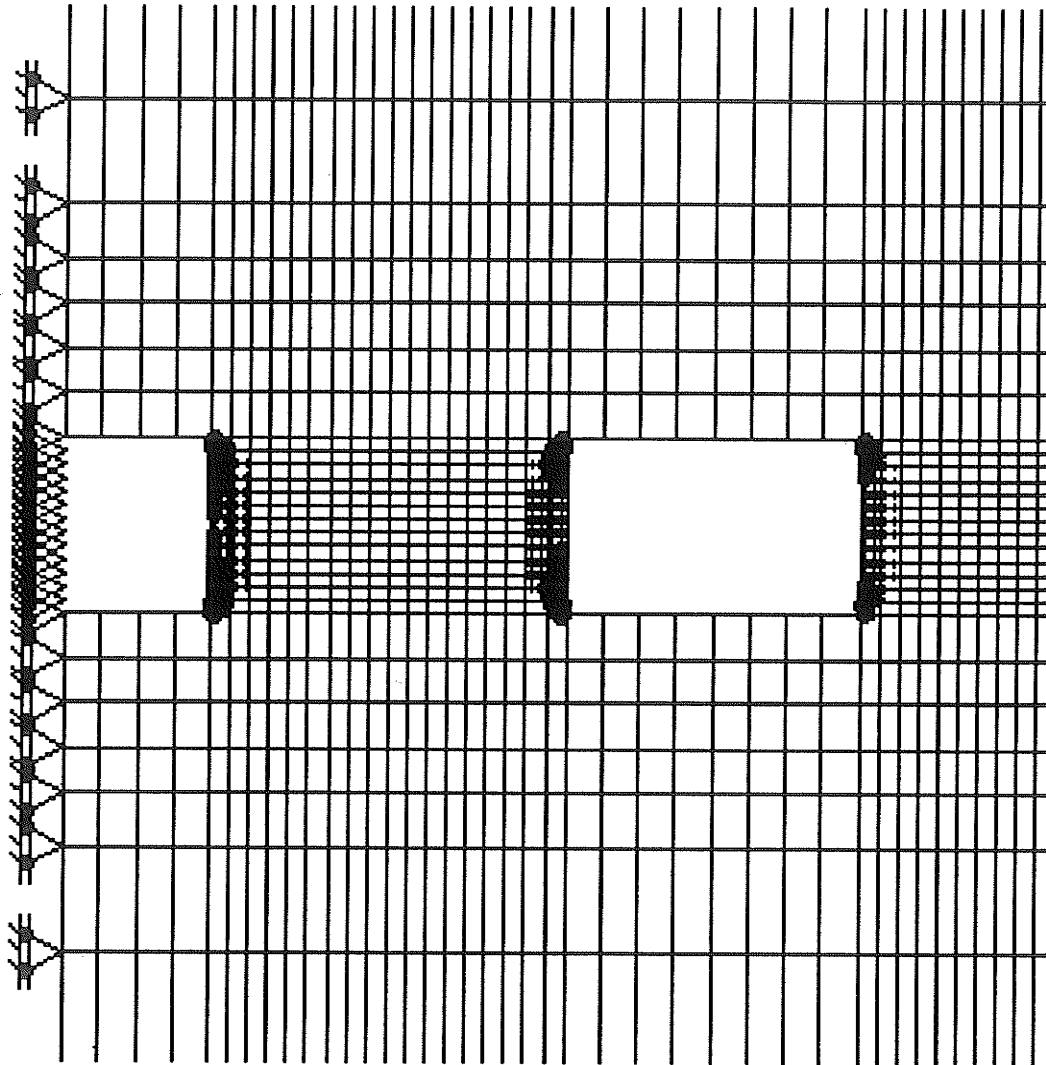


**Figure 9.13** Plastic strain distribution immediately after room excavation, signifying the initiation of corner ductile shear zones. The size of black dots is proportional to the magnitude of plastic strain at the Gauss points.

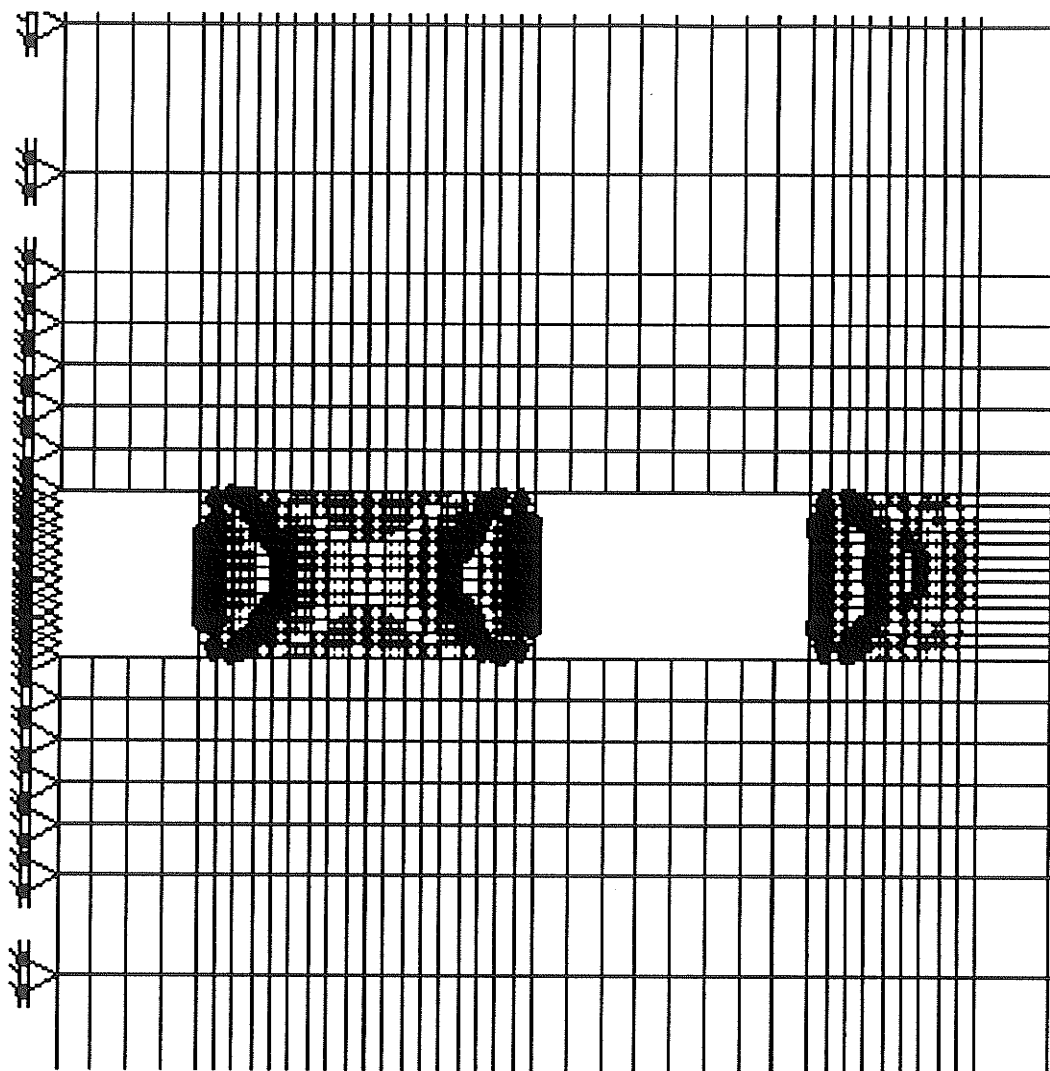


**Figure 9.14** Localizations of plastic strain along diagonal directions at pillar edges 60 days after room excavation, symbolizing the failure pattern of corner ductile shear zones observed from field observations in Chapter 8.

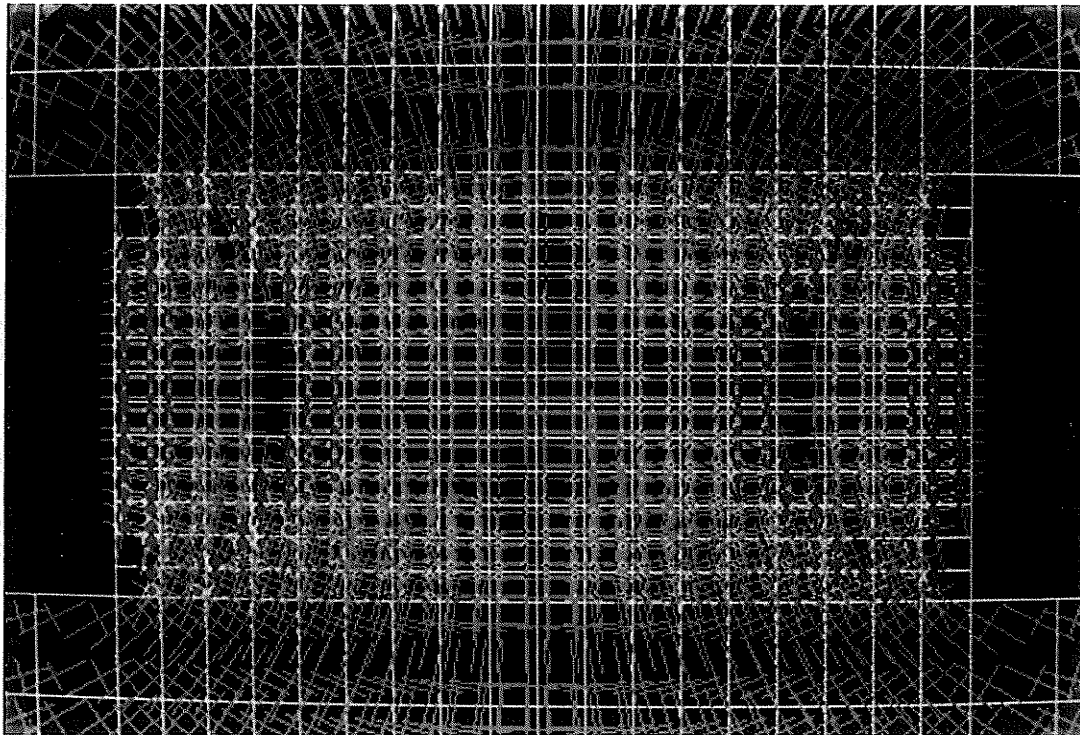


**Figure 9.15** Principal stress distribution (green lines) in the yield pillar and accumulated plastic strain (red dots).

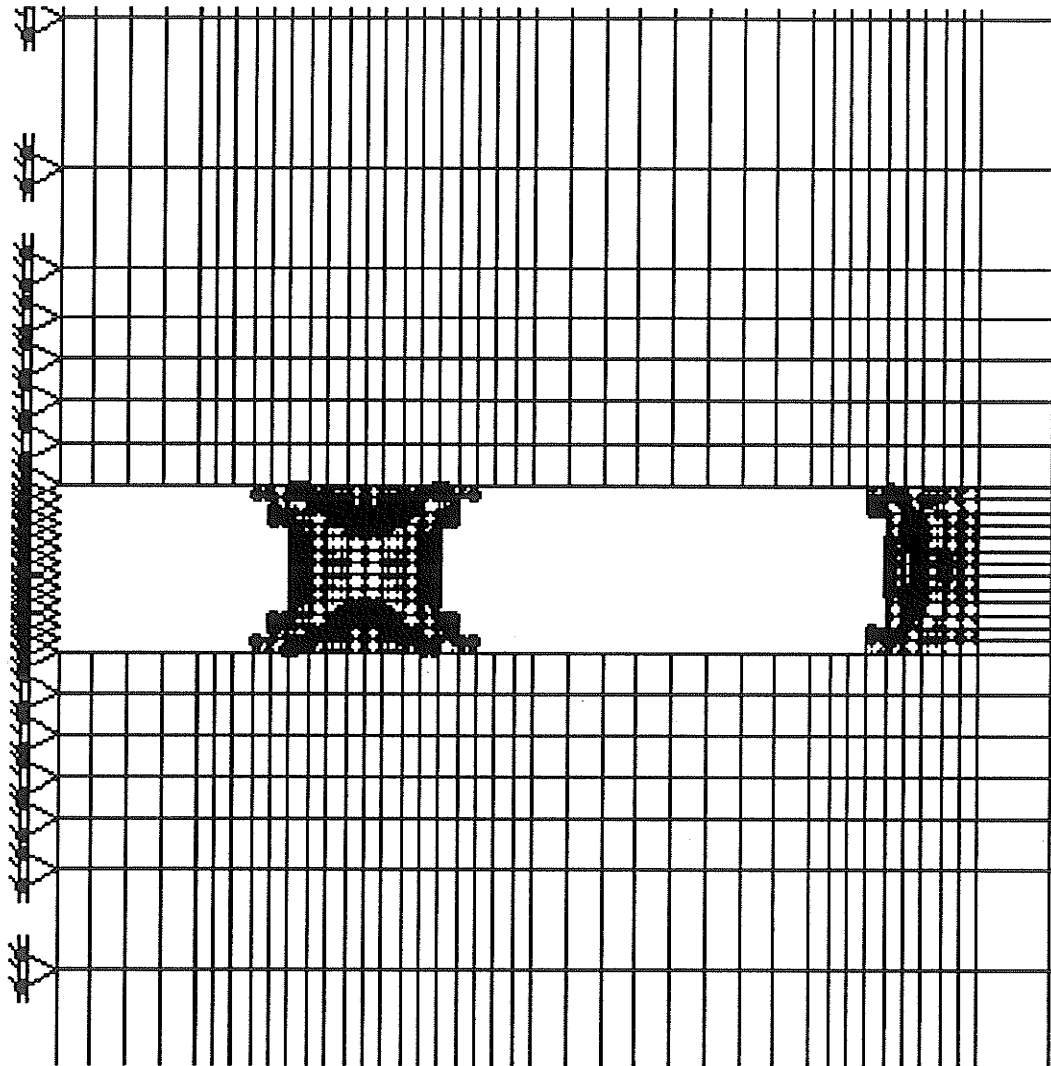


**Figure 9.16** Second generation of plastic strain localization (70 days after room excavation).

pillar were removed after 90 days. Continued analysis after this second removal of the detached blocks did not induce further strain localization in the remaining yield pillar, although a third generation localization zone was induced in the abutment (Figure 9.17). In the yield pillar, the localization bands at the top and bottom were enhanced as pillar deformation increased. The pillar was relatively stable although deformation was increasing. The fracture or strain localization pattern in the yield pillar did not change any further with time. The yield pillar functioned as a stable, *soft-support* through out the rest of the analysis. However, the process of localization and formation of isolated wedges might continue in the abutment. To study this process, a finer mesh and larger model would need to be set up and analyzed.

### 9.6.2 Stress distribution

Figures 9.18 and 9.19 show the variation of vertical stress ( $\sigma_y$ ) along the central height of the potash zone. Immediately after room excavation and before formation of apparent strain localization bands (Figure 9.18a), peak stresses were located at the boundaries of the openings and stresses gradually reduced to the *in situ* stress in the abutments away from the openings. As deformation increased (30 days after excavation, Figure 9.18b), stresses in the yield pillars increased and the locations of the peak stresses gradually moved into the pillars due to yield of material at pillar edges. After 60 days (Figure 9.18c), the two isolated pillars yielded and exhibited a single stress peak at their centres; stresses dropped considerably near the locations of strain localized bands due to stress redistribution (Figure 9.15). In the abutments, the locations of peak stresses

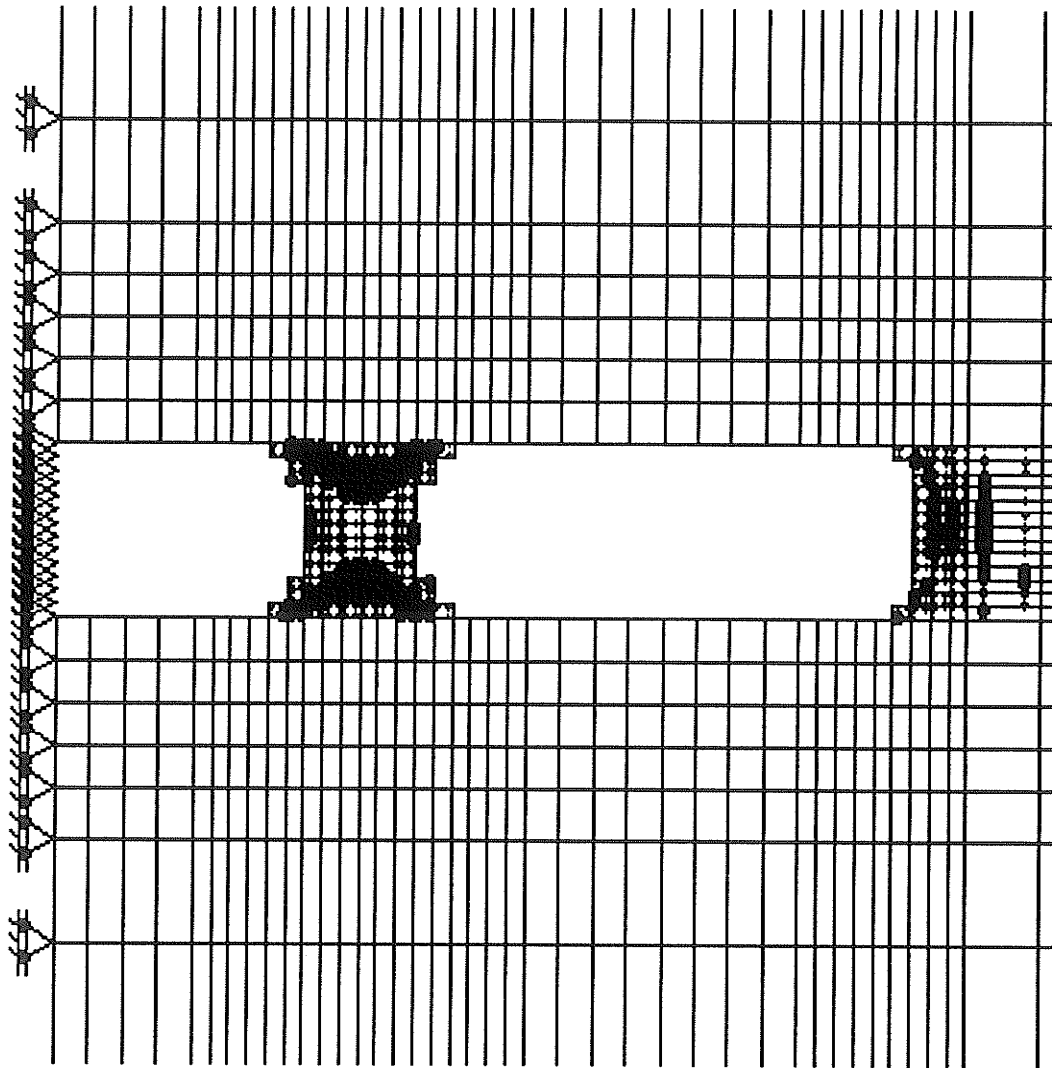


**Figure 9.17** Third generation of plastic strain localization. Fracture pattern appears to be stable in the yield pillar (110 days after initial room excavation).

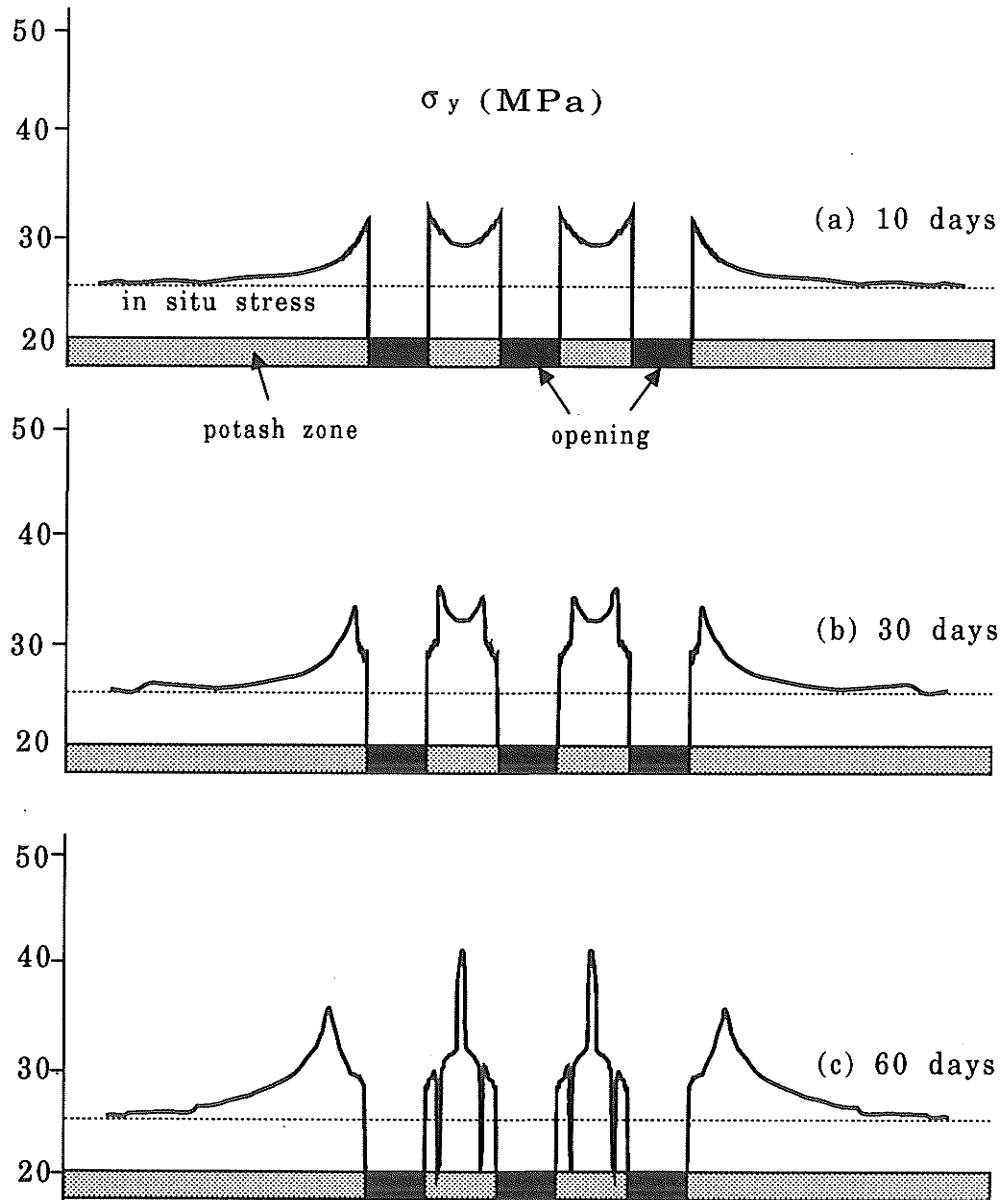


**Figure 9.18** Variation of vertical stress ( $\sigma_y$ ) distribution along the central height of the potash zone, (a) 10 days after excavation, (b) 30 days after excavation, (c) 60 days after excavation.

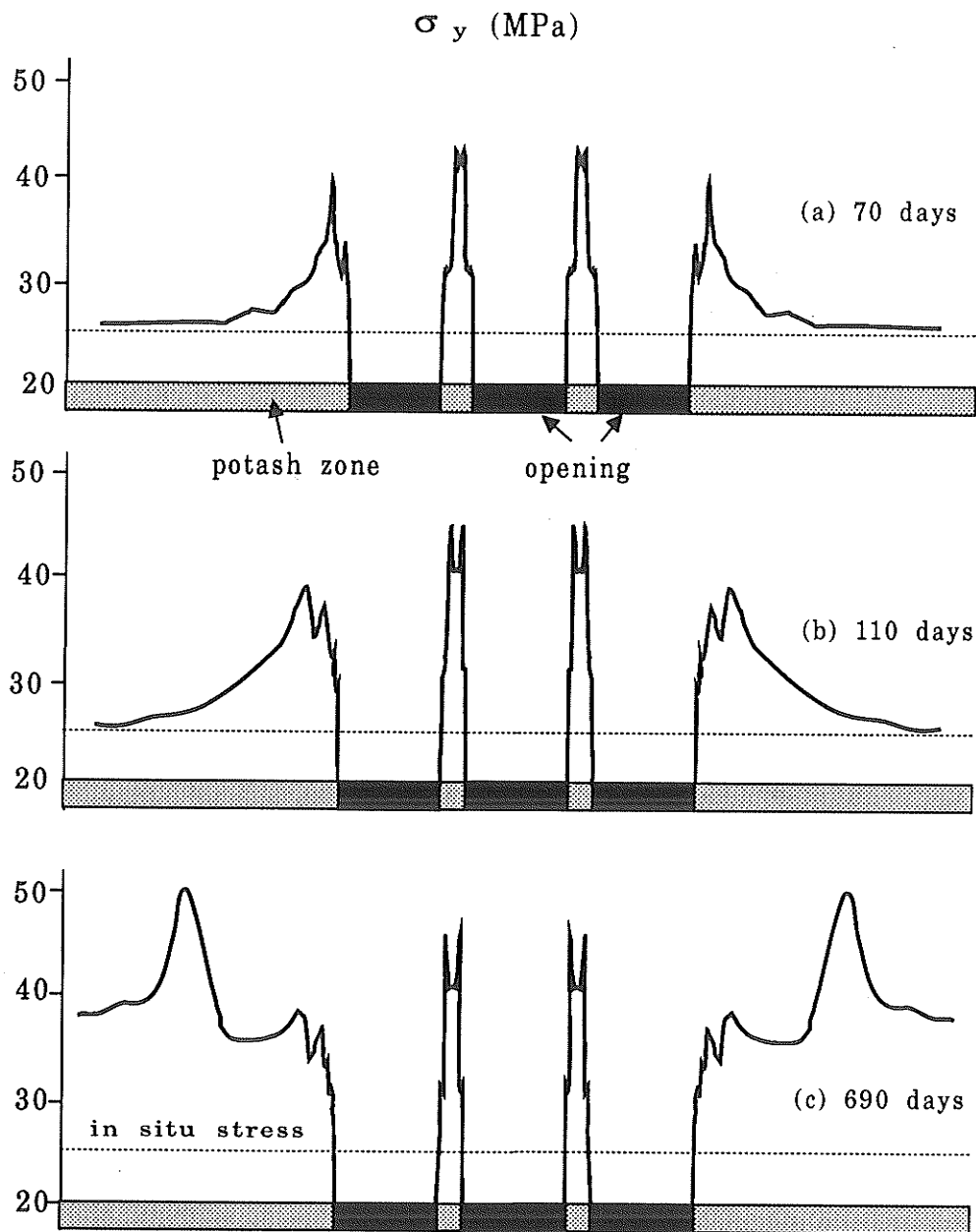
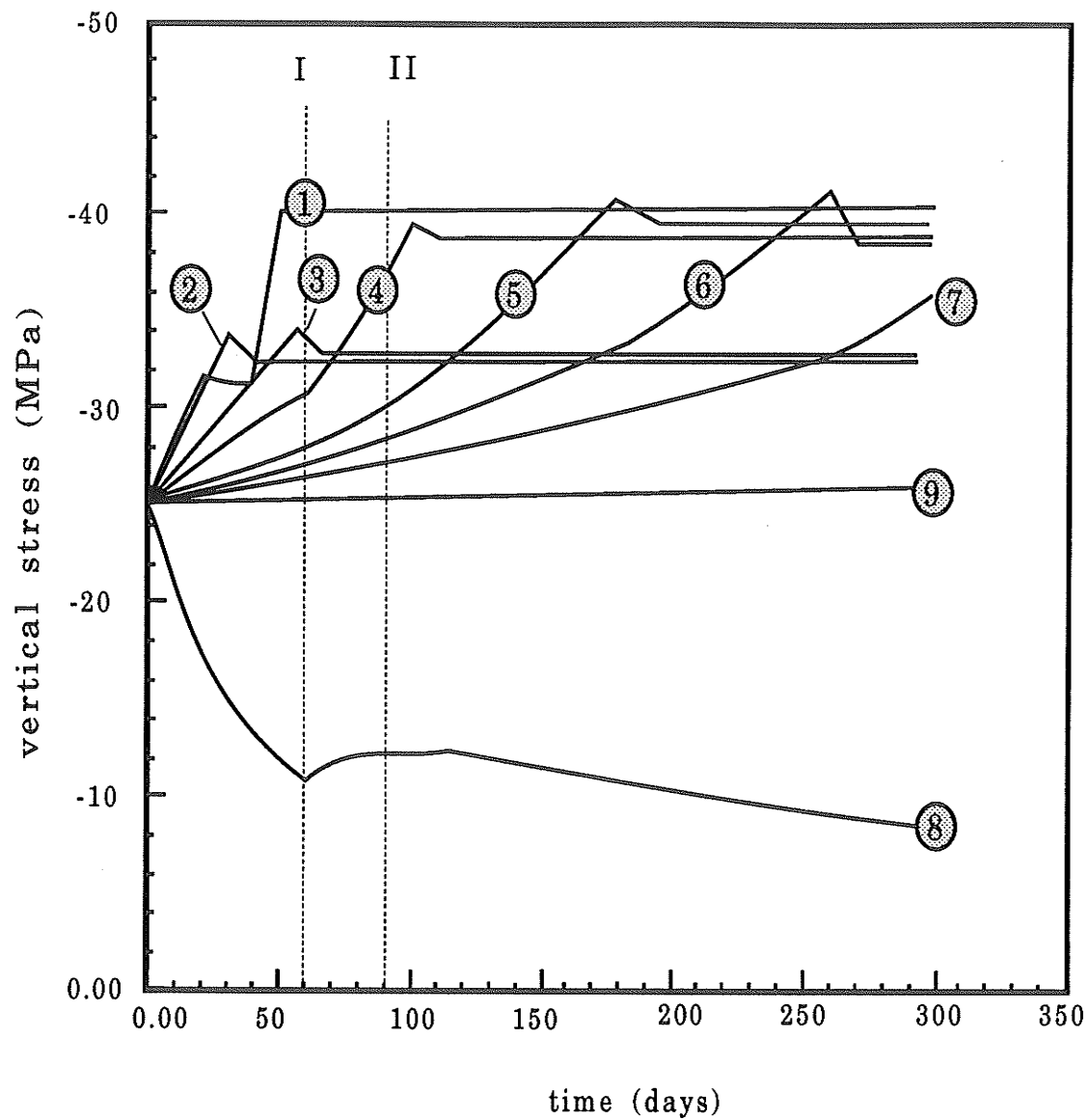


**Figure 9.19** Variation of vertical stress ( $\sigma_y$ ) distribution along the central height of the potash zone, (a) 70 days after excavation, (b) 110 days after excavation, (c) 690 days after excavation.

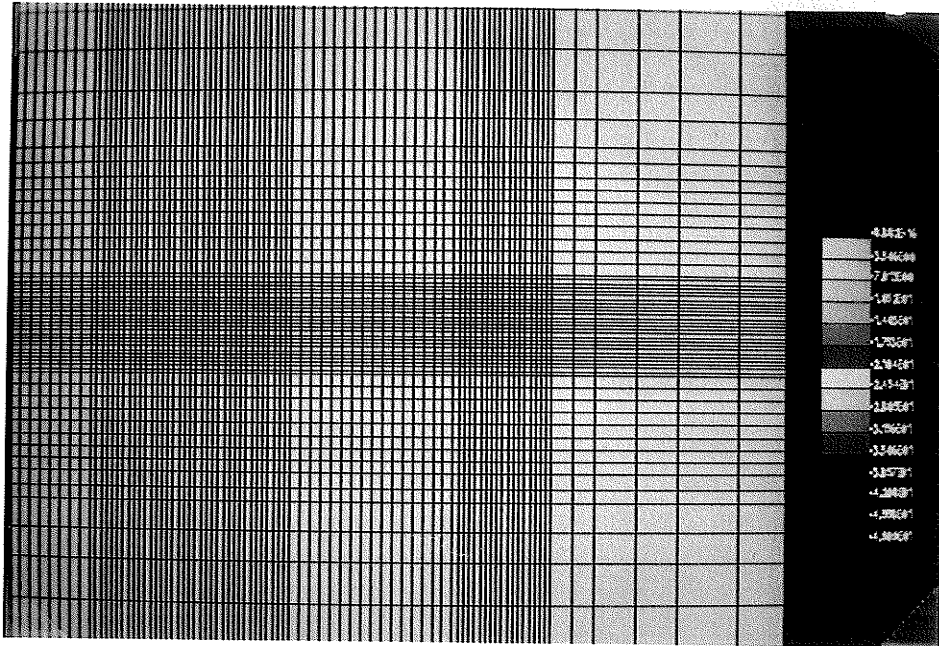
moved further away from the openings. The magnitude of peak stresses in both yield pillars and abutments increased. With the removal of the first shear wedges at the pillar boundaries (Figure 9.16), vertical stress in both yield pillars and abutments increased again (Figure 9.19a). Similar changes were observed immediately after removal of the second generation of shear wedges (Figure 9.19b). As deformation increased without additional changes in opening geometry (i.e., no more elements were removed), stresses in yield pillars and near the edges of the abutments gradually reached a constant state and stabilized. However, vertical stress continued to increase in the interior of the abutments and the locations of these peak stresses moved from the openings with time, indicating an increase in the area of yielded ground (Figure 9.19c).

Figure 9.20 shows the stress history at various locations shown by the numbers in Figure 9.12. Stress at most locations near openings stabilized (i.e., reached a constant value) or kept decreasing, while stresses continued to increase in the interior of the abutments.

Figures 9.21-9.25 show a set of contour maps of vertical stress around openings which further indicates stress changes during progressive pillar deformation. Figure 9.21 illustrates the uniform *in situ* stress state prior to room excavation. Yellow represents virgin stress levels, blues represent lower compressive stresses less than virgin *in situ* stress, while greens are higher than virgin levels. Figure 9.22 shows that the vertical stress increased in the pillars immediately after excavation. Shortly after excavation, two peak stresses developed in the yield pillar, and stresses near pillar edges dropped to about the pre-mining stress level (Figure 9.23). Figure 9.24 shows that later a single peak stress



**Figure 9.20** History of vertical stress ( $\sigma_v$ ) at various locations shown by the numbers in Figure 9.12. I - Removal of first set of shear wedges, II - removal of second generation of shear wedges.



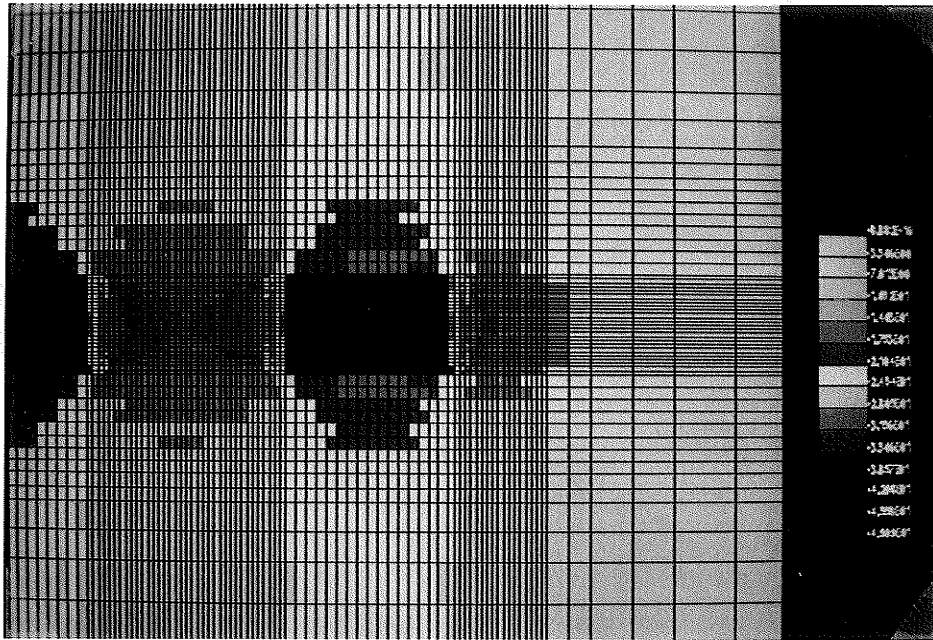


**Figure 9.23** Contour map of vertical stress 30 days after room excavation. Two peak stresses occurred in the yield pillar, stresses near pillar edges dropped due to yield.

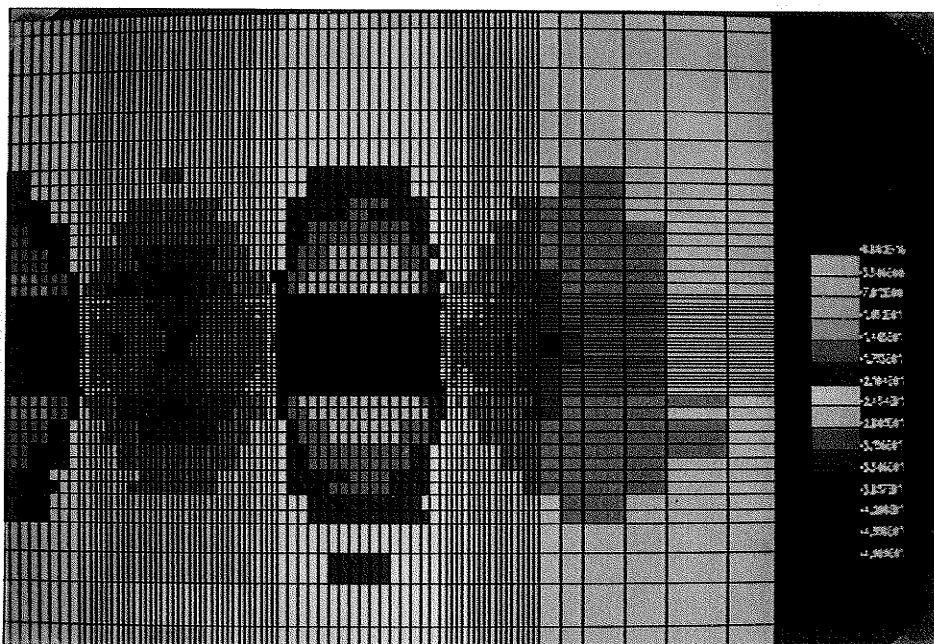


**Figure 9.24** As pillar deformation increased (60 days after room excavation), the entire pillar yielded, forming a single peak stress at pillar centre.

formed at the pillar centre. As pillar deformation increased, the zone of yielded ground increased further, with stress relieved ground around all three openings. Also, the location of peak compressive stress moved from the yield pillar into the abutments and kept moving away from the openings with time (Figure 9.25).

The changes in vertical stress distribution indicate that yielding around the openings results in transfer of load onto the abutments. It is also of interest to note that horizontal tensile stress in the roofs of openings did not occur until the yield pillar reached a stable state ( $> 110$  days). Therefore, it is not likely that vertical tensile cracking would occur in the roof. Shear displacement along weak layers due to sagging of roof (and floor) into the openings are likely.

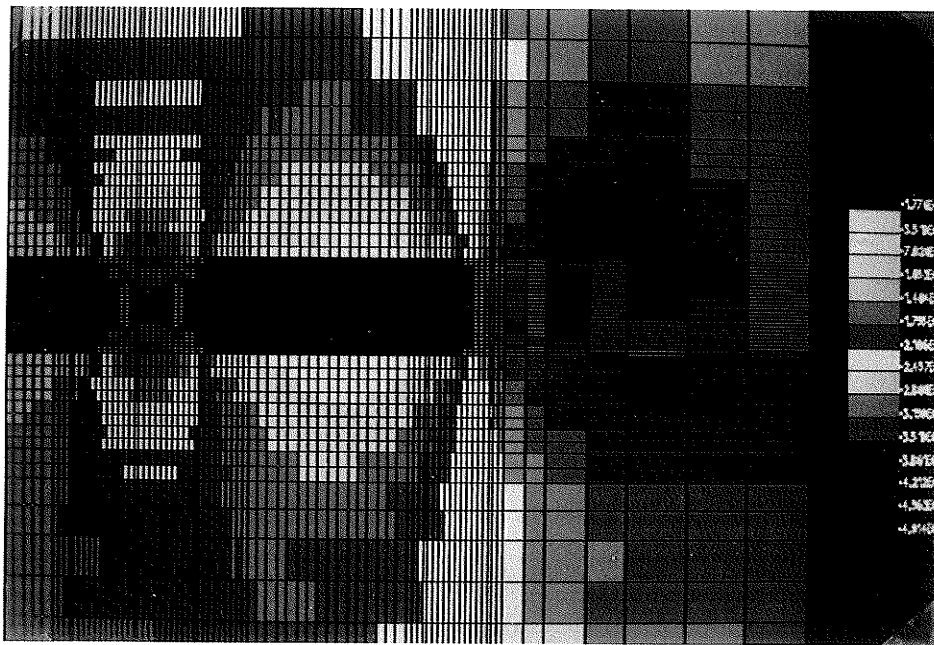
### **9.6.3 Convergence**

Figure 9.26 shows the history of convergence between roof and floor at the 6 pairs of locations shown by the letters in Figure 9.12. At all the locations, the rate of convergence was decreasing when the analysis terminated after 280 days of simulation.

## **9.7 Discussion**

### **9.7.1 Effect of clay layers**

As observed in Chapter 8, there are a few clay layers in the potash zone (Figures 8.6, 8.7 and 3.3). The thickness of these clay layers varies from place to place but averages 2-3 cm. Since the visco-plastic version of SIMEX, in its present form, is a general continuous model without the capability of including slipping interfaces, the effect



**Figure 9.25** As pillar deformation increased further (120 days after excavation), zone of yielding ground increased, stress relieved ground over all three openings, and the location of peak compressive stress moved away from the openings.

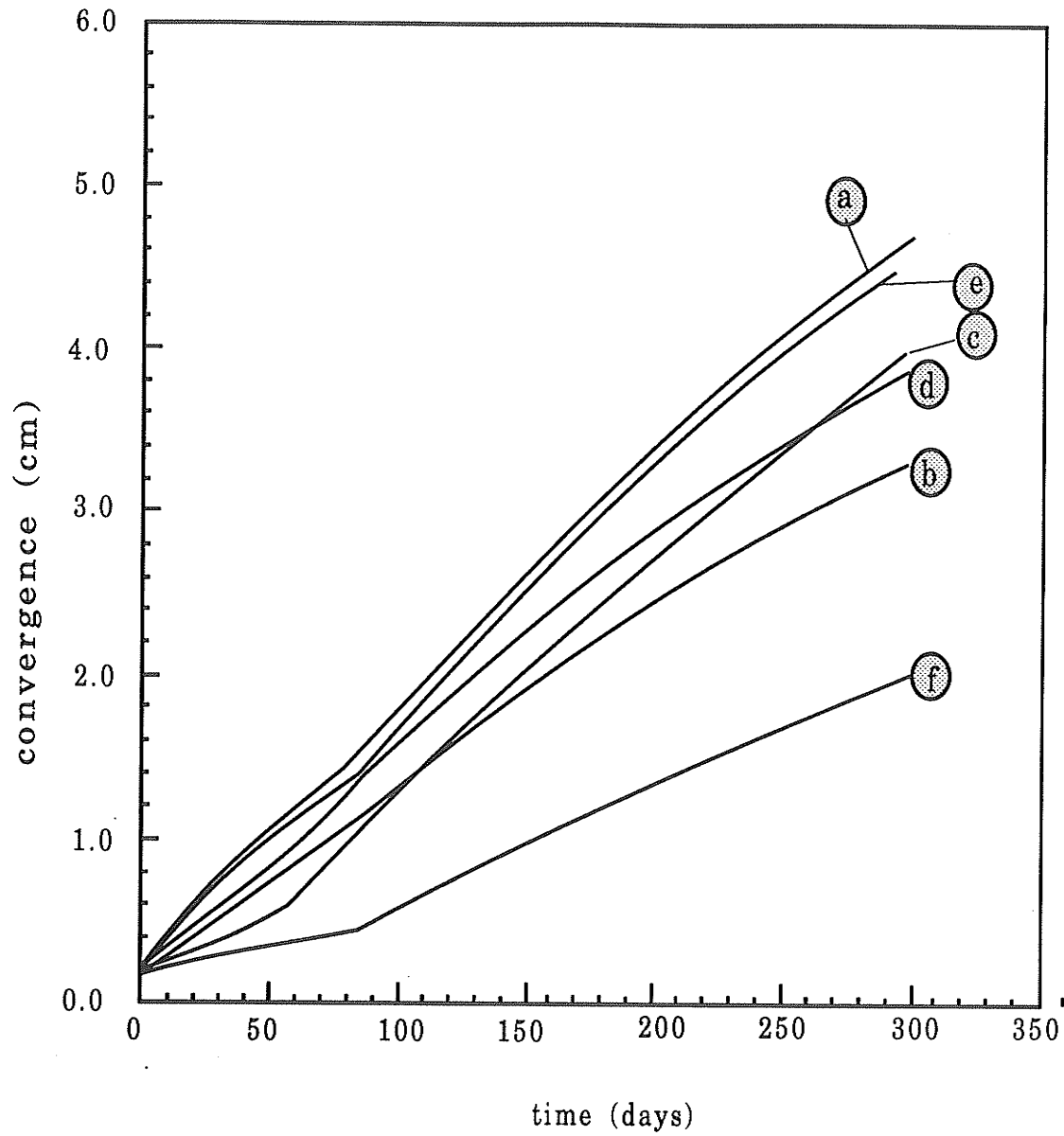


**Figure 9.26** History of convergence between roof and floor at various pairs of locations shown by letters in Figure 9.12.

of clay layers on yield pillar deformation was not considered in the analysis of yield pillar deformation. However, trial modelling has been conducted in which a clay layer has been included by using a weak layer of elements at both the top and bottom of the potash zone (with Young's modulus  $E=2.5$  GPa, Poisson's ratio  $\nu=0.3$ , cohesion  $c=0.1$  MPa, friction angle  $f=20^\circ$  and fluidity parameter  $\gamma=5.5 \times 10^{-2}$ , Figure 9.27). No slip is permitted between this layer and the potash. Figure 9.28 shows the distribution of viscoplastic strain 60 days after room excavation. Comparing this figure to Figure 9.14, it may be stated that the magnitude of plastic strain near the top and bottom of the pillar reduced due to the existence of the clay layers. Figure 9.29 shows the plastic strain 70 days after room excavation. Strain localization bands that occur at the top and bottom of the yield pillar without clay layers (Figure 9.16) are vanishingly small when the clay layers are present.

### 9.7.2 Discrepancies between field observations and FEM results

Bands of strain localization at pillar edges parallel to the opening walls (Figure 9.14 and 9.16) appeared in the FEM modelling, contrary to what has been observed *in situ* (an isolated shear wedge, Figure 8.8 and Stage 2 in Figure 8.22). There are two possibilities for such incompatibility between the FEM modelling results and *in situ* observations: (1) stress analysis shows that high stress did occur at pillar edges immediately after room excavation (Figure 9.18a). This stress level may cause brittle cracking (for example slabbing) parallel to the opening wall. In reality, when such cracks form, slabs will soon fall into the opening and will not contribute to further pillar

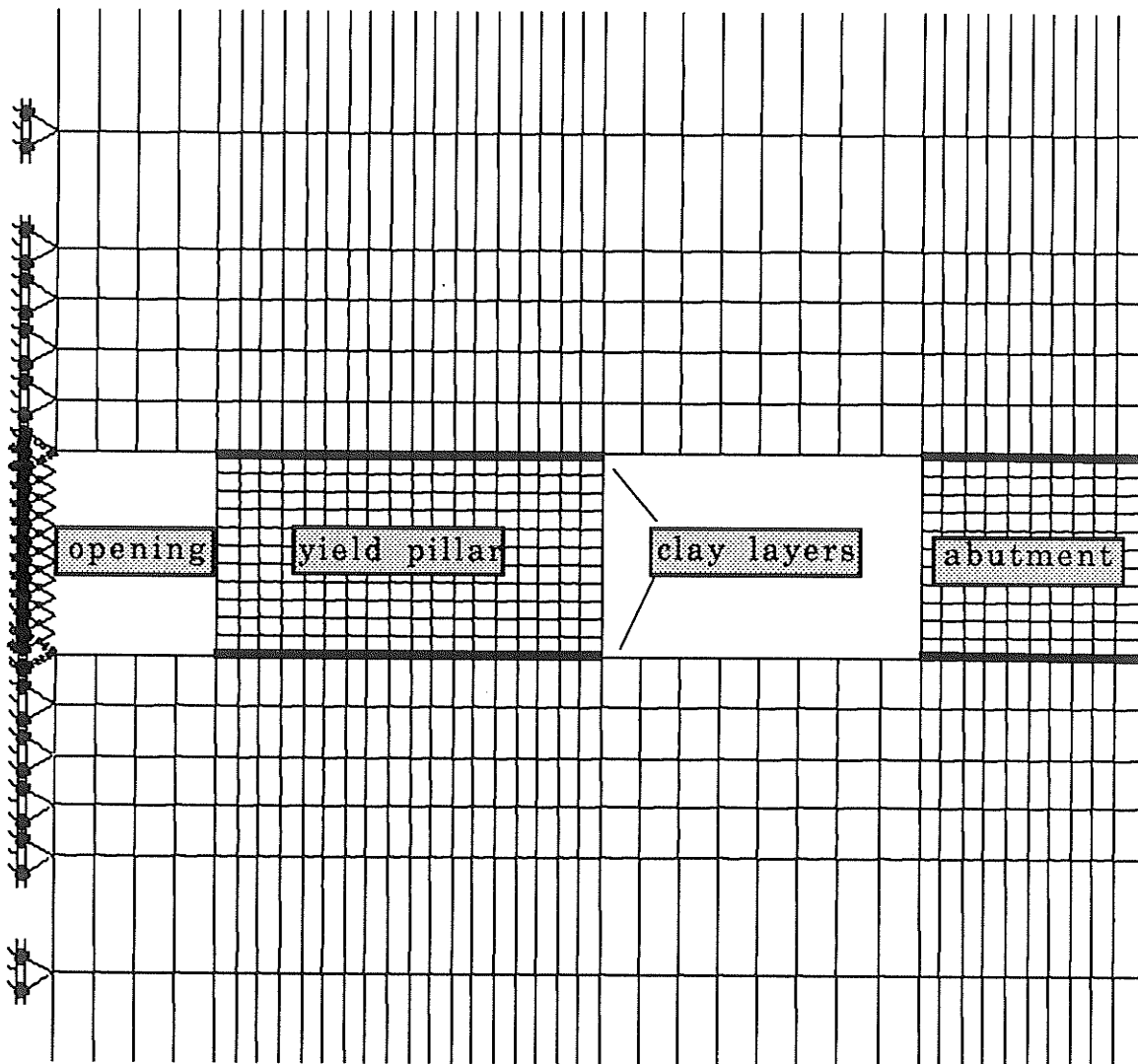


**Figure 9.27** Finite element mesh showing clay layers, openings, yield pillar, abutment and surrounding rock.

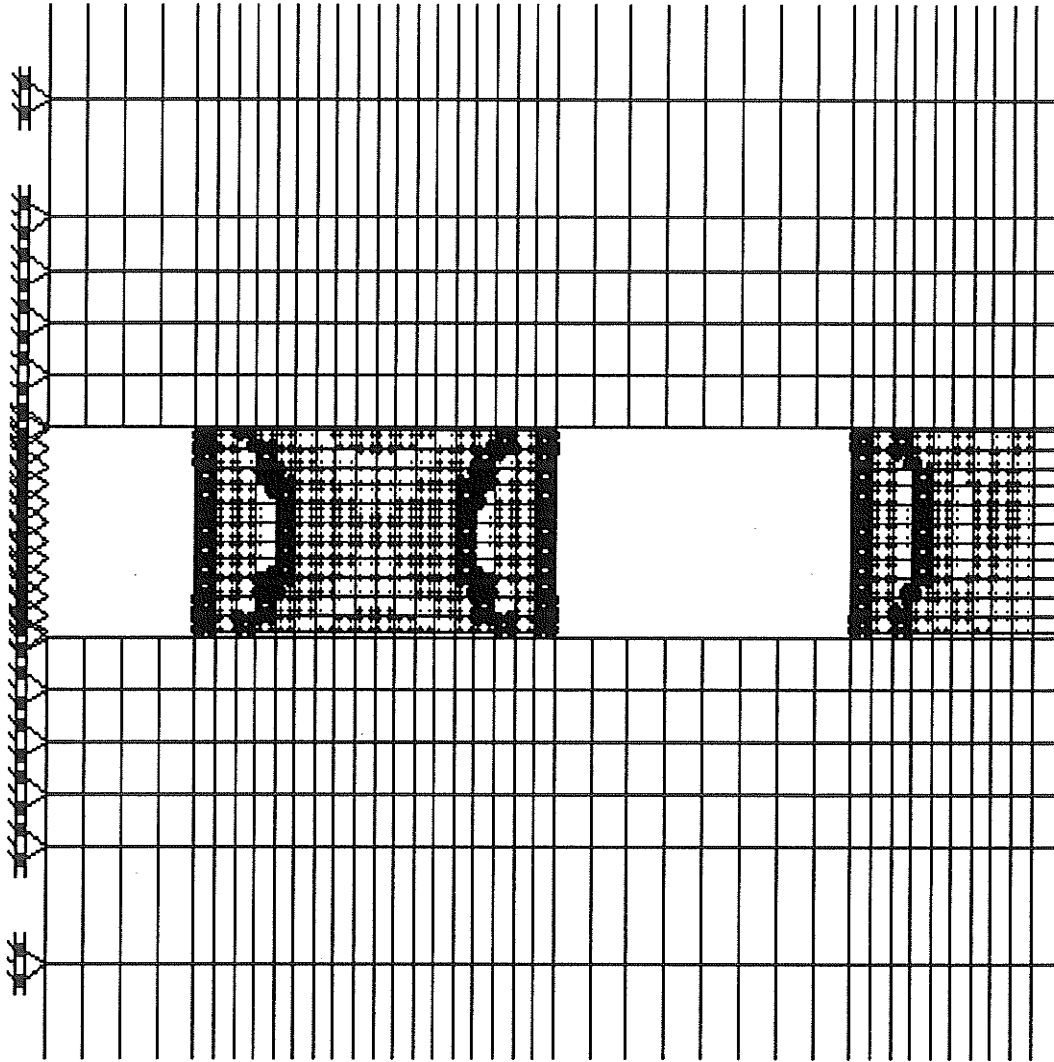


**Figure 9.28** Localization of plastic strain 60 days after room excavation in the yield pillar model that includes clay layers at the top and bottom of the potash ore zone (See Figure 9.27). Compared to Figure 9.14, the plastic strain near top and bottom reduced due to the presence of clay layers.

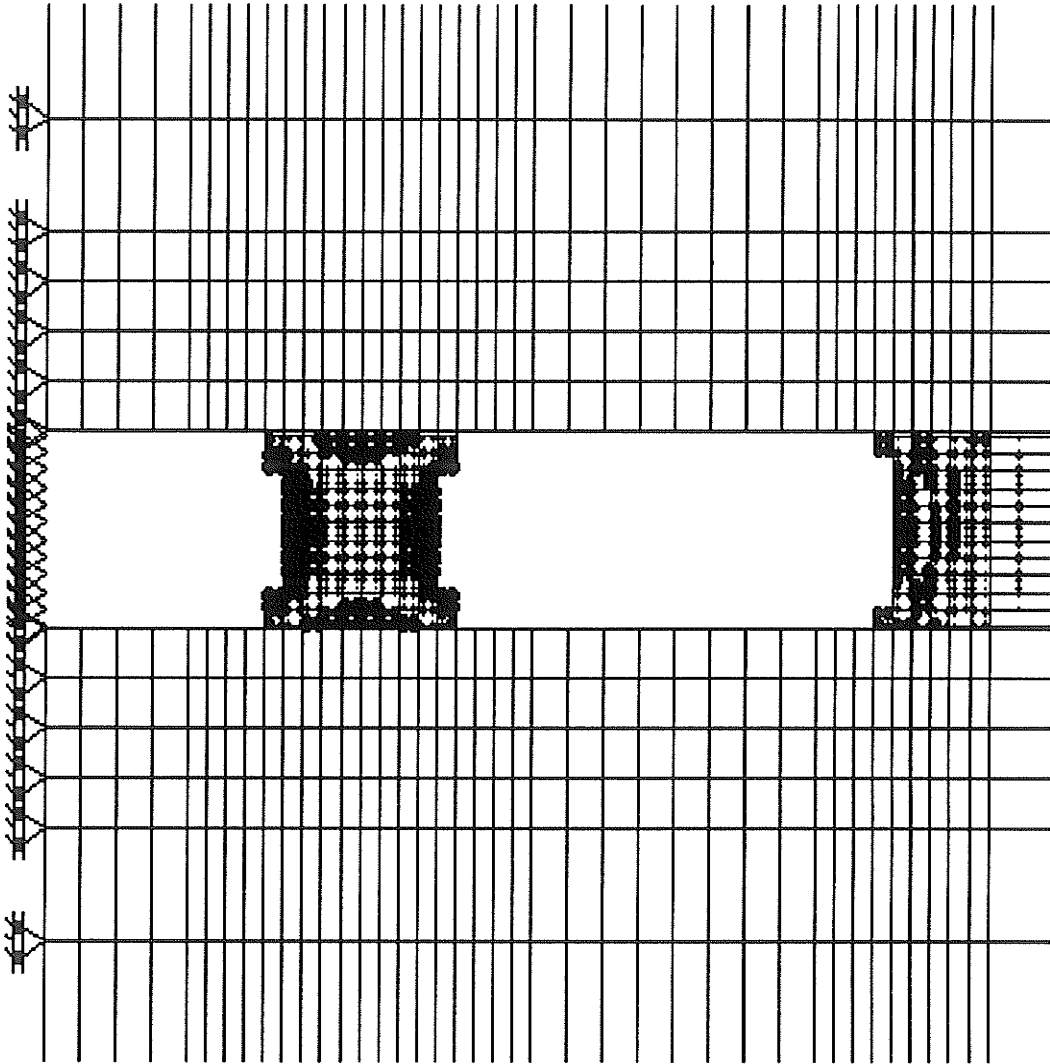


**Figure 9.29** Distribution of plastic strain 70 days after the initial room excavation in the yield pillar model that includes the effect of clay layers at the top and bottom of the potash zone.

deformation. These complex cracking and collapsing processes could not be taken into account by the **SIMEX** code. (2) the FEM results also reflect the use of infinitesimal strain to model a plastic deformational process that generates finite deformations and the disadvantages of using the Lagrangian description (displacement of a point is described by its initial position and time) instead of the Eulerian description (displacement of a point is described by its current position and time), especially for large deformation problems. If the Lagrangian description is used, the finite element mesh for the next time step should be updated by the deformations resulting from the previous time step. This is because the geometry of the original finite element mesh could be very different from the current geometry of the pillar after the accumulation of viscoplastic strains over time. For example, the geometry of the yield pillar in Figure 9.16 should represent the geometry of the yield pillar at Stage 3 in Figure 9.22. This clearly is not the case and cannot be unless the deformed mesh is used as the current finite element mesh at each time step.

### **9.7.3 Effects of viscoplastic roof and floor**

To simplify the analysis, the overlying and underlying strata were assumed to be a weak, linear elastic material in the viscoplastic numerical modelling with **SIMEX** (Figure 9.11). It was shown that these simulations replicated the observed pillar behavior quite well. However, the roof and floor in the Saskatchewan potash mines are not linear elastic materials. At the Cominco Mine the immediate roof is a salt layer (about 1 metre thick) followed by 15 metres of potash and potash rubble with clay layers. The

underlying strata are also potash with clay layers (Figure 3.2 and 3.3). The effects of the viscoplasticity of roof and floor on the progressive failure of the yield pillar have been examined by modelling a viscoplastic roof and floor in the numerical model used earlier (Figure 9.11). A few trial runs suggested that only the cohesion of the overlying and underlying rocks will significantly influence the distribution of viscoplastic strain. Friction angle was shown to have a smaller role. More detailed simulations were therefore carried out with various cohesion values for the roof and floor, while fixing the other properties as follows: angle of internal friction,  $\phi=20^\circ$ , fluidity parameter  $\gamma=5.5 \times 10^{-2}$  (similar to that of the potash ore zone), Young's modulus,  $E_1=30$  GPa, and Poisson's ratio  $\nu_1=0.3$ . The material parameters for the potash ore zone (B in Figure 9.11) were the same as in the previous simulation with an elastic roof and floor.

At very low values of cohesion (e.g.,  $c_1=2$  MPa, similar to that of the potash ore zone), plastic strain occurred in both roof and floor. Figure 9.30 shows that plastic strain occurred at room corners in the yield pillar immediately after room excavation, as well as in the roof and floor. Figure 9.31 shows the distribution of plastic strain 60 days after room excavation. Compared to Figures 9.14, in which the roof and floor are linear elastic, the pattern of localized plastic strains within the yield pillar did not change when a viscoplastic roof and floor was simulated. However, with the viscoplastic roof and floor, yielding also occurred in the roof and floor.

The isolated wedges on both sides of the yield pillar and in the abutment as well as a layer of roof and floor, where plastic strain occurred, were removed in the "60-day" simulation and the analysis continued. Figure 9.32 shows that the yield pillar stabilized

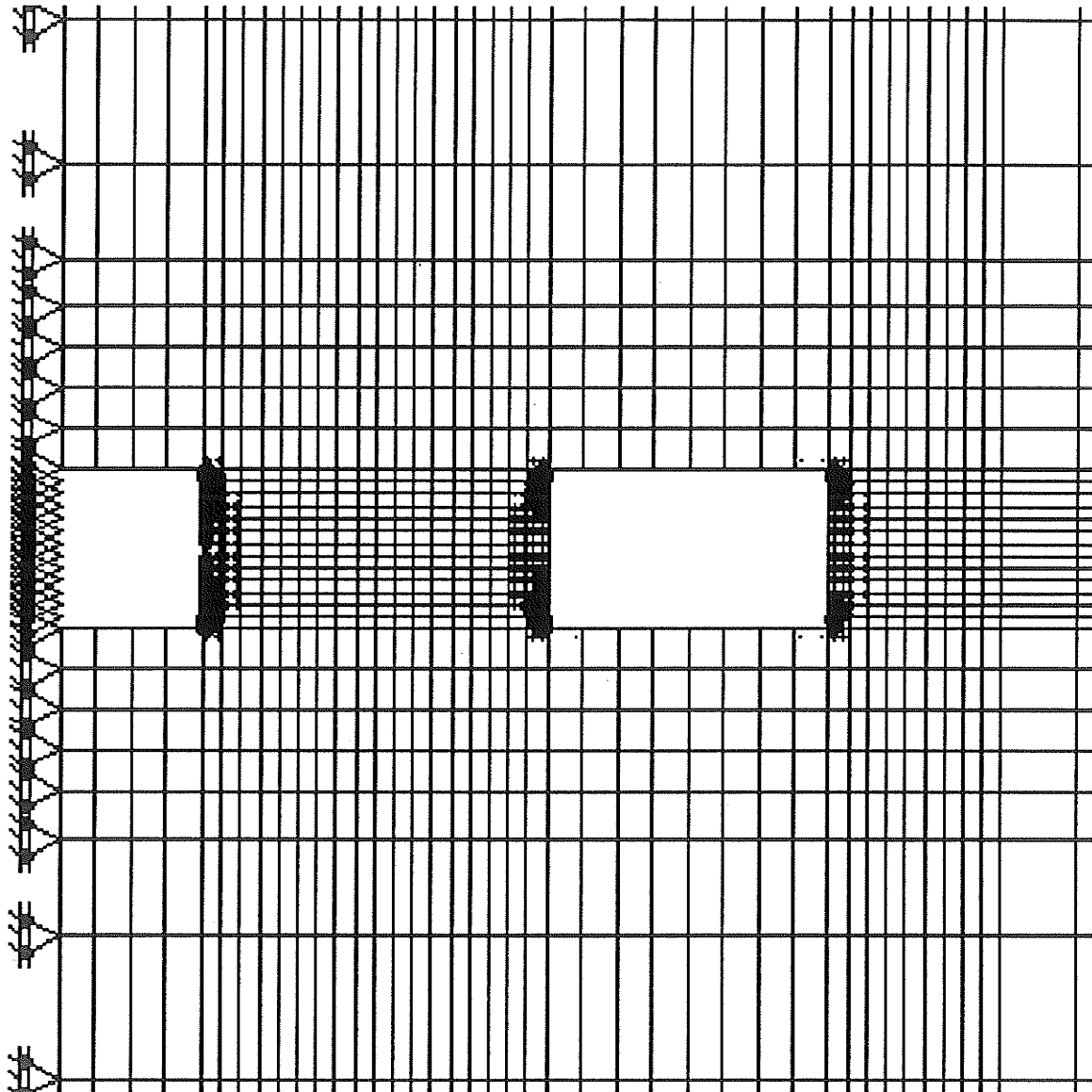


**Figure 9.30** Plastic strain distribution immediately after room excavation in the model with viscoplastic roof and floor. It signifies the initiation of corner ductile shear zones. Local plastic strain also occurs in the roof and floor.

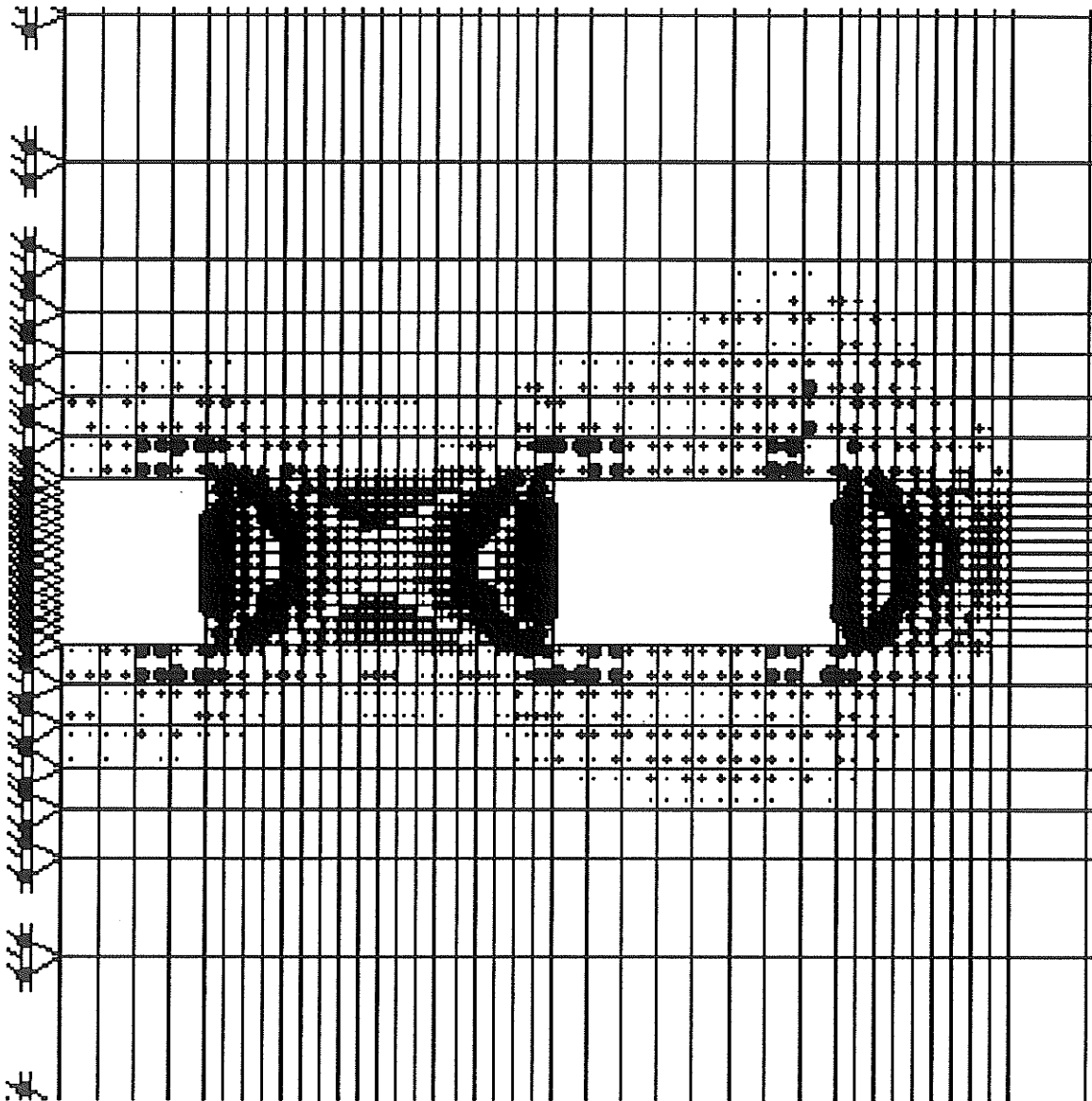


**Figure 9.31** Localization of plastic strain in diagonal directions at pillar edges 60 days after room excavation in the model with viscoplastic roof and floor. Failure also occurs in the roof and floor areas.

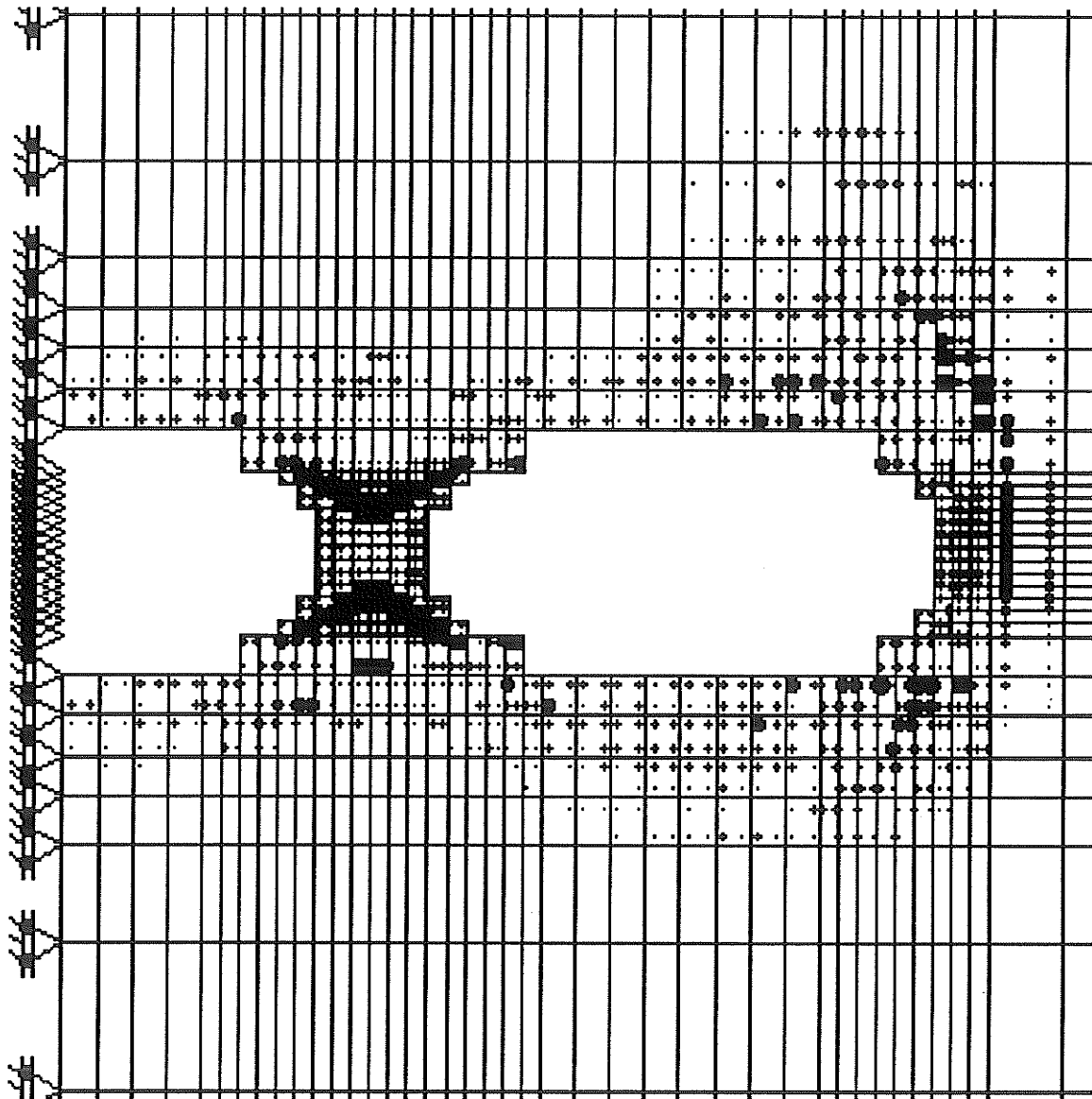


**Figure 9.32** Third generation of plastic localization for the model with viscoplastic roof and floor. Fracture pattern appears to be stable in the yield pillar (110 days after initial room excavation).

following the formation of the shallowly inclined strain localization bands at the top and bottom of the yield pillar. This state is similar to that shown in Figure 9.17 for an elastic roof and floor. Plastic strain occurred in the roof and floor and extended gradually with time. These figures show that the failure pattern and failure process within the yield pillar and abutment pillar obtained with a viscoplastic roof and floor are similar to those obtained with an elastic roof and floor, except that failure also occurred in the roof and floor for the viscoplastic case. The magnitude of plastic strain in the roof and floor depends largely on the cohesion of the material. It decreases significantly as the cohesion increases. For example, plastic strain in the roof and floor vanishes completely when the cohesion increases to 5 MPa.

Using viscoplastic roof and floor materials instead of linear elastic properties changes the distribution of stress around the openings and local stress histories. With the viscoplastic roof and floor, the extension of the de-stressed area (shown in Figures 9.21 - 9.25 for the elastic case) occurs at a lower rate. The rate depends on the material parameters (cohesion, angle of internal friction, and fluidity parameter). However, stress distribution within the yield pillar itself is not affected significantly (compare Figures 9.33, 9.34, and 9.35 with Figure 9.18, 9.19, and 9.20 respectively).

## 9.8 Chapter Summary

The following conclusions can be drawn from the numerical simulation of pillar deformation and fracturing:

- (1) The initiation and propagation of corner shear zones can be simulated on the

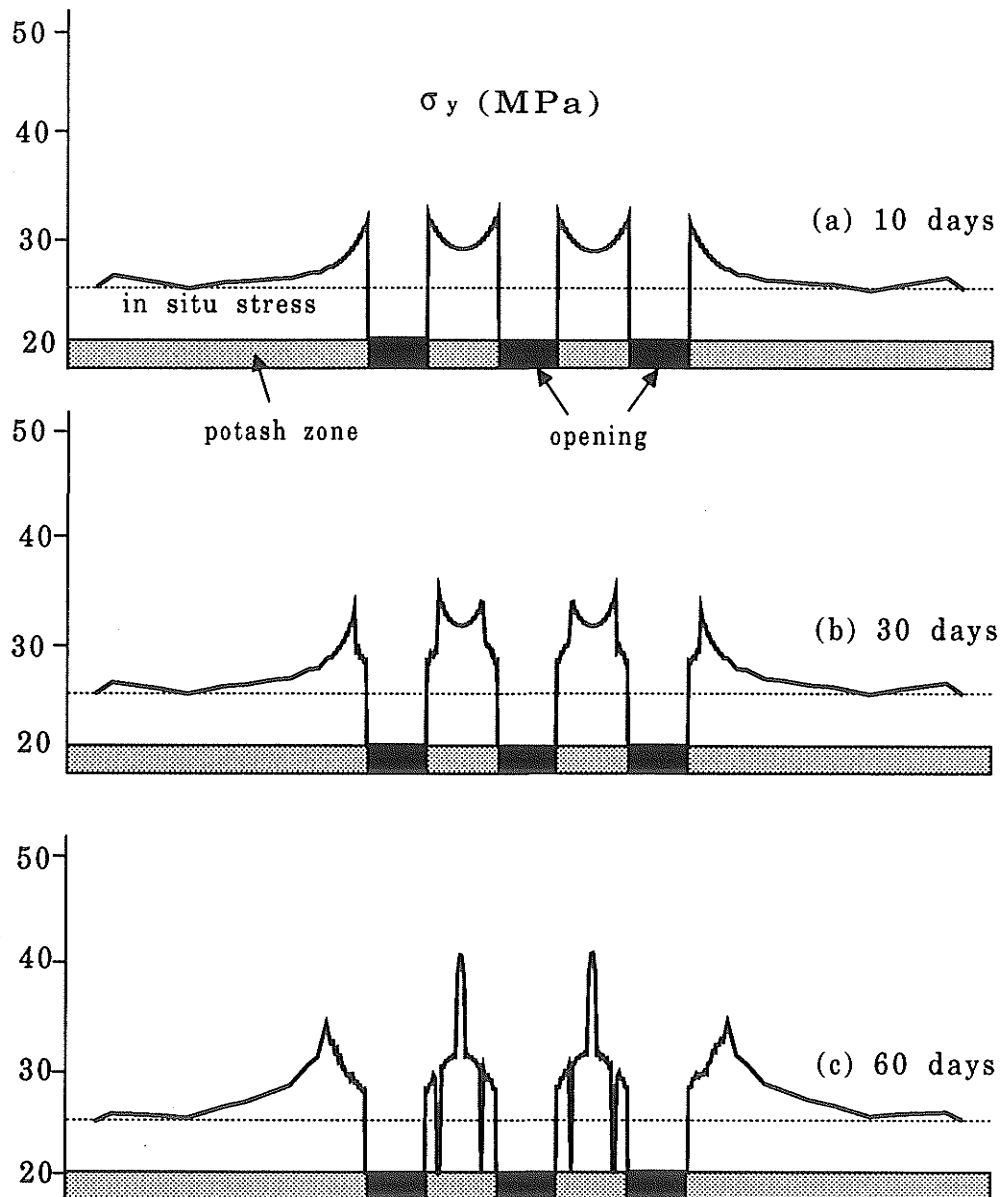


**Figure 9.33** Vertical stress ( $\sigma_y$ ) distribution along the central height of the potash zone for the model with viscoplastic roof and floor. (a) 10 days after excavation, (b) 30 days after excavation, (c) 60 days after excavation.

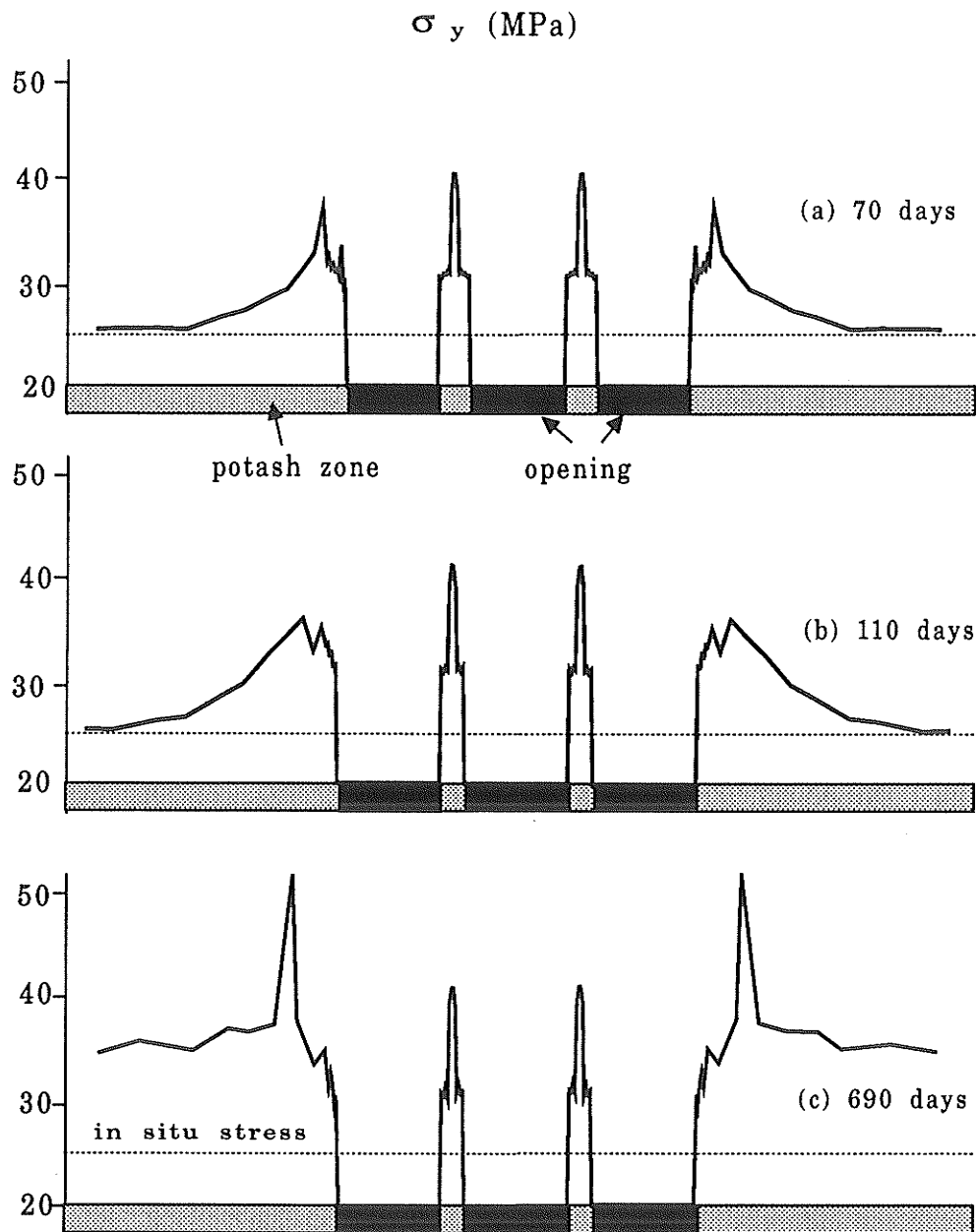


**Figure 9.34** Vertical stress ( $\sigma_y$ ) distribution along the central height of the potash zone for the model with viscoplastic roof and floor. (a) 70 days after excavation, (b) 110 days after excavation, (c) 690 days after excavation.

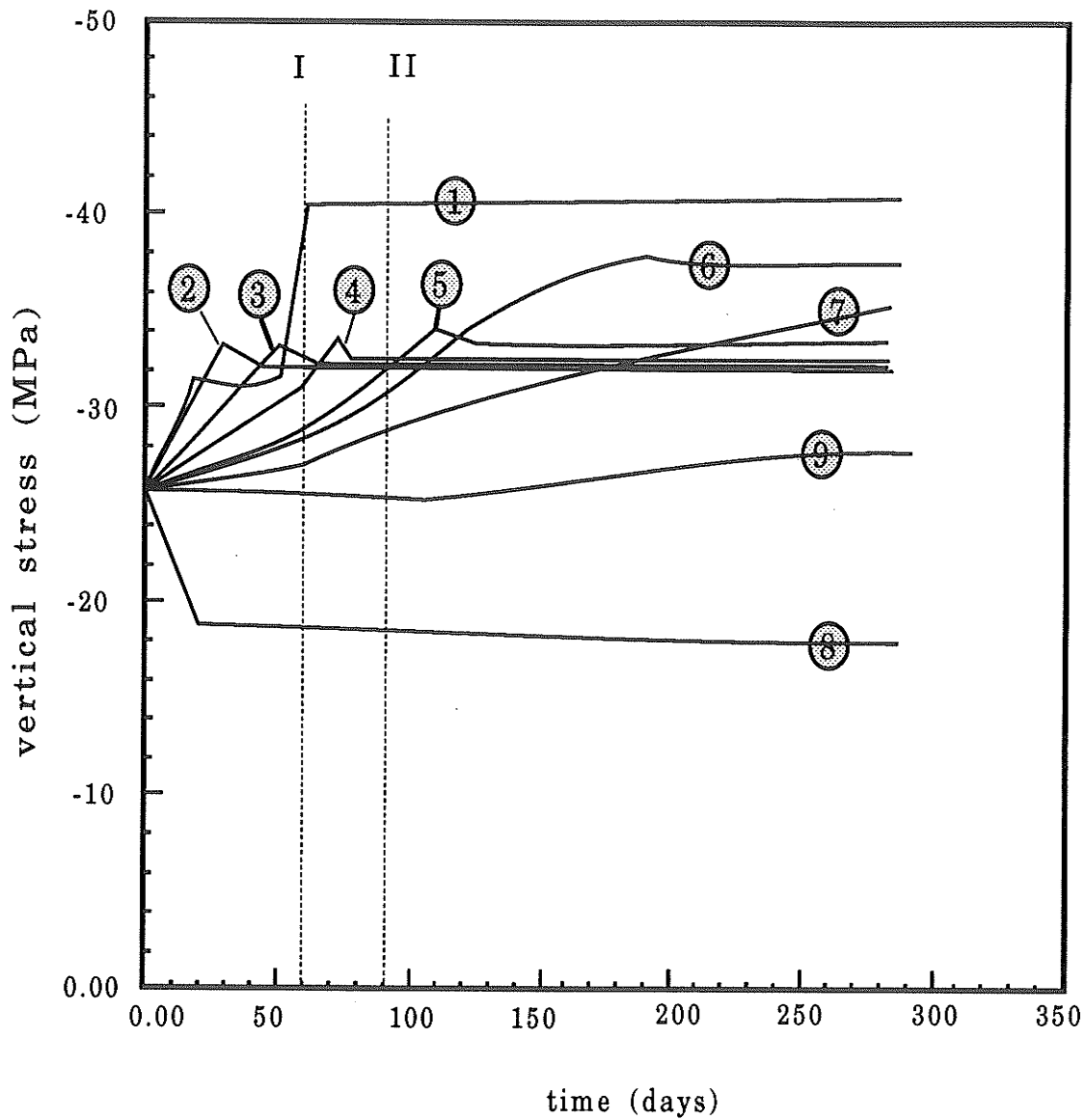


**Figure 9.35** History of vertical stress at various locations shown by the numbers in Figure 9.12 for the model with viscoplastic roof and floor. I - Removal of first set of shear wedges, ii - Removal of second generation of shear wedges.

basis of the theory of linear elastic fracture mechanics. Finite element modelling indicated that the corner fractures are mode II fractures (shear). However, LEFM does not provide a correct prediction for the direction of crack propagation. Therefore, in determining the direction of fracture propagation, the assumption that fractures propagate along the direction of the maximum compressive stress was followed. Once corner fractures propagated to the middle height of the pillar, stresses were relieved in the isolated wedges or shear wedges that developed at the edges of the pillar.

(2) Simulation of progressive, viscoplastic pillar deformation reproduced all four stages of the yield pillar deformational model proposed in Chapter 8 (Figure 8.22). The computer modelling reproduced the initiation and extension of corner ductile shear zones in terms of the development of plastic strain localization bands. After collapse of the second generation of shear wedges, stresses around the openings reached quasi-stable levels while displacements continued to increase. No further strain localization developed at the sides of the yield pillar at this stage. Instead, strain localization occurred at pillar top and bottom and formed a relatively stable failure mode. This observation suggest an additional pillar deformational stage (Stage 5) should be included in the yield pillar deformational model (Figure 9.36). The processes of failure through strain localization bands, isolated wedges, and wedge collapse may continue at the edges of the abutment pillar after the yield pillar has reached "stabilized". Stress analysis shows that as deformation of the yield pillar progresses, the location of the peak stress transfers from the yield pillar to the abutment pillar, and that the peak stress over the abutment moves away from the opening with time. This signifies the progressive extension of yielding

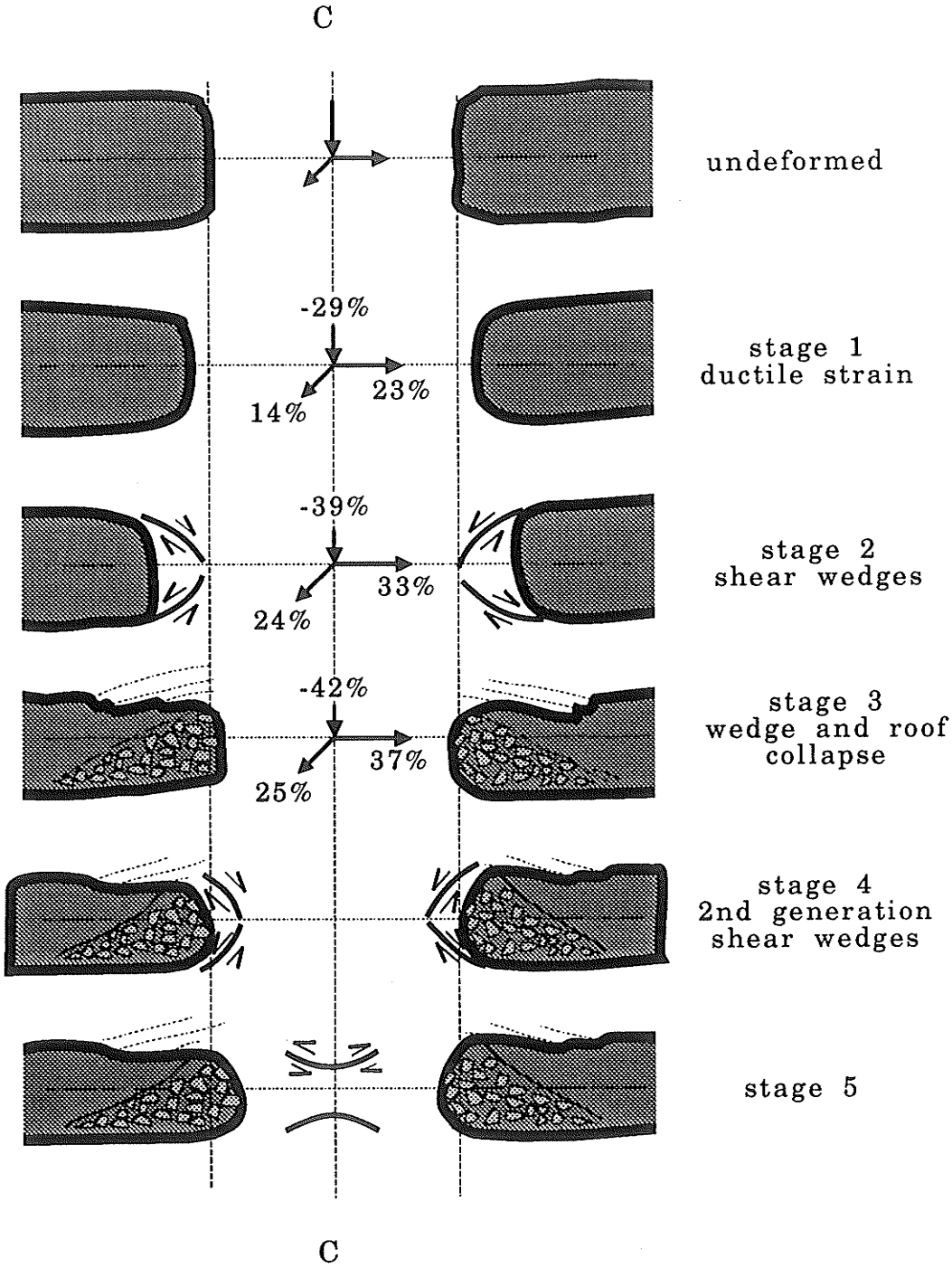


**Figure 9.36** Modified yield pillar deformation model. Finite element simulation reproduced all four stages of pillar deformation proposed in Figure 8.22. An additional deformation stage may be included (Stage 5), indicating a final stable failure mode.

around the openings.

(3) The failure pattern in both yield and abutment pillars is highly sensitive to material properties (cohesion and friction), opening dimensions, clay layers, sequencing of excavation, and deformational rates (as expressed by the fluidity parameter). Failure pattern within the yield pillar is not very sensitive to the viscoplasticity of roof and floor. However, a viscoplastic roof and floor induce plastic strains in the roof and floor and slow down the extension of the de-stressed area around the openings.

## 10. DISCUSSION, CONCLUSIONS AND FUTURE WORK

### 10.1 Discussion

The overall goal of this thesis was a selective study of *in situ* and laboratory potash behavior, with special reference to mining induced deformation in Saskatchewan potash mines. Under this overall goal, five major research objectives were identified through a critical examination of the existing potash literature in Chapter 2 and a realistic consideration of the specific problems in potash mining in Saskatchewan in Chapter 3. These objectives were then addressed in Chapters 5-9 by means of laboratory experiments, *in situ* observations, and analytical/numerical simulations. Each chapter treated a specific problem concerning either laboratory or *in situ* deformational characteristics of Saskatchewan potash and salt rocks. Together, these 5 chapters contribute to a better understanding of the behavior of mine openings in salt rocks. The following is a general critique of the deformational properties of salt, underground excavation in salt, and numerical modelling of salt excavation in the light of the results from the research described in this thesis.

#### 10.1.1 Deformational properties of salt

Salt rocks in this study include halite and potash. Halite is composed mainly of pure halite crystals (sodium chloride) with grain sizes ranging from 2 to 20 mm in diameter, has an average uniaxial tensile strength of 1-2 MPa, and an average compressive strength of about 30 MPa. Potash is composed predominantly of medium to

coarse grained sylvite (potassium chloride) and halite (sodium chloride), with some carnallite and interstitial clay. The grain size of potash is similar to that of halite. The average uniaxial tensile strength is also 1-2 MPa and the average uniaxial compressive strength is around 25 MPa.

### **Elastic deformation**

Various studies indicate that most salt rocks show approximately linear and isotropic elastic deformation prior to yield. The elastic constants are nearly independent of salt types and their sources (Senseny et al. 1992; Hansen and Carter 1984), but are dependent on loading rate and to a lesser degree on confining pressure. While these statements appear to be true for the initial elastic response of Saskatchewan potash in compression, the elastic deformation is very limited (only up to 30% of the ultimate strength in compression, Table 5.1 and Figure 5.4). Halite from the Cominco Mine shows an apparent bi-linear elastic response with a Young's modulus in tension being only half of the Young's modulus in compression (Tables 6.2-6.4). This is a rather interesting finding, especially for Saskatchewan potash mines where halite forms the immediate roof of the potash openings. As a result of bimodularity, roof deflection is actually larger than predicted by assuming unimodularity (Figures 7.18 and 7.29), and the possibility of vertical tensile cracking on the exposed roof surface is reduced (Figure 7.30). For potash from the Cominco Mine, the assumption of unimodularity appears to be correct. However, potash behaves linear elastically to failure in tension, while plastic deformation dominates in compression (Figure 6.11).

Bimodularity has also been measured on granite and limestone (Tables 6.8 and 6.9), on marble, quartzite, sandstone (Haimson and Tharp 1974), and on many other materials such as bone (Simkin and Robin 1973), composites (Jeness and Kline 1974), and concrete (Guo and Zhang 1987).

Bimodular elasticity should be considered where the state of stress is tension or mixed compression and tension because it influences stress distribution and displacements. Such effects have been demonstrated in indirect rock tensile strength tests (Figures 7.23, 7.24, 7.26 and 7.27), in beam behavior (Figures 7.10-7.13, 7.17 and 7.18), in roof failure and floor heave (Figure 7.29 and 7.30), and in hydraulic fracturing from boreholes for *in situ* stress determination and reservoir stimulation (Haimson and Tharp 1974). Effects of bimodular elasticity should also be considered in underground gas/compressed air storage, hydro-power tunnels, fragmentation or cutting by blasting, drilling, TBM's, roadheaders, and allowable mud pressures in wellbores, etc.

Stress relaxation tests on Saskatchewan potash suggest that potash may not have a creep limit, i.e. its long-term strength might be zero (Chapter 5). Therefore, potash creeps at any load. The elastic deformation of potash is time dependent.

### **Inelastic deformation**

Potash and salt usually show a large amount of permanent deformation, depending on temperature, stresses (both mean stress and deviatoric stress), moisture, deformational rate, and stress history (Senseney et al. 1992). The magnitude of accumulated plastic strain in a conventional uniaxial compression test can reach 12% (Figure 9.5). In potash yield

pillars at the Cominco Mine, permanent strains over 8 years of deformation were estimated at more than 40% from rock fabric analyses (Tables 8.2, 8.4 and 8.6).

Deformation of solids is commonly viewed as governed by physical processes at the atomistic scales through a variety of *deformational mechanisms*. The deformational mechanisms of a particular solid depend largely on the crystallographic system of its major mineral components. Both halite and sylvite form isometric crystals. Their identified mechanisms include glide along  $\{110\} \langle 110 \rangle$  systems that can produce a transient (strain hardening) phenomenon; cross slip that corresponds to the brittle-to-ductile transition; diffusion controlled mechanisms (climb and diffusion) that are responsible for steady-state creep at high temperature; and dynamic recrystallization that might correspond to a softening process (Senseny et al. 1992). While these mechanisms and their speculated deformational phenomena maybe applicable to the plastic deformation of pure halite or pure sylvite, potash shows a much more complicated deformational mechanism due to the fact that sylvite grains and halite deform very differently during deformation. Fabric analyses and visual inspection of deformed potash surfaces show that sylvite grains deform in a ductile fashion without loss of continuity, while halite grains deform in a brittle fashion by fracturing and rotation and displacement among the broken fragments (Section 8.7.2, Figures 8.20 and 8.21). The overall permanent strain in potash, therefore, includes a combined results of brittle deformation of halite, plastic deformation of sylvite and grain boundary sliding. Deformational mechanisms of halite grains include fracturing and displacement and rotation of fragments. Sylvite deformational mechanisms are yet to be determined.

The different deformational mechanisms of sylvite and halite grains in potash make the application of constitutive laws based on deformational mechanisms for single minerals difficult, although such constitutive laws have been accepted as superior over other constitutive models, including various empirical and rheological models, as reviewed in Section 2.2.2.

Both elastic and inelastic properties of salt rocks are highly loading rate and load dependent. While much effort has been put on creep properties, stress relaxation has been overlooked. As illustrated in Chapter 5, stress relaxation tests have many advantages over creep tests in addressing time dependent properties at various stages of deformation. The present situation is that a huge body of creep data has been accumulated with limited progress in our understanding. Diverting some of the research attention from creep to relaxation may result in a milestone in salt research.

### 10.1.2 Underground excavation in salt

Due to the unique *flow* properties of salt rocks, deep underground excavations in such rocks are typically associated with gradual closure. This gradual closure could result in loss of access to mine entries, loss of storage volume in storage caverns, borehole closure, subsidence and its associated effects on overburden hydrology (Baar 1966 and 1970). However, the *flow* properties can be advantage in mine planning and layout to ensure safety during the service period and increase extraction.

An example of such design methodology is the *stress control technique* that has been developed over the last three decades. In addition to the fact that the technique

improves extraction ratios and achieves the necessary safety, it is also economic because it utilizes the existing ground to stabilize mine openings rather than by the use of artificial ground supports. However, the successful application of the stress control technique largely depends on understanding the *in situ* behavior (deformation and fracture) of the host rocks and surrounding strata. *In situ* documentation of deformational features at both a mesoscopic scale and a microscopic scale is therefore of utmost importance.

The deformation and failure process of a yield pillar can be controlled by proper selection of design parameters, including geometry and dimensions of rooms and pillars, sequence and speed of excavation, and probably most importantly, by using back fill. The yield pillar study in Chapters 8 and 9 indicates that pillar deformation involves ductile flattening of pillar interiors, repeated development of shear zones and shear wedges at pillar margins and the detachment or collapse of these shear wedges. This deformational process reduces the thickness of yield pillars, enlarges the area of yield around the openings, increases the possibility of separation of roof and floor strata along bedding surfaces, and may result in long-term, although slow, surface subsidence. Ultimately, fracture of the overlying Downson Bay limestone formation, induced seismicity, and pathways for water inflow (Yuan and Lajtai 1991) may develop. However, these are matters of some complexity and conjecture.

Yield pillars should be designed in such a way that they can yield at a designed rate while excavating the protected rooms and on the other hand, they should be able to achieve long-term stability to reduce long-term subsidence. Placing salt tailings as backfill in mined-out openings can provide confinement to yield pillars and, together with the

yield pillars, support the overburden. Returning salt tailings back underground also reduces the environmental problems associated with surface tailing piles. Because backfill salt tails can become solid over time due to crystallization, backfilling may also allow second-pass mining to extract some or all the pillars left after the first-pass mining (Van Sambeek 1992; Kaskiw et al. 1989)

The proper design needs accurate estimations of the progressive deformation of salt, including strain rate, convergence, stress changes, failure processes around openings, and the consolidation of backfill. Such estimations require numerical simulations that are based on both *in situ* and laboratory data for calibration.

### 10.1.3 Numerical modelling in salt excavation

Numerical tools are essential in most rock mechanics and rock engineering problems. For excavation in salt rocks, the indispensability of numerical tools is notable due to the complex non-linear, viscoplastic stress-strain relationships of these materials. As physical modelling experiments are usually costly and difficult to perform, numerical simulation becomes an essential ingredient for providing valuable information more economically. However, numerical simulation should be complemented by laboratory tests and *in situ* observations. Numerical simulation might not be a precise, quantitative tool, but is, at least, more valuable as a qualitative tool, to reproduce specific features of deformation and failure, to help understanding of the mechanisms of deformation and to explore potential trade offs and alternatives in mine layouts. This limitation of numerical modelling is due to the fact that simulation in rock mechanics and rock

engineering usually falls into a *data limited* category where models can not be validated and used with confidence, because one seldom knows enough about a rock medium to model it unambiguously (Starfield and Cundall 1988).

Such a modelling philosophy was a guideline in modelling yield pillar behavior in Chapter 9. The modelling provided a better understanding of progressive pillar deformation and failure and the associated stress redistribution and convergence of mine openings. The results can be used to guide future pillar design.

A comprehensive research approach that combines the results of laboratory testing, *in situ* observations and analytical/numerical simulation has been followed in this thesis. Such a comprehensive, three-step research methodology seems to be essential for most rock engineering projects. Laboratory tests provide basic mechanical models and necessary parameters and *in situ* documentation provides essential data for theoretical/numerical modelling. The modelling results, in turn, contribute to better understanding and more realistic mine design.

## 10.2 Conclusions

(1) The general nature of potash deformation reflected by axial stress vs. axial, lateral and volumetric strain curves in a reverse loading test is similar to that of conventional compression tests obtained by Lajtai et al. (1991a), i.e., composed of pre-fractured, yielding, microfracture propagation, dilatancy and post failure stages.

(2) Potash behavior under a reverse loading path is strongly rate dependent, as reflected by the dependence of initial axial deformational moduli, the ductile yield point,

and post-peak behavior on the rate at which the deviatoric stress was applied to the specimens. The initial axial deformational moduli ranged from 29 GPa at the fastest stress rate to 12 GPa at the lowest stress rate; the deviatoric stress at the ductile yield point ranged from 7.6 MPa at the fastest stress rate to 2.3 MPa at the slowest stress rate, and the lowest stress rate induced the largest amount of ductile strain after yield, while the highest stress rate induced the smallest amount of ductile strain before the ultimate failure point.

(3) The general nature of the axial stress-axial strain curve from multiple-stage repeated relaxation tests is similar to those obtained from direct reverse loading tests. The inserted relaxation phases do not have a significant effect on the stress-strain curve. This phenomenon indicates a potential advantage in using inserted relaxation tests to investigate time dependent behavior at various stages of deformation during a single test. The same task by creep testing would be extremely time consuming and several tests would be required instead of one.

(4) The relationship between normalized stress drop ( $\sigma_1/\sigma_u$ ) and logarithm of time is linear. This suggests that the stress rate may not become zero before stress becomes zero, and therefore, that Lanigan potash has no creep limit, i.e. its longterm strength is zero. The Bingham model that has been well-accepted for salt rock analysis may not be valid for Lanigan potash since in this model the longterm strength is equivalent to the yield stress.

(5) The relaxation behavior of Lanigan potash before failure can be approximated by a strain-hardening constitutive law postulated by Haupt, with the effect of confining

pressure incorporated.

(6) The new combined compression-tension testing technique allows the direct measurement of deformational moduli in tension and in compression of rocks from the same sample in the same compression frame. Using this test, bimodularity has been demonstrated in halite, granite, and limestone.

(7) The bimodular constitutive model **MWCM** has been incorporated into the finite element program SIMEX. The program's accuracy has been validated against analytical solutions.

(8) Some aspects of the practical significance of rock bimodularity have been investigated analytically and numerically. It has been shown that rock bimodularity has significant effects on the interpretation of indirect rock tensile tests and roof behavior around underground openings. For rocks in which Young's modulus in tension is less than that in compression, the tensile strength derived from the beam bending, hydraulic extension, Brazilian and ring tests is overestimated if bimodularity is ignored. The actual tensile strength can be estimated only if the ratio of Young's moduli in tension and in compression is known. Ignoring bimodularity underestimates roof deflection and overestimates the possibility of tensile cracking in the roof at low horizontal stresses.

(9) Pillar deformation at the Cominco Mine over a period of 8 years has been shown to involve bulk rock flattening, development of shear zones at pillar corners, development of shear wedges at pillar margins, and the detachment of those shear wedges into adjacent rooms.

(10) Bulk rock strain in pillars has been achieved through a combination of brittle

deformation of halite, plastic deformation of sylvite and grain boundary sliding.

(11) Deformational mechanisms in halite include fracturing and displacement and rotation of fragments. Sylvite deforms continuously through mechanisms yet to be determined.

(12) The bulk rock strain has led to the development of a fabric anisotropy that can be detected by the centre-to-centre method or by the grain shape method. The fabric anisotropy ellipsoids determined by the two methods have similar orientations but different dimensional ratios.

(13) Both types of ellipsoids indicate flattening according to the Flinn classification system. Shortening has occurred in the vertical to subvertical orientation, greatest elongation has taken place in the horizontal to subhorizontal direction normal to the original openings, and lesser elongation has taken place parallel to the original openings.

(14) Neither type of fabric anisotropy ellipsoid is fully sensitive to strain produced by grain boundary sliding, consequently neither registers total bulk rock strain. However, the shape ellipsoids are useful in tracking sylvite strain variations during progressive pillar failure and have been included in the proposed progressive yield pillar deformation model.

(15) The initiation and propagation of corner shear zones observed in potash yield pillars can be simulated numerically on the basis of the theory of linear elastic fracture mechanics. Finite element modelling indicated that the corner fractures are pure mode II fractures (under shear stress). However, LEFM does not provide a correct prediction for the direction of crack propagation. In determining the direction of fracture propagation,

the assumption that fracture propagates along the direction of the maximum compressive stress direction was followed. Once corner fractures propagated to the middle height of the pillar, stresses were relieved in the isolated wedges or shear wedges at the margins of the pillar.

(16) Simulation of progressive, viscoplastic pillar deformation reproduced all four stages of the conceptual yield pillar deformational model proposed in Chapter 8 (Figure 8.22). The computer model demonstrated the initiation and extension of corner ductile shear zones through the development of narrow bands of plastic strain localization. Stress analysis also showed that as yield pillar deformation increased, the location of the peak stress transferred from the yield pillar to the abutment pillar, and continued to move into the abutment with time, signifying the progressive extension of yielding around openings.

### **10.3 Recommendation for Future Research**

Although considerable progress has been made in understanding salt mechanics and related engineering problems, there are many aspects that remain unknown. It is probably fair enough to say that what we have not understood yet is much more than what we have come to understand. The topics for research range from basic mechanical to engineering related problems. Furthermore, new topics reveal themselves as research progresses. Following is a list of some of the remaining problems relating to this study, which appear to be interesting and worth further research:

1. Multiple-stage, repeated relaxation tests have many advantages over creep tests or single stage relaxation tests. More such tests would be very useful for confirming the

non-existence of a creep limit in potash and to validate and modify the stress-strain equations proposed in Chapter 5 and other existing constitutive models. The development of any valuable constitutive models should actually be based on both sufficient creep and relaxation data. Constitutive equations and their derivation should include both a creep term and a relaxation term independently. Furthermore, any relaxation as well as creep tests would be more meaningful if they are accompanied by microfabric analyses of deformed rock samples to identify deformational mechanisms dominating at various stages of deformation.

2. All the repeated-relaxation tests in this study were performed along the pre-failure part of the stress-strain curve. Some relaxation tests along the unloading part of the stress-strain curve (after failure) would be very useful for studying post-failure time dependent characteristics. In order to do this, the initial hydrostatic stress in the tests should be higher, say at least 35 MPa.

3. It would be useful to apply the new combined compression-tension testing technique to other rock types to build a data base on rock bimodularity and to accumulate rock elastic parameters in tension. These data are still not available for most rocks.

4. The general characteristics of a compressive stress-strain curve for potash appear similar to that of halite. However, potash deforms quite differently in tension than in compression. Its behavior in tension is also very different from halite deformation in tension. Potash tensile stress-strain curves show a linear-elastic response up to the final failure. Exploring the reason for these differences would be very useful because it raises questions as to the common belief that elastic properties of salt rocks are independent of

location and type of salt. In the author's opinion, this should be carried out by micro-fabric analyses to identify the deformational mechanisms that might account for such differences.

5. Studies of the influence of material bimodularity in other rock engineering problems, such as in hydraulic fracture and rock fragmentation, would have both theoretical and practical value.

6. Deformational mechanisms in potash are still not clear, especially in sylvite crystals. The fact that both sylvite and halite are optically isotropic means that a methodology such as TEM will be required to identify specific mechanisms. Estimation of grain boundary sliding and strain accumulated in other mineral components, including interstitial clay, would help in understanding the representation of object strain results and centre-to-centre strain results and their relation to overall bulk rock strains.

7. The numerical simulation in this study broadly reproduced the phenomena observed within yield pillar sections in the Cominco Mine. Further research could include the effects of material parameters (fluidity, angle of internal friction, and cohesion), opening and pillar geometry, sequence of excavation, neighboring panels, and further consideration of the effect of clay layers.

8. In modelling corner ductile shear zones, the phenomenon of strain localization was utilized. However, the development of strain localization in the present form of SIMEX largely depends on mesh size and orientation. Incorporating various theories of strain localization phenomena would be most desirable in order to improve simulation models.

9. Finally, simulation of yield pillars with backfilling would yield very interesting information for controlling subsidence and increasing extraction ratios.

## REFERENCES

- Adler, L. 1970. Double elasticity in drill cores under flexure. *Int. J. Rock Mech. Min. Sci.*, **7**, 357-370.
- Ahmed, M. 1990. A study of possible failure mechanisms for mining-induced seismicity in Saskatchewan. *Ph.D Thesis*, Department of Civil Engineering, University of Manitoba, Winnipeg, Manitoba.
- Ambartsumyan, S.A. 1966. Equations of the plane problem of the multimodulus theory of elasticity. *Izvestiya Akademii Nauk Armanskoi SSR, Mekhanika*, **19**, 3-19 (Translation available from the Aerospace Corp., El Segundo, Calif. as LRG-67-T-14).
- Arthur, J.R.F., Dunstan, T., Al-Ani Q.A.J. and Assadi A. 1977. Plastic deformation and failure in granular media. *Geotechnique*, **27**, 53-74.
- Ashby, M.S. 1972. A first report of deformation mechanism maps. *Acta. Metal*, **20**, 887-897.
- Aubertin, M., Gill, D.E. and Ladanyi, B. 1989. The active stress concept and the creep of rock salt. *Proceedings*, Sixth Int. Congr. on Rock Mechanics, Montreal, Canada, Balkema, Rotterdam, 1501-1503.
- Aubertin, M., Gill, D.E. and Ladanyi, B. 1991. A unified viscoplastic model for the inelastic flow of alkali halides. *Mech. of Mater.* **11**, 63-82.
- Ayari, M.L. 1991. SIMEX (SIMulation of Mining EXcavation) Menu, Elastic Version. *Internal Report*, Geological Engineering, University of Manitoba.
- Ayari, M.L. 1992. SIMEX Menu, Viscoplastic Version. *Internal Report*, Mechanical Engineering, University of Manitoba.
- Baar, C.A. 1966. Measurements of rock pressure and pillar loads in deep potash mines. *Proceeding*, II Salt Symposium, Northern Ohio Geological Society, 18-33.
- Baar, C.A. 1970. Correct interpretation of data for better understanding of salt pillar behavior in mines. *Proceeding*, III Salt Symposium, Northern Ohio Geological Society, 280-289.
- Baar, C.A. 1971. Creep measured in deep potash mines vs. theoretical predictions. *Proceedings*, 7th Canadian Rock Mech. Symp., 23-77.
- Baar, C.A. 1972. Dangerous applications of laboratory parameters to the design of deep mines. *Internal Report*, E 72-6, Saskatchewan Research Council.

Baar, C.A. 1973 Analysis of time-dependent deformations of opening in salt media; investigation into the mechanism of creep deformation in carnallite, and practical applications. Discussion, *Int. J. Rock Mech. Min. Sci. & Geomech. Abs.*, **10**, 251-254.

Baar, C.A. 1977. *Applied Salt-Rock Mechanics - 1: The In-situ Behavior of Salt Rocks*, Elsevier Scientific, Amsterdam, 294 p.

Bakhtar, K. 1979. Development of long term creep-testing facilities for evaluation of inelastic behavior in salt. *M.S. Thesis*, Department of Mineral Engineering, The Pennsylvania State University, August, 227 p.

Bakhtar, K. Hardy, H.R., Richardson, A.M., Mrugala, M.J. 1988. Experimental results and modelling of long-term creep behavior of rock salt, Key Questions in Rock Mechanics: *Proceedings*, 29th US Symposium, Minneapolis, 13-15 June, 1988, Publ. Rotterdam: A.A. Balkema, 169-178.

Balthasar, K., Haupt, M., Lempp, C. and Natau, O. 1987. Stress relaxation behavior of rock salt: comparison of in situ measurements and laboratory test results. *Proceedings*, Sixth International Congress on Rock Mechanics, **1**, 11-13.

Bardet, J.P. and Mortazavi, S.M. 1987. Simulation of shear band formation in overconsolidated clay. *Constitutive Laws for Engineering Materials. Theory and Applications*, Desai, C.S. and Saxena, S.K., eds, **2**, 805-812.

Barsoum, R.J. 1977. Triangular quarter point elements as elastic and perfectly-plastic crack tip elements. *Int. J. Num. Meths. in Engr.* **11**(1).

Beek, M.A., Garbe, B., Geier, W., Hunsche, U. and Plischke, I. 1984. In-situ deformation measurements of a rock salt pillar using methods of coherent optics. *Optoelektronik in der Technik*; 6. Int. kongr. -Laser 83, Springer Verl., Berlin, 3 Tab, 9 Abb, 170-181.

Beer, F.D. and Johnston, E.R.Jr. 1981. *Mechanics of Materials*, McGraw-Hill Inc.

Bert, C.W. and Reddy, V.S. 1980. Cylindrical shells of bimodular composite material. *Proceedings*, Prepv-ASCE Conv. & Expo., Hollywood, Fla, Oct. 27-31, 1980 Publ by ASCE, New York, prepv.80-623, 139.

Bert, C.W. and Kumer M. 1981. Vibration of cylindrical shells of bimodular composite materials. *Collet Tech Pap AIAA ASME ASCE AHS Struct Dyn Mater Conf 22nd Pl3 and AIAA Dyn Spec Conf*, Allaufa, Ga Apr.6-10, 1981 Publ by AIAA(cpp812) NY Pap 81-0525, 147-154.

- Bert, C. W., Reddy, J. N., Chao, W. C. and Reddy, V. S. 1981. Vibration of thick rectangular plates of bimodulus composite material. *ASME Pap n81-APM-28* for meet Jun 22-27, 1981, 6p. Also: *J Appl Mech Trans ASME* 48, 371-376.
- Bert, C.W. and Tran, A.D. 1982. Transient response of a thick beam of bimodular material. *Earthquake Engineering and Structural Dynamics*, **10**, 551-560.
- Bert, C. W. 1983a. Prediction of bending rupture strength of non-linear materials with different behavior in tension and compression, *Int J Non Linear Mech*, **18**, 353-361.
- Bert, C. W. 1983b. Bending of laminated thick beams of bimodular material, *Rebello, Clifford J. Eng Struct*, **5**, 227-231.
- Bert, C.W. 1985. On mechanics of composite structures. *Proceedings of the 19th Midwestern Mechanics Conference*. Sept. 9-11, Columbus.
- Bert, C. W. and Ko, C. L. 1985. Buckling of columns constructed of bimodular materials. *International Journal of Engineering Science*, **23**, 641-657.
- Bieniawski, Z.T. 1984. *Rock Mechanics Design in Mining and Tunneling*, A.A. Balkema, Rotterdam and Boston, 272 p.
- Booker, J.R., Carter, J.P., Small, J.C., Brown, P.T. and Poulos, H.G. 1989. Some recent applications of numerical methods to geotechnical analysis. *Research report - University of Sydney, School of Civil and Mining Engineering*, n 598, May, 34 p.
- Boucly, P. 1984. In situ experience and mathematical representation of the behavior of rock salt used in storage of gas. *Proceedings, 1st Conf. on the Mechanical Behavior of Salt*, Trans Tech Publications, Clausthal, Germany, 453-471.
- Bradshaw, R. L., Boegly, W. J. and Empson, F. M. 1964. Correlation of convergence measurements in salt mines with laboratory creep data. *Proceedings, 6th Symp. Rock Mechanics*, Rolla, Missouri, 501-514.
- Brady, B.H.G. and Brown, E.T. 1985. *Rock Mechanics for Underground Mining*, Allen and Unwin, London, 527 p.
- Brown, E.T., Ed. 1987. *Analytical and Computational Methods in Engineering Rock Mechanics*, Allen and Unwin, London, Boston, Sydney, Wellington, 259 pp.
- Burshtein, L. S. 1967. Rock strength under axial tension and flexure. *Fiziko-Tekhnicheskie Problemy*, 53-61.

Carneiro, F. 1947. Une Nouvelle methode d'essai pour determiner la resistance a la traction du beton. *Reunion des Laboratoires d'Essai de Materiaux*, Paris.

Carter, B.J., Lajtai, E.Z. and Petulikov, A. 1991a. Primary and remote fracture around underground cavities. *Int. J. Numerical and Analytical Methods in Geomechanics*, **15**, 21-40.

Carter, B.J., Duncan, E.J.S. and Lajtai, E.Z. 1991b. Fitting strength criteria to intact rock. *Geotechnical and Geological Engineering*, **9**, 73-81.

Carter, B.J. and Lajtai, E.Z. 1991. Time and stress dependent of fracture propagation in potash rock, Fracture in Potash. *Report*, Department of Geological Engineering, University of Manitoba.

Carter, B.J. 1992a. Size and stress gradient effects on fracture around cavities. *Rock Mechanics and Rock Engineering*, to be published.

Carter, B.J. 1992b. Physical and numerical modeling of fracture in rock, with special emphasis on the potash mines of Saskatchewan. *Ph.D Thesis*, Department of Civil Engineering, the University of Manitoba.

Carter, B.J., Lajtai, E.Z. and Yuan, Y. 1992. Tensile fracture from circular cavities loaded in compression. *International Journal of Fracture* (in press).

Carter, N.L. and Hansen, F.D. 1983. Creep of rocksalt. *Tectonophysics*, **92**, 275-333.

Chaudler, N.A. 1989. An energy approach to sleeve fracture stress measurements. *Ph.D. Thesis*, Department of Civil Engineering, the University of Manitoba.

Chen, G. and Karmis, M. 1988. Computer modelling of yield pillar behavior using post-failure criteria. *Proceedings*, 7th International Conference on Ground Control in Mining, edited by Syd S. Peng, 116-125.

Chen R., Ayari, M. L. and Stimpson, B. 1991. Influence of material bimodularity on the behavior of underground mining structures. *Proceedings*, 13th Canadian Congress of Applied Mechanics, June 2-6, 720-721.

Chen, Rui, Brisbin, W.C. and Stimpson, B. 1993. Mining induced deformation in potash yield pillars, Vanscoy, Saskatchewan. *Canadian Geotechnical Journal*, (in press, to appear in April, 1993).

Chen, Rui and Stimpson, B. 1993a. Indirect tension tests on rock - analytical/numerical correction for material bimodularity. *ASTM Geotechnical Testing Journal*, (in press, to appear in June, 1993).

Chen, Rui and Stimpson, B. 1993b. Effect of different compression and tension moduli on indirect rock tensile strength tests. *Rock Mechanics and Rock Engineering*, (in press).

Cloos, E. 1947. Oolite deformation in the South Mountain fold, Maryland. *Geological Society of America Bulletin*, 58, 843-918.

Coates, D.F. 1965. Pillar loading, Part I - literature survey and new hypothesis. *Report*, Mines Branch Research Report R168, Canada, Department of Mines and Technical Surveys, Ottawa, October 1965.

Cominco Ltd. 1985. Collection and evaluation of field data around excavations in potash to evaluate excavation performance or concepts for new mining layouts. *Internal Report*.

Conover, D.P., Haramy, K.Y. and Hanna, K. 1989. Methods to determine pillar stress distribution and its effect on stability. Rock Mechanics as a Guide to Efficient Utilization of Natural Resource, *Proceedings*, 30th Symposium on Rock Mechanics, Published by A.A. Balkema, 419-426.

Coolbaugh, M.J. 1967. Special problems of mining in deep potash, rock mechanics investigation of structural properties of potash and salt under high stress conditions. *AIME Transactions*, Society Mining Engineering, 238, 323-329.

Cristescu, N.D. 1992. *Rock Viscoplasticity*, Notes for Tempus Summer School, June, Bucharest University, 98 p.

Cundall, P. A. 1976. Explicit finite difference methods in geomechanics. *Numerical Methods in Geomechanics*, C. Desai edit, ASCE, New York, 1, 132-150.

Cundall, P.A. 1987. Distinct element models of rock and soil structure. *Analytical and Computational Methods in Eng. Rock Mech*, E. Brown edit, Allen & Unwin, London, 130-163.

Cundall, P.A. and Hart, R.D. 1983. Development of generalized 2-D and 3-D distinct element programs for modeling jointed rock. *Report*, U.S. Army Engineers Waterways Exp. Stat. Tech.

Cundall, P.A. 1989. Numerical experiments on localization in frictional materials. *Ingenieur-Archiv*, 59, 148-159.

Daemen, J.J.K. and Fairhurst, C. 1971. Influence of failed rock properties on tunnel stability. *Proceedings*, 12th U.S. Rock Mech. Symp, 855-875.

Daemen, J.J.K. 1975. Tunnel support loading caused by rock failure. *Report*, Tech. Rep-MRD-3-75, Missouri River Div., U.S. Corps Engs, Omaha.

- Dawson, P.R. and Munson, D.E. 1983. Numerical simulation of creep deformation around a room in a deep potash mine. *Int. J. Rock Mech. Min. Sci. & Geomech. Abstr.*, **20**, 33-42.
- De Borst, R. 1988. Bifurcations in finite element models with a non-associated flow law. *Int. J. Num. Anal. Meths. Geomech.*, **12**, 99-116.
- De Souza, E.M. 1991. Automated system to monitor mine instrumentation. *Mining Technology*, **73**, n 849, Oct., 8 p.
- De Souza, E.M. 1992. Data acquisition system for geotechnical instrumentation and design. *CIM Bulletin*, **85**, 43-47.
- Denkhaus, H. 1962. A critical review of the present state of scientific knowledge related to the strength of the mining pillars. *Jl S. Afr. Inst. Min. Metall*, **63**, 59-75.
- Desai, C.S., Somasundaram, S. and Frantziskonis, G. 1986. A hierarchical approach for constitutive modeling of geologic materials. *Int. J. Numer. Analyt. Meth. in Geomech.* **10**, 225-257.
- Desai, C.S. and Zhang, D. 1987. Viscoplastic model for geologic materials with generalized flow rule. *Int. J. Numer. Analyt. Meth. in Geomech.* **11**, 603-620.
- Detournay, E. and Fairhurst, C. 1987. Two-dimensional elastoplastic analysis of a long cylindrical cavity under non-hydrostatic loading. *Int. J. Rock Mech. of Min. Sci. and Geomech. Abstr.*, **24**, 197-211.
- Dreyer, W. and Borchert, H. 1965. Development of new types of measurement apparatus to determine the absolute stress in salt pillars. (In German), *Kali und Steinsalz*, **4**, 112-114.
- Duncan, E.J.S. 1990. Deformation and Strength of Saskatchewan Potash Rock. *Ph.D Thesis*, Department of Civil Engineering, University of Manitoba.
- Duncan, E.J.S. and Lajtai, E.Z. 1991. The creep of Saskatchewan potash rock in uniaxial compression. Fracture in Potash, *Report*, Department of Geological Engineering, the University of Manitoba.
- Dunn, C.E. 1982. Geology of the Middle Devonian Dawson Bay Formation in the Saskatoon potash mining district, Saskatchewan. *Report*, Sask. Energy, and Mines, 194 p.
- Dunn, C.E. 1983. The Dawson Bay Formation and its relationship to the underlying Prairie Evaporite in the Saskatoon area, Saskatchewan. *Proceedings*, First International

Potash Technology Conference, Potash'83, 41-46.

Duvall, W.Z. 1948. Stress analysis applied to multiple openings and pillars. *Report*, USBM, R1 4387, November.

Erdogan, F. and Sih, G.C.. 1963. On the crack extension in plates under plane loading and transverse shear. *A.S.M.E. J. Basic Engr.*, **85**, 519-527.

El-Tahan, W.W., Staab, G.H., Advani, S.H. and Lee, J.K. 1989. Structural analysis of bimodular materials. *Journal of Engineering Mechanics*, **115**, 963-981.

Erslev, E.A. 1988. Normalized center-to-center strain analysis of packed aggregates. *Journal of Structural Geology*, **10**, 210-209.

Erslev, E.A. 1989. *Instruction Manual for INSTRAIN 2.5*. Copyright 1987-89 Eric Erslev, Colorado State University.

Ewy, R.T. and Cook, N.G.W. 1990. Deformation and fracture around cylindrical openings in rock, Parts I and II. *Int. J. Rock Mech. Min. Sci. & Geomech. Abstr.*, **27**, 387-427.

Fairhurst, C. 1961. Laboratory measurements of some physical properties of rock. *Proceedings*, Fourth Symp. Rock Mechanics Bull. **76**, Mineral Ind. Experiment Station, Pennsylvania State U., University Park.

Fairhurst, C. 1991. Private communications.

Feder, G. 1978. Shear fracture of rock mass in vicinity of deep cavities - test results and analytical concepts (in German). *Rock Mechanics*, Suppl. **6**, 71-102.

Felsmechanik, L.F. 1988. Uniaxial relaxation tests on rock salt. *Proceedings*, Second Conference on the Mechanical Behavior of Salt, Federal Institute of Geosciences and Natural Resources, Hanover, September 1984, Trans Tech Publications, Clausthal, Germany.

Findley, W.N. and Khosla, G. 1955. Application of the superposition principle and theories of mechanical equation of state, strain, and time hardening to creep of plastics under changing loads. *J. of Appl. Physics*, **26**, 821-832.

Franklin, J.A. and Dusseault, M.B. 1989. *Rock Engineering*, McGraw-Hill Publishing Company.

Franklin, J.A. and Dusseault, M.B. 1991. *Rock Engineering Application*, McGraw-Hill Publishing Company.

Frocet, M.M. 1948. *Photoelasticity*. 2, New York, John Wiley and Sons Inc. London, Chapman and Hall Ltd. 121-129.

Fry, N. 1979. Random point distributions and strain measurement in rock. *Tectonophysics*, **60**, 806-80

Fuzesy, A. 1982. Potash in Saskatchewan. *Report*, Saskatchewan Energy and Mines, Report No. 181, p 46.

Gendzwill, D. J. 1978. Winnipegosis mounds and Prairie Evaporite Formation of Saskatchewan - seismic study. *American Association of Petroleum Geologists Bulletin*, **62**, 73-86.

Gendzwill, D. J., Horner, R.B. & Hasagawa, H.S. 1982. Induced earthquakes at a potash mine near Saskatoon, Canada. *Canadian J. Earth Sciences*, **19**,

Gendzwill, D.J. 1984. Induced seismicity in Saskatchewan potash mines. *Proceedings*, First International Congress on Rockbursts and Seismicity in Mines, N. C. Gay and Z.H. Wainwright edit, Johannesburg, 1982, SAIMM. Johannesburg.

Gendzwill, D.J. and Prugger, A.F. 1987. Seismic studies in Saskatchewan potash mines. *Presentation*, Workshop of Mining Induced Seismicity, Montreal.

Gendzwill, D.J. and Prugger, A.F. 1988. Seismic activity in a flooded Saskatchewan potash mine. *Proceedings*, 2nd International Symposium of Rockbursts and Seismicity in Mines, Minneapolis, 8-10 June 1988, 139-148.

Gendzwill, D.J. 1989. Seismic case history of some Saskatchewan potash mines. *Abstracts*, Annual Meeting of the Canadian Society of Exploration Geophysicists, Calgary, Alberta, 55 p.

Gendzwill, D.J. and Lundberg, R.M. 1989. Seismic anomalies of Saskatchewan Winnipegosis mounds, Geophysical Atlas of Western Canada Hydrocarbon Reservoirs. *Report*, Canadian Society of Exploration Geophysicists.

Goodman, R.E. and Shi, G.H. 1985. *Block Theory and Its Application to Rock Engineering*, Prentice-Hall, Inc., Englewood Cliffs, New Jersey 07632.

Gordaninejad, F. and Bert, C.W. 1989. A new theory for bending of thick sandwich beams. *International Journal of Mechanical Sciences*, **31**, 925-934.

Gordaninejad, F. 1989. Nonlinear bending of anisotropic bimodular composite-material plates. *Computers and Structures*, **33**, 615-620.

Griffiths, D.V. 1981. Computation of strain softening behavior. *Implementation of Computer Procedures and Stress-Strain Laws in Geotechnical Engineering*, Desai, C.S. and Saxena, S.K. eds, 2, 591-603, Acorn Press.

Gumusoglu, M.C.; Bray, J.W. and Watson, J.O. 1987. Analysis of underground excavations incorporating the strain softening of rock masses. *Proceedings*, 6th ISRM Cong., Montreal, 2, 923-928.

Guo Zhen-hai and Zhang Xiu-gin, 1987. Investigation of complete stress deformation curves for concrete in tension. *ACI Materials Journal*, 84, July-Aug., 278-285.

Haimson, B.C. and Tharp, T.M. 1974. Stresses around boreholes in bilinear elastic rock. *Society of Petroleum Engineers Journal*, 14, 145-151.

Hambley, D.F., Dusseault, M.B. and Mraz, D.Z. 1988. Characterization of salt rock creep behavior. Key Questions in Rock Mechanics: *Proceedings*, 29th US Symposium, Published by A.A. Balkema, 179-189.

Hambley, D.F. 1989. Pillar design for mines in saltrock. *Mining Science and Technology*, 9, 111-135.

Hansen, F.D. 1977. Case history - rock mechanics examination of the Jefferson Island Salt Mine: II. Laboratory evaluation of strength and creep deformation characteristics of dome salt under confining pressure, Office of Waste Isolation. *Report Y/OWI/SUB-77/22303/5*, 141 pp.

Hansen, F.D. and Mellegard, K.D. 1980. Creep of 50-mm diameter specimens of some salt from Avery Island, Louisiana. *Report*, RE/SPEC, ONWI-104.

Hansen, F.D. and Carter, N.L. 1980. Creep of rock salt at elevated temperature. *Proceedings*, 21st U.S. Symp. on Rock Mechanics. May 28-30, University of Missouri - Rolla. Preprint.

Hansen, F.D. and Carter, N.L. 1984. Creep of Avery Island rocksalt. *Proceedings*, First Conference on the Mechanical Behavior of Salt, Hardy and Langer edit, Trans Tech Publications, 53-69.

Hansen, F.D. and Senseny, P.E. 1983. Petrofabrics of deformed salt. *Proceedings*, the First International Potash Technology Conference, edited by McKercher, 347-353.

Hardikar, M.A., Fahreuthold, E.P. and Grany, K.E. 1987. Microcomputer control of triaxial rock compaction and creep tests. *Proceedings*, 28th US Symposium on Rock Mechanics/Tucson/29 June - 1 July.

- Hardy, Jr. H. R. and Jayaraman, N. I. 1970. An Investigation of Methods for the Determination of the Tensile Strength of Rock. *Proceedings*, 2nd Cong. Rock Mech., Beograd, paper no. 5-12.
- Hardy, H.R., Jr. and Langer, M. (ed.) 1984. *Proceedings*, First Conference on the Mechanical Behavior of Salt, Pennsylvania State University, Trans Tech Publications, Clausthal, Germany.
- Hardy, H.R., Jr. and Langer, M. (ed.) 1988. *Proceedings*, Second Conference on the Mechanical Behavior of Salt, Federal Institute of Geosciences and Natural Resources, Hannover, Trans Tech Publications, Clausthal, Germany.
- Hart, R.D. 1990. Lecture: Discontinuum analysis for deep excavations in jointed rock. *Rock at Great Depth*, Maury & Fournaintraux (eds) Balkema, Rotterdam, 1123-1130.
- Haupt, M. and Natau, O. 1988. Uniaxial relaxation tests on rock salt. *Proceedings*, Second Conference on the Mechanical Behavior of Salt. 179-185.
- Haupt, M. 1991. A constitutive law for rock salt based on creep and relaxation tests. *Rock Mechanics and Rock Engineering*, 24, 179-206.
- Herget, G. et al. 1985. *Seminar*, Canadian Potash Mining and Ground Control.
- Herrmann, W., Wawersik, R.R. and Lauson, H.S. 1980. A model for transient creep of southeastern New Mexico rock salt. *Report*, SAND-80-2172, Sandia National Laboratories, Albuquerque, New Mexico, 47 p.
- Herrmann, W. and Lauson, H.S. 1981. Analysis of creep data for various natural rock salts. *Report*, SAND81-2567, Sandia National Laboratories, Albuquerque, New Mexico.
- Hill, R. 1962. Acceleration waves in solids. *J. Mech. Phys. Solids*, 10, 1-16.
- Hoek, E. and Brown, E.T. 1980. *Underground Excavations in Rock*, Inst. Min. Metall., London, 527 p.
- Hobbs, D.W. 1964. The tensile strength of rocks. *Int. J. Rock. Mech. Mining Sci.* 1, 385-396.
- Holter, M.E. 1969. The Middle Devonian Prairie Evaporite of Saskatchewan. *Report*, Saskatchewan, Mineral Resources Department, report 123, 133 p.
- Horseman, S. and Passaris, E. 1984. Creep tests for storage cavity closure prediction. *Proceedings*, First Conference on the Mechanical Behavior of Salt, Trans. Tech. Publications, Clausthal, West Germany, 119-157.

- Hudson, J.A. 1989. *Rock Mechanics Principles in Engineering Practice*, Butterworths.
- Hunsche, U., Plischke, I, Nipp, H.K. and Albrecht, H. 1985. An in-situ creep experiment using a large rock-salt pillar. *Proceedings*, Sixth International Symposium on Salt, May, Toronto, Canada.
- Hunsche, U. and Albrecht, H. 1990. Results of true triaxial strength tests on rock salt. *Engineering Fracture Mechanics*, 35, 867-877.
- Hunsche, U. 1991a. Volume change and energy dissipation in rock salt during triaxial failure tests. *Proceedings*, Coll. 'Mechanics of Creep Brittle Materials 2', A. Cocks and A. Ponter edited, Leicester (UK), set. 172-182.
- Hunsche, U. 1991b. True triaxial failure tests on cubic rock salt samples - experimental methods and results. *Proceedings*, IUTAM-Symposium, Hannover, Aug. Berlin.
- Hussian, M.A., Pu, S.L. and Underwood, J. 1974. Strain energy release rate for a crack under combined mode I and II. *Fracture Analysis*, ASTM STP 560, 2-28.
- Ingraffea A. R. 1983. Numerical modeling of fracture propagation. *Rock Fracture Mechanics* (ed. by H.P. Rossmanith), Springer-Verlag, Berlin.
- Jeness, J.R., Jr. and Kline, D.E. 1974. Comparison of static and dynamic mechanical properties of some epoxy-matrix composites. *Journal of Testing and Evaluation*, 2, 483-488.
- Jaeger, J.C. and Cook, N.G.W. 1979. *Fundamentals of Rock Mechanics*, third edition, Chapman and Hall, London, 170 p.
- Jones, R.M. 1977. Stress-strain relations for materials with different moduli in tension and compression. *AIAA Journal*, 15, 16-23.
- Jortner, J. 1972. Uniaxial and biaxial stress-strain data for ATS-Sgraphite at room temperature. *Report*, MGCG3564, McDonnell-Douglas Astronautics Co.
- Kaiser, P. K. 1979. Time-dependent behavior of tunnels in jointed rock masses. *Ph.D. Thesis*, Department of Civil Engineering, University of Alberta.
- Kaiser, P.K. 1987. Detection of rock mass rupture modes. *Proceedings*, 6th International Rock Mechanics Congress of ISRM, Montreal.
- Kaiser, P.K. 1988. Overview of rock mass failure mechanisms. Professional Development *Seminar* on Rock Mass Failures in Hard Rock Mining at Canadian Mining and Industrial Equipment Exhibition, June 1-3, Sudbury.

Kaskiw, L., Morgan, R. and Ruse, D. 1989. Backfilling at IMC (Canada) K2 potash Mines. *Proceedings*, 4th International Symposium on Innovations in Mining and Backfill Technology, Montreal, Quebec.

Katsube, T.J. and Hume, J.P. 1987. Canadian Centre for Mineral and Energy Technology, Mining Research Laboratories Divisional *Report* MRL 87-52, 49-110.

Khan, F.K. and Irani, F.K. 1988. Failure behavior of rocks at ambient temperature. *Mechanics of Materials*, **6**, 271-283.

Khan, A. S. and Yuan, S. 1988. Three-dimensional finite element program for brittle bimodal rock-like materials. *International Journal for Numerical and Analytical Methods in Geomechanics*, **12**, Nov-Dec 599-609.

Kicker, D.C. and Park, D.W. 1986. Yield pillar simulation using physical modelling. Rock Mechanics: Key to Energy Production. *Proceedings*, 27th U.S. Symposium on Rock Mechanics, Published by the Society of Mining Engineering, 224-230 p.

King, M. S. and Acar, K. Z. 1971. Creep properties of Saskatchewan potash as a function of changes in temperature and stress. *Proc. 3rd Symp. on Salt*, Clev., Ohio, North. Ohio Geol. Soc., 226-235.

King, M.S. 1973. Creep in model pillars of Saskatchewan potash. *Int. J. Rock Mech. Min. Sci. & Geomech Abstr.*, **10**, 363-371.

Kripakov, N.P. 1981. Finite element analysis of yield pillar stability. *Computers and Structures*, **13**, 575-593.

Kripakov, N.P. and Melvin, M.T. 1983. A computer procedure to simulate progressive rock failure around coal mine entries. *Proceedings*, 1st Conf. on Use of Computers in Coal Industry, Y.J. Wang and R.L. Sanford, Editors, West Virginia Univ., Morgantown, WV, 1983, 487-502.

Kroll, D.W. 1987. Basic geomechanical properties of the Dawson Bay Formation. *M.Sc. Thesis*, Department of Civil Engineering, University of Manitoba.

Labuz, J.F. 1985. A study of the fracture process zone in rock. *Ph. D. thesis*, Northwestern University.

Ladanyi, B. and Gill, D.E. 1983. In-situ determination of creep properties of rock salt. *Proc. 5th Cong. ISRM*, **1**, Melbourne, A219-A225.

Lajtai, E.Z. 1982. The fracture of Lac du Bonnet granite. *Report to Atomic Energy of Canada Ltd.*, Whiteshell Nuclear Research Establishment, 126 p.

Lajtai, E.Z. and Duncan, E.J.S. 1988. Mechanism of deformation and fracture in potash rock. *Can. Geotech. J.* **25**, 262-278.

Lajtai, E.Z., Shields, D.H. and Stimpson, B. 1988. Mine stability in potash mining. *Report*, Progress Report CRD-8506, Departments of Civil and Geological Engineering, University of Manitoba.

Lajtai, E.Z., Carter, B.J. and Duncan, E.J.S. 1991a. Mapping the stage of fracture around cavities. *Engineering Geology*, **31**, 277-289.

Lajtai, E.Z., Duncan, E.J.S. and Carter, B.J. 1991b. The effect of strain rate on rock strength. *Rock Mechanics and Rock Engineering*, **24**, 99-109.

Lajtai, E.Z. 1989 and 1990. Project report on mining-induced fracture - year 1 and year 2, NSERC File # 661-107/87.

Lajtai, E.Z. ed. 1991. Fracture in Potash. NSERC Research Report, Department of Geological Engineering, University of Manitoba.

Lajtai, E.Z. 1992. Personal communication.

Lama, R.J. and Vutukuri, V.S. 1978. Tensile strength of rock. *Handbook on Mechanical Properties of Rock*, Trans Tech Publications, 1, 87-140.

Lane, D.M. 1959. Dawson Bay Formation in the Quill Lades - Qu'Appelle area. *Report*, Saskatchewan, Mineral Resources Department, 28, 49 p.

Langer, M. 1982. Geotechnical investigation methods for rock salt. *Bull. Int. Assoc. Engng. Geology*, **25**, 155-164.

Langer, M. 1984. Rheological behavior of rock salt. *Proceedings*, First Conference on the Mechanical Behavior of Salt, Publ by Trans Tech Publications, Clausthal-Zellerfeld, West Germany, and Gulf Publ Co, Houston, TX, USA and London, Engl, 201-240.

Langer, M. 1986. Rheology of rock-salt and its application for radioactive waste disposal purposes. *Proceedings*, Int. Symp. on Eng. in Complex Rock Formations, Nov, Beijing, Science Press, Beijing.

La Pointe, P.R. 1988. A method to characterize fracture density and connectivity through fractal geometry. *Int. J. Rock Mech. Min. Sci. & Geomech. Abstr.* **25**, 421-429.

Landner, E.N. and Brady, B.H.G. 1984. Memory aspects of salt creep. *Proceedings*, 1st Cong. on the Mechanical Behavior of Salt, Trans Tech Publications, Clausthal, West Germany.

Lisle, R. J. 1977. Estimation of the tectonic strain ratio from the mean shape of deformed elliptical markers. *Geologieen Mijnbouw*, **56**, 140-144.

Logie, C.V. and Matheson, G.M. 1983. A critical review of current state-of-the-art design of mine pillars. *Stability in Underground Mining*, C.O. Brawner (edi), Edwards Brothers Inc., Ann Arbor, Michigan, 359-382.

Lomenick, T. F. and Bradshaw, R. L. 1969. Deformation of rock salt in openings mined for the disposal of radioactive wastes. *Rock Mech.* **1**, 5-30.

Lu, Paul H. 1986. Biaxial-loading measurement for mine-pillar stability evaluation - case studies, International Symposium on Application of Rock Characterization in Mine Design. *Proceedings*, of the Symposium held at the SME-AIME Annual Meeting, New Orleans, LA, USA, Mar, Publ by Soc of Mining Engineers of AIME, Littleton, CO, 142-151.

Luong, M.P. 1988. Direct tensile and direct shear strengths of Fontainebleau sandstone. Key Questions in Rock Mechanics. *Proceedings*, 29th U.S. Symposium on Rock Mechanics, Cundall et al edited, 237-246.

Lux, K.H. and Heusermann, S. 1983. Creep tests on rock salt with changing load as a basis for the verification of theoretical material laws. *Proceedings*, Sixth Int. Symp. on Salt, **1**, 417-435.

Mackintosh, A.M. & McVITTIE, G.A. 1983. Geological anomalies observed at the Cominco Ltd. Saskatchewan potash mine. *Proceedings*, first International Potash Technology Conference, Potash '83, 59-64.

Mandel, J., 1966, Conditions the stabilite et postulat de Drucker, *Proc. IUTAM Symp. on Rheology and Soil Mechanics* (Eds. J. Kravtchenko and P.M. Sirieys), Springer-Verlag, Berlin, 1966, 58-68.

Mandelbrot, B.B. 1983. *The Fractal Geometry of Nature*. W.H. Freeman and Company.

Martin, C.D. and Christianson, R. 1991. Overcoring in highly stressed granite - the influence of microcracking. *International Journal of Rock Mechanics and Mining Sciences & Geomechanics Abstracts*, **28**, 53-70.

McKercher, R.M. (ed). 1983. *Proceedings*, First International Potash Technology Conference, Pergamon Press Canada Ltd.

Mellegard, K.D., Senseny, P.E. and Hansen, F.D. 1981. Quasi-static strength and creep characteristics of 100-mm diameter specimens of salt from Avery Island, Louisiana. *Report*, RE/SPEC, ONWI-250.

Mellor, M. and Hawkes, I. 1971. Measurement of tensile strength by diametrical compression of discs and annuli. *Engineering Geology*, **5**, 173-225.

Molenkamp, F., 1985, Comparison of frictional material models with respect to shear banding initiation. *Geotechnique*, **35**, 127-143.

Mollard, J. 1988. Photolineament studies and the regional tectonic framework in southern Saskatchewan, *Abstract*, the Fifteenth Annual Meeting of the Canadian Geophysical Union, Saskatoon, Saskatchewan, 34 p.

Morgenstern, N.R. and Sepehr, K. 1991. Time-dependent hydraulic fracturing in potash mines. *Int. J. Rock Mech. Min. Sci. & Geomech. Abstr.* **28**, 187-197.

MPC. 1988. (micro-film).

Mraz, D.Z. and Dusseault, M.B. 1986a. Effect of geometry on the bearing capacity of pillars in saltrock. *Presentation*, In: Can. Inst. Min. - Rock Mech. Strata Control Workshop (Saskatchewan, Sack.).

Mraz, D.Z. and Dusseault, M.B. 1986b. Long term behavior of a test room in potash, *Rock Mechanics: Key to Energy Production* (H.L. Hertman ed), Society of Mining Engineers, Littleton, CO, 405-414

Mraz, D. and Eng P. 1984. Solutions to Pillar Design in Plastically Behaving Rocks. *Rock Mechanics and Strata Control*, *CIM Bulletin*, August.

Mroz, Z. & Nawrocki, P. 1989. Deformation and stability of an elasto-plastic softening pillar. *Rock Mechanics and Rock Engineering*, **22**, 69-108.

Mrugala, M. 1985. A laboratory study of the time-dependent behavior of salt. *Ph.D Thesis*, Dept. of Mineral Engineering, the Pennsylvania State University.

Mrugala, M. and Hardy, H.R., Jr. 1988. Effect of test duration on the viscoelastic parameters of salt. *Proceedings*, Second Conference on the Mechanical Behavior of Salt, Federal Institute of Geosciences and Natural Resources, Hannover, September 1984, Trans Tech Publications, Clausthal, Germany.

Munson, D.E. 1979. Preliminary deformation-mechanism map for salt. *Report*, SAND-79-0076, Sandia National Laboratories, Albuquerque, New Mexico, 37 p.

Munson, D.E. and Dawson, P.R. 1984. Salt constitutive modelling using mechanism maps. *Proc.*, 1st conf. on the Mechanical Model Behavior of Salt, Trans Tech Publications, Clausthal, West Germany.

Needleman, A. and Tvergaard, V. 1984. Finite element analysis of localization in plasticity. *Finite Elements: Special Problems in Solid Mechanics*, Oden, J. T. and Garey, G.F. eds, 94-157, Prentice-Hall, Englewood Cliffs, NJ.

Neelamegan, M., Ohama, Y., Demura, K., Suzuki, S. and Shirai, A. 1984. Deformation and durability of polymer-impregnated ferrocement, *ACI Journal*, Nov.-Dec.

Novak, R.C. and Bert, C.W. 1968. Theoretical and experimental bases for more precise elastic properties of epoxy. *J. of Composite Materials*, 2, 506-508.

Obert, L. 1964. Deformational behavior of model pillars made from salt, trona and potash Ore. *Proc. 6th Symp. Rock Mechanics*, Univ. of Missouri, Rolla, 539-60.

Obert, L. 1965. Creep in model pillars. *Report*, U.S. Bur. Mines, Invs. No. 6703

Ortiz, M., Leory Y. and Needleman, M. 1986. A finite element method for localized failure analysis, *Computer Methods in Applied Mechanics and Engineering*, 61, 189-214.

Owen, D.R.J. and Fawkes, A.J. 1983. *Engineering Fracture Mechanics: numerical methods and applications*, Pineride Press Ltd. Swansen, U.K.

Pan, Y.W. and Dong, J.J. 1991. Time-dependent tunnel convergence. part I and II, *Int. J. Rock Mech. Min. Sci. & Geomech. Abstr.*, 28, 409-475.

Pande, G. N., Beer, G. and Williams, J.R. 1990. *Numerical Methods in Rock Mechanics*, John Wiley & Sons Ltd.

Papanastasiou, P. C. and Vardoulakis, I. 1992. Numerical treatment of progressive localization in relation to borehole stability. *Int. J. Numerical and Analytical Methods in Geomechanics*, 16, 389-424.

Park, D.W. and Ash, N.F. 1985. Stability analysis of entries in a deep coal mine using finite element method, *Mining Sci. & Tech.*, 3, 11-20.

Passaris, E.K.S. 1977. The effect of directional aeolotropy on the mechanical behavior of rocksalt. *Proceedings*, Conference on Rock Engineering, British Geot. Soc & Dept of Mining Engineering, Newcastle Upon Tyne, U.K. 11-31.

Passaris, E.K.S. 1979. The rheological behavior of rocksalt as determined in an in situ pressurized test cavity. *Proceedings*, 4th Int. Cong. on Rock Mechanics, 1, A.A. Balkema, Rotterdam, 257-264.

Pietruszczak, S. and Mroz, Z. 1980. Numerical analysis of elastic-plastic compression of pillar accounting for material hardening and softening. *Int. J. Rock Mech. Min. Sci.*

& *Geomech. Abstr.* 17, 199-207.

Pietruszczak, S. and Mroz, Z. 1981. Finite element analysis of deformations of strain softening materials. *Int. J. Num. Anal. Meth. in Geom.*, 7.

Prevost, J. 1984. Localization of deformation in elastic-plastic solids. *Int. J. Numer. Anal. Meth. Geomech.*, 8, 187-196.

Prugger, F. F. & Prugger, A. F. 1991. Water problems in Saskatchewan potash mining - what can be learned from them? *CIM Bulletin*, 84, 58-66.

Pushkarev, V.I. and Afanesev, B.G. 1973. A rapid method of determining the long-term strength of weak rocks. *Soviet Mining Science*, 9, 558-560.

Ramsay, J.G. 1967. *Folding and Fracturing of Rocks*. McGraw-Hill, New York.

Ramsay, J.G. 1983. *The Techniques of Modern Structural Geology*. v 1: Strain Analysis, pp 73, Academic Press, London.

Rice, J.R. 1976. The localization of plastic deformation. *Theoretical and Applied Mechanics*, ed. by W.T. Koiter, North-Holland Publishing Company, 207-220.

Richardson, L.F. 1910. The approximate arithmetical solution by finite differences of physical problems involving differential equations with an application to the stresses in a masonry dam. *Trans. Roy. Soc. A*, 210, 307-357.

Roegiers, J.C. 1990. Lecture: stability and failure of circular openings. *Rock at Great Depth*, 1, Maury & Fourmaintraux (eds), Balkema, Rotterdam. 1115-1122.

Rousset, G., Bazargan - Sabet, B. and Lenain, R. 1989. Time - dependent behavior of rocks: laboratory tests on hollow cylinder. *Rock Mechanics as a Guide for Efficient Utilization of Natural Resources: Proc, 30th U.S. Symposium, Morgantown, 19-22 June*, Publ. Rotterdam: A. A. Balkema 385-391.

Rudnicki, J.W. and Rice, J.R. 1975. Conditions for the localization of deformation in pressure-sensitive dilatant materials. *J. Mech. Phys. Solids*, 23, 371-394.

Russel, J.E. and Lomenick, T.F. 1984. Analysis of long-term creep tests on model pillars. *Proceedings, 1st Conf. on the Mechanical Properties of Salt*, Pennsylvania State University, Nov., Trans Tech Publications, Clausthal, Germany.

Saint-Venant, B. 1864. *Notes to Navier's Resume des Lecons Dela Resistance des Corps Solides*. 3rd Ed., Paris, 175 p.

Sakurai, S. and Tanigawa, M. 1989. Back analysis of deformation measurements in a large underground cavern considering the influence of discontinuity of rocks. *Doboku Gakkai Rombun-Hokokushu/Proceedings*, Japan Society of Civil Engineers, 75-84. (in Japanese)

Salamon, M.D.G. 1967. A method of designing room and pillar workings. *Jl S. Afr. Inst. Min. Metall.*, **68**, 68-78.

Santarelli, F.J. and Brown, E.T. 1987. Performance of deep wellbores in rock with a confining pressure-dependent elastic modulus. *Proc.*, 6th ISRM Cong., Montreal, 1217-1223.

Senseny, P.E. 1984. Specimen size and history effects on creep of salt. *Proceedings*, First Conference on the Mechanical Behavior of Salt, Pennsylvania State University, November, Trans Tech Publications, Clausthal, Germany, 369-379.

Senseny, P.E. 1988. Creep properties of four salt rocks. *Proceedings*, Second Conference on the Mechanical Behavior of Salt, Hardy and Langer (eds), Trans Tech Publications, Clausthal, Germany, 431-444.

Senseny, P.E., Hansen, F.D., Russell, J.E., Carter, N.L. and Handin, J.W. 1992. Mechanical behavior of rock salt: phenomenology and micromechanisms. *Int. J. Rock Mech. Min. Sci. & Geomech. Abstr.*, **29**, 363-378.

Sepehr, K. 1988. Non-linear and time-dependent finite element modelling of underground excavations with special reference to induced seismicity in potash mining. *Ph.D Thesis*, Department of Civil Engineering, University of Manitoba, Winnipeg, Manitoba.

Sepehr, K. and Stimpson, B. 1988a. Induced seismicity in potash mining - a finite element study. *International Journal of Mining and Geological Engineering*, **6**, 27-40.

Sepehr, K. and Stimpson, B. 1988b. Roof deflections and sag in jointed horizontally bedded strata - a numerical study. *Rock Mechanics and Rock Engineering*, **21**, 207-218.

Serata, S. 1968. Application of continuum mechanics to design of deep potash mines in Canada. *Int. J. Rock Mech. Min. Sci.*, **5**, 293-314.

Serata, S., Sakurai, S. and Adachi, T. 1972. Theory of aggregate rock behavior based on absolute three-dimensional testing (ATT) of rock salt. *Basic and Applied Rock Mechanics*, Edited by K.E. Gray. The Amer. Inst. Mining, Metallurgical and Petroleum Engineers Inc. New York, 431-473.

Serata, S. and Cundey, T.E. 1978. Rheological method of salt cavity design for underground storage of solid, liquid and gaseous matters. *Proceedings*, 19th Symp. on

Rock Mechanics, Reno, Nevada, 187-192.

Serata, S. 1983. Stress control methods: quantitative approach to stabilizing mine openings in weak ground. *Stability in Underground Mining*, C. Brawner (ed.), 52-98.

Sharan, S.K. 1989. Finite element analysis of underground openings. *International Journal for Numerical and Analytical Methods in Geomechanics*, **13**, 565-570.

Shi, G.C. 1973. Some basic problems in fracture mechanics and new concepts. *Eng. Fract. Mech.*, **5**, 365-377.

Shuttle, D.A. and Smith, I.M. 1988. Numerical simulation of shear band formation in soils, *Int. J. Numer. Anal. Meth. Geomech.*, **12**, 611-626.

Simkin, A. and Robin, G. 1973. The mechanical testing of bone in bending. *Journal of Biomechanics*, **6**, 31-39.

Singh, J.G. and Upadhyay, P.C. 1986. Bending of thick rock slabs. *Mining Science and Technology*, **3**, 255-265.

Sobotkal, Z. 1985. Rheology of Materials and Engineering Structures.

Srinivasan, R.S. and Ramachandra, L.S. 1989. Axisymmetric buckling and post-buckling of bimodulus annular plates. *Engineering Structures*, **11**, 195-198.

Starfield, A.M. and Cundall, P.A. 1988. Towards a methodology for rock mechanics modelling. *Int. J. Rock Mech. Min. Sci. & Geomech. Abstr.* **25**, 99-106.

Stimpson, B. and Ahmed, M. 1992. Fracture of a linear Voussoir arch: a laboratory and numerical study. *Canadian Geotechnical Journal*, **29**, 188-194.

Stimpson, B. and Chen, Rui, 1993. Measurement of rock elastic moduli in tension and in compression and its practical significance. *Canadian Geotechnical Journal* (accepted, will appear in April, 1993).

Sundaram, R.N. and Corrales, J.M. 1980. Brazilian tensile strength of rocks with different elastic properties in tension and compression, Technical Note. *Int. J. Rock Mech. Min. Sic & Geomech. Abstr*, **17**, 131-133.

Thomas, T.Y. 1961. *Plastic Flow and Fracture in Solids*, Academic Press.

Tsang, P. Peng, S. S. and Hsiung, S. M. 1989. Yielding pillar application under strong roof and strong floor conditions - a case study. *Rock Mechanics as a Guide for Efficient*

Utilization of Natural Resource: *Proceedings*, 30th U.S. Symposium, Morgantown, 19-22 June, Publ. Rotterdam: A. A. Balkema, 411-418.

Van Sambeek, L., Fossum, A., Callahan, G. and Ratigan, J. 1992. Salt mechanics: empirical and theoretical developments. *Proceedings*, 7th International Symposium on Salt, Kyoto, Japan April 6-9.

Van Sambeek, L. 1992. Testing and modeling of backfill used in salt and potash mines. *Proceeding*, International Symposium on Rock Support, 16-19 June, Sudbury, Canada, 583-589.

Vardoulakis, I. 1980. Shear band inclination and shear modulus of sand in biaxial tests. *Int. J. Num. Anal. Meths. Geomech.* **4**, 103-119.

Vardoulakis, I. 1981. Bifurcation analysis of the plane rectilinear deformations in dry sand. *Int. J. Solid Struct.* **17**, 1085-1111.

Vardoulakis, I., 1984, Rock bursting as a surface instability phenomenon, *Int. J. Rock Mech Min. Sci. Geomech. Abstr.* **21**, 137-144.

Vardoulakis, I., Goldscheider, M. and Gudehus, G. 1978. Formation of shear bands in sand bodies as a bifurcation problem. *Int. J. Num. Anal. Meths Geomech.*, **2**, 99-128.

Vermeer, P.A. 1982. A simple shear-band analysis using compliances. *Proceedings*, IUTAM Sump. Deformation and Failure of Granular Materials (Eds. P.A. Vermeer and H. J. Luger), Balkema Publ., Rotterdam, 493-499.

Verral, R.A., Fields, R.J. and Ashby, M.F. 1977. Deformation mechanism maps for LiF and NaCl. *J. Amer. Ceramic Soc.*, **60**, 211 p.

Vutukuri, V. S., Lama, R. D. and Saluja, S. S. 1974. *Handbook on Mechanical Properties of Rock: testing techniques and results*, Trans. Tech. Pub. Vol. I, 87-140.

Wawersik, W.R. 1968. Detailed analysis of rock failure in laboratory compression tests. *Ph. D. thesis*, University of Minnesota.

Wawersik, W.R. and Hannum, D.W. 1980. Mechanical behavior of New Mexico rock salt in triaxial compression up to 200 c. *Journal of Geophysical Research*, **85**, 891-900.

Wawersik, W.R., Herrmann, W., Montgomery, S.T. and Lauson, H.S. 1982. Excavation design in rock salt - laboratory experiments. *Proceedings*, Int. Symp. Rock Mechanics Related to Caverns and Pressure Shafts, Aachen, Balkema, Rotterdam.

Wawersik, W.R. and Preece, D.S. 1984. Creep testing of salt. *Proceedings*, First Conf.

- on the Mechanical Behavior of Salt. Trans Tech Publ., Clausthal-Zellerfeld, 421-449.
- Wawersik, W.R and Zeuch, D.H. 1986. Modelling and mechanistic interpretation of creep of rock salt below 200°C. *Tectonophysics*, 121, 125-152.
- Wawersik, W.R. 1988. Alternatives to a power-law creep model for rock salt at temperatures below 160°C, in The Mechanical Behavior of Salt. *Proceedings*, Second Conference, edited by Hardy and Langer, Hanover, Federal Republic of Germany, Trans Tech Publications, Clausthal, Federal Republic of Germany, 103-128.
- Williams, J.R. 1988. Contact analysis of large numbers of interacting bodies using discrete modal methods for simulating material failure on the microscopic scale. *Eng. Comput.*, 5, 198-209.
- Wilson, E.B. 1988. The tensile behavior of locked oil sands from the McMurray Formation. *M.Sc. thesis*, Department of Mechanical Engineering, University of Manitoba.
- Winkel, B.V., Gerstle, K.H. and Ko, H.Y. 1972. Analysis of time-dependent deformations of openings in salt media. *Int. J. Rock Mech. Min. Sci.*, 9, 249-260.
- Worsley, N. and Fuzesy, A. 1979. The potash-bearing members of the Devonian Prairie Evaporite of southeastern Saskatchewan, south of the mining area. *Economic Geology*, 74, 377-388.
- Xiong, L. and Hunsche, U. 1988. Creep behavior of salt under true triaxial stress. *Proceedings*, Second Conference on the Mechanical Behavior of Salt, Hardy and Langer edited, Trans Tech Publications, 235-243.
- Yu, Y.S., Ong, C.G. and Mottahed, P., 1988, Viscoelastic finite element analysis in design of potash mines. *Eng. Comput.*, 5,
- Yuan, Y.G. and Lajtai, E.Z. 1991. Numerical modeling of mining-induced fracture propagation. Fracture in Potash. *Report*, Department of Geological Engineering, University of Manitoba.
- Zienkiewicz, O.C. 1992. Computational mechanics today. *International Journal for Numerical Methods in Engineering*, 34, 9-33.